PROGRAMA DE DOCTORADO EN TECNOLOGÍAS DE LA INFORMACIÓN Y LAS COMUNICACIONES

TESIS DOCTORAL

DESARROLLO DE FILTROS DE MICROONDAS BASADOS EN CAVIDADES RESONANTES PARA LA DETECCIÓN DE AXIONES

Presentada por Jose María García Barceló para optar al grado de Doctor
por la Universidad Politécnica de Cartagena

Dirigida por:
Dr. Antonio José Lozano Guerrero

Codirigida por:
Dr. Alejandro Álvarez Melcón
Dr. Benito Gimeno Martínez

Cartagena, 2023

DOCTORAL PROGRAMME IN INFORMATION AND COMMUNICATION TECHNOLOGIES

PhD THESIS

DEVELOPMENT OF RESONANT CAVITY-BASED MICROWAVE FILTERS FOR AXION DETECTION

Presented by Jose María García Barceló
to the Technical University of Cartagena in fulfilment of
the thesis requirement for the award of PhD

Supervisor:
Dr. Antonio José Lozano Guerrero

Co-supervisors:
Dr. Alejandro Álvarez Melcón
Dr. Benito Gimeno Martínez

Cartagena, 2023

CONTENTS

LIST OF FIGURES

LIST OF TABLES

RESUMEN

Esta tesis doctoral aborda varias investigaciones para la detección de axiones y para la mejora de comunicaciones satelitales mediante el uso de cavidades resonantes en tecnología guía de onda. El axión es una partícula hipotética teorizada para resolver el problema CP fuerte (Charge conjugation Parity symmetry) en la cromodinámica cuántica (QCD) y que, de existir, podría ser componente de la materia oscura. En esta línea, el desarrollo de detectores axiónicos de materia oscura, comúnmente denominados haloscopios, se ha encontrado en auge en los últimos 20 años. En este trabajo se han desarrollado diversos métodos para la mejora de estos haloscopios empleando estructuras basadas en subcavidades conectadas por irises. Por otro lado, es bien sabido que el espectro electromagnético en las comunicaciones por satélite se encuentra saturado debido a la alta demanda de radiocomunicaciones hoy en día. Además, el coste de puesta en órbita de un satélite crece exponencialmente con el peso abordo de éste, cuya reducción será clave en cualquier programa espacial. Así, en esta tesis se abordan diversos diseños de filtros paso banda en guía de onda para la optimización del peso, volumen y huella abordo de los futuros satélites de comunicaciones.

El espectro frecuencial barrido por la comunidad axiónica en busca de la ansiada partícula (el axión) es cada día mayor y hace que exista una alta competencia para participar en esta búsqueda con detectores de altas prestaciones. Además, las condiciones extremas a las que debe ser sometido un detector de axiones de materia oscura para que se cumplan las condiciones de detección (temperaturas criogénicas, campo magnetoestático alto, etc.) complican aún más esta tarea. Algunos de los parámetros que rigen el rendimiento de un haloscopio basado en cavidades resonantes son su volumen, factor de calidad y factor de forma. Durante la elaboración de este trabajo se han diseñado, fabricado y caracterizado diversas topologías novedosas para la creación de estos detectores, optimizando los tres parámetros mencionados, consiguiendo resultados satisfactorios. Esta tesis doctoral ha sido realizada en el marco de trabajo del grupo axiónico RADES (Relic Axion Detector Exploratory System). Se han llevado a cabo tareas de investigación para la mejora del factor de calidad en estructuras fabricadas en las primeras etapas por este grupo experimental mediante la aplicación de diversos tratamientos, como la aplicación de soldaduras.

Además de la optimización de los parámetros en haloscopios, estos necesitarán escanear un espectro de frecuencias, como se ha mencionado anteriormente, para lo cual se deberá implementar sistemas de sintonía que permita el cambio de frecuencia de resonancia y otros sistemas para el ajuste del acoplamiento de entrada / salida del sistema (otro de los parámetros críticos del detector). Existen dos tipos de sintonía frecuencial, mecánica y electrónica. Para los sistemas de sintonía mecánicos, se han realizado estudios del

comportamiento de los prototipos fabricados cuando estos se abren mediante un corte vertical, lo cual cambiará su frecuencia de búsqueda del axión. Por otro lado, para los sistemas de sintonía electrónicos se han desarrollado diversos diseños para la introducción de materiales ferromagnéticos y ferroeléctricos, que cambiarán la frecuencia de operación mediante el cambio de permeabilidad y permitividad del medio, respectivamente, aplicando un cambio de voltaje o temperatura. Se ha hecho un estudio mucho más extenso para estos últimos. Los sistemas electrónicos permiten evitar ciertos problemas que ocurren en los de tipo mecánico, como pueden ser fallos de movimiento a temperaturas criogénicas o la falta de escalabilidad. Para los elementos ferroeléctricos, se ha llegado a un diseño novedoso que ha aportado gran valor a la comunidad científica para la aplicación de este tipo de materiales en cualquier haloscopio. Además, se han desarrollado sistemas de acoplamiento entre subcavidades con láminas ferroeléctricas, evitando la fabricación de irises, los cuales pueden dar problemas en ciertos sistemas. Para los sistemas de ajuste de acoplamiento de entrada / salida, se ha desarrollado un prototipo preliminar que ha aportado buenos resultados experimentales. Asimismo, se han llevado a cabo otras tareas de investigación para el desarrollo de otras técnicas de mejora de haloscopios. Una de ellas es la del rechazo de resonancias no deseados cerca del modo axiónico por medio de la combinación de varios puertos coaxiales con el método phase-matching, para el cual se han realizado diversas simulaciones y fabricaciones, extrayendo resultados positivos que hacen viable dicho método. Otros estudios secundarios han sido los de la implementación de QuBits para reducir la temperatura del sistema (parámetro clave para el rendimiento), el uso de elementos HTS (High Temperature Superconductor) para aumentar el factor de calidad, el diseño de haloscopios a frecuencias en las bandas UHF y W, y el análisis electromagnético del acoplamiento axion-photon en haloscopios mediante el método BI-RME (Boundary Integral-Resonant Mode Expasion) 3D.

Finalmente, como spin-off del desarrollo de haloscopios, se han realizado diversos estudios para el diseño, fabricación, caracterización y mejora de filtros paso banda para comunicaciones satelitales empleando la misma tecnología (cavidades resonantes acopladas por irises en guía de onda). Se ha han desarrollado varios filtros evanescentes basados en impresión 3D o fabricación aditiva de bajo coste, y mecanizado CNC (Computer Numerical Control). A estos filtros se les ha aplicado un sistema de sintonía de tornillos que ha permitido la mejora de la respuesta eléctrica de filtrado. Por otro lado, se ha llevado a cabo el diseño de un filtro asimétrico doblado horizontalmente para la implementación de ceros de transmisión, consiguiente un alto rechazo fuera de la banda de paso. Estos filtros son gran valor para la comunidad científica ya que permiten avanzar en el estado del arte de filtros con altas prestaciones (bajo peso, volumen y huella) para comunicaciones satelitales.

- Palabras clave: axiones; detectores de materia oscura; haloscopios; interacción axion-photon; cavidades resonantes; ferroeléctricos; sintonización; acoplamientos; filtros paso banda; filtros de microondas; filtros resonadores; filtros de guía de onda; ceros de transmisión; guía de ondas de modo evanescente; impresión 3D.

ABSTRACT

This PhD thesis addresses several investigations for the detection of axions and for the improvement of satellite communications using resonant cavities in waveguide technology. The axion is a hypothetical particle theorized that could explain the strong CP problem (Charge conjugation Parity symmetry) in quantum chromodynamics (QCD) and which, if it exists, could be a component of dark matter. In this line, the development of axion dark matter detectors, commonly called haloscopes, has been booming in the last 20 years. In this work, several methods have been developed for the improvement of these haloscopes using structures based on subcavities coupled by irises. On the other hand, it is well known that the electromagnetic spectrum in satellite communications is saturated due to the high demand for radio communication systems. In addition, the cost of putting a satellite into orbit grows exponentially with the weight on board, the reduction of which will be key in any space program. Thus, this PhD thesis deals with different waveguide bandpass filter designs for optimizing the weight, volume, and on-board footprint of future communication satellites.

The frequency spectrum swept by the axion community in search of the coveted particle is increasing day by day, which means that there is a high level of competition to develop high-performance detectors. In addition, the extreme conditions to which a dark matter axion detector must be subjected in order to meet the detection conditions (cryogenic temperatures, high magnetostatic field, etc.) further complicate this task. Some of the parameters that govern the performance of a haloscope based on resonant cavities are its volume, quality factor and form factor. During the development of this work, several novel topologies have been designed, manufactured, and characterized for the creation of these detectors, optimizing the three above-mentioned parameters, achieving satisfactory results. This PhD thesis has been carried out within the framework of the RADES (Relic Axion Detector Exploratory System) axion group. Research work has been carried out to improve the quality factor in structures manufactured in the first stages of this experimental group through the application of various treatments, such as soldering.

In addition, as the axion mass is unknown, it is important to scan in frequency to search for the axion over a range as large as possible, as mentioned above, for which tuning systems must be implemented to allow resonant frequency shift and other arrangements for adjusting the input / output coupling of the system (another key haloscope parameter). There are two types of frequency tuning, mechanical and electronic. For mechanical tuning systems, studies have been carried out on the behaviour of the fabricated prototypes when they are opened by a vertical cut, which will change their axion search frequency. On the other hand, for electronic tuning systems, various designs

have been developed for the introduction of ferromagnetic and ferroelectric materials, which will change the operating frequency by changing the permeability and permittivity of the medium, respectively, by applying a change of voltage or temperature. A much more extensive study has been made for the use of ferroelectric tuning systems. Electronic systems avoid certain problems that occur in mechanical systems, such as motion failure at cryogenic temperatures or lack of scalability. For ferroelectric elements, a novel design has been achieved which has brought great value to the scientific community for the application of this type of material in any haloscope. Also, coupling systems have been developed between subcavities with ferroelectric films, avoiding the need to manufacture irises, which can cause problems in certain systems. For the input / output coupling adjustment systems, a preliminary prototype has been developed which has provided good experimental results. Other research works have also been carried out on the development of other haloscope enhancement techniques. One of them is the rejection of unwanted resonances near the axion mode by means of the combination of several coaxial ports with the phase-matching method, for which several simulations and fabrications have been carried out, obtaining positive results that make this method feasible. Other secondary studies have been the implementation of QuBit devices to reduce the system temperature (another key parameter for haloscope performance), the use of HTS (High Temperature Superconductor) elements to increase the quality factor, the haloscope design at frequencies in the UHF and W bands, and the electromagnetic analysis of axion-photon coupling in haloscopes using the BI-RME (Boundary Integral-Resonant Mode Expansion) 3D method.

Finally, as a spin-off from the development of haloscopes, several studies have been carried out for the design, manufacture, characterization, and improvement of bandpass filters for satellite communications using the same technology (resonant cavities coupled by irises in waveguide). Several evanescent filters based on 3D printing or low-cost additive manufacturing and CNC (Computer Numerical Control) machining have been developed. A screw tuning system has been applied to these filters to improve the electrical filtering response. On the other hand, the design of a horizontally folded asymmetric filter for the implementation of transmission zeros, to increase the rejection capabilities of the filter, has been carried out. These filters could be of great value to the scientific community as they allow to advance in the state of the art of high-performance filters (low weight, volume, and footprint) for satellite communications.

- Keywords: axions; dark matter detectors; haloscopes; axion-photon interaction; resonant cavities; ferroelectrics; tuning; couplings; bandpass filters; microwave filters; resonator filters; waveguide filters; transmission zeros; evanescent mode waveguide; 3D-printing.

ACKNOWLEDGMENTS

Me gustaría agradecer a todas las personas que han hecho posible la realización de esta tesis doctoral. En primer lugar, a mis directores, los profesores Dr. Antonio José Lozano Guerrero, Dr. Alejandro Álvarez Melcón, y Dr. Benito Gimeno. Antonio, muchas gracias por tu apoyo diario e incondicional durante todos estos años. Tú más que nadie sabes todas las vicisitudes por las que he pasado durante la realización de esta tesis doctoral, y tu constante fe y soporte han hecho posible que haya llegado a este punto de mi carrera investigadora. Alejandro, por ser mi persona de referencia en la ciencia e investigación desde el primer día que decidí embarcarme en este, aunque vertiginoso, maravilloso mundo. Tus innumerables consejos y empatía han hecho que mi rumbo nunca se desvíe. Benito, por todas tus recomendaciones y por ser una persona tan cercana. Tu experiencia en el mundo de la Física ha hecho que mi interés por esta rama de la ciencia aumente aún más.

Mencionar también a mis compañeros doctorandos a lo largo de mis estudios de doctorado en Cartagena: Gabi, Alejandro P., Antonio R., Pablo N., Joserra, Rafa, Clara, Celia, Miguel, Antonio O., etc. Gracias a todos vosotros por los buenos momentos y hacer un entorno de trabajo más amigable.

También a mis compañeros de investigación seniors en Cartagena: Prof. Dr. Alejandro D. por confiar en mí para la realización de este proyecto. Tu gran capacidad de organización y liderazgo ha hecho que este trabajo pueda ser llevado a cabo mucho más eficientemente. Prof. Dr. Juan M., por tu amplia experiencia en la investigación, que me ha servido para guiarme en muchos aspectos del doctorado. Prof. Dr. Fernando Q., por tus consejos y los buenos momentos que hemos pasado junto a Alejandro A. en las reuniones. Al técnico D. Juan Albaladejo, que me ha echado un mano en la fabricación de multitud de estructuras que han servido para avanzar en la investigación de este trabajo.

On the other hand, I would like to express my deepest gratitude to all the collaborators of the RADES team (Igor, Babette, Juan Daniel, etc.). I must also say that it has been an honour to meet all my colleagues from this group at CERN (Geneva, Switzerland), where I did 3 research stays: Sergio, Babette, Walter, Jessica, Chloe, etc. Thank you very much to all of you for making life abroad more bearable and for your great empathy. I have felt at home during my stays there. I want to emphasize that I will be eternally grateful to Dr. Walter W., who has given me hundreds of tips regarding the world of radiofrequency; your knowledge should be framed in a museum. I would also like to mention my deepest gratitude for the hospitality offered by Dr. Babette D., who from the first day I arrived in

Geneva was supporting me as one of the team.

Por supuesto, agradecer a toda mi familia. En primer lugar, a mis padres. Gracias, mamá, Maria Victoria. Ni todos los trabajos de doctorado del mundo podrían describir lo que siento por ti y lo agradecido que estaré toda mi vida por tu ayuda. Gracias, papá, Jose María. Por tu cariño, apoyo, e incontables consejos cuando más los necesitaba. Agradecer también a mi hermana Maria Victoria, a mi sobrina Adriana, a mi abuelita Loli, a mi Titi, a Javi, a mis primos Angelito y María, a mis tías Mari Paz y Cloti, a mis abuelos Ángel, Jose María y Carmen, a quienes siempre tendré presentes en mi corazón, y a toda mi familia en general. Mucha gracias por vuestro cariño.

Agradecer también a todos mis amigos, los más y menos cercanos. Siempre os tendré en el corazón, acabemos donde acabemos trabajando cada uno de nosotros. Y gracias a ti, Dr. Carlos J., por animarme a hacer el doctorado.

Y a Lucía, mi amor, mi cielo. Eres una referencia para mí en la vida. Soy la persona más afortunada del mundo por tenerte a mi lado. Gracias por ser la persona más dulce del planeta Tierra. Tu cariño y tus palabras día a día han hecho que esta tesis doctoral navegue a velocidad de crucero. No siento más que orgullo hacia ti por donde has llegado en tu vida profesional. Eres una científica excepcional y tengo claro que vas a llegar a donde te propongas en la vida.

DEDICATION

*"There is a driving force stronger than steam,
electricity and atomic energy: the willpower.
- Albert Einstein*

To my grandfather Ángel

ACRONYMS

P   Parity

CP   Charge conjugation times Parity

CDM   Cold Dark Matter

WIMPs   Weakly Interacting Massive Particles

LSW   Light Shining through Walls

BNL   Brookhaven National Laboratory

CAST   CERN Axion Solar Telescope

IAXO   International AXion Observatory

RADES   Relic Axion Detector Exploratory Setup

CERN   Conseil Européen pour la Recherche Nucléaire

ADMX   Axion Dark Matter eXperiment

KSVZ   Kim-Shifman-Vainshtein-Zakharov

DFSZ   Dine-Fischler-Srednicki-Zhitnitsky

KLASH   KLoe magnet for Axion SearcH

HAYSTAC Haloscope At Yale Sensitive To Axion Cdm

ORGAN   Oscillating Resonant Group AxioN

QUAX   QUaerere AXions

CAPP   Center for Axion and Precision Physics

HTS   High Temperature Superconductors

BI-RME   Boundary Integral-Resonant Mode Expansion

RF   RadioFrequency

SM   Standard Model

EM   ElectroMagnetic

NASA   National Aeronautics and Space Administration

ALP   Axion-Like Particles

QCD   Quantum ChromoDynamics

PQ   Peccei and Quinn

DAQ   Data Acquisition System

FFT   Fast Fourier Transform

LNA   Low Noise Amplifier

LHC   Large Hadron Collider

SMA   SubMiniature version A

VNA   Vector Network Analyzer

R&D   Research and Development

SAW   Surface Acoustic Wave

IL   Insertion Loss

CAD   Computer-Aided Design

MEMS   MicroElectroMechanical Systems

AM   Additive Manufacturing

GPS   Global Positioning System

GLONASS   GLObal NAvigation Satellite System

VSAT   Very Small Aperture Terminal

UPCT   Universidad Politécnica de Cartagena

UPV   Universidad Politécnica de Valencia

APM   Alta Precisión del Mecanizado S.L.

EDM   Electrical Discharge Machining

IBS   Institute for Basic Science

DC   Direct Current

BST   Barium Strontium Titanate or $Ba_xSr_{1-x}TiO_3$

STO   Strontium Titanate or $SrTiO_3$

KTO   Potassium Tantalate or $KTaO_3$

YIG   Yttrium Iron Garnet

PMMA   PolyMethyl MethAcrylate

CTO   Calcium Titanate or $CaTiO_3$

MoM   Method of Moments

YBCO   Yttrium Barium Copper Oxide

GND   GrouND

CNC   Computer Numerical Control

FDM   Fused Deposition Modeling

SLA   StereoLithogrAphy

SIW   Substrate Integrated Waveguide

RL   Return Loss

SFR   Spurious Free Range

1

INTRODUCTION

1.1 STATE OF THE ART

Both particle physics and cosmology are very interested in the discovery of the axion. The axion is a hypothetical pseudoscalar particle [1, 2] that was first proposed to clarify why the strong interactions preserve Parity (P) and Charge conjugation times Parity (CP) [3]. A parity transformation (also known as a parity inversion) in physics is the flipping of the sign of one spatial coordinate. On the other hand, charge conjugation is a transformation that replaces all particles with their corresponding antiparticles, altering the sign of all charges: not just electric charges, but also charges relevant to other forces. The term CP then refers to the combination of charge conjugation symmetry and parity symmetry. In the case of the axion, this particle would be a candidate for Cold Dark Matter (CDM) if its mass were in the range of $1 - 1000$ μeV [4]. The axion is now the most plausible candidate for the composition of CDM, and this has led to a profusion of searches throughout the globe. This is due to recent reductions in the accessible parameter space for the Weakly Interacting Massive Particles (WIMPs), which are hypothetical particles candidates to be dark matter. There is no official definition a WIMPs particle, but in general, it is a new elementary particle that interacts with gravity and any other force (or forces) that may or may not be part of the Standard Model (SM) [5].

Axions are believed to have a weak electromagnetic (photons) and Dirac fermionic (nucleons, electrons, ...) coupling in addition to their gravitational interaction with baryonic matter. In this PhD thesis, efforts are concentrated on the axion coupling into two photons provided by the Lagrangian density

$$\mathcal{L}_{a\gamma\gamma} \propto g_{a\gamma} a \vec{E} \cdot \vec{B}_e, \tag{1.1}$$

where $g_{a\gamma}$ is the axion-photon coupling coefficient, a the axion field, $\vec{E}$ the electric field generated by the axion, and $\vec{B}_e$ the external magnetic field (magnetic flux density).

It has become clear that the axion detection is quite difficult. In the past, it was believed that CDM axions were invisible to all detection methods due to their extremely weak interactions with matter and radiation and lifetimes that are far larger than the duration of the universe [5]. However, the pursuit of axion-photon coupling has evolved over the last thirty years, with three distinct detection approaches used depending on the origins

of these particles and their estimated masses. Sikivie [6] suggested two of them in the mid-1980s, axion helioscopes and haloscopes based on the inverse Primakoff effect [7]. The other, the Light Shining through Walls (LSW) experiment [8–10], is based on both direct and inverse Primakoff effects. Helioscopes and haloscopes detect axions from natural sources (such as the sun and relic axions, respectively, being the latter the axions that originated in the early era of the universe and lying nowadays in the galaxies), whereas LSW produces axions on its own in the laboratory.

An optical barrier separates two Fabry-Perot cavities in the LSW experiment. The first cavity generates axions, which are detected in the second cavity. The axion-photon coupling is used for both creation and detection [9].

Experiments with helioscopes hunt for axions created by the inverse Primakoff effect in the inner layers of the Sun from plasma photons. Following preliminary experiments at the Brookhaven National Laboratory (BNL) in 1992 [11] and in the SUMICO experiment in Japan [12–14], the third generation CERN Axion Solar Telescope (CAST) experiment achieved the best results in this type of detection to date, with limits for axion-photon coupling of $< 6.6 \times 10^{-11}$ GeV^{-1} in the mass range < 0.02 eV [15], and $< 2.3 \times 10^{-10}$ GeV^{-1} for 0.02 eV $< m_a < 0.64$ eV [16]. The International AXion Observatory (IAXO) experiment will be the start of the future of solar axion research [17].

An axion haloscope detector converts axions to photons via the inverse Primakoff effect in a microwave cavity immersed in a high static magnetic field. The Relic Axion Detector Exploratory Setup (RADES) collaboration began in 2016, bringing together research groups from Spanish universities and research organisations as well as Conseil Européen pour la Recherche Nucléaire (CERN) researchers. The reference [18] includes a full state of the art report on the many axion detection experiments that have been completed or are in the process of being developed and executed. Secondly, the references [19–21] provide updated and comprehensive evaluations. The goal of the RADES teamwork is to find the axion in our galactic halo, which is a candidate for forming dark matter [22, 23]. As a result, the experiment should obviously be based on a haloscope configuration. The main goal of haloscope studies is to discover axions in the galactic halo by encouraging axion-photon conversion in the presence of a strong magnetostatic field. When this conversion happens in a resonant device, such as a microwave resonant cavity, the strength of the electromagnetic field is increased. Furthermore, because of the predicted extremely low axion-photon coupling and therefore the electromagnetic power to be detected, it is necessary to work under cryogenic limits to decrease the thermal noise and thus boost the signal to noise ratio (S/N).

The Axion Dark Matter eXperiment (ADMX) team had already finished the exploration successfully in the $1.9 - 3.65$ eV mass range ($460 - 890$ MHz) at the beginning of the RADES group, with exclusion limits attaining those of the Kim-Shifman-Vainshtein-

Zakharov (KSVZ) model [24]. It profited from the knowledge gained from two novel experiments at BNL [25] and the University of Florida [26]. The prospects of the advanced prototype (ADMX-Gen2) have the potential to achieve the Dine-Fischler-Srednicki-Zhitnitsky (DFSZ) model in the $1.4 - 25$ eV axion mass range [24].

Since the beginning of the RADES collaboration [27], there has been a significant increase in research with cavity haloscopes with many new resonant cavity ideas, such as the KLoe magnet for Axion SearcH (KLASH) project [28] at lower axion masses than ADMX, and the teams Haloscope At Yale Sensitive To Axion Cdm (HAYSTAC) [29], Oscillating Resonant Group AxioN (ORGAN) [30], QUaerere AXions (QUAX) [31] and Center for Axion and Precision Physics (CAPP) [32].

1.2 OBJECTIVES

The main goal of this PhD thesis is to evolve the RADES haloscope structures to be more competitive in the axion community. For this purpose, several prototypes have been studied, designed, and manufactured for testing novel concepts. In order to develop the haloscope design theory, an exhaustive investigation has been carried out to find the boundaries in the improvements of the key haloscope parameters: volume, quality factor and form factor. This study tries to serve as a guide to improve the design of a haloscope cavity at any searching frequency. In addition, several prototypes have been produced for the validation of the theoretical results. On the other hand, in order to gain more experience in the field of multicavity design and fabrication for axion search purposes, another goal of this PhD thesis is the testing and implementation of various treatments on the first structures of the RADES group.

In addition, the development of an input / output coupling readjustment system and an electronic frequency tuning system using ferromagnetic materials has also been pursued. Another major objective of this work has been the design of an electronic tuning system based on ferroelectric materials. Also, this technology has been employed for the improvement of the interresonator irises needed in multicavity haloscopes.

On the other hand, as a minor target in the PhD thesis more investigations for enhancing other concepts in the RADES group have been carried out. Several studies (including experimental results) have been conducted for the development of a technique that rejects unwanted modes by the use of the phase-matching method, combining ports in a single haloscope. This group has focused until two years ago on the search for axions at X-band frequencies. Recently, however, new prototypes have been developed working at lower (UHF-band) and higher (W-band) frequencies to cover other frequency spectral ranges. In addition, other improvements in the haloscope experiment design have been realized: High Temperature Superconductors (HTS) structures (to enhance the quality factor of the resonances) and QuBit systems (to improve the thermal noise decreasing the cryogenic

temperature limit). Also, an efficient full-wave modal technique has been studied for the analysis of the electromagnetic coupling axion-photon in a haloscope cavity due to an axion field: the Boundary Integral-Resonant Mode Expansion (BI-RME) 3D method.

Finally, a spin-off from the multicavity haloscope designs has emerged. These structures based on several cavities interconnected by window irises are very commonly employed in RadioFrequency (RF) bandpass filters for satellite applications. The development of several of these filters was another important goal in this PhD thesis which has been carried out along with manufacturing and testing.

1.3 THESIS OUTLINE

This PhD thesis is structured as follows:

Chapter 1 provides an introduction to this PhD thesis including the state of the art, objectives and the structure in which it is organised.

Chapter 2 presents the theoretical basis for dark matter axions and the systems that aim to detect them. Also, the principles of the bandpass filters for satellite communications and its connection with the haloscope designs are detailed.

Chapter 3 states the advances realised in this work in the haloscope parameters (volume, form factor and quality factor). A novel and adjustable external port system is presented. In addition, the description of the systems developed in the RADES group for the haloscope designs is provided.

Chapter 4 shows a detailed discussion of the electronic tuning system generated from this PhD thesis with the use of ferroelectric materials. There is also presented how these elements have been employed as interresonator couplings to replace the iris windows (which often cause problems in manufacturing) allowing the adjustment of the coupling value, thanks to the possibility of varying their electrical properties.

Chapter 5 points secondary studies that have arisen from the need to further improve haloscope designs and explore other regions of the spectrum where axions could be found. Also, a full-wave modal method has been investigated for the efficient analysis of the axion-photon coupling in a haloscope structure.

Chapter 6 details the properties and development of the bandpass filters for satellite communications. Experimental results are exposed in this chapter, testing the performance compared with theory and simulations.

Chapter 7 concludes this PhD thesis. It begins by summarising the work efforts. Then, there are addressed in detail various subjects and areas with regard to the haloscope design that may be relevant for future research efforts, and there are highlighted potential features that have not been completely explore.

THEORETICAL MOTIVATION

2

2.1 DARK MATTER

Physics has long attempted to answer Nature's most fundamental questions. With the advancement of technology over the last century, physicists have been able to examine subatomic processes in ways that were unimaginable previously. Thanks to the theoretical formalism along with the experimental results, the development of a model that explains the many forces, matter components, and their interactions was possible: the SM, which is the best characterization of subatomic physics so far. The fermions (quarks and leptons) that make up known matter and the gauge bosons that convey particle interaction (ElectroMagnetic (EM), strong and weak forces) are the elements of the SM. However, today there are numerous phenomena that the SM cannot clarify (like gravity). Despite this, new concepts and models are being studied and discovered, like the prediction in 1960 and subsequent discovery in 2012 (at CERN) of the Higgs boson, which justify the particle masses. These new discoveries involve an extension of the SM [5].

Although the axion was initially proposed for another purpose (CP problem), it was subsequently determined that the particle would be an outstanding candidate for CDM in our universe, which arises from a model that parameterize the evolution of the *Big Bang*. Researchers discovered evidence that just 5 % of our galaxy mass is related to visible or ordinary matter (recollected in the SM). The remaining 95 % is made up of two undetected elements known as *dark matter* (25 %) and *dark energy* (70 %). The former is made up of one or more undiscovered massive particles that interact only by means of gravitational forces. The latter is even less perceptible and it is seen as an evenly dispersed field throughout space, giving birth to a repulsive force that counterbalances gravity and causes the universe to expand [33]. The rotating velocity of particles at various distances in some galaxies, which deviates from Keplerian expectations, provides evidence for dark matter (see Figure 2.1). Vera Rubin, an American astronomer who pioneered the measurement of star rotation inside a galaxy, was the first to discover this phenomena [34]. Her observations revealed that galaxy rotation curves remained flat, contradicting the theoretical model and providing the most direct and robust evidence for dark matter existence. Beyond the cluster bulge of these galaxies, the velocity is nearly constant. The findings strongly suggested a huge amount of non-observable matter. Another sign of this element is the high gravitational distortion of light from remote galaxies (*gravitational lensing*) [35]. In Figure 2.2, an image of the galaxy cluster *SMACS 0723* taken with the

James Webb Space Telescope of the National Aeronautics and Space Administration (NASA) is shown, where gravitational lensing of light is evident without a clear logic. Weak lensing analyses anticipate several times more mass than is really present. In addition, there are other evidences that support the idea of dark matter (like the Cosmic Microwave Background Anisotropy [36]). Nevertheless, current physics theories are unable to address the problems of what dark energy is and what dark matter is made of, whose finding could imply the discovery of the millennium in Physics.
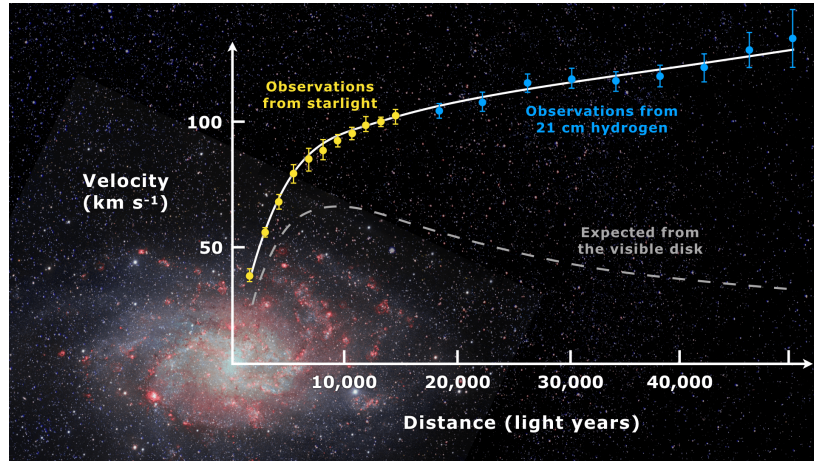
Figure 2.1: Rotation curve of the *M33* galaxy. Taken from [37].

Figure 2.2: Deep field image of the the galaxy cluster *SMACS 0723* from the *James Webb Space Telescope* of the NASA. This picture supposes the deepest and sharpest infrared image of the distant universe so far by the date of the publication of this PhD thesis. The combined mass of this galaxy cluster acts as a gravitational lens. Taken from [38].

Observations in cosmology and astrophysics have revealed that dark matter has played an essential role in the evolution of our universe. Dark matter interacts with conventional matter via gravitational force, and hence plays an important role in the construction of the

cosmic structures visible today. However, no evidence of a non-gravitational interaction between dark matter and conventional matter has been found thus far. The term *dark* refers to the fact that it does neither absorb or emit radiation in any substantial way across the EM spectrum. Additionally, dark matter must have a lengthy lifetime in order to yield the findings observed from all cosmic time scales until today.

Various alternatives within and outside the SM have been presented since the hypothesis of dark matter's theory. The bulk of these choices, however, were ruled out by observation or experimental results [39]. Several dark matter hypotheses remain viable, with WIMPs and the axion regarded as the most powerful. Figure 2.3 depicts the candidates that could be dark matter today.
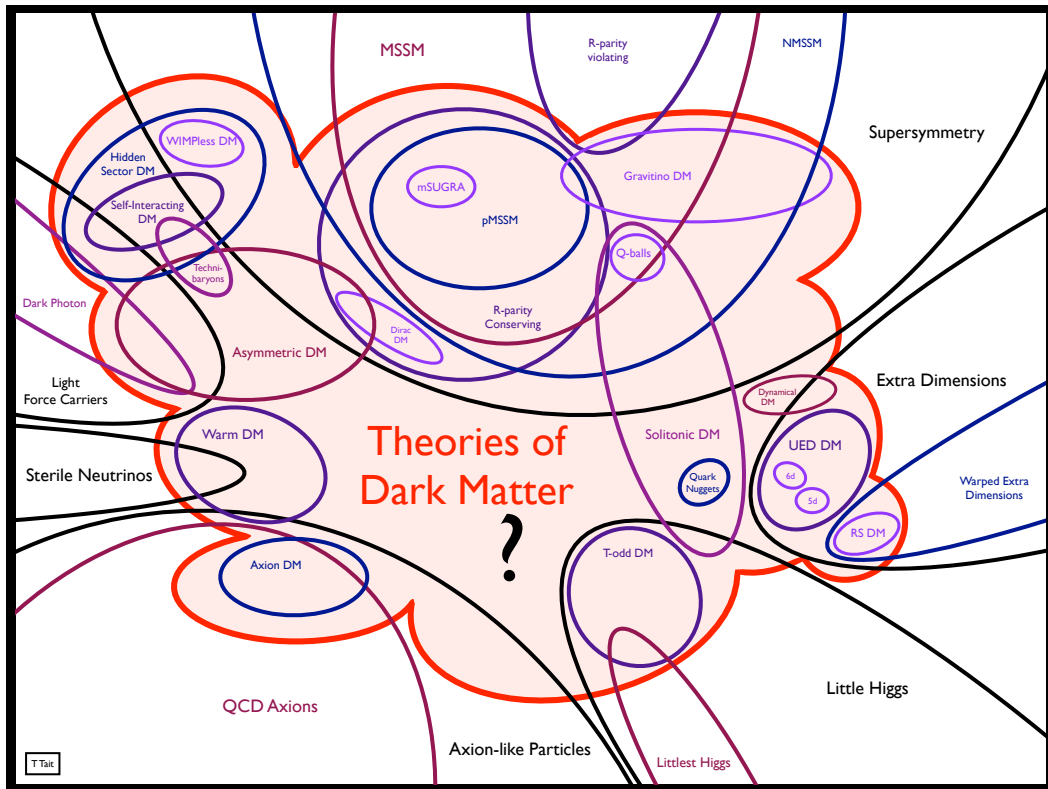
Figure 2.3: Landscape of the dark matter candidates. Image credit: Tim M. P. Tait, University of California, Irvine (2016).

WIMPs are made up of a set of hypothesised particles that were created thermally in the primitive Universe, such as the neutralino and the gravitino. Supersymmetry predicts the most significant WIMPs ideas that are currently feasible. Current experiments have imposed significant limits on WIMPs [40] and supersymmetry [41], proposing that the theory may need more refinement.

Axions were initially proposed as dark matter in 1983 [4]. Because of its easy extension of the SM, the axion particle naturally contains all of the features of dark matter, and it is a preferred candidate due to its straightforward solution to the strong CP problem. The axion

is theorized to form a Bose-Einstein condensate, which might differentiate it from other CDM solutions due to their phase space structure, which is corroborated by astronomical observations [42]. String theory has recently improved the theory of CDM axions in addition to other hypothetical particles known as Axion-Like Particles (ALP).

2.2 AXIONS

The axion is a hypothetical pseudoscalar particle that was first proposed to explain why P and CP are maintained by strong interactions within the context of the SM of particle interactions. The Quantum ChromoDynamics (QCD) Lagrangian contains a CP symmetry breaking the element [43]

$$\mathcal{L} = ... + \frac{\bar{\theta}g^2}{16\pi^2}G^a_{\mu\nu}\tilde{G}^{a\mu\nu} + ...,\tag{2.1}$$

where $\bar{\theta} \in [-\pi, +\pi]$ is a parameter that arises from the non-abelian gauge theory [44, 45] and $G^a_{\mu\nu}$ is the gluon field strength tensor and $\tilde{G}^{a\mu\nu}$ is its dual.

Since the neutron is made of quarks, it should show the CP symmetry violation as well. The presence of an electric dipole moment in this particle would, in fact, break the CP symmetry, and the strength of the moment might be used to calculate $\bar{\theta}$ [46–48]. So far, no tests have found a neutron electric dipole moment, with an upper bound, at 90% confidence interval, of 3×10^{-26} e-cm [49, 50]. The calculated $\bar{\theta}$ upper limit is $\sim 10^{-10}$ rad, which is several orders of magnitude less than projected. This exceedingly narrow upper restriction on this parameter is referred to as the *strong CP problem*.

Peccei and Quinn (PQ) [3] suggested an answer to this issue. Their solution is based on introducing to the early universe a new $U(1)$ symmetry, where making field-dependent term a/f_a, $\bar{\theta}$ acquires a dynamical behaviour, being a a complex pseudo-scalar field produced by the symmetry and f_a an energy scale (directly related with temperature). When the cosmos cooled below f_a, the PQ symmetry was spontaneously broken, leading a to gain a minimum value and $\bar{\theta}$ to zero. Independently, Weinberg [1] and Wilczek [2] demonstrated that breaking the PQ symmetry resulted in the production of a new Goldstone boson known as *the axion*.

The axion mass results from the violation of PQ symmetry by instanton effects and it can be approximated as [5]

$$m_a \approx 6\,\frac{10^6\,GeV}{f_a}.\tag{2.2}$$

The PQ symmetry was originally thought to break surrounding the weak scale, about $f_a \approx 250$ GeV, resulting in the mass of the axion of $m_a \approx 100$ keV [51]. This is the so-called Peccei-Quinn-Weinberg-Wilczek model, which has been ruled out thanks to some experiments [52].

Nowadays models enable the energy scale to be several orders of magnitude greater than the weak scale, which predicts a significantly lower axion mass from the previous model. Furthermore, as f_a grows, so does the difficulty of finding the axion. The KSVZ model [53, 54] and the DFSZ model [55, 56] are the two most widely recognised axion models nowadays.

On the other hand, axions would need to be numerous at all time scales in the post-inflationary cosmos to solve the strong CP problem. Generally, axions created by the breaking of the PQ-symmetry would be non-baryonic, non-relativistic and collisionless. The gravity forces dominate the axion particle, which has an exceedingly weak coupling to the electromagnetic and weak forces. As a result, the axion produced by the Peccei-Quinn mechanism that solved the strong CP problem is a suitable aspirant for dark matter.

The PQ-symmetry breaking theory does not predict the mass of axions, however astronomical observations and particle physics experiments have restricted the f_a, and consequently m_a. The lifetime of the neutrino burst from the supernova *SN1987A* established the bottom bound of $f_a \gtrsim 10^9$ GeV [51]. The highest limit is set by the cosmic energy density issue. The cosmic energy density of axions grows as the axion mass drops; if $f_a \gtrsim 10^{12}$ GeV, the axion energy density would be too high causing the collapse of the primordial universe (overclosure) [22, 23, 57]. This leads to an approximate axion mass range of $m_a \in [1, 1000]$ μeV.

The axion was previously thought to be undetected due to its weak coupling to the SM particles and forces, giving birth to the term *invisible axion*. The different couplings vary depending on the model but, at the dark matter mass range, for all the axion models the coupling to SM particles and forces is $\lesssim 10^{-12}$ GeV^{-1}, and frequently much lower [58]. The natural lifespan of an axion is proportional to its mass by

$$\tau_{a\gamma\gamma} \approx \left(\frac{10^5 \, eV}{m_a} \right)^5 \, sec. \tag{2.3}$$

The decay period to convert to a SM particle for CDM axions within the permitted range of masses is several orders of magnitude higher than the age of the universe, implying that dark matter axions are undetected.

Sikivie proposed in 1983 utilising the inverse Primakoff effect to dramatically improve the electromagnetic coupling, which led to several direct detection hypotheses of the axion particle [6]. The axion-photon conversion Lagrangian determines this coupling, as indicates equation 1.1. Employing a static magnetic field B_0, this Lagrangian becomes $\mathcal{L}_{a\gamma\gamma} = g_{a\gamma\gamma} a \vec{E} \cdot \vec{B}_0$. Figure 2.4 shows the axion-photon conversion in two scenarios: vacuum and static magnetic field. The presence of a magnetic field boosts this conversion, providing to the axion a significant higher lifetime compared to the vacuum case.
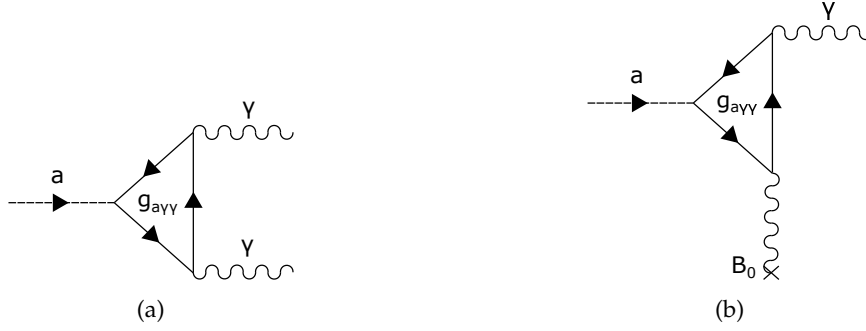
Figure 2.4: Axion-photon conversion represented with Feynman diagrams at: (a) vacuum, and (b) static magnetic field B_0.

For the KSVZ model, the axion-photon coupling coefficient takes $g_{a\gamma\gamma} = 0.38\frac{m_a}{GeV^2}$ [53, 54], while for the DFSZ model this parameter acquires a value of $g_{a\gamma\gamma} = 0.14\frac{m_a}{GeV^2}$ [55, 56].

Due to the non-relativistic nature of axion dark matter, the photon frequency of the axion-photon conversion can be computed by [24]

$$f \approx \frac{m_a c^2}{h},$$ (2.4)

where $c = 2.99792458 \times 10^8$ m/s is the speed of light in vacuum and $h = 6.62607015 \times 10^{-34}\ \frac{m^2 Kg}{s}$ is the Planck constant. In this equation, the axion mass m_a is expressed in Kg, and it can be converted to eV by $1Kg = 5.60958616 \times 10^{35} eV$. The frequency f is expressed in Hz.

Two experiments were suggested by Sikivie based on direct detection, the haloscopes and the helioscopes, employing the inverse Primakoff effect. For the haloscope case, it is employed a microwave cavity immersed in a high static magnetic field to boost the axion-photon conversion and to facilitate its detection. On the other hand, the helioscope detectors are telescopes immersed in a high magnetic field that transform solar axions (that are not CDM axions) created at the inner layers of the sun into photon.

Currently, the most competitive axion detectors are the ADMX [24], for the haloscope case, and the CAST [15] (now decommissioned) and the IAXO [59], for the helioscope case. The latter is a near-future project that will start with a first prototype called BabyIAXO [59], which will be used for both helioscope and haloscope experiments, as in the CAST magnet. Cryogenic devices are used in both detectors to decrease the background noise and gain a very sensitive signal at the detection. Figure 2.5 shows that there is still a considerable portion of the axion-photon coupling space that is unexplored. The axion distinct phenomenology needs focused and specialised investigations in order to find it.

As it can be seen in Figure 2.5b, the ADMX experiment is the only haloscope detector that has reached the KSVZ and DFSZ models. In fact, the CAPP experimental group published recently a paper describing an axion dark matter search using a haloscope at DFSZ sensit-

(a)

(b)
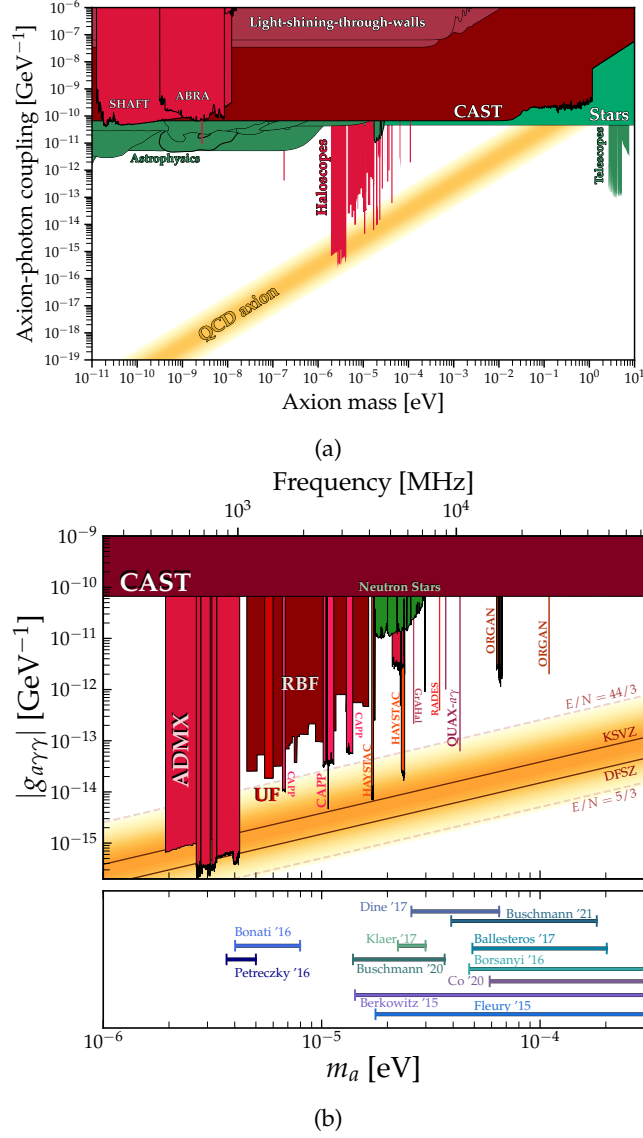
Figure 2.5: Landscape of the axion-photon coupling coefficient ($g_{a\gamma\gamma}$) versus the axion mass (m_a) for: (a) a wide range of axion masses, and (b) zoom in at the haloscope region. The yellow bands show the benchmark of the QCD model, where the KSVZ and DFSZ models lie. At the bottom of (b), several theory prediction references of the axion dark matter mass are represented. In [60] a multitude of exclusion plots can be consulted, including these figures.

ivity [61]. However, several advances in various haloscope groups are being made in order to reach these models, where the axion is expected to be found with much more certainty according to the axion theory. In this PhD thesis, it is intended to cover this aspect in the RADES group, where sensitivities are expected to reach both models in its new generation detectors.

2.3 HALOSCOPE DESIGN

A resonant haloscope experiment, as defined in [27] for the RADES case, consists of a microwave resonant cavity with an applied high and static magnetic field at cryogenic

temperatures, and connected by a port to a receiver or Data Acquisition System (DAQ) that amplifies / filters / down-converts the signal avoiding the introducing of noise as much as possible. This receiver also makes the Analog / Digital conversion and a Fast Fourier Transform (FFT) for the post-processing. In Figure 2.6 an illustration of a rectangular cavity haloscope experiment is shown. The RF signal of the cavity, ideally as a result of
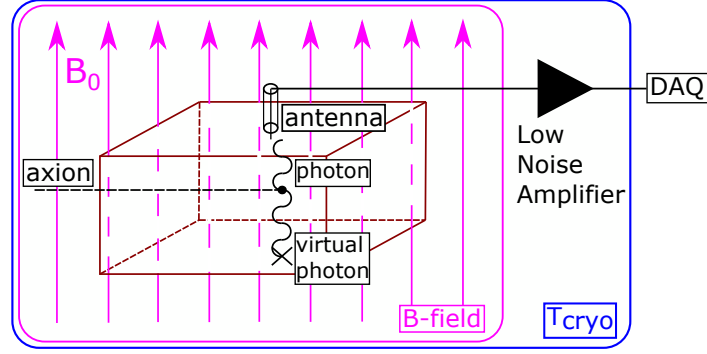
Figure 2.6: Illustration of an usual cavity haloscope experiment.

the inverse Primakoff effect, is extracted by a coaxial port in this example. A Low Noise Amplifier (LNA) is positioned out of the magnetic field, but at the cryogenic environment, for a correct amplification before the DAQ.

A haloscope often employs a superconducting solenoidal or dipole magnet to take advantage of its high static magnetic field. This is the case of CAST, which apart from being used for helioscope experiments, has two dipole bores with a $\sim$ 9 T magnetic field at $T \approx 1.8$ K where haloscopes can be positioned for data campaigns, as depicts Figure 2.7.
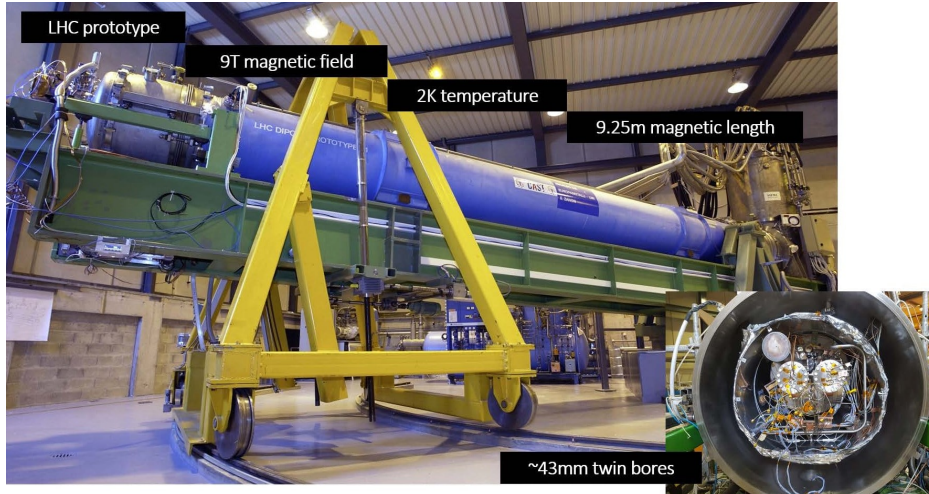
Figure 2.7: CAST, a decommissioned dipole magnet of the Large Hadron Collider (LHC) mounted in a movable system for the tracking of the sun for helioscope experiments. Inset: Front view of the magnet when the tape is removed (opened). The two parallel cylindrical bores of diameter $\phi = 42.5$ mm and length $L = 9.25$ m, where the haloscope detectors are inserted, can be observed here. Taken from [62].

Each bore has a inner (valid space to insert prototypes) diameter of $\phi = 4.3$ cm and a cross-section area of 14.52 cm^2. Because the current carrying wires are Niobium Titanium, the magnet becomes superconductive at temperatures below 4.5 K. It is ramped up to 13 kA current, producing an 8.8 T magnetic field across a length of 9.26 m aligned in the transversal direction.

CAST was suggested in 1999 [63, 64] as a helioscope experiment and has been collecting data since 2003. In recent years, RADES and CAPP, two axion haloscope teams, make use of these two bores for searching axions. However, CAST programs were cancelled by CERN one year ago due to lack of physics results.

Despite technical advances in X-ray detectors, the CAST sensitivity to solar axions is severely constrained by its volume and magnetic field. Its successor, the future IAXO experimental design, consists of a superconductive 8 coil toroidal magnet with bore diameters of $\phi = 60$ cm. The average magnetic field is ~ 2.5 T, with a length of 20 m. The IAXO experiment has the potential to outperform the existing CAST limit by more than an order of magnitude. Currently, an intermediate step called BabyIAXO is being designed and tested [59]. RADES cavities are expected to be mounted in the BabyIAXO and IAXO bores in the future. Figures 2.8a and 2.8b depict a conceptual design of each magnet.

(a)   (b)
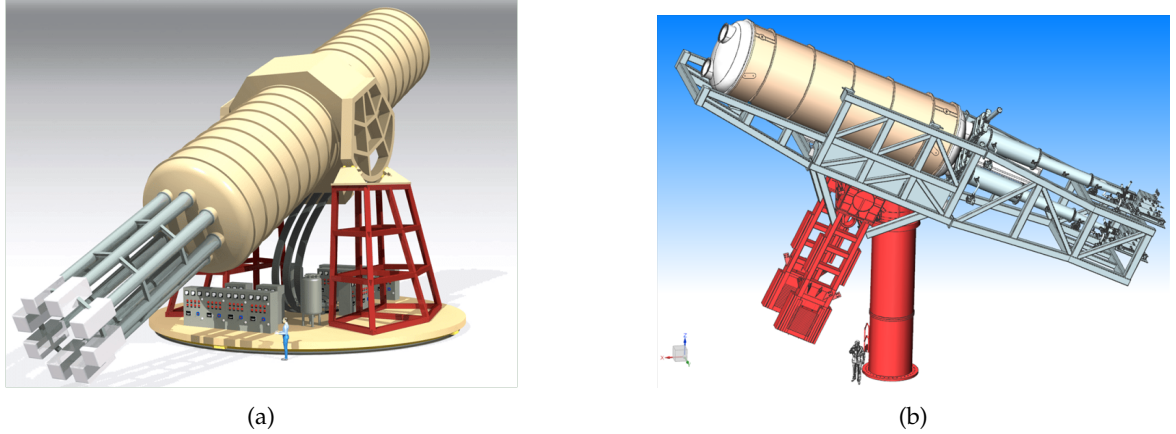
Figure 2.8: (a) Conceptual design of the IAXO and (b) its intermediate experiment BabyIAXO. (a) and (b) taken from [65] and [59], respectively.

Regardless of the magnet to be used, the major aims in the design of a haloscope experiment may be summarised as maximising the received EM power from the axion-photon interaction, optimising the haloscope sensitivity, and maximising the scanning rate over the mass range of interest. It is therefore critical to understand the relationships between these three factors and the design parameters.

2.3.1 *Detected power*

The generated power with the axion-photon coupling in a resonant cavity haloscope may be calculated as [66, 67]

$$P_g = g_{a\gamma\gamma}^2 \frac{\rho_a}{m_a} B_e^2 CV \frac{Q_c Q_a}{Q_c + Q_a}, \tag{2.5}$$

where ρ_a is the density of the axion dark matter, V the volume of the haloscope cavity, C the geometric or form factor, Q_c the quality factor of the resonance mode in the cavity, and Q_a the quality factor of the axion resonance. The form factor is a normalised quantity that measures the parallelism between the magnetostatic field $\vec{B}_e$ where the haloscope is immersed and the desired RF electric field $\vec{E}$ caused by the axion field at the cavity:

$$C = \frac{|\int_V \vec{E} \cdot \vec{B}_e \, dV|^2}{\int_V ||\vec{B}_e||^2 \, dV \, \int_V \varepsilon_r ||\vec{E}||^2 \, dV}. \tag{2.6}$$

In equation 2.6, the parameter of the numerator suffers a conversion from complex numbers to magnitude ($|\cdot|$ operator), while in the denominator parameters it is applied the operator standard vector norm ($||\cdot||$), defined in the 3D complex vector space. In addition, the real part of the the relative permittivity or dielectric constant parameter (ε_r) is included in this equation to take into account the cavity medium (for vacuum, $\varepsilon_r = 1$).

This P_g power will be divided into two parts: (1) power dissipated by the lossy cavity (metallic walls if no lossy dielectric materials are present), and (2) extracted power by the port experiment. For frequencies below 30 GHz, a coaxial monopole or loop antenna coupled to a coaxial line is usually employed, which will then transmit the RF signal to the receiver. The detected RF power at the port is obtained as

$$P_d = \kappa g_{a\gamma\gamma}^2 \frac{\rho_a}{m_a} B_e^2 CV \frac{Q_l Q_a}{Q_l + Q_a} \tag{2.7}$$

where κ is the external coupling at the port, and Q_l is the loaded quality factor (that considers the effect of the port). In order to achieve the maximum power transfer, a critical coupling regime is necessary. For this purpose, the port coupling should acquire a value of $\kappa = 0.5$, which must be maintained as long as the haloscope is taking data seeking axions. Actually, this parameter is extremely sensitive to minor mechanical or temperature variations. As a result, developing mechanical or electrical devices for adjusting the port coupling at any time becomes very important or desirable.

In general, Q_a ($\sim 10^6$) is much higher than Q_l. This reduces the detected power to a

$$P_d = \kappa g_{a\gamma\gamma}^2 \frac{\rho_a}{m_a} B_e^2 CV Q_l \tag{2.8}$$

2.3.2 *Axion-photon coupling sensitivity*

Another important parameter in a haloscope experiment is the signal to noise ratio, which can be expressed as

$$\frac{S}{N} = \frac{P_d}{P_N} = \frac{P_d}{k_B T_{sys} \sqrt{\frac{\Delta v}{\Delta t}}}, \tag{2.9}$$

given by the equation of the Dicke's radiometer [68], where k_B is the Boltzmann constant, T_{sys} the noise temperature of the experimental system, Δv the reception bandwidth and Δt the observation or search time. Taking into account that the reception bandwidth should coincide with the axion resonance bandwidth ($\Delta v_a = \frac{m_a}{Q_a}$) and introducing 2.8 into 2.9, the axion-photon coupling equation is obtained as

$$g_{a\gamma\gamma} = \left(\frac{\frac{S}{N} k_B T_{sys}}{\kappa \rho_a C V Q_l} \right)^{\frac{1}{2}} \frac{1}{B_e} \left(\frac{m_a^3}{Q_a \Delta t} \right)^{\frac{1}{4}}. \tag{2.10}$$

The axion-photon coupling can also be expressed by its dimensionless form:

$$C_{a\gamma\gamma} = 5 \cdot 10^{15} \frac{g_{a\gamma\gamma} \left(GeV^{-1} \right)}{m_a \left(\mu eV \right)} = 5 \cdot 10^{15} \left(\frac{\frac{S}{N} k_B T_{sys}}{\kappa \rho_a C V Q_l} \right)^{\frac{1}{2}} \frac{1}{B_e} \left(\frac{1}{Q_a m_a \Delta t} \right)^{\frac{1}{4}}. \tag{2.11}$$

From all these equations we can extract that the detected RF power only depends on parameters that are intrinsic to the axion ($g_{a\gamma\gamma}$, ρ_a and m_a) and experimental parameters in the haloscope detector (B_e, C, V and Q_l). However, the axion-photon coupling relies, apart from all the above parameters, on experimental parameters at the receiver ($\frac{S}{N}$, T_{sys} and Δt).

2.3.3 *Scanning rate*

The ultimate goal of a haloscope is to explore the greatest feasible mass range as fast as possible. The sweeping of the mass spectrum can be accomplished using appropriate tuning mechanisms (mechanically or electronically) that vary the resonance frequency of the cavity, being the $\frac{dm_a}{dt}$ parameter the scanning rate, referred as a haloscope figure of merit.

The axion mass range examined in a data campaign employing a cavity which resonance is centred at m_a, is equivalent to the cavity bandwidth:

$$dm_a = \frac{m_a}{Q_l}. \tag{2.12}$$

On the other hand, from equation 2.9, the necessary time for achieving a specific $\frac{S}{N}$ value can be extracted:

$$dt = \frac{m_a}{Q_a} \left(\frac{\frac{S}{N} k_B T_{sys}}{P_d} \right)^2. \tag{2.13}$$

Thus, the scanning rate can be expressed as

$$\frac{dm_a}{dt} = \frac{Q_a}{Q_l} \left(\frac{P_d}{\frac{S}{N} k_B T_{sys}} \right)^2 = Q_a Q_l \kappa^2 g_{a\gamma}^4 \left(\frac{\rho_a}{m_a} \right)^2 B_e^4 C^2 V^2 \left(\frac{S}{N} k_B T_{sys} \right)^{-2}. \tag{2.14}$$

2.4 WAVEGUIDE COUPLED CAVITIES AS HALOSCOPES

To summarise the previous section, the experimental settings that maximise the detected power, sensitivity, and scanning rate may be found in 2.8, 2.11, and 2.14, respectively. The external magnetic field B_e is clearly the most influential parameter on the cavity, followed by V and Q_l, the C parameter for the operation mode, and the system temperature T_{sys}, which is primarily determined by the physical temperature of the cavity and the noise temperature of the LNA (see Figure 2.6), according to the Friis formula [69].

The magnetic volume $B_e^2 V$ is a figure of merit for the magnet in these types of experiments. However, it is frequently difficult to construct a haloscope that entirely fills the bore space (due to the dependence between its volume and resonant frequency), therefore the magnet potential is underutilised. This was the situation and the motivation for the RADES initiative. Considering the upper limit in $g_a\gamma\gamma$ for the ADMX possibilities in the next years [24], RADES intended to scan higher masses, which leads to lower volumes in the resonant cavities, because the resonant frequency relies, in general, inversely on the cavity size.

2.4.1 *Single cavities*

The two most commonly used types of microwave cavities for haloscopes are the cylindrical and rectangular types, which are depicted in Figure 2.9.
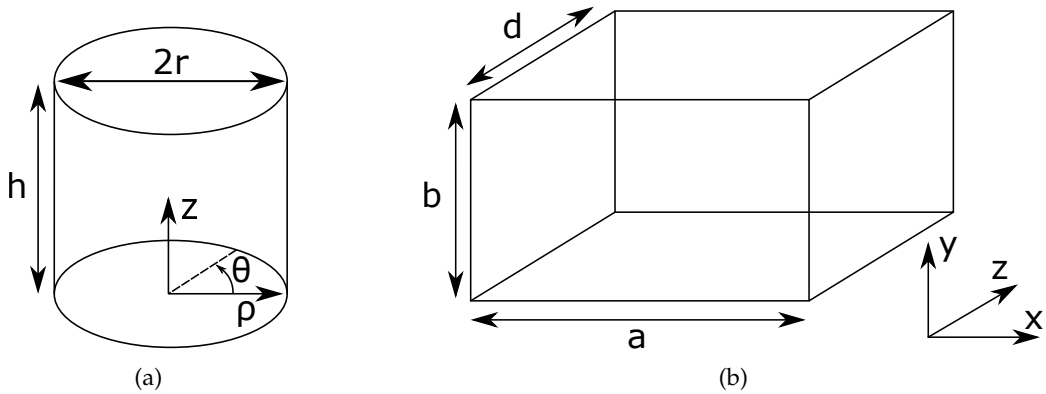
Figure 2.9: a) Cylindrical cavity of radius r and height h, and (b) rectangular cavity of width a, height b and length d.

Their resonant frequencies for TE_{mnp} and TM_{mnp} modes can be expressed as follows [70]:

$$f_{TE_{mnp}}^{cyl} = \frac{c}{2\pi \sqrt{\varepsilon_r \mu_r}} \sqrt{\left(\frac{p'_{mn}}{r}\right)^2 + \left(\frac{p\pi}{h}\right)^2}, \qquad \begin{matrix} m = 0,1,2,... \\ n = 1,2,3,... \\ p = 1,2,3,... \end{matrix} \qquad (2.15)$$

$$f_{TM_{mnp}}^{cyl} = \frac{c}{2\pi \sqrt{\varepsilon_r \mu_r}} \sqrt{\left(\frac{p_{mn}}{r}\right)^2 + \left(\frac{p\pi}{h}\right)^2}, \qquad \begin{matrix} m = 0,1,2,... \\ n = 1,2,3,... \\ p = 0,1,2,... \end{matrix} \qquad (2.16)$$

$$f_{TE_{mnp}}^{rec} = \frac{c}{2\sqrt{\varepsilon_r \mu_r}} \sqrt{\left(\frac{m}{a}\right)^2 + \left(\frac{n}{b}\right)^2 + \left(\frac{p}{d}\right)^2}, \qquad \begin{matrix} m = 0,1,2,... \\ n = 0,1,2,... \\ p = 1,2,3,... \end{matrix} \qquad (2.17)$$

m and *n* not zero simultaneously

$$f_{TM_{mnp}}^{rec} = \frac{c}{2\sqrt{\varepsilon_r \mu_r}} \sqrt{\left(\frac{m}{a}\right)^2 + \left(\frac{n}{b}\right)^2 + \left(\frac{p}{d}\right)^2}, \qquad \begin{matrix} m = 1,2,3,... \\ n = 1,2,3,... \\ p = 0,1,2,... \end{matrix} \qquad (2.18)$$

where m, n, and p are integers that denote the number of maxima of the electric field in the θ, ρ, and z axis for cylindrical cavities, and in the x, y, and z axis for rectangular cavities, respectively, μ_r is the relative magnetic permeability ($\mu_r = \varepsilon_r = 1$ is assumed), p_{mn} and p'_{mn} represent the $n-th$ zero ($n = 1,2,3,...$) of the first kind Bessel function J_m, and its derivative J'_m, respectively, of order m ($m = 0,1,2,3,...$), r and h are the radius and height of the cylindrical cavity, respectively, and a, b and d are the width, height and length of the rectangular cavity, respectively. Usually rectangular cavities working with the TE_{101} fundamental resonance at 8.4 GHz (34.74 μeV) have been used in RADES. For the ADMX experiment, employing the TM_{010} mode, an estimated exploration mass of 30 μeV (7.25 GHz) is achieved with a cavity diameter of 3.17 cm, which would underutilise the available 60 cm diameter of their magnet bore.

Solenoid magnets are used in the majority of haloscope investigations, such as ADMX [71] and HAYSTAC [72]. Because these magnets generate an axial ($\hat{z}$) magnetic field (see Figures 2.10a and 2.10c) the typical type of cavity is cylindrical, and it is positioned to make its $z-$axis parallel to the longitudinal axis of the magnet bore. In this method, a TM mode with an axial electric field gives the best form factor C value. More specifically, this is achieved with the TM_{010} mode. As it is said previously, in the early stages of the RADES project a powerful accelerator dipole magnet (see Figures 2.10b and 2.10d) was available: the CAST magnet, which produces an 8.8 T transverse ($\hat{y}$) magnetic field. The rectangular cavity, where TE_{m0p} modes shown a vertical polarisation in the E-field, is a more suitable cavity for this type of magnets.
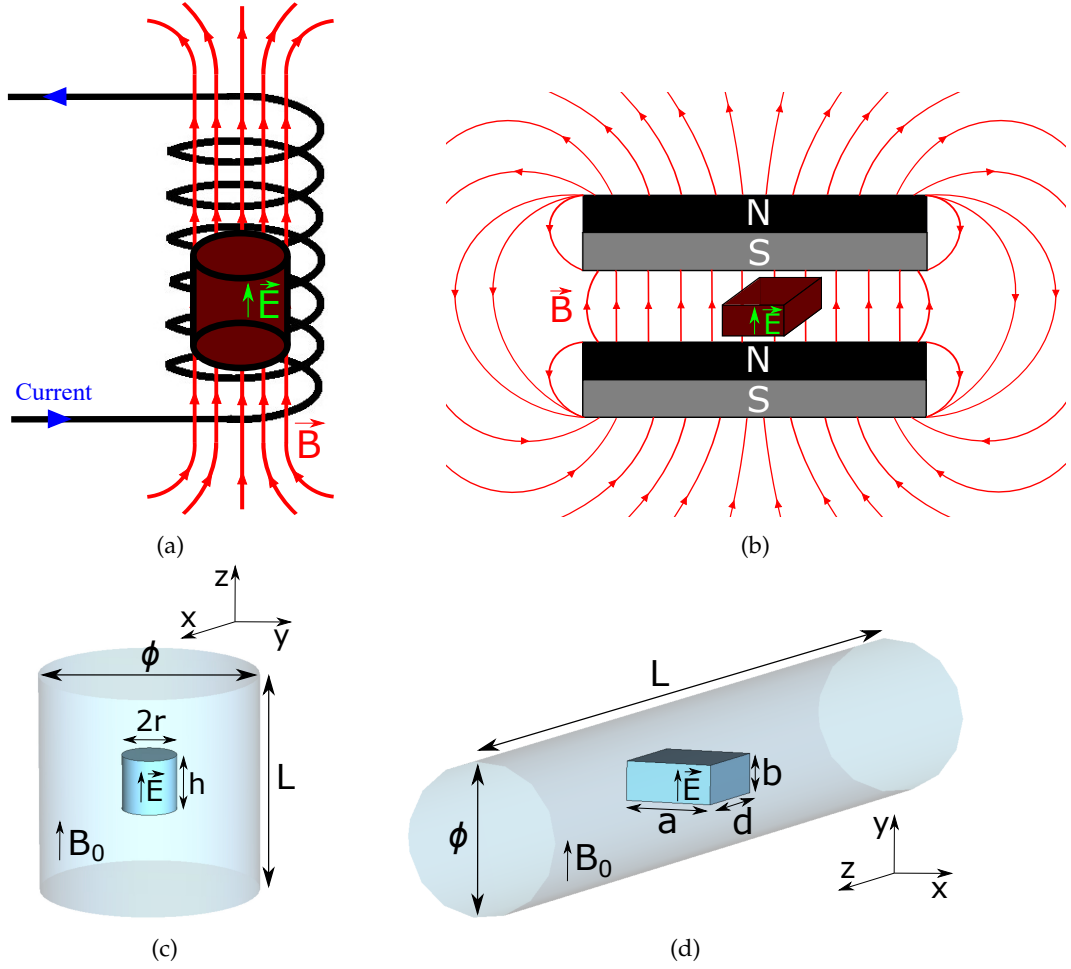
Figure 2.10: (a) Solenoid magnet with axial magnetic field, and (b) dipole magnet with transversal magnetic field. (c) Model of a solenoid magnet bore, and (d) model of a dipole magnet bore. In these examples, a cavity is inserted to show how the cavity E-field and the bore B_0-field lines are parallel in all the cases. (a) and (b) are taken and modified from [68] and, (c) and (d) from [73].

In the rectangular cavity case, to achieve the highest form factor, the TE_{101} mode should be used. To design a haloscope to search axions at $m_a = 30$ μeV, the cavity should be a parallelepiped with $a = 29.3$ mm, making $a = b = d$ to increase the volume as much as possible. This fits into the dipole bore of diameter of 42.5 mm from the CAST magnet [63], although the bore is much underutilised taking into account that the length of the cavity is very small compared to the magnet diameter (9.3 m). Furthermore, in order to avoid mode mixing from degenerate modes, the dimensions a and b must be sufficiently distinct ($a \approx 2b$). As a drawback, this decreases the cross-section of the cavity and, as a result, its volume.

Considering that a rectangular cross-section is not optimized to cover the total circular cross-section of the magnet bore, the RADES motivation is based on increasing the volume of the cavity in the longitudinal axis of the magnet without changing the resonant frequency (or axion search mass) and other cavity parameters such as Q_l and C.

It seems intuitively plausible that the first idea for increasing the haloscope volume in the CAST bore is to increase the length dimension d of the cavity. For the TE_{101} mode, it can be easily seen that the resonant frequency is reduced from equation 2.17 to $f_{TE_{101}} \approx \frac{c}{2a}$ when $a \ll d$. To maintain the same frequency, the width dimension a has to be reduced a little. Anyway, the large value of d in comparison yields to a high increasing in the volume parameter. For example, at 8.4 GHz (X-Band) or $m_a = 34.76$ μeV, which is the operation frequency of the first RADES haloscope, a width and length of $a = d = 25.24$ mm can be used, providing a volume (assuming $b = \frac{a}{2}$) of $V = 5.97$ mL. However, using $d = 100a$, the width is converted to $a = 17.85$ mm, the length is $d = 100 \times 17.85 = 1785$ mm, and the volume is $V = 284.37$ mL, which produces an increasing of a factor 47.63. However, there is an important drawback for long cavities: the mode clustering in frequency due to higher modes TE_{10p}, which may impede the characterisation of the manufactured cavity Q_l as well as its external coupling factor κ. This concept is represented by

$$\Delta f = \frac{|f_a - f_{neighbour}|}{|f_a|} \times 100, \tag{2.19}$$

where Δf is the mode clustering expressed in [%], f_a is the operation frequency where the axion is being searched and $f_{neighbour}$ is the next resonant mode frequency. Following the same example, for not long cavities at 8.4 GHz ($d = 25.24$ mm) the mode proximity with the axion mode TE_{101} is $\Delta f = 58.11$ %, while for $d = 100a$ this parameter takes $\Delta f = 0.015$ %, a value that might cause problems in the manufactured prototype due to the overlapping of the resonances hampering the identification of the quality factor in the response and decreasing the form factor of the axion mode. Because of this problem, RADES proposed an alternative for increasing the haloscope length (and its volume) solving the mode clustering issue: the multicavity idea.

2.4.2 *Multicavities*

The multicavity structures are based on a number N of interconnected subcavities. These structures are frequently utilised in telecommunication for microwave and millimetre wave filtering. In such scenario, the goal is to implement a bandpass filter with parameters that specify the passband, stop band, pass ripple, and stop band attenuation [74]. In the next section, more information about the study and design of such structures can be found.

When working with haloscopes, the goal is to create an extremely selective filter (high loaded quality factor Q_l), centered at the axion mode frequency. The reference [27] presents the mathematical formalism for the study and design of this type of multicavity structures. If the subcavities have the same size, the haloscope resonant frequency is that of the cell cavity, and the total volume is the sum of the volumes of all the subcavities (i.e., $V_{total} \approx NV_{cell}$), while the resonance frequency remains the same. Furthermore, the multicavity haloscope Q_l must be roughly equal to that of each subcavity. On the other hand, the port that extracts the axion signal can be positioned in any subcavity, which

gives a considerable scope to choose an appropriate position inside the magnet bore for the haloscope. This is possible thanks to the fact that each subcavity has the E-field maximum for the TE_{101} mode at their centers for a critically coupling status, while in a single cavity there is only a small region where the maximum field lies also at the cavity center [27].

Apart from higher order resonant modes TE_{mnp} or TM_{mnp} that can be excited in the cavity due to the dimension of the subcavity, the multicavity may have multiple mode configurations for the same resonant mode, depending on the couplings between subcavities. These configurations are based on the polarization or phase of the field (positive or negative) of each subcavity. Each configuration corresponds with a specific combination of different polarizations. The mode configuration with all positive (or all negative) electric fields in the subcavities will be chosen since it creates a constructive sum in the form factor term $|\int \vec{E} \cdot \vec{B}_e dv|^2$ (see equation 2.6), which provides the maximum C value. In reality, it is assumed that the overall form factor will be roughly the same as one of each subcavity, which, for the TE_{101} mode, it is $C_{TE_{101}} = \frac{64}{\pi^4}$, calculated analytically from 2.6.

The multicavity idea is very similar to the notion of coherently summing N signals derived from N identical subcavities, but in a single structure, which avoids the problem to maintain the coherence in the sum. In recent years, more multicavity approaches for the haloscope design have been reported, including [75, 76].

The design of the interresonator couplings in RADES is based on the alignment of the electric field in all the subcavities to reach the all-positive configuration. These couplings between neighbour subcavities can be accomplished using rectangular irises, as illustrated in Figure 2.11. Irises invariant in y-axis (Figure 2.11a) have an inductive behaviour, but

<div align="center">(a)   (b)</div>
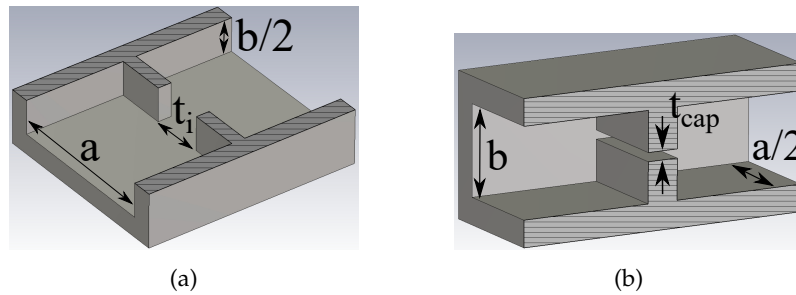
Figure 2.11: Simplest iris couplings between neighbour subcavities: (a) inductive window, and (b) capacitive window. For an easier visualization of the inner geometry, the structures are cut in two symmetric halves. The dashed regions denote the symmetry planes. Taken and modified from [77].

those invariant in x-axis (Figure 2.11b) have a capacitive behaviour due to the vertical polarisation of the electric field in the TE_{101} mode. For this reason, the former are called inductive irises and the latter capacitive irises.

The first RADES haloscope was designed (using the formalism in [27]), optimised (using CST Studio [78]), built, and characterised in 2018 [27]. Later, this structure was employed for a data taking campaign in CAST, whose data results were published in [79]. This haloscope is the first haloscope based on the multicavity idea and it consists in a 5-subcavities structure interconnected by inductive irises, as shown in Figure 2.12.

(a)   (b)
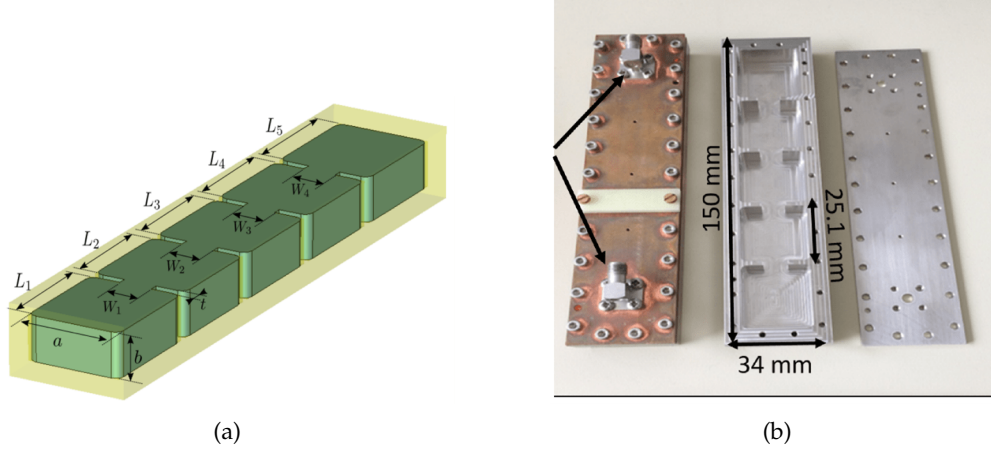
Figure 2.12: First RADES multicavity haloscope based on 5-subcavities and 4 inductive irises as inter-resonator couplings: (a) 3D model with dimensions, and (b) manufactured prototype. The dimensions of the structure are $a = 22.99$ mm, $b = 10.25$ mm, $L_1 = L_5 = 26.82$ mm, $L_2 = L_3 = L_4 = 25.14$ mm, $W_1 = W_2 = W_3 = W_4 = 8.14$ mm and $t = 1.95$ mm.

In Figure 2.12a a 3D scheme and the dimensions of the designed structure can be found. The technical drawings for the manufacturing of this haloscope are depicted in Appendix I: Technical Drawings (see Figures A.1 and A.2). The final manufacturing dimensions take into account the slight deviations due to the thermal contraction in the structure, from room temperature ($T = 300$ K) to cryogenic temperature ($T = 2$ K). The prototype was manufactured in stainless steel $316LN$ material, which is a particular strong version of $316L$ to avoid magnetic interferences at the CAST magnet and the structural deformation due to magnetic quenches. To increase the electrical conductivity of the material (and thus the quality factor) a 30 μm copper layer is applied after the manufacturing. Also, this multicavity was produced with two 90° SubMiniature version A (SMA) coaxial ports, each, in one of the extreme subcavities, as depicted in Figure 2.12b. One of them is used for testing purpose and the other one for the extraction of the signal.

Figure 2.13 illustrates the five configuration modes of the resonant mode TE_{101} for this structure. The form factor is also included in this figure, where it can be observed how C is maximum for the all-positive configuration. Here it is important to remark that the number of configuration modes corresponds with the number of subcavities N.
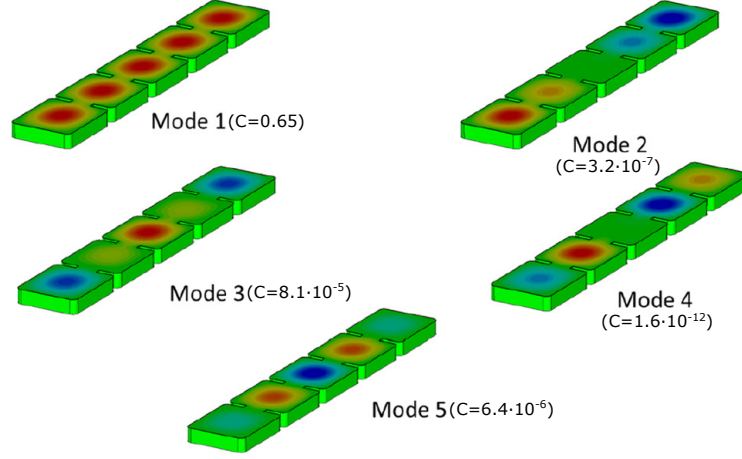
Figure 2.13: Vertical polarization of the electric field pattern (E_y) of the five configuration modes of TE_{101} resonant mode in the first RADES 5-subcavities multicavity. The form factor of each configuration is included for comparison. The red fields denote positive E-field levels, the green fields zero and the blue negative levels. Taken and modified from [27].

Figure 2.14[1] shows the measured and simulated transmission coefficient (employing both ports), applying a temperature of $T = 2$ K. In this picture, it can be seen the noise
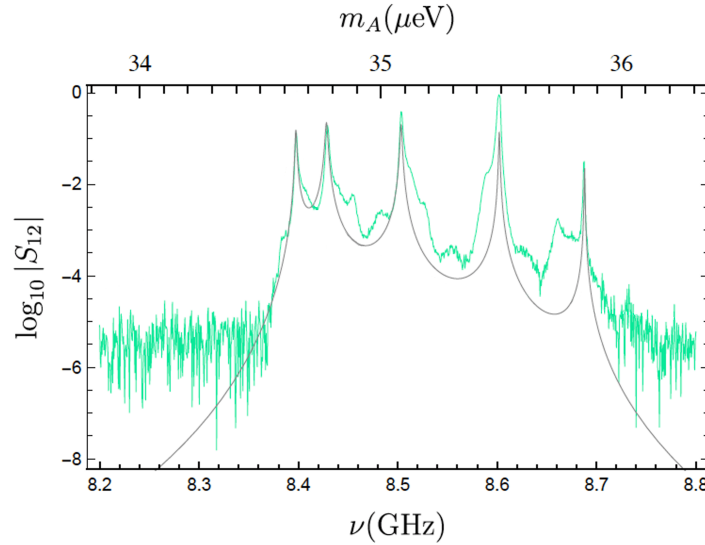
Figure 2.14: Transmission coefficient magnitude S_{12} at $T = 2$ K versus the frequency and the axion mass: measured (light green) and simulated (black). Taken and modified from [27].

from the measured results (taken with a Vector Network Analyzer (VNA)) included by the cable and intermediate elements (connectors, flanges, LNA, and so on).

---

1 To measure the transmission response of a haloscope, the S_{21} parameter, i.e. the transmission power between port 1 and port 2, is usually measured. However, for the results shown in Figure 2.14, a measurement was taken where the numbering of the two ports was swapped. This does not change the behaviour of the haloscope at all, as it is merely a numbering issue.

Despite the multicavity idea reduces the mode clustering, similarly to the long cavities and its next modes, there is a limitation. When the number of subcavities N rises, the concentration of the configuration modes increases equally. Figure 2.15 depicts the $N = 30$ configuration modes of a haloscope based on 30 subcavities with 29 inductive irises, this is, an all-inductive multicavity as the first RADES haloscope. The transmission coefficient
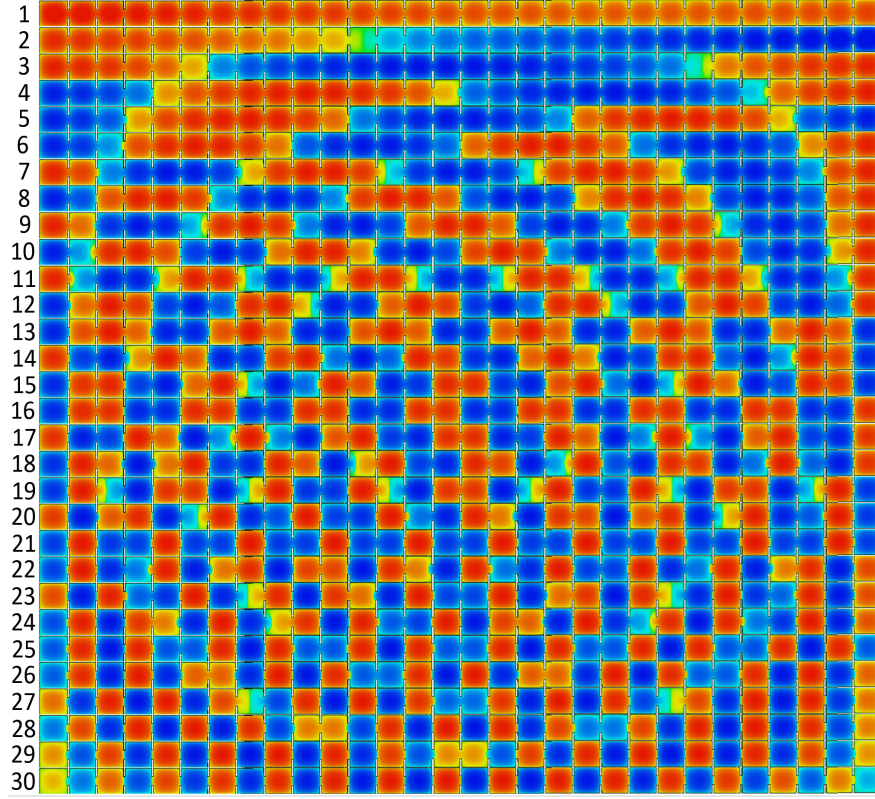
Figure 2.15: Vertical polarization of the electric field pattern (E_y) of the $N = 30$ configuration modes of TE_{101} resonant mode at a 30-subcavities haloscope. The numbers at left column are referred to the configuration modes in order, from the lower to the higher frequency. The 30 right columns represent each subcavity. The red areas denote a positive level in the electric field, and the blue areas with a negative level. The form factor for all the configurations is almost zero, except for the first one, $C_{mode1} = 0.65$.

of this structure is presented in Figure 2.16, where a clear mode clustering between the configuration modes of the TE_{101} resonant mode can be observed. Each resonance of this spectrum corresponds with each configuration mode. This scenario gets worse with the manufactured structure and considering the data taking settings, resulting in more possibilities to produce overlapping between the resonances, making obtaining the quality factor or coupling factor from measurements difficult, apart from the possibility of reducing the form factor.

A similar situation is presented with an all-capacitive structure for $N = 30$ subcavities, with a simple difference: the axion mode will be the last mode configuration, instead of being in the first position as in the all-inductive multicavity.
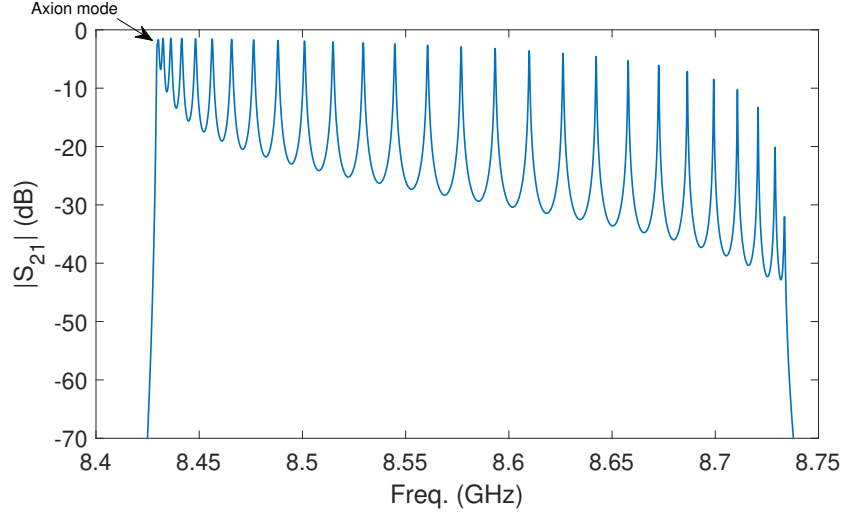
Figure 2.16: Magnitude of the transmission coefficient S_{21} at $T = 2$ K versus the frequency of an all-inductive multicavity based on $N = 30$ subcavities.

Using alternating interresonator couplings (capacitive and inductive irises) is an efficient solution to improve the mode clustering close to the axion mode [80]. Unlike previous scenarios, the axion mode is now located at the centre of the band, where there is a higher mode separation. The first haloscope with this alternating principle designed, optimised and manufactured by the RADES team was a 6-subcavities structure with 3 capacitive and 2 inductive irises (see Figure 2.17a), that was produced in 2018. Later, an evolution of this structure based on $N = 30$ subcavities with 15 capacitive
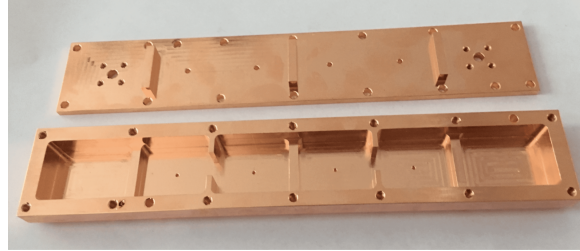
(a)
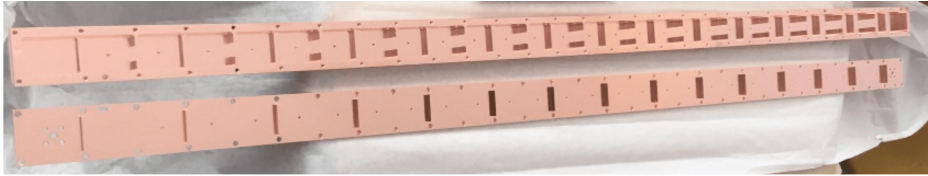
(b)

Figure 2.17: Manufactured prototypes of the alternating haloscopes based on: (a) $N = 6$ subcavities and (b) $N = 30$ subcavities. The technical drawings for the manufacturing of these haloscopes are depicted in Appendix I: Technical Drawings (see Figure A.3 for the $N = 6$ haloscope, and Figures A.4 and A.5 for the $N = 30$ haloscope).

and 14 inductive irises (see Figure 2.17b) was manufactured in 2019 at the CERN workshop.

In Figure 2.18a the six E-field patterns of the configuration modes for the $N = 6$ structure and its form factor values are depicted. In this case, the 4th configuration

(a)

(b)
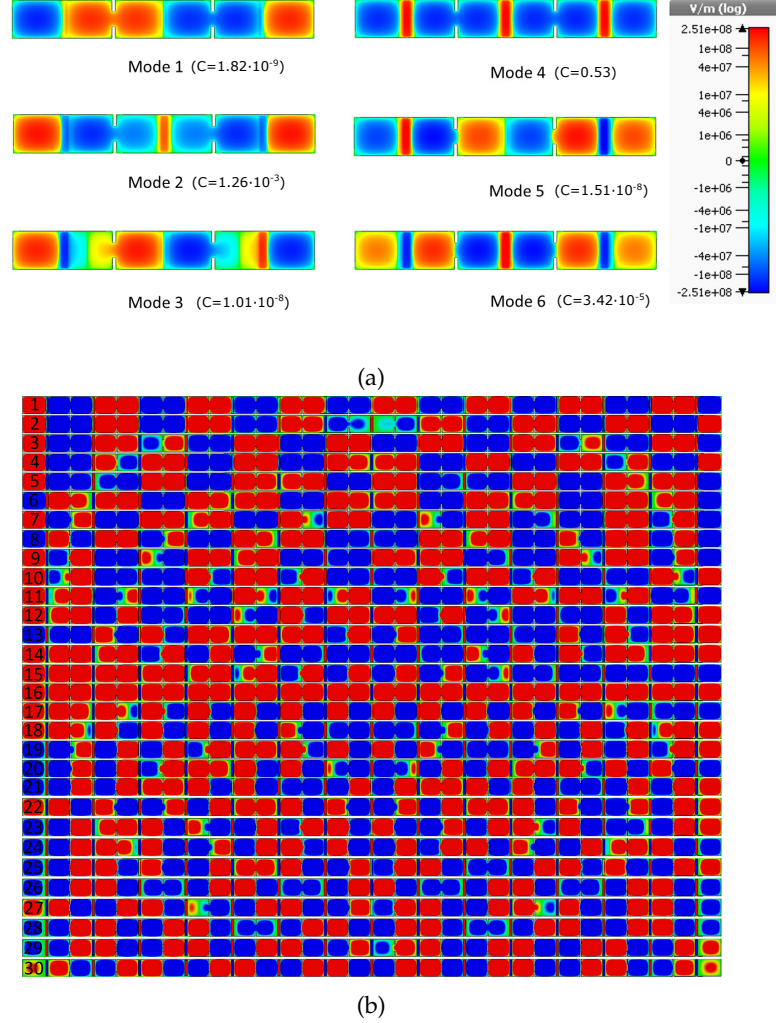
Figure 2.18: Vertical polarization of the electric field pattern (E_y) of the six (a) and thirty (b) configuration modes of TE_{101} resonant mode in the: (a) $N = 6$ haloscope and (b) $N = 30$ haloscope. The form factor of each configuration is included for comparison in the small structure. The red fields denote positive E-field levels, the green fields zero and the blue negative levels. In (b) the numbers at left column are referred to the configuration modes in order, from the lower to the higher frequency. The 30 right columns represent each subcavity. The form factor for all the configurations is almost zero, except for the axion one. (a) is taken and modified from [80].

corresponds with the axion mode (the configuration that possesses the maximum C). On the other hand, Figure 2.18b depicts the thirty E-fields of the configuration modes in the second version of the alternating haloscopes. In this case, the 16th configuration corresponds with the axion mode.

Figure 2.19a shows the spectra of the small alternating structure in the frequency region of interest, where an improvement in mode clustering can be observed. In Figure 2.19b the same plot is shown but for the $N = 30$ version, where an enhancement in the mode
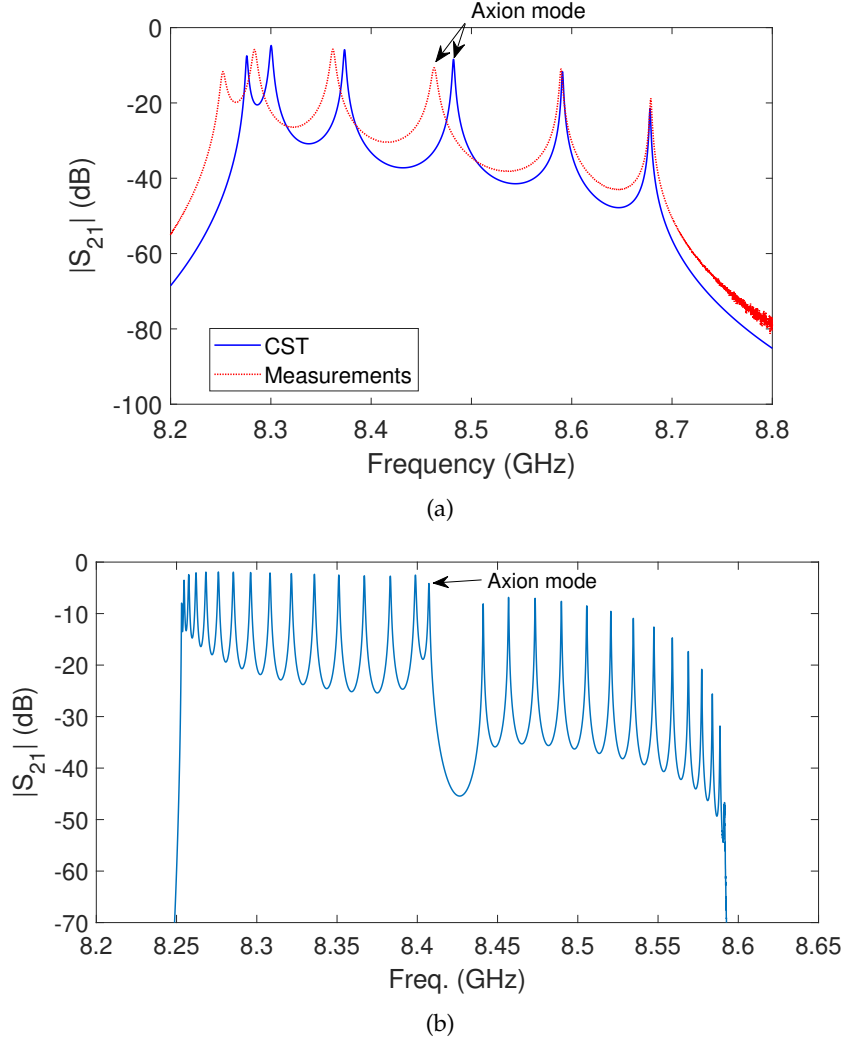
Figure 2.19: Transmission coefficient magnitude S_{12} at $T = 2$ K versus the frequency for: (a) $N = 6$ haloscope and (b) $N = 30$ haloscope. In (a) the dotted red line corresponds with the measurements and the solid blue line with the simulation results. In (b) only the simulation results are shown. (a) is taken and modified from [80].

separation can be observed as well. In the all-inductive $N = 30$ structure the Δf parameter acquires a value of 0.006 % (470 KHz), while in the alternating structure it is $\Delta f = 0.183$ % (15.34 MHz), an increase of factor $\times 31$ in mode separation between the axion mode and the next neighbouring mode.

Despite the mode clustering and volume improvements, these interresonator irises are prone to manufacturing issues, particularly when both kinds (inductive and capacitive) are used (alternating) [80]. In this scenario, the fabrication necessitates completely 3D machining procedures with multiple axis cut planes. In investigations with the alternating 6-subcavities and 30-subcavities haloscopes, inadequate contact between metallic surfaces resulted in a decrease in the flow of surface currents, and hence a decrease in the unloaded quality factor. In this PhD thesis, several solutions are presented to cover these issues: parallel manufacturing cuts to the electric field lines, the soldering and the modularity (see section 3.2), and the use of ferroelectric films (see section 4.2), making extremely easy

to manufacture rectangular housings.

Following the promising results of the last years, the RADES collaboration is nowadays focused on increasing the sensitivity of its haloscopes, on expanding the mass range through mechanical or electrical tuning systems, on designing new haloscope concepts for other mass regions (UHF and W bands), and on developing numerical methods for an efficient and accuracy solution in the axion-photon interaction that induces an electromagnetic field (the BI-RME 3D method [81]). The two first topics (sensitivity improvement and tuning development) are the main objectives of this PhD thesis.

As previously stated, the sensitivity of the experiment in terms of haloscope parameters is determined by its volume, quality factor, and port coupling. Considering the first RADES haloscopes prepared for the CAST bore, a different approach can be applied in the future BabyIAXO magnet, whose magnetic field pattern is defined by a superconducting toroidal magnet [59]. If tall (high b dimension) multicavities are employed, the volume and quality factor can be considerably enhanced. Because it is being used the TE_{101} resonant mode, the detection frequency is independent of the cavity height, relying solely on its width and length. The haloscope height can be adjusted in this manner until it approaches the magnet bore diameter. However, due to the novel resonant TE_{1n1} and TM_{1n1} resonant modes (with $n = 1, 2, 3, ...$) at extremely high cavities, mode clustering around the TE_{101} mode will occur, so an exhaustive investigation to achieve the optimal dimensions of the haloscope and to study its limits should be carried out (this analysis is presented in section 3.1). Furthermore, the multicavity idea may be adapted for other interresonator coupling directions, resulting in 2D structures that cannot only improve their volume and utilise the magnet bore space, but also add transmission zeros in the detector response for the rejection of undesired modes.

To conclude, as it is said previously, the sensitivity of the coaxial port coupling to probe location, size, and shape makes it necessary to create mechanical devices for controlling this coupling when data are taken for maintaining as much as possible the critically coupling case. When a frequency range is examined by a tuning mechanism this movable coupling device is required. The use of nanopositioners for the development of a moving coupling system is currently being designed by the RADES team (see section 3.4). Mechanical and EM mechanisms based on ferroelectric and ferromagnetic materials are being investigated for the tuning system (see section 4.1).

2.5 WAVEGUIDE FILTERS FOR SATELLITE COMMUNICATIONS

Satellite communications emerged in the 1970s and 1980s, boosting the area of Research and Development (R&D) for microwave filtering networks. The size and mass of the on-board equipment is a key cost issue for many satellite applications. Furthermore, RF power generation in space is quite costly, thus minimal losses in high RF power devices

are similarly important. Another critical consideration is that the equipment must work flawlessly in orbit for the duration of the satellite lifespan (typically around 12 years or more). During this time period, there were several developments and innovations in the field of filtering and multiplexing networks. Dual and trial-mode waveguide filters with arbitrary amplitude and phase responses, dielectric resonator filters, contiguous and non-contiguous channel multiplexing networks, Surface Acoustic Wave (SAW) filters, HTS filters, and a wide range of filters in coaxial, waveguide, planar, and microstrip technology were among those developed. The development of materials and procedures for large-scale manufacturing techniques, as well as cost-effectiveness for microwave filters in terrestrial systems, was driven by the advent of broad wireless cellular communication networks in the 1990s [74].

Later, when microwave communications systems extended around the world, there was a scarcity of EM spectrum available for a variety of services (telecommunications, broadcasting, security, and so on). This has resulted in increased RF signal processing and filtering needs in order to make the most use of the frequency spectrum. As a result, a race to design filters with the lowest Insertion Loss (IL) feasible inside the passband and the largest rejection possible within the stop band began [74].

In the realm of microwave communications systems, Computer-Aided Design (CAD) and tuning employing electromagnetic methods has played a critical role. Several advances in the production procedures of space microwave equipment have been implemented during the previous decade in order to attain cheaper prices. The application of cutting-edge technology in MicroElectroMechanical Systems (MEMS) and HTSs continues to fuel the area of R&D for microwave filter miniaturisation [74].

On the other hand, Additive Manufacturing (AM) procedures have been around for a long time, although they were not acknowledged as 3D printing techniques until 2012. Today, several sectors are focusing their efforts on incorporating additive structures into their line of business goods [82]. Although AM has not been widely used in the field of RF applied in space communications in the last ten years due to issues with availability of base materials and surface roughness, some structures with complex geometries can only be manufactured using this technology. This allows the employment of geometries that could not previously be afforded without the usage of this form of production, as well as obtain superior results for certain applications. As a result, these novel AM processes offer greater flexibility in the construction of new microwave filters in guided technology, as well as a smaller size. This has an obvious direct advantage in that the lower the weight and volume, the less expensive is to launch satellites into orbit [83].

Satellite communications play an important role in the current society, with numerous applications ranging from TV signal broadcasting to scientific exploration of outer space, including mobile communications, satellite assisted navigation systems (Global

Positioning System (GPS), GLObal NAvigation Satellite System (GLONASS), or Galileo), military applications, Very Small Aperture Terminal (VSAT) networks, and high capacity data transmission systems. As a result, it will be critical to conduct research initiatives to produce new RF components that may be utilised to improve future satellites.

The present PhD thesis investigates the methodologies for the study and design of novel components for the RF payloads of future communications satellites in the context mentioned above. This effort will be particularly focused on the development of novel bandpass filter systems, as a haloscope spin-off, for RF payloads of the future satellite communications systems. In Figure 2.20 an example of a RF bandpass filter based on waveguide technology at X-band is shown (Figure 2.20a depicts the 3D model of the structure and Figure 2.20b displays its electrical response). Attending Figure 2.12, a

(a)

(b)
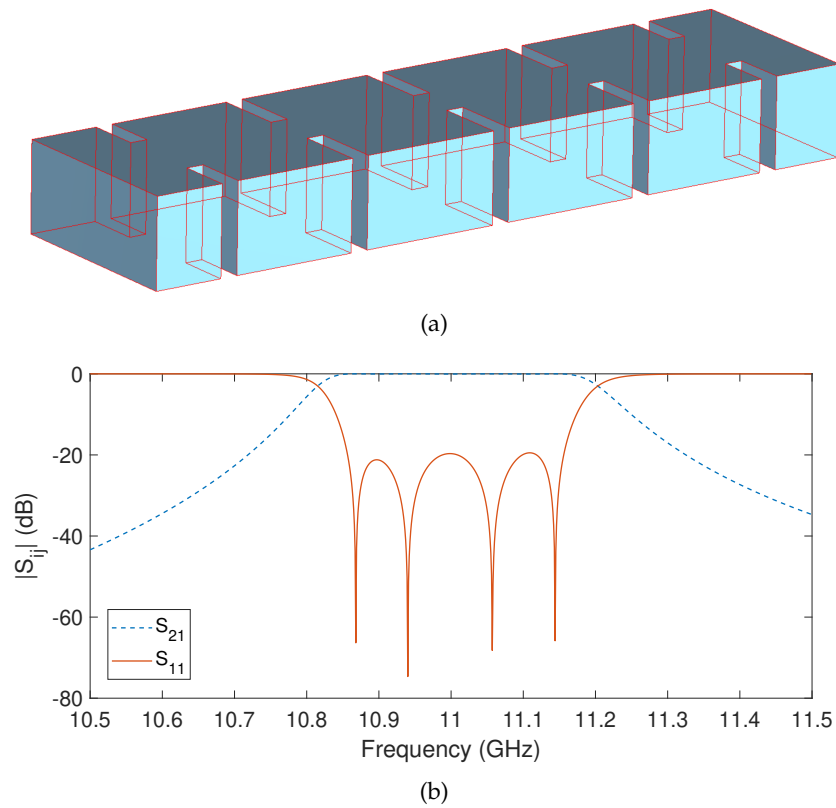
Figure 2.20: Example of a RF bandpass filter based on 4 resonant cavities with an all-inductive behaviour: (a) 3D model, and (b) electrical response of the filter.

clear similarity can be observed between the structure of a RADES multicavity haloscope and the one of a waveguide bandpass filter. However, their responses (Figures 2.14 and 2.20b, respectively) are designed working with different principles. In haloscopes, a unique resonance is desired for the axion detection to maximize its sensitivity, while for RF bandpass filters several resonances are needed to design the passband with an specific bandwidth, a parameter that is selected as a target in the designing process. The description of other parameters in RF bandpass filters is presented in section 6.

The creation of these components is typically time and resource intensive owing to the difficulties in designing the components, particularly due to their high sensitivity, and the requirement for correct electromagnetic modelling to forecast their circuit responses. This needs research into more efficient numerical procedures for completing the design of these components more quickly and reliably. Although there are currently many different methods for designing RF filters ([74, 84–87]), one of the project goals is to investigate new filter design techniques, as well as their suitability for the production of the above-mentioned components using dielectric parts with 3D techniques, incorporating complex geometries.

Furthermore, as previously said, dielectric elements with certain properties will be integrated in the new designs to regulate certain filter characteristics and, as a consequence, obtain superior results in bandpass filter response. The benefits are connected to the size of the final filters and the improvement of the spurious free range, selectivity in the passband, and filtering function rejection [88, 89].

Finally, the proposed project would prioritise experimental validation of the devices developed during the work. To that purpose, several prototypes will be built and then tested using the RF equipment available in the research group. The goal will be to demonstrate the practical feasibility of the new designed devices, with the goal of making them useful to the space industry.

3

IMPROVEMENTS IN DARK MATTER HALOSCOPES

The improvement in haloscope performance is one of the fundamental lines in all experimental groups searching for dark matter axions. Considering equation 2.10, the following parameters can be extracted to enhance the performance of a haloscope experiment:

- **Volume (V)**: the volume is a parameter that can be controlled with the dimensions of the haloscope cavity. The selection of the value for this parameter should take into account other criteria, like the scanning frequency and the magnet bore size.

- **Form factor (C)**: this parameter depends on the electromagnetic field distribution into the cavity volume and its parallelism with the static magnetic field of the external magnet. In multicavity structures, an optimum design should be carried out for the alignment of the electric field in all the subcavities. Then, in these cases the haloscope dimensions control the C parameter. Considering an homogeneous static magnetic field, for single cavities, the form factor will be maximum.

- **Loaded quality factor (Q_l)**: this parameter depends not only on the dimensions of the cavity but also on its material and operating temperature. In addition, the quality factor is critical in the manufacturing process, where an important reduction is usually obtained ($\sim 50\%$ from theoretical or simulated values) due to the necessity to apply cuts in the cavity walls, and thus interrupt the continuity of surface currents when the joint of the pieces is not perfect.

- **Mode clustering (Δf)**: the separation of the axion mode from the non-desired modes is a key issue that should be minimized to avoid the reduction of the form and quality factors due to the electromagnetic distortion of the axion mode from other mode interactions. This parameter sets the limits in the the maximum achievable volume of a haloscope cavity. Special attention should be paid to this parameter when using a tuning system to sweep a frequency range as in some cases mode crossings may exist, where a non-desired mode may go from being above the axion mode to being below it when a new frequency is scanned.

- **Magnetic field (B_e) and bore size of the magnet**: the properties of the employed magnet are an important aspect in a haloscope experiment. For large bores it is very difficult to maintain a high magnetic field. However, small magnets can provide a high magnetic field. Then, there is a trade-off with magnet volume and magnetic field when selecting a dipole or solenoid magnet. There are a multitude of magnets in the axion community, which will be reviewed in the following section.

- **Tuning system**: since the location of the axion in the electromagnetic spectrum is unknown, a scan of the widest possible range of masses (or frequencies) must be performed. Then, the optimization of the employed tuning system in a haloscope experiment is an essential feature for an efficient axion searching. In this PhD thesis, mechanical and electrical tuning systems are presented. The reduction of the time employed to shift the scanned frequency to a new frequency step is also crucial since there is a limited time in a data campaign.

- **External port coupling (κ)**: the objective for this parameter is to maintain its value in $\kappa = 0.5$, where a critical coupling status is acquired. To achieve this, an adjustable system is needed to correct the port position when performing a frequency sweep with the appropriate tuning system, in which the electromagnetic field of the mode will change and hence the maximum coupling condition.

- **System temperature (T_{sys})**: the temperature of the components in the haloscope experiments (like the cavity, LNA amplifier and cables) sets the value of this parameter. The temperature of the components is mainly controlled by the cryostat system at the employed magnet. For example, in the CAST dipole magnet the temperature was $T = 1.8$ K at the bore section where the cavity is inserted. Also, thermal plates are needed for a thermal transition in order to match the cables from the cryogenic temperatures to the room section.

- **Signal to noise ratio ($\frac{S}{N}$)**: as equation 2.9 depicts, $\frac{S}{N}$ depends on the above parameters (V, C, Q_l, B_e, κ, and T_{sys}) plus on the reception bandwidth (Δv), which can be controlled at the receiver.

- **Data taking time (Δt)**: this parameter is the time spent in a data campaign searching axions at a particular frequency into the selected spectrum range. The idea is to maximise the other parameters (volume, form factor, etc.) as much as possible to be able to accommodate Δt and the scanned frequency range to the needs imposed in a measurement campaign, where there will be a limited time to take data. The objective is to achieve in the axion-photon sensitivity ($g_{a\gamma\gamma}$) the models KSVZ and DFSZ (see Figure 2.5b).

The first five parameters (V, C, Q_l, Δf and the features of the magnets) are the main topic of the next section, where the volume limits are searched employing multitude of developed concepts considering several magnet sizes currently used in the axion community. In section 3.2 an extensive analysis is carried out to study the quality factor in manufacturing structures and several solutions are proposed for improving it. In addition, in section 5.2.3 the use of High Temperature Superconducting elements is exposed as a method for increasing the quality factor in the RADES structures [90]. The next two topics on the above list (tuning systems and external port coupling) are treated in sections 3.3 and 3.4, respectively. On the other hand, a new investigation line is understudy in the RADES team for a considerable reduction of the temperature in the haloscope experiments to mK values: the use of QuBits [91, 92], which affects mainly to the T_{sys} and $\frac{S}{N}$ parameters, which

is exposed in section 5.2.1. Finally, the improving of Δt is not covered in this work since it is a parameter that can only be controlled with the accessibility to a magnet. Generally, several axion teams required the use of the same magnet (this is the case of CAST or the future BabyIAXO magnet), so its use is limited in time.

3.1 VOLUME, FORM FACTOR AND QUALITY FACTOR OPTIMISATION

One of the primary goal of this work is to investigate the feasibility of expanding the volume of a haloscope based on rectangular geometries (which were the first used in the RADES collaboration), resulting in an increase in axion detection sensitivity. In addition, other essential ideas are covered, such as the improvement in mode clustering or mode separation, which is a vital characteristic of a haloscope to avoid the degradation of the form and quality factors [80]. The maximum volume allowed in a haloscope design is primarily determined by four factors: the cavity shape (rectangular or cylindrical), the electromagnetic operation mode and frequency, whether or not the multicavity concept is used, and the geometry and type of magnet (and thus the direction of the magnetic field) where the axion data taking will be conducted.

As it is said in section 2.4, the mode and type of cavities usually employed in dipole and solenoid magnets are the TE_{101} mode with rectangular cavities (see Figure 2.10d) and the TM_{010} mode with cylindrical cavities (see Figure 2.10c), respectively, since it maximizes the form factor because of the direction of the magnetic field of the magnets. However, there are some cases where rectangular haloscopes (working with the TE_{101} mode) could fit into a solenoid magnet depending of the size of the bore. In this sense, a proper study should be carried out in the current axion community magnets for selecting the most appropriated bore in our haloscope design. In the case of the dipole magnet CAST employed by the RADES team several years ago, it possesses a very limited bore diameter compared with other magnets, but with a very large length, involving to apply the idea of the multicavity concept in the longitudinal axis ($z-$axis in Figure 2.10d). However, a different designing approach (regarding the cavity volume limits) can be applied in larger bores, for example in the future BabyIAXO magnet, whose magnetic field pattern is defined by a superconducting toroidal magnet [59], although it can be approximated as a dipole magnet for simplicity in this PhD thesis. Its huge bore, compared to CAST, makes possible the application of other ideas that combine tall and/or long cavities with the multicavity concept in any axis. In Table 3.1 the information of the most well-known magnets employed by different axion groups is described. A constant magnetic field $\vec{B}_e = B_e \hat{y}$ in dipole and quasi-dipole [59] magnets was chosen as an approximation for calculating the form factor in this PhD thesis.

In such table, the custom figure of merit of the magnets takes into account the influence of the parameters B_e, V and T_{sys} in equation 2.10, assuming a hypothetical cavity filling the entire magnet bore and that the temperature and magnetic field is stable and homogen-

Magnet	Type	B_e (T)	T (K)	ϕ (mm)	L (m)	$\frac{B_e^2 V}{T}$ ($\frac{T^2 m^3}{K}$)	References
BabyIAXO	Quasi-dipole	~ 2.5	4.2	600	10	4.207	[59]
CAST (cancelled)	Dipole	9	1.8	42.5	9.25	0.591	[63]
SM18	Dipole	11	4.2	54	2	0.132	[90]
MRI (ADMX-EFR)	Solenoid	~ 9	0.1	650	0.8	215.03	[93]
ADMX (1st gen)	Solenoid	8	0.1	600	1.1	199.05	[94]
ADMX-HF	Solenoid	9	0.025	175	0.4	31.17	[94, 95]
Canfranc	Solenoid	10	0.01	130	0.15	19.9	[96]
CAPP-8TB	Solenoid	8	0.05	165.4	0.476	13.1	[97]
ORGAN	Solenoid	14	0.03	65	0.445	9.633	[30, 98]
Oxford-Instr.	Solenoid	12	4.2	320	0.75	8.27	[99]
HAYSTAC	Solenoid	9	0.127	140	0.56	5.496	[72]
18T HTS (ADMX)	Solenoid	~ 18	0.11	70	0.467	5.294	[100, 101]
QUAX	Solenoid	~ 1	0.12	150	0.5	0.075	[102]

Table 3.1: Details of some magnets in the axion community: name and type of magnet, magnetic field B_e in Teslas, temperature T in Kelvins, diameter ϕ in milimeters, length L in meters, and figure of merit of the magnet in $\frac{T^2 m^3}{K}$. The figure of merit employed here is in accordance with equation 2.10, assuming that a hypothetical haloscope possesses the same volume of the magnet.

eous in all the volume. In reality, this is not possible due to geometrical incompatibilities, and B_e and T_{sys} deviations. However, as a first approximation it shows the potential of each magnet. In Figure 3.1 several pictures of real magnets are shown: the ADMX solenoid magnet with its setup (see Figure 3.1a) and a dipole magnet (CAST) with the RADES setup (see Figures 3.1b, 3.1c and 3.1d).

In general, the dipole magnet bore is much longer than its radii. This is the case with the CAST and BabyIAXO magnets, which have diameters of 42.5 and 600 mm and lengths of 9.25 and 10 m, respectively [59, 63]. The length and the diameter of the solenoid magnet bores, on the other hand, are very comparable. This is the case with the Canfranc and MRI (ADMX-EFR) magnets, which have diameters of 130 and 650 mm, respectively, and lengths of 150 and 800 mm [93, 96]. The initial concept for utilising the space in dipole magnets is to expand the overall length of the haloscope. The length of the subcavities can be expanded for this purpose by using the multicavity idea [27, 80]. In fact, one of the first attempts to exploit long cavities in the axion community was to design, develop and implement a toroidal-shaped cavity [103, 104]. However, it will be demonstrated that the use of novel topologies, such as tall structures on dipole and solenoid magnets, are also highly attractive notions.

The volume constraints in a haloscope based on a single cavity (with regard to the mode clustering) are illustrated in section 3.1.1. Some significant principles are introduced in section 3.1.2 to construct a haloscope based on the multicavity concept in order to enhance its capacity as much as feasible. A first step for setting the foundations for the development of the previous constructions to use even more of the space available in the bore of the magnets is further explored in section 3.1.3.
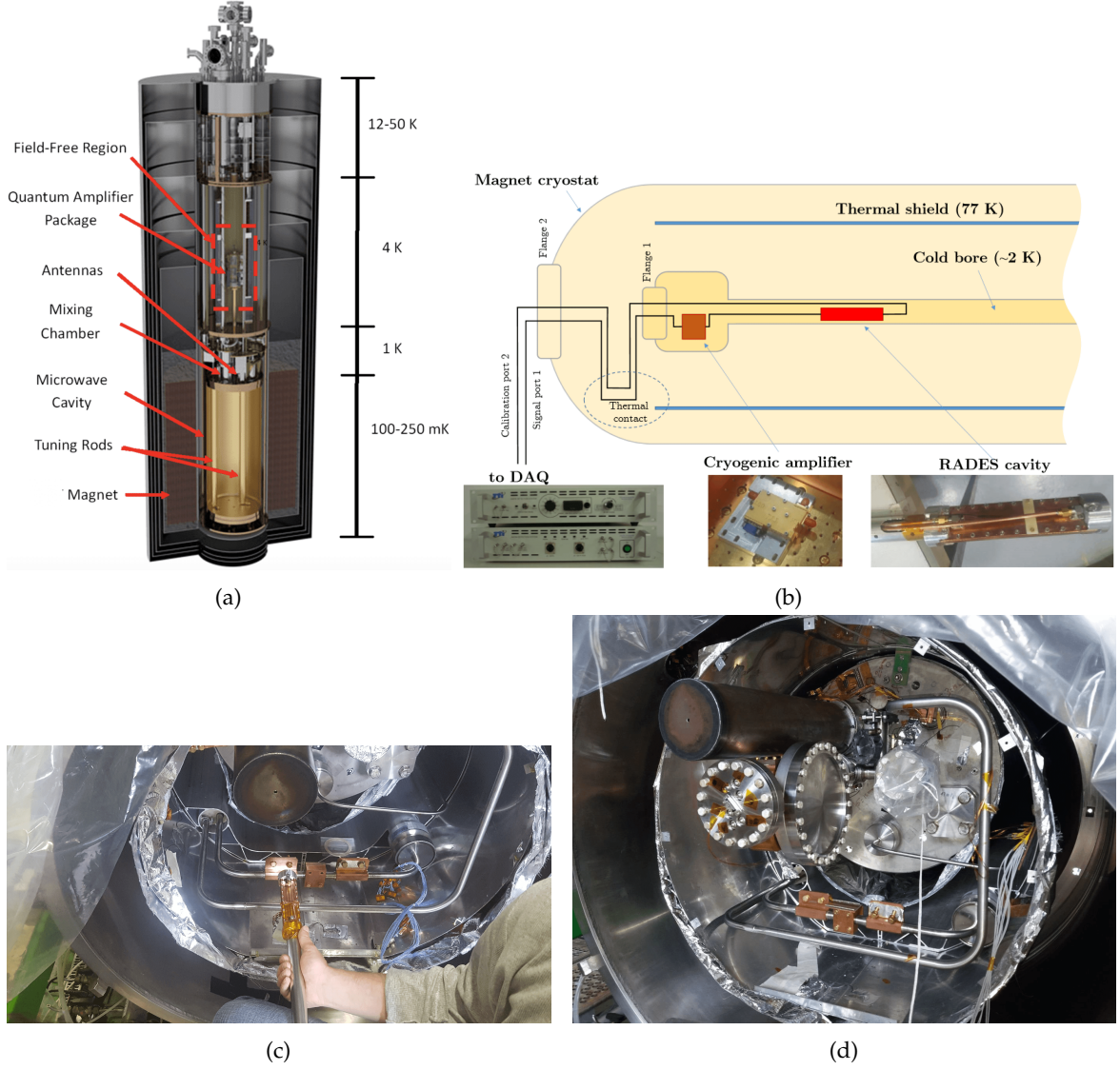
Figure 3.1: Schemes of real magnets: (a) ADMX solenoid magnet with descriptions of its sections, (b) diagram of the CAST magnet with a RADES installation, (c) picture of a RADES member introducing the 5-subcavities haloscope into one of the two 42.5 mm CAST bores, and (d) picture of the CAST bore closed showing the flange (*Flange* 1 from (b)) where the cables are connected for the internal electronics.

3.1.1 *Volume limits in single cavities*

The TE_{101} mode is used for rectangular cavities functioning in dipole magnets because it optimises the form factor specified in equation 2.6. Since $n = 0$ (see equation 2.17), the height of the cavity b has no effect on the resonant frequency $f_{TE_{101}}$ for this mode, hence it can be adjusted as desired to increase the cavity volume. There is a limit, however, where the height of the cavity cannot be raised owing to the proximity of the higher modes with $n \neq 0$ (in this case, closeness with the TE_{111}), which may impede accurate mode identification and may even diminish the form factor in some situations.

In addition, when considering equation 2.17 it is discovered that the simplest way to expand the haloscope length without decreasing the resonant frequency of the TE_{101} mode is to slightly reduce the width. Because this reduction is little in comparison to the length gained, the overall volume will grow. Furthermore, when the cavity length is substantially greater than the width, the resonant frequency becomes independent of the cavity length $f_{TE_{101}} \approx \frac{c}{2a}$. Again, the closeness of the next resonant mode (mode clustering with the TE_{102}) imposes a length constraint. Several ways for raising the volume of haloscopes without reducing the resonance frequency of the TE_{101} mode will be described in the following subsections.

3.1.1.1 Long cavities

As previously mentioned, the mode separation (Δf) between the modes TE_{101} and TE_{102} determines the ability to extend the length, d, of a rectangular single cavity. This parameter is computed with equation 2.19. The relative mode separation for a rectangular cavity as a function of d/a is plotted in Figure 3.2a, which is valid for any resonant frequency of TE_{101} and height b.

(a)   (b)
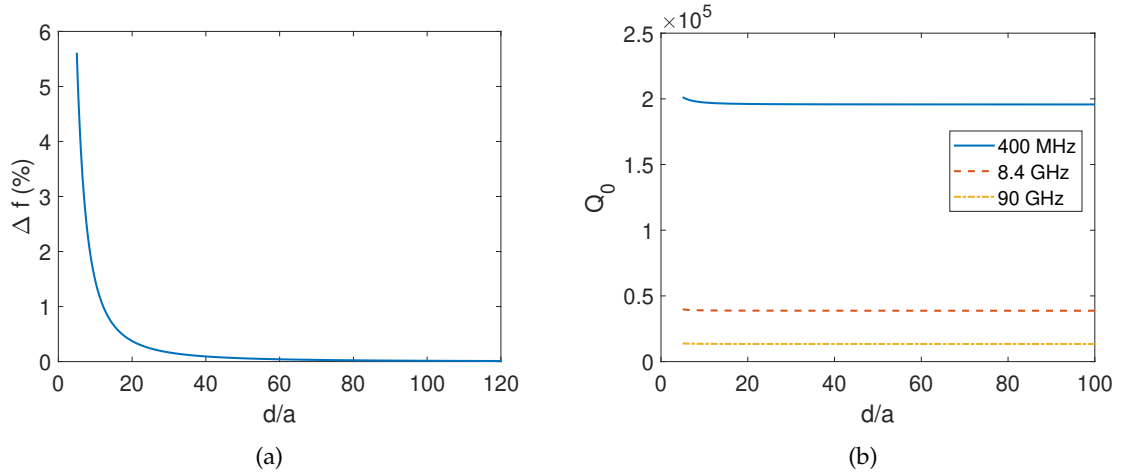
Figure 3.2: (a) Relative mode separation between modes TE_{101} and TE_{102} of a rectangular cavity versus d/a (valid for any frequency), and (b) unloaded quality factor of the TE_{101} mode versus d/a for 3 frequencies (0.4, 8.4 and 90 GHz).

The findings reveal that when d/a grows, the mode separation decreases rapidly. If the following mode is far enough away in frequency, the value of C for any cavity size will reach the theoretical maximum: $C_{TE_{101}} = 64/\pi^4 = 0.657$, calculated from equation 2.6.

The Q_0 factor of a TE_{10p} mode in a rectangular waveguide cavity resonator with no dielectric losses is given by [70]

$$Q_0 = \frac{1}{2}\sqrt{\frac{\pi\,\sigma}{\varepsilon_0\,f_{10p}}} \frac{b\left(a^2+d^2\right)^{3/2}}{ad\left(a^2+d^2\right)+2b\left(a^3+d^3\right)}, \tag{3.1}$$

where σ is the electrical conductivity of the haloscope housing or cavity walls (we assume $\sigma = 2 \times 10^9$ S/m in this study, which corresponds to the copper case at cryogenic temperatures), $\varepsilon_0 \approx 8.854 \times 10^{-12}$ F/m is the electric permittivity in vacuum, f_{10p} is the resonant frequency of a TE_{10p} mode, and p is the number of the sinusoidal fluctuations along the longitudinal $z-$axis ($p = 1$ for the operation mode). Furthermore, equation 3.1 demonstrates that the unloaded quality factor drops with increasing frequency, which is equal to decreasing the cavity width. Figure 3.2b shows that the Q_0 parameter is also length independent for large d values.

As an example, the Q_0 value of the TE_{101} mode for a rectangular cavity of width $a = 17.85$ mm and height $b = 10.16$ mm (operating at $f_{TE_{101}} = 8.4$ GHz, X-band) is $Q_0 \approx 3.9 \times 10^4$ for any d between $500 - 2000$ mm (or d/a between $28 - 112$). For $f_{TE_{101}} \approx 400$ MHz (UHF-band) and $f_{TE_{101}} \approx 90$ GHz (W-band) the quality factor acquires values around $Q_0 = 2 \times 10^5$ and $Q_0 = 1.3 \times 10^4$, respectively, for the same range of d/a, as it can be seen in Figure 3.2b.

The lowest acceptable mode separation is determined by the measured quality factor in production, which depends on the housing material and manufacturing process quality. Larger Q_0s provide sharper resonances, allowing modes to get closer in frequency. In general, due to limitations in the fabrication process, we should expect the unloaded quality factor of the produced prototype to be around half of the theoretical. These limitations are usually the roughness at inner walls, the quality in soldering, and the metallic contact if screws are used. The form factor as a function of d/a for four Q_0 values is displayed in Figure 3.3a as a quantification of the mode clustering on the energy loss. This graphic demonstrates how the decrease in C is smaller for high Q_0 values. The form
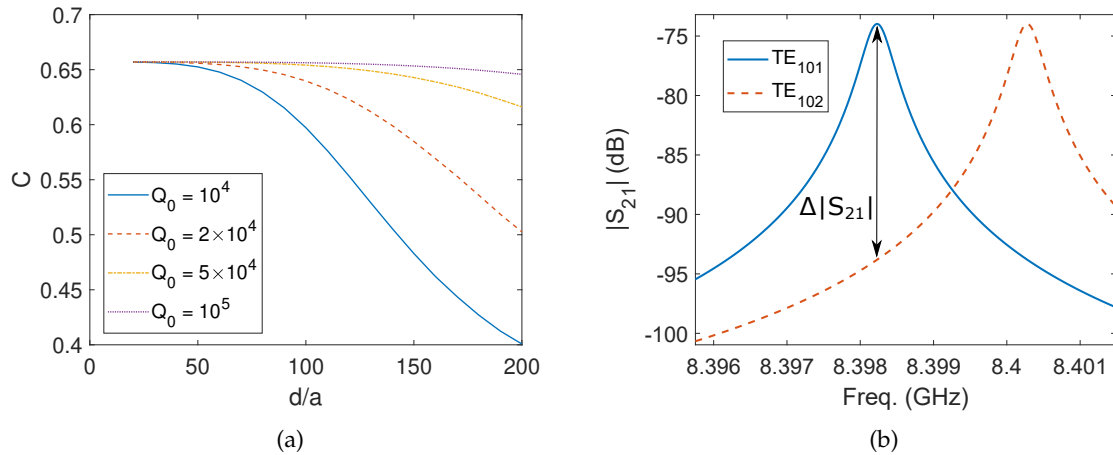
Figure 3.3: (a) C parameter as a function of d/a for four Q_0 values, and (b) example of two modes very close whose resonances have an amplitude difference of $\Delta|S_{21}| = 20$ dB at the resonant frequency of the mode TE_{101}.

factor in Figure 3.3a was calculated using equation 2.6, taking into account the disturbance of the electric field (and therefore its C detriment) caused by the impact of the following resonant mode E-field (the one from the TE_{102} mode in this example) when they are quite

near. As a result of this behaviour, the E-field effect of the next mode is greater if the difference in dB in the S_{21} parameter of both modes TE_{101} and TE_{102} at $f_{rTE_{101}}$ ($\Delta|S_{21}|$) is less. Because of mode clustering, we chose a form factor of $C = 0.65$ as our lowest admissible reduction value. The cavity length is thought to be expanded even if C declines, as long as the $Q_0 \times V \times C$ factor (the figure of merit of a haloscope) continues to rise. To be cautious, the above value is maintained as a conservative limit. This constraint also guarantees that the resonant frequency f_r and the quality factor Q_0 values are measured correctly in the manufactured structure. In any case, if the cavity response shows two resonances that are extremely near or even mixed (owing to lower than expected quality factors), there are ways to recover the original form of each resonance and compute these two parameters [105]. Figure 3.3b shows an example of two modes whose resonances are very close for an operation frequency of 8.4 GHz with $Q_0 = 2 \times 10^4$ and $d = 1400$ mm (or $d/a \approx 79$), resulting in a $C = 0.65$ ($\sim$ 99 % of $C_{max} = 0.657$). Figure 3.3 graphs aid in selecting the guard frequency to prevent a large form factor decrease.

An X-band example is created to demonstrate this subject, with $a = 17.85$ mm, $b = 10.16$ mm, and $d = 1400$ mm. The spacing between the axion mode and its first neighbour in this design is 2.05 MHz (or 0.024 %). Furthermore, the volume value for this prototype is $V = 253.9$ mL, representing a 38 improvement in C over a standard WR-90 cavity ($a = 22.86$ mm, $b = 10.16$ mm, and $d = 28.55$ mm, which gives a volume of $V = 6.73$ mL). An overview of the acquired upgrades in this comparison is presented in Table 3.2.

a (mm)	b (mm)	d (mm)	V (mL)	Q_0	C	$Q_0 \times V \times C$ (L)
22.86	10.16	28.55	6.63	4.6×10^4	0.657	200.37
17.85	10.16	1400	253.9	3.9×10^4	0.65	6436.37

Table 3.2: Summary of the parameters obtained in a rectangular resonant cavity with a working frequency of 8.4 GHz for two cases: standard WR-90 cavity and very long cavity (large d).

This large cavity fits loosely in the CAST dipole magnet, as it is shown in Table 3.1. For a solenoid magnet, however, the cavity length should be decreased to match the bore diameter. In MRI (ADMX-EFR), for example, a longitudinal limit of $d \approx \phi_{MRI} = 650$ mm is enforced. Because of the magnetic field direction, the longitudinal axis of the cavity should be oriented in any radial axis of the solenoid magnet (x or $y-$axis in Figure 2.10c), as mentioned in the previous subsection. In this situation, there is a lot of remaining space along the solenoid magnet longitudinal axis ($z-$axis in Figure 2.10c). In any case, the extra volume from a conventional cavity is still significant.

The haloscope sensitivity reached in the limit situation presented in Table 3.2 is quite good at one frequency, but great attention must be paid if a specific frequency range is to be swept because there are likely to be multiple mode crossings. As a result, while developing one of these structures, the dimensions will be constrained by a trade-off between the volume obtained and the number of mode crossings tolerated, while also considering the magnet bore size.

3.1.1.2 *Tall cavities*

The vertical dimension b, like the longitudinal dimension of a single cavity, can be raised up to a limit dictated by the closeness of the next modes (mode separation between the TE_{101} and the TE_{111}/TM_{111}). The width a value is not lowered in the case of tall cavities as it controls the cutoff frequency of the TE_{10} mode and influences the resonant frequency of the cavity. As the height b value increases, the Q_0 value increases up to half of the limit, as illustrated in Figure 3.4a. As an example at 8.4 GHz (X-band), an unloaded quality factor

(a)   (b)
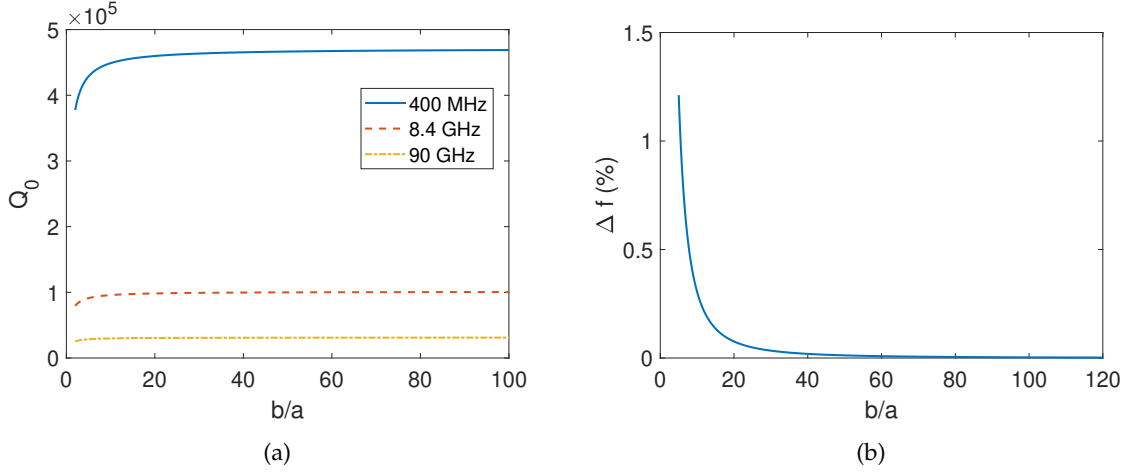
Figure 3.4: (a) Unloaded quality factor of the mode TE_{101} versus the b/a parameter for several frequencies (0.4, 8.4 and 90 GHz), and (b) mode separation between the modes TE_{101} and TE_{111}/TM_{111} of a single cavity versus b/a for X-band ($d = 28.55$ mm).

of $Q_0 = 10^5$ is achieved for heights b ranging from 500 mm to 2000 mm. The value of this parameter for ~ 400 MHz (UHF-band) and ~ 90 GHz (W-band) is roughly $Q_0 = 4.7 \times 10^5$ and $Q_0 = 3.1 \times 10^4$, respectively, as it is shown in Figure 3.4a. For clarity, the frequency closeness with the nearest mode for X-band frequencies (where a length $d = 28.55$ mm is employed) is also displayed in Figure 3.4b. Analogously to the results from Figure 3.2a, the findings reveal a behaviour with a quick increase in mode separation for low b/a values, while for high values Δf begins to stabilise at values tending to zero.

The same condition of $C_{min} = 0.65$ is enforced to discover the minimal permitted mode separation. Figure 3.5 plots the form factor parameter versus b/a for four Q_0 values, considering that the E-field contribution that now negatively impacts C is the one from the TE_{111} mode. As with long cavities, this graphic illustrates that for large Q_0 values, the impairment in C is lesser.

When the same analysis for long cavities at X-band is done to establish the lowest accepted mode separation, the limit is obtained with $b = 1500$ mm (or $b/a = 66$), taking into consideration a Q_0 after manufacturing of $Q_0^{real} \approx 50000$ (half of the simulated one).

For this example, the mode separation between the axion mode and the next resonant mode is 0.59 MHz (or 0.007 %), which has been obtained employing the dimensions
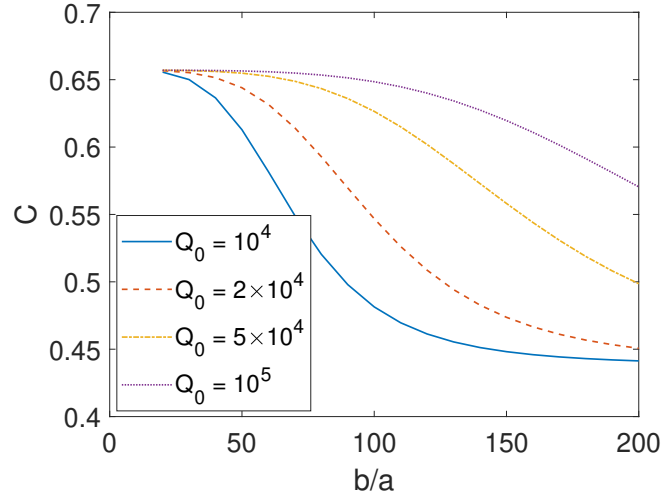
Figure 3.5: C parameter as a function of b/a for four Q_0 cases.

$a = 22.86$ mm, $b = 1500$ mm, and $d = 28.55$ mm. In this scenario, the volume is $V = 978.98$ mL, representing a 148 improvement over a standard WR-90 cavity. Table 3.3 shows a summary of these enhancements.

a (mm)	b (mm)	d (mm)	V (mL)	Q_0	C	$Q_0 \times V \times C$ (L)
22.86	10.16	28.55	6.63	4.6×10^4	0.657	200.37
22.86	1500	28.55	978.98	10^5	0.65	6.4×10^4

Table 3.3: A comparison of the parameters of a standard rectangular resonant cavity operating at 8.4 GHz with a very tall cavity (high b value) resonating at the same frequency.

With a focus on Table 3.1 it is clear how the height of this tall cavity must be reduced until it fits into the solenoid magnet along longitudinal axis. In MRI (ADMX-EFR), for example, a maximum cavity height of $b = L_{MRI} = 800$ mm is enforced. In any case, the added volume from a standard cavity is once again quite large. The only alternative with a significant benefit for a dipole magnet is BabyIAXO, whose diameter bore ($\phi_{BabyIAXO} = 600$ mm) may be employed to accommodate this tall cavity in the radial orientation ($y-$axis in Figure 2.10d). Thus, with this situation, there is a lot of vacant space on the dipole longitudinal axis ($z-$axis in Figure 2.10d), which may also be used with the novel concepts given in the next subsections.

Similarly to the structures from the previous section, the sensitivity value obtained in the cavity haloscope for the scenario illustrated in Table 3.3 is very high at one frequency, however numerous mode crossings might arise if a tuning device is used. As a result, throughout the design phase, the dimensions will be constrained by a trade-off between increasing the volume, the number of mode crossings, and the size of the magnet.

3.1.1.3 *Large cavities*

The last method for boosting the volume of a single cavity is to raise both the length and height dimensions simultaneously. As previously stated, the width of a very long cavity should be significantly lowered to retain the same resonant frequency, which, on the other hand, is not affected by the height, as stated in the preceding sections. The mode clustering issue must now take into account two mode approximations to our working mode: the TE_{102} (due to the longitudinal dimension d) and TE_{111} (due to the vertical dimension b) modes. The relative mode separation follows the behavior seen in Figure 3.6a for X-band frequencies ($d = 28.55$ mm). The results reveal that when d/a
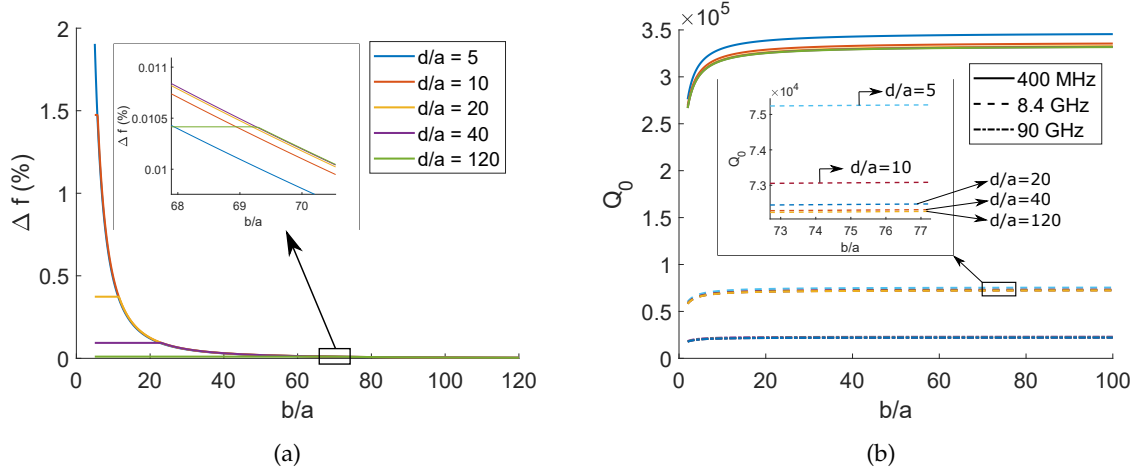
Figure 3.6: (a) Relative mode separation for X-band frequencies ($a = 17.85$ mm) between modes TE_{101} and TE_{102} or TE_{111} (the closest one, which depends on the b/a and d/a parameters). (b) TE_{101} mode quality factor versus b/a at several frequencies (0.4, 8.4, and 90 GHz) for five d/a examples. The insets in both plots indicate a zoom to differentiate all of the d/a situations. In (a) a clear change in the curve behaviour can be observed due to the proximity of different modes (TE_{102} or TE_{111}) to the TE_{101} mode.

and/or b/a grow, the mode separation decreases rapidly.

Figure 3.6b depicts the behavior of the unloaded quality factor in these scenarios. For the X-band case, a width of $a = 17.85$ mm is required to maintain $f_r = 8.4$ GHz. The cavity gives a $Q_0 = 7.2 \times 10^4$ for d and b between $500 - 2000$ mm, as illustrated in the inset of Figure 3.6b. The Q_0 is significantly lower than in the tall cavity because the width has been slightly lowered to compensate for the increase in length.

Furthermore, we accept a form factor of $C = 0.65$ in order to establish the minimum mode separation. Now, the contributions of the electric field that have an unfavorable effect on C come from both the TE_{102} and TE_{111} modes. The behavior of the parameter C with d/a, b/a, and Q_0 is comparable to the case shown in Figures 3.3a and 3.5. The limit for 8.4 GHz is attained with the values $b = 1100$ mm and $d = 1600$ mm, with an unloaded quality factor after manufacturing of $Q_0^{real} \approx 3.6 \times 10^4$ (half of theoretical). An overview of the realized improvements is provided in Table 3.4. The $Q_0 \times V \times C$ factor is increased by

7336 when compared to the standard cavity.

a (mm)	b (mm)	d (mm)	V (mL)	Q_0	C	$Q_0 \times V \times C$ (L)
22.86	10.16	28.55	6.63	4.6×10^4	0.657	200.37
17.85	1100	1600	3.14×10^4	7.2×10^4	0.65	1.47×10^6

Table 3.4: A comparison of the parameters of a standard rectangular resonant cavity operating at 8.4 GHz with a very long and tall cavity (high d and b values) resonating at the same frequency.

With these results and data from Table 3.1, it is clear that in dipole magnets the best orientation for this type of cavity is obtained by aligning both longitudinal axis of the magnet bore and the cavity since it provides the highest dimension values, and both the magnetic field of the magnet and the E-field of the cavity are parallel. In BabyIAXO, for example, the height of the cavity can be raised up to $b = 600$ mm ($y-$axis in Figure 2.10d), and the length can be set to its limit $d = 1600$ mm ($z-$axis in Figure 2.10d), giving a volume value of $V = 1.71 \times 10^4$ mL with $a = 17.85$ mm, which involves a volume enhancement of 2580 over a standard cavity. The cavity height in a solenoid magnet must match the bore longitudinal axis ($z-$axis in Figure 2.10c), and the length of the haloscope can fill all of the bore radial axis (x or $y-$axis in Figure 2.10c). At the MRI (ADMX-EFR) solenoid magnet, for example, a haloscope of $a = 17.85$ mm, $b = 800$ mm, and $d = 650$ mm may be fitted, implying a volume of $V = 9282$ mL. This yields to a reduction in volume by half as compared to the BabyIAXO dipole magnet. However, this reduction can be offset by the low ADMX operating temperature (lower T_{sys} in equation 2.10) and high magnetic field values (see Table 3.1).

Figure 3.7 illustrates various sketches of each type of cavity employing the dimensions at the studied limit values: long, tall, and large (long and tall) single cavities.

Lastly, as with tall or long cavities, the haloscope sensitivity achieved in the example given in Table 3.4 is quite good at one frequency, although multiple mode crossings may occur with a tuning mechanism. As a result, the final dimensions of the designed cavity should take into account the trade-off between volume, mode-crossing, and magnet size.

3.1.2 *Volume limits in 1D multicavities*

Over the previous six years, the RADES team has used the multicavity idea to expand the volume of haloscopes along the longitudinal axis without diminishing the frequency [68]. Unlike the long cavity approach, $z-$axis multicavity designs may utilise wider rectangular waveguides (for instance, the standard WR-90 employed for X-band).

This experimental group has designed and built many small haloscope prototypes (see Figures 2.12b and 2.17), being the first three an all-inductive structure with five subcavities and two alternating structures based on two different number of subcavities ($N = 6$ and
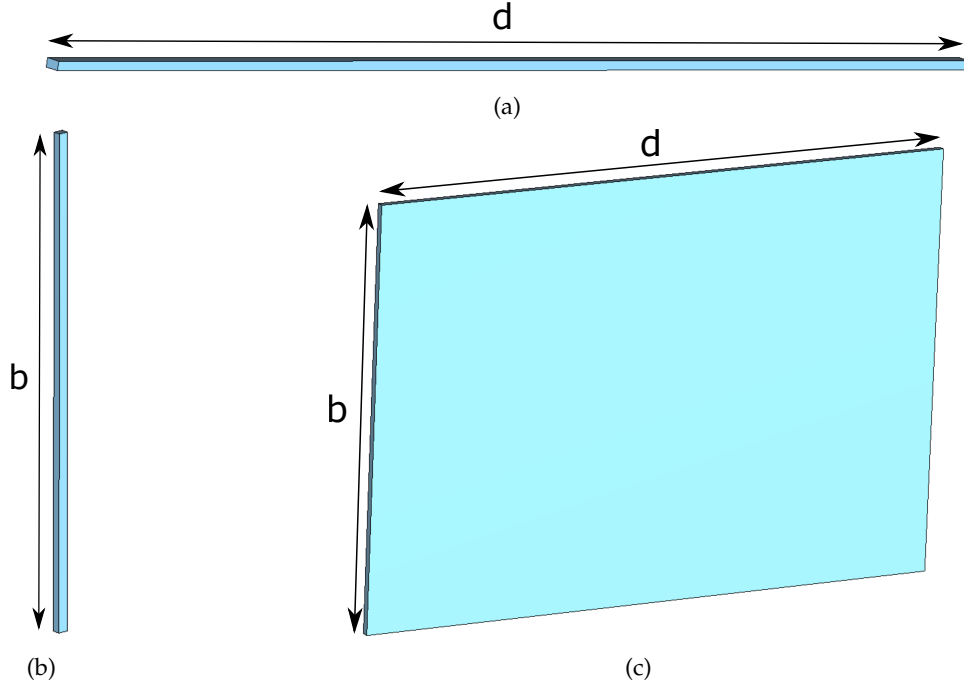
Figure 3.7: (a) Long resonant cavity of $d = 1400$ mm, (b) tall structure of $b = 1500$ mm and (c) Large (long and tall) cavity of $b = 1100$ mm and $d = 1600$ mm.

$N = 30$, where N is the number of subcavities). In [27, 68, 79, 80, 106], the results of the first two structures can be consulted.

The coupling matrix was used as a supporting tool in the design of the haloscope multicavity constructions. In [27, 74], the theoretical notions of this technique can be found. For the 1D multicavities case, the following matrix was used to enhance geometrical parameters in the structures explored in this work:

$$
\mathbf{M} = \begin{pmatrix}
\Omega_1 & M_{1,2} & 0 & 0 & \cdots & 0 & 0 & 0 \\
M_{1,2} & \Omega_2 & M_{2,3} & 0 & \cdots & 0 & 0 & 0 \\
0 & M_{2,3} & \Omega_3 & M_{3,4} & \cdots & 0 & 0 & 0 \\
0 & 0 & M_{3,4} & \Omega_4 & \cdots & 0 & 0 & 0 \\
\vdots & \vdots & \vdots & \vdots & \ddots & \vdots & \vdots & \vdots \\
0 & 0 & 0 & 0 & \cdots & \Omega_{N-2} & M_{N-2,N-1} & 0 \\
0 & 0 & 0 & 0 & \cdots & M_{N-2,N-1} & \Omega_{N-1} & M_{N-1,N} \\
0 & 0 & 0 & 0 & \cdots & 0 & M_{N-1,N} & \Omega_N
\end{pmatrix},
\tag{3.2}
$$

where $M_{i,j}$ are the values of the impedance inverters in the normalised low-pass prototype network and Ω_q is the discrepancy between the resonant frequency in the q-th subcavity and the frequency of the axion mode [74]. The physical interresonator coupling k used in the design is related to $M_{i,j}$. A low-pass to band-pass transformation ($\Omega = \left(\frac{f}{f_{axion}} - \frac{f_{axion}}{f} \right) \frac{1}{f_B}$, where $f_B = \frac{BW}{f_{axion}}$ is the fractional bandwidth and BW is the bandwidth) is commonly performed to extract its value [74]. All multicavity designs in this work use a bandwidth of $BW = 100$ MHz. The relationship with the coupling value is given by [74]:

$$
M_{i,j} = \frac{k_{i,j}}{f_B},
\tag{3.3}
$$

where $k_{i,j}$ denotes the physical coupling between the resonators i and j. More information about these factors is detailed in [74]. The value of the parameter Ω_q can be obtained by using the condition $\mathbf{M} \times \mathbf{1}_N^T = \mathbf{0}_N^T$, where $\mathbf{1}_N$ is a 1-vector and $\mathbf{0}_N$ is a 0-vector, both with a size of N [27, 74]. The dimension of this matrix ($N \times N$) is determined by the number of subcavities N. Furthermore, the element values outside the three main diagonals are 0. This means that resonators that are not adjacent have no physical coupling.

At first look, it may appear that resonant mode clustering would be unproblematic because the TE_{102} mode is far distant due to the short length of the subcavities. However, the multicavity provides extra resonant modes related with the coupled subcavity system eigenmodes, known as *configuration modes* [27]. All the TE_{mnp} resonant mode have these configuration modes. As the number of subcavities rises and the interresonator coupling value k falls, their resonant frequencies approach the axion eigenmode. The theory and techniques for obtaining the physical coupling k are detailed in [80]. For each TE_{mnp} mode, the number of configuration modes in a multicavity is the same as the number of subcavities.

Higher interresonator couplings result in shorter subcavities (in length) to maintain the same resonant frequency due to the loading effect of the iris windows [74]. For 8.4 GHz (our example), where lengths may vary by 1 or 2 mm, this effect is minor. However, for very large k values, the coupling iris must be opened extensively resulting in a severe loading effect. This impact will have to be considered even for relatively low k values in other frequency bands, such as UHF. Thus, there is again another trade-off between volume and mode separation. Figure 3.8 compares an example of the figure of merit ($Q_0 \times V \times C$) of single and multicavity designs at 8.4 GHz as a function of total volume (increasing the length for the single cavity case and the number of subcavities for the multicavity case) [1]. A physical coupling value of $|k| = 0.0377$ has been used, a similar parameter to the one usually employed in RADES [80].

The following steps comprise the procedure of the multicavity design: firstly, the axion search frequency (in our case, for the resonant mode TE_{101}) and a interresonator coupling k value (physically realisable) are selected [27]. Second, the coupling matrix approach is used to calculate the subcavity natural frequencies, as detailed in [27]. Lastly, an iterative optimization process is performed in which the subcavities and the irises are tuned to resonate at the desired frequency and to produce the desired physical coupling, respectively.

Instabilities in design outcomes are detected as a result of high sensitivity in the C parameter during the optimization process, which becomes more difficult as the number of subcavities increases (as it is shown in Figure 3.8). Overcoming these challenges would result in an enhancement similar to the theoretical multicavity case, which is superior than

---

1 A similar investigation might be conducted by increasing the height b and the number of subcavities N in the vertical direction, correspondingly.
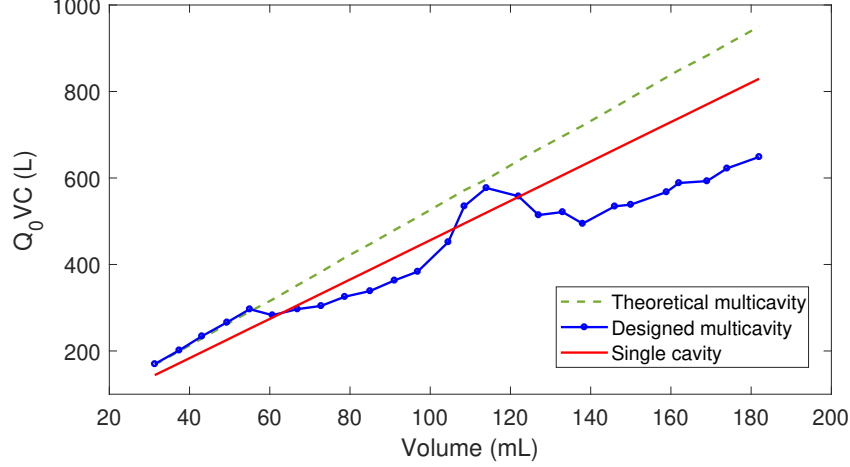
Figure 3.8: $Q_0 \times V \times C$ factor of a single cavity versus multicavity structures (theoretical and designed). Each spot at the designed multicavity results (blue curve) represents a specific number of subcavities ($N = 5$ to 30 subcavities, from left to right). The case $N = 5$, the starting point, is the first RADES haloscope design, which can be observed in Figure 2.12b. Its response is detailed in [27].

the improvement attained with a single cavity, and therefore the multicavity idea appears to be the best option for boosting the sensitivity of the axion detector. Concerning the quality factor, it has been determined from Figure 3.8 that it is unaffected by N. For this comparison, the multicavity has a somewhat larger value since it has a standard width $a = 22.86$ mm (for the single cavity design based on a long length, it must be decreased to $a = 17.85$ mm) and the Q_0 is significantly dependent on this dimension, as discussed in earlier sections. According to these considerations (see Table 3.2), the unloaded quality factor assumes values around 4.6×10^4 for $a = 22.86$ mm and $Q_0 \approx 3.9 \times 10^4$ for $a = 17.85$ mm. As a result, Q_0 represents the difference in the slope of the $Q_0 \times V \times C$ behaviour between single cavities and multicavities.

Regarding the mode clustering problem, there is a method to relocate the TE_{101} mode neighbour configuration modes away from the axion mode for multicavities. This approach is based on switching the signs of the iris couplings, which is accomplished realistically by employing the two types of irises explained in [80] (capacitive and inductive windows). The axion is at the first configuration mode of the TE_{101} resonant mode for an all-inductive haloscope (which has $k < 0$), and at the last one for an all-capacitive structure ($k > 0$). The axion mode in an alternating inductive/capacitive structure, on the other hand, is the one at the middle (for N being odd) or the mode at the position $\frac{N}{2} + 1$ (for N being even), where the mode separation is greater. Figure 3.9a depicts an example of the magnitude of the S_{21} parameter versus the frequency for the three preceding scenarios (all-capacitive, all-inductive, or alternating irises) in a $N = 6$ multicavity employing irises with $|k| = 0.0377$. As it can be observed, the axion mode is provided by the all-inductive and all-capacitive multicavities at their first and last resonances, respectively, whilst the alternating structure provides it at $\frac{N}{2} + 1 = 4$. The relative mode clustering between

45
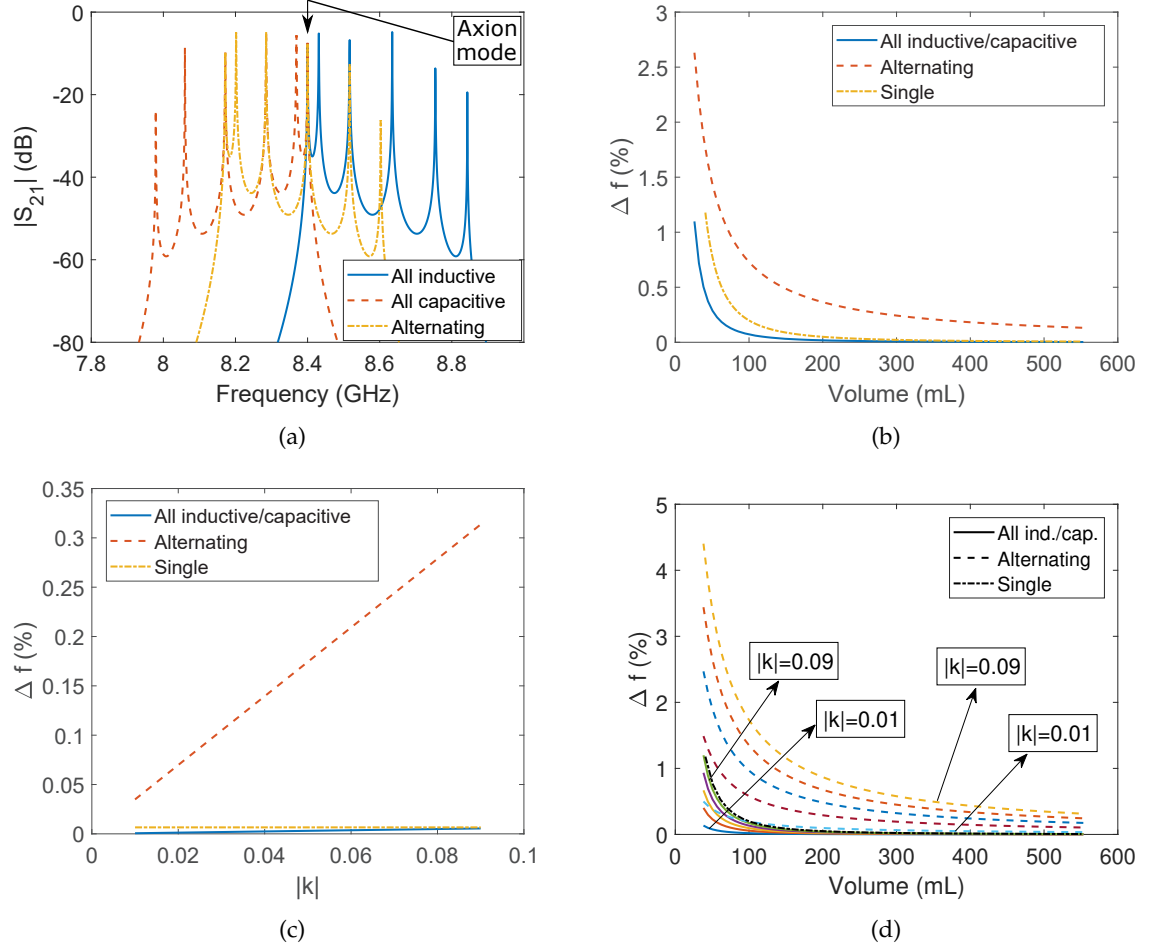
Figure 3.9: Comparative of the all-inductive, all-capacitive and alternating inductive / capacitive irises cases for a multicavity operating at 8.4 GHz making use of a physical coupling value of $|k| = 0.0377$: (a) magnitude of the S_{21} parameter in dB versus the frequency for a $N = 6$ multicavity of each type, (b) relative mode separation between the closest eigenmode to the axion one versus volume, (c) relative mode separation versus the absolute value of the physical coupling k for $N = 90$, and (d) relative mode clustering between the axion one and its closest neighbour mode as a function of the volume for various k values (and types). For all the multicavity cases, several $|k|$ values have been used (from bottom to top: $|k| = 0.01, 0.03, 0.05, 0.07$ and 0.09). The single cavity case with a high d value has been included in the plots (b), (c) and (d) for a better understanding. In (c), a length $d = 2700$ mm has been employed for the single cavity to provide the same volume value than the multicavity case.

the axion mode and the closest configuration mode is depicted in Figure 3.9b[2] for the previous three scenarios compared with a long single cavity structure operating at X-band frequencies.

In addition, the dependency of the relative mode separation with the k parameter is displayed in Figure 3.9c. Also, Figure 3.9d shows the behaviour of raising the volume with several $|k|$ values and different design types. The multicavity findings from these

---

2 For the multicavity scenario in this plot, a plausible assumption has been made: identical subcavity volume for any N. In reality, the length difference is minimised during the computation of the final volume, which is the factor represented by this figure.

plots were derived using the formulation presented in [27] (for the all-inductive and the all-capacitive scenarios) and [80] (for the alternating scenario).

As depicts Figure 3.9b, the alternating notion significantly improves mode separation. However, the fabrication of combined capacitive and inductive irises is complex, making the building of alternating multicavities more difficult than the all-inductive multicavity scenario. Furthermore, while the largest frequency separations are obtained with the larger values of $|k|$, as it is shown in Figures 3.9c and 3.9d, in a real design of haloscopes based on the multicavity concept, intermediate physical coupling values are selected such that the loading impact of the iris windows does not significantly limit the subcavity lengths, as previously explained [27].

Another benefit of the multicavity idea over single cavities is that it makes it simpler to extract RF power (through a coaxial to waveguide transition, for instance) in a critical coupling regime or $\kappa = 0.5$. This is due to the fact that in a multicavity haloscope, the E-field level of the TE_{101} mode has a maximum value in each subcavity, but in a single cavity there is only one maximum. With increasing $|k|$, the E-field level at the centre of the subcavities drops. Therefore, there is another trade-off between relative mode clustering (which requires a great $|k|$ value) and coupling power extraction (which is easier with small $|k|$ values).

Following the idea of 1D multicavity for $z-$axis connected subcavities, it is expanded in the following sections for long, tall, and large subcavities coupled in several axes.

3.1.2.1 *Long subcavities*

The combination of both multicavity and long single cavity approaches must be treated as a unique concept for exploiting the space offered by the dipole or solenoid magnet bores. This technique is based on extending the subcavity lengths in the multicavity structure while decreasing the width slightly to retain the correct axion frequency. As previously stated, the reduction in the waveguide width a of the subcavities results in a little decrease of the unloaded quality factor.

The subcavities of a 1D multicavity structure can be coupled (or stacked) in three ways: length, height, or width. This sort of stacking is seen in the multicavities from Figure 3.10a, which are composed by three long subcavities. Examples of each form of stacking in dipole and solenoid magnet bores are presented from Figure 3.10b to 3.10g[3]. The stacking in length scenario has been used in RADES so far (see produced structures in Figures 2.12b and 2.17) for the CAST dipole bore, using the orientation from Figure 3.10b.

---

3 With the purpose of aligning the E-field of the haloscope cavity with the magnetostatic field of the solenoid, the vertical direction of the multicavity ($y-$axis in Figure 3.10a) is oriented towards the longitudinal direction of the bore ($z-$axis in Figure 2.10a).
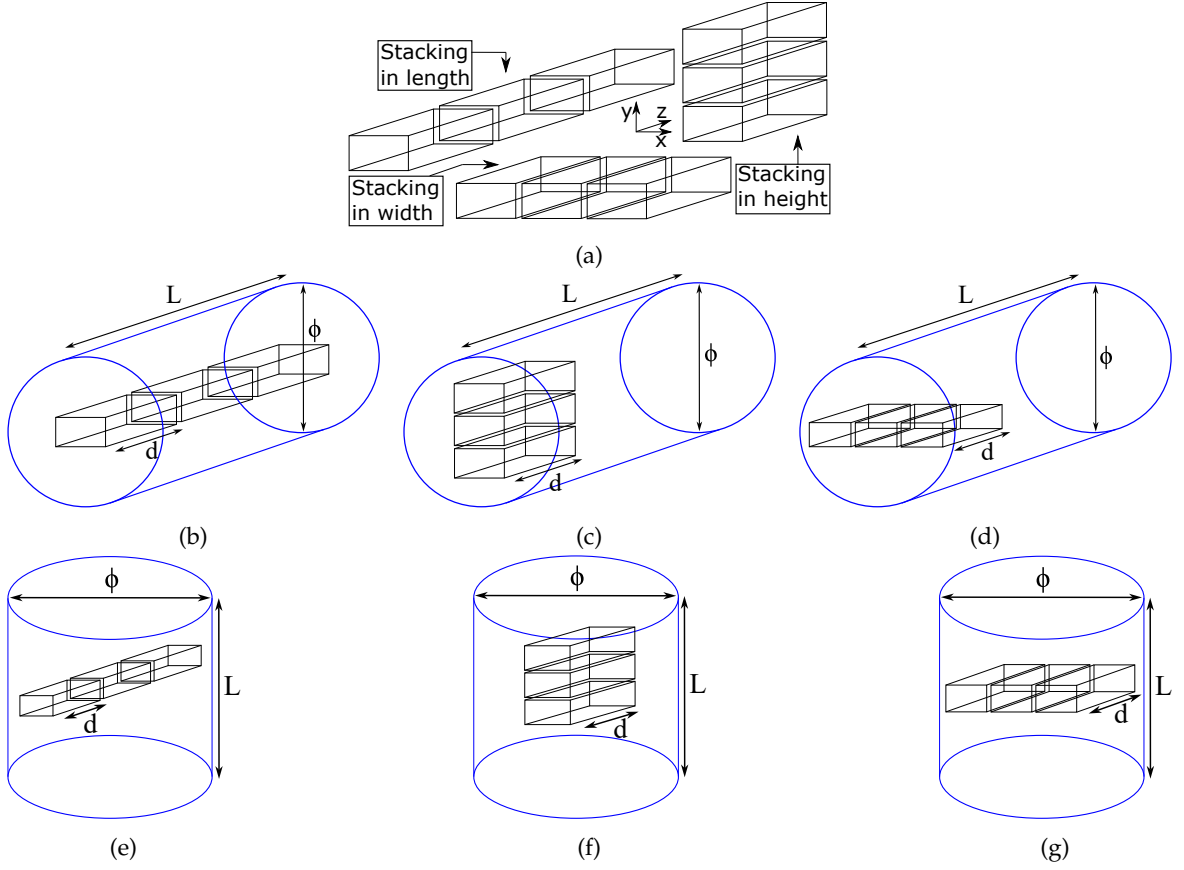
Figure 3.10: (a) Types of stackings in a multicavity example based on $N = 3$ subcavities with a high length value. Accommodation of the previous multicavities in dipole and solenoid magnets. For dipole bores: (b) stacking in length, (c) in height, and (d) in width. For solenoid bores: (e) stacking in length, (f) in height, and (g) in width.

For the same working frequency, longer subcavities result in lower $|k|$ values in a multicavity using the length direction ($z-$axis in Figure 3.10a). This is caused by the distance between the E-field maximum and the iris window, since with longer subcavity lengths, less energy reaches the coupling windows. There is a length limit beyond which the coupling windows cannot produce the right k value for any shape. As a result, exceedingly large subcavities cannot be used in a multicavity stacked in length. At the designing process, the greatest length at which the physical coupling is still possible with the iris windows must be determined. The number of subcavities N has no influence on this effect.

In the case of this type of multicavity designs, due to the large length of the bores, there is plenty of space to increase the number of subcavities and their lengths in a dipole magnet (10 m in the case of BabyIAXO bore length). For solenoid magnets, however, the multicavity notion employing the longitudinal axis for subcavity stacking (see Figure 3.10e) is not the optimum option since the diameter is the limiting dimension. Therefore, a maximum haloscope length of 650 mm is set for the biggest solenoid magnet from Table 3.1, the MRI (ADMX-EFR) magnet, whose diameter has the same value. This is simply accomplished with a single cavity. If using 1D multicavities with stacking in length is required, a multicavity design with not very long subcavities ($N = 13$ subcavities

of length $d = 50$mm, for instance) could be carried out, though it will be demonstrated below that there are more useful configurations to rise up the volume of a multicavity haloscope in solenoids.

The energy that reaches the coupling windows is quite high for the other two stacking alternatives (x and $y-$axis in Figure 3.10a) because of the shorter space from the subcavity center (highest E-field region) to the iris. Thus, regardless of the k value, any subcavity length may be used. Nonetheless, due to the magnet size of both dipoles and solenoids, there are certain constraints for these novel staking orientations. For the in height stacking (see Figure 3.10c) and the in width stacking (see Figure 3.10d) scenarios within dipole bores, the longitudinal axis of the magnet must be used for the limiting of the subcavity length, and the diameter plane for the stacking direction of all the subcavities. This indicates a lot of flexibility in terms of length d ($L_{BabyIAXO} = 10$ m), but also a restriction in the maximum number of subcavities N ($\phi_{BabyIAXO} = 600$ mm).

In solenoid magnets, for the scenario with long subcavities employing the in height stacking (see Figure 3.10f), the longitudinal axis of the multicavity can be directed in any radial bore axis (d restricted to $\phi_{MRI} = 650$ mm) and the stacking of the subcavities can be oriented in the longitudinal magnet axis (N limited to $L_{MRI} = 800$ mm). However, when stacking a multicavity with long subcavities in width for solenoid bores (see Figure 3.10g), both subcavity stacking and its longitudinal axis must take any radial magnet axis. Because of the cylindrical form of the bore, both d and N are constrained to a smaller value rather than $\phi_{MRI} = 650$ mm. Only one subcavity might be inserted if its length spans the whole radial axis ($d \approx \phi_{MRI} = 650$ mm). Nevertheless, by reducing this dimension to a more reasonable value, N can be raised. If a footprint with a square area is used at the MRI solenoid bore, for example, a maximum length value of $d = \frac{\phi_{MRI}}{2}\sqrt{2} = 459.62$ mm (equation for the fitting of a square inside a circle) can be implemented. In this example, a more powerful design might be created by employing various lengths for each subcavity and utilising practically the whole bore diameter plane to increase the volume of the structures (reserved as future work).

Figures 3.11a, 3.11b and 3.11c show a comparison study of these three cases of coupling orientations for X-band frequencies in a multicavity with $N = 2$ (for simplicity) and an inductive or capacitive iris varying the volume, which depends only on the length because the height ($b = 10.16$ mm), width ($a = 22.86$ mm), and N are all fixed. These conclusions hold true for both dipole and solenoid bores assuming an approximation of $\vec{B}_e = B_e\,\hat{y}$ for dipole magnets and $\vec{B}_e = B_e\,\hat{z}$ for solenoid magnets. In such scenario, the C value is the same in both cases.

According to the outcomes from Figure 3.9b, the mode separation imposes a limit in N (the number of subcavities) and in d (the subcavity length) in multicavities employing long subcavities, in the same way to the limit in the single cavity lengths (detailed in
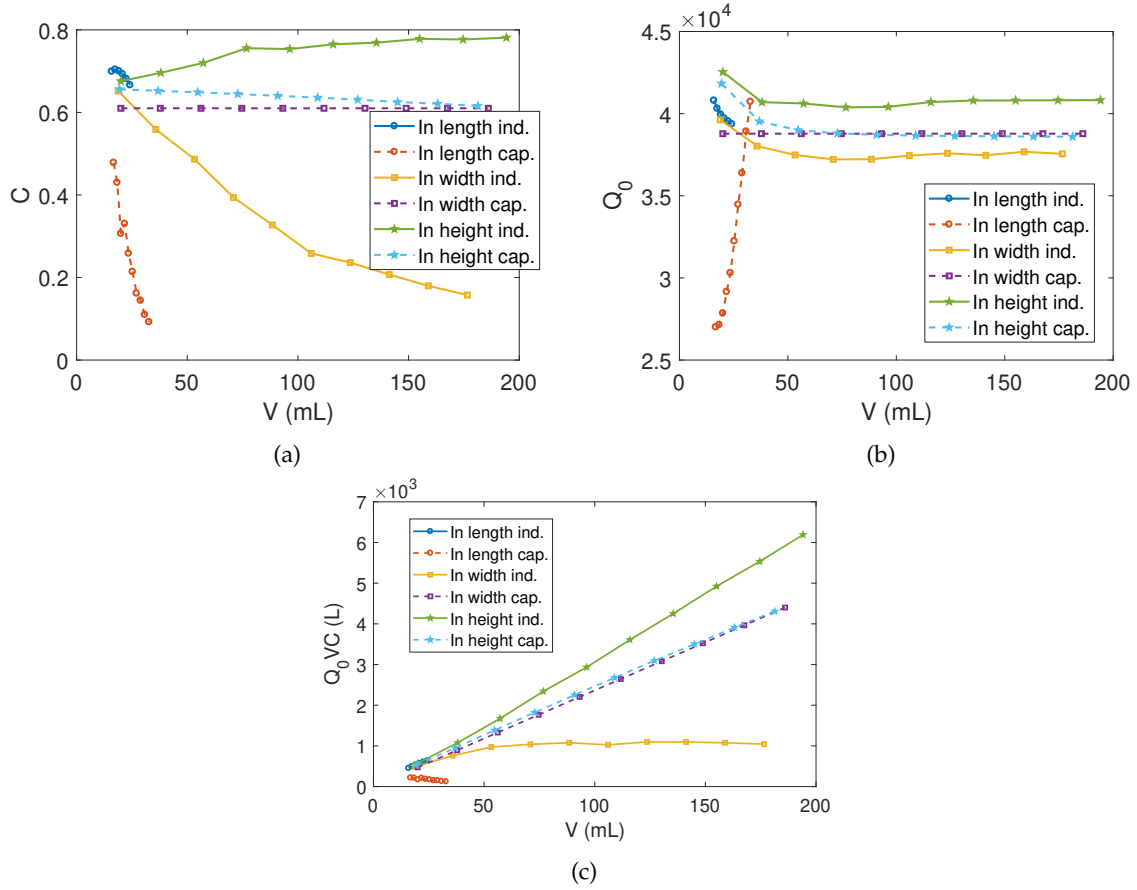
Figure 3.11: Influence of each form of coupling (inductive and capacitive) on the design factors for the three subcavity stacking possibilities (in length, in width, and in height) in a multicavity based on two long subcavities (with a height of $b = 10.16$ mm and a width of $a = 17.85$ mm): (a) form factor, (b) unloaded quality factor, and (c) $Q_0 \times V \times C$ factor. The volume value depends only on the subcavity length since N is now fixed.

subsection 3.1.1.1). Nonetheless, the magnet size is often far smaller than these limitations for any stacking orientation. For simplicity, the examples from Figures 3.11a, 3.11b and 3.11c employ a $N = 2$ multicavity.

This study used a physical coupling value of $|k| = 0.025$, which is a common value utilised in the RADES team. Figure 3.11 demonstrates how the curves (both inductive and capacitive) for the in length stacking option are restricted to volume values below 50 mL. This is due to the previously mentioned length constraint in the subcavities for this type of coupling stacking (the needed coupling $|k| = 0.025$ cannot be reached with longer lengths). There is no similar restriction for the other four curves, therefore this study may be repeated with greater volumes if required. The results from the $Q_0 \times V \times C$ parameter in Figure 3.11c show that the in height orientation stacking is the best choice for lengthy subcavities. However, depending on the kind and size of the magnet bore, the $x-$axis direction may be preferable.

It is not evident how to build an inductive/capacitive iris for the vertical coupling stacking. As a result, a prior study was conducted to determine the inductive and

capacitive behaviour by adjusting the position and size of a rectangular iris window. For the inductive case, a window with a quasi-square form is placed in the centre of the subcavity (as depicted in Figure 3.12a). For the capacitive iris case, a narrow rectangular

Inductive iris   Capacitive iris

(a)   (b)
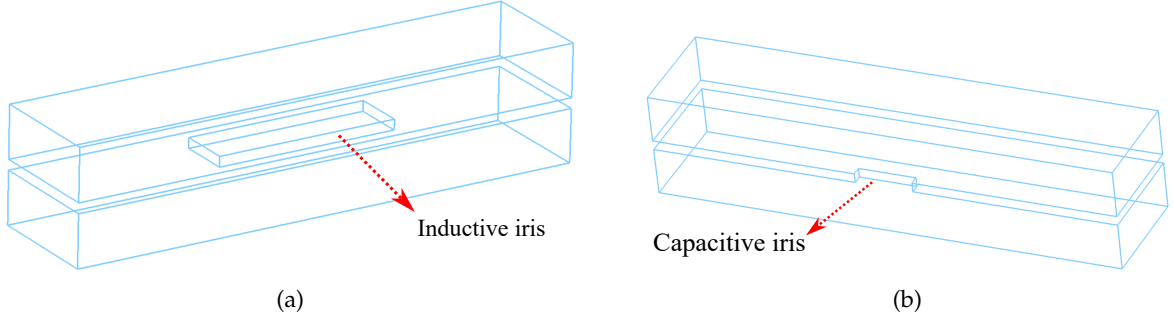
Figure 3.12: 3D model of a $N = 2$ multicavity employing the in height stacking with (a) an inductive iris, and (b) a capacitive iris.

form moved to one side along the width is needed (as it is depicted in Figure 3.12b).

All of these investigations were conducted for the all-inductive and all-capacitive multicavity scenarios. However, as previously demonstrated, the alternating case gives the greatest mode separation between configuration modes close to the axion resonance. As a proof of concept, it was designed a long (with $d = 100$ mm) alternating haloscope structure employing the in height stacking with $N = 4$ subcavities.

A 0.025 value was used for the interresonator iris couplings $|k|$. The coupling matrix extracted for this case (using equation 3.3) is given by

$$\mathbf{M} = \begin{pmatrix} -0.5 & 0.5 & 0 & 0 \\ 0.5 & 0 & -0.5 & 0 \\ 0 & -0.5 & 0 & 0.5 \\ 0 & 0 & 0.5 & -0.5 \end{pmatrix}. \tag{3.4}$$

This matrix was used for the structure designing with the procedures provided in [27, 74]. An alternating behaviour can be noticed (positive and negative sign for the capacitive and inductive irises, respectively) for the non-zero off-diagonal elements.

Figures 3.13a and 3.13b depict the haloscope final aspect, demonstrating the geometry and position of each form of the iris windows in this type of multicavity (stacking in height). Figure 3.13c depicts the magnitude of the simulated S_{21} parameter versus the frequency.

According to Figures 3.13a and 3.13b, the dimensions of the structure are as follows: subcavity lengths $d = 100$ mm, subcavity heights $b = 10.16$ mm, width of the inner subcavities $a_{in} = 18.3$ mm, width of the external or outermost subcavities $a_{ext} = 17.9$ mm, length of the two capacitive irises $C_{zcap} = 12.4$ mm, width of the two capacitive irises $C_{xcap} = 2$ mm, length of the inductive iris $C_{zind} = 35.5$ mm, width of the inductive iris
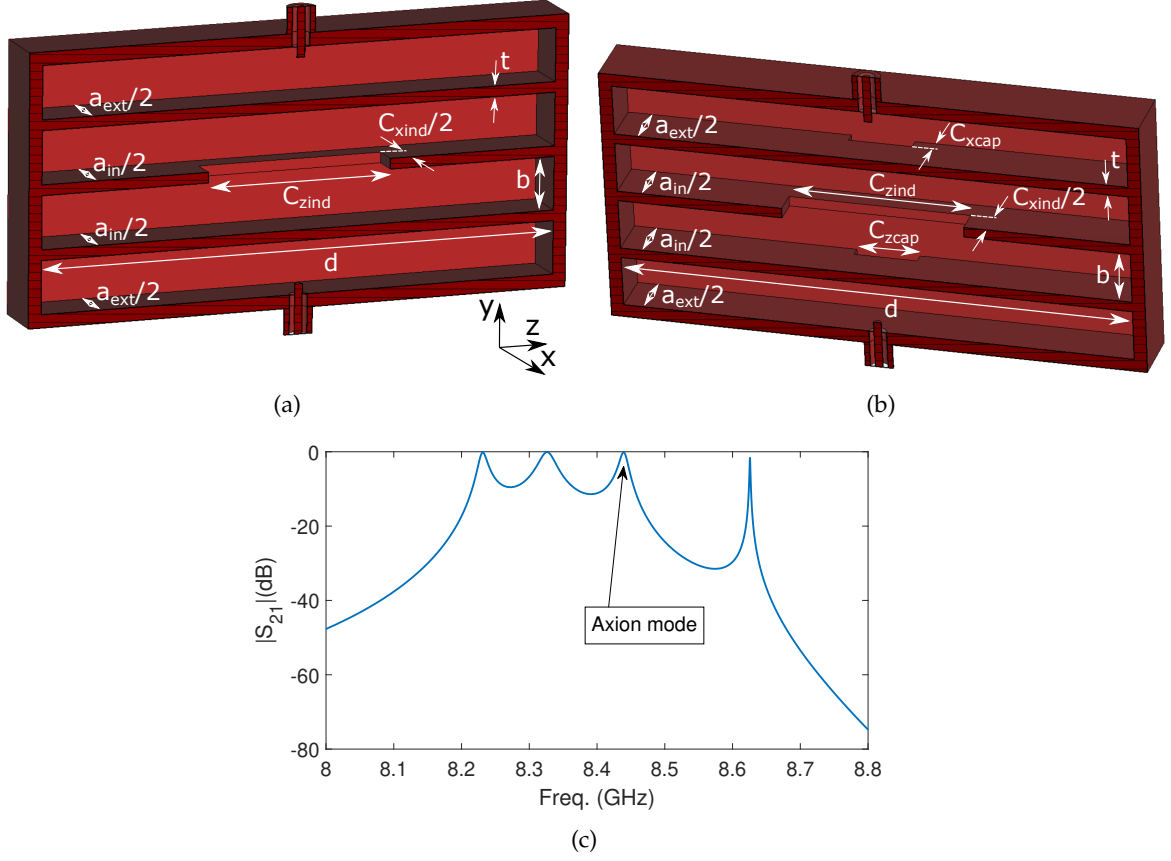
Figure 3.13: Long multicavity design with an alternating behaviour based on $N = 4$ subcavities stacked in height with two capacitive and one inductive iris windows: (a) left half of the haloscope, (b) right half of the haloscope, and (c) magnitude of the S_{21} parameter versus the frequency.

$C_{xind} = 10$ mm and iris thickness $t = 2$ mm.

As it can be observed, there are four resonances within the $8 - 8.8$ GHz frequency band, which corresponds to the number of subcavities $N = 4$. These resonances are the four configuration modes of the TE_{101} resonant mode in the multicavity. When the amplitude of the E-field of these four eigenmodes is examined (see Figure 3.14), the axion mode is recognised as the third (the case where all the subcavities are in synchronisation [80]), confirming the alternating behaviour (being N an even value). Table 3.5 lists the configuration modes of the TE_{101} mode shown in Figure 3.14.

Frequency (GHz)	Configuration
8.231	[+ − − +]
8.326	[+ − + −]
8.439	[+ + + +]
8.626	[+ + − −]

Table 3.5: Report of the TE_{101} configuration modes shown in Figure 3.14.
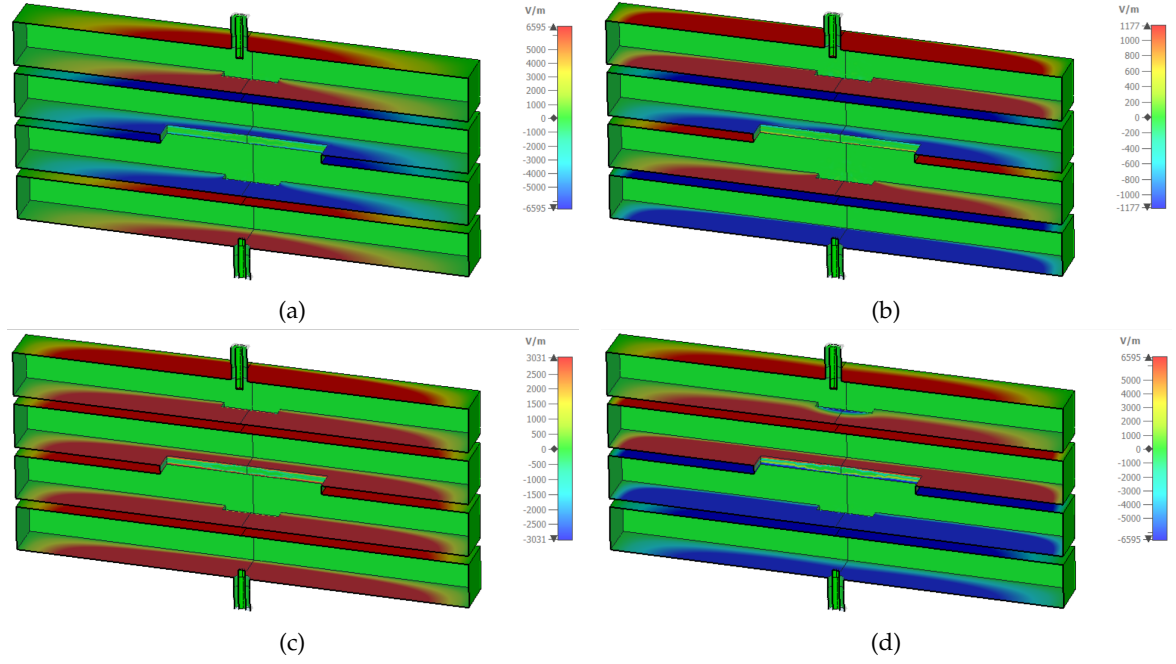
Figure 3.14: Configuration mode E-fields (magnitude component) of the designed haloscope depicted in Figure 3.13: (a) [+ − − +], (b) [+ − + −], (c) [+ + + +] and (d) [+ + − −], where the signs "+" and "−" symbolize, for each subcavity, a positive and negative electric field level, respectively.

The mode clustering of this haloscope design ($\Delta f = 1.3$ % or 113 MHz) is far from our limitations because of the limited number of subcavities ($N = 4$). On the other hand, since the length value is not very high ($d = 100$ mm), the closeness of the following resonant mode (the first configuration mode of the TE_{102} mode) is irrelevant as there is enough distance in frequency (and beyond the frequency span shown in Figure 3.13c).

The observed axion mode resonant frequency is at $f = 8.439$ GHz, being an excellent result compared to the objective of 8.4 GHz. The unloaded quality and form factors are $Q_0 = 39579$ and $C = 0.654$, respectively, which are consistent with the findings from Figure 3.11 for the stacking in height case in the scenarios with inductive and capacitive windows for $d = 100$ mm (where for two subcavities the volume is $V \approx 37$ mL). This lends support to the theoretical study offered in this subsection. The haloscope overall volume is $V = 74$ mL, and the total $Q_0 \times V \times C$ factor is 1915.47 L, or 9.56 times that of a single cavity with the standard WR-90.

3.1.2.2 *Tall subcavities*

The tall structure, as explained in subsection 3.1.1.2, is a viable option for expanding the haloscope volume. This approach may also be used to increase the subcavities height in 1D multicavity designs. As with the long subcavities discussed before, there are three options for stacking the subcavities in a tall multicavity: in length, in height, and in width, which are exposed in Figure 3.15a with an example of $N = 3$ tall subcavities. Examples for these stacking orientations in dipole and solenoid magnet bores are shown from
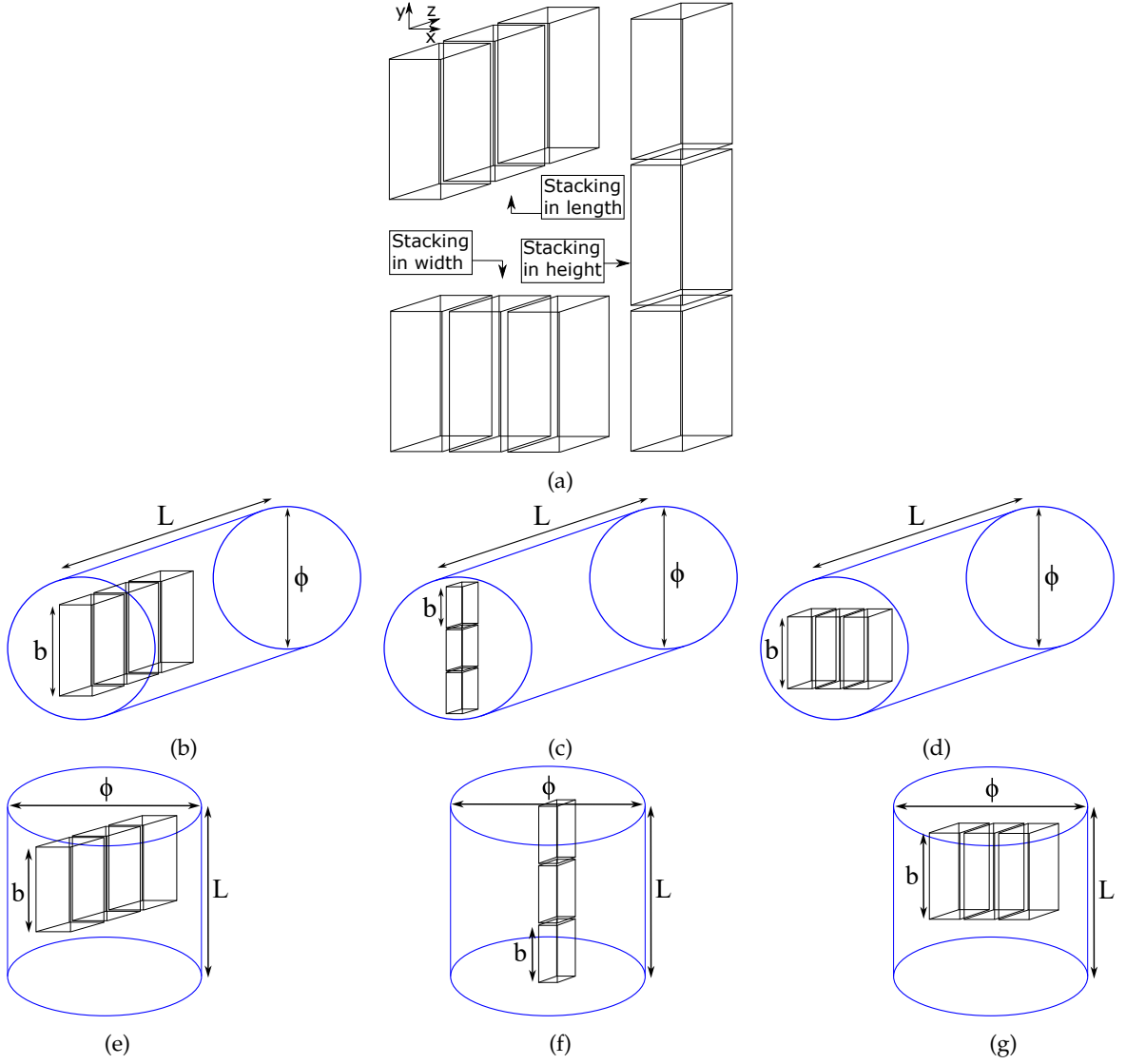
Figure 3.15: (a) Stacking options in a multicavity design based on $N = 3$ tall subcavities. Application of these scenarios in dipole and solenoid bores. Dipole cases: (b) stacking in length, (c) in height, and (d) in width. Solenoid cases: (e) stacking in length, (f) in height, and (g) in width.

Figure 3.15b to Figure 3.15g.

In the case of dipoles, the tall multicavity with stacking in length (see Figure 3.15b) should guide its vertical dimension towards the $y-$axis, limiting the height b value ($\phi_{BabyIAXO} = 600$ mm for the biggest dipole from Table 3.1), while the subcavity stacking orientation must be parallel to the longitudinal axis of the magnet, which implies a great freedom to increase N ($L_{BabyIAXO} = 10$ m). For tall multicavities with stacking in height within dipoles (see Figure 3.15c), the vertical dimensions of the haloscope and the stacking must be parallel to the $y-$axis of the magnet, resulting in a significant restriction in both parameters b and N (a total height of $\phi_{BabyIAXO} = 600$ mm could be used for the haloscope). If using multicavity haloscopes stacked in height is required, not too tall subcavities ($N = 15$ design with $b = 40$ mm, for instance) could be employed, though it

will be demonstrated below that there are more practical scenarios to enhance the total volume in dipoles. Lastly, in dipole bores for tall subcavities with stacking in width (see Figure 3.15d), both the height and the stacking direction must be guided to the transverse plane of the magnet, but in opposite directions (seeing Figure 2.10d, $y-$axis for b, the subcavity heights, and $x-$axis for N, the stacking of the subcavities). Because this scenario is quite similar to the long multicavities with the stacking in width case employing a solenoid magnet (see Figure 3.10g) described in the previous subsection, equivalent considerations are used here for limiting the parameters b and N, taking the cylindrical form of the magnet bore into account.

Tall multicavities with stacking in length for solenoid magnets (see Figure 3.15e) must have their heights guided towards the longitudinal magnet axis (limiting the subcavity height to $b = L_{MRI} = 800$ mm) and the stacking orientation towards any radial magnet axis (limiting the number of subcavities N considering the bore diameter $\phi_{MRI} = 650$ mm). For tall multicavities with stacking in height for solenoid magnets (see Figure 3.15f), both the height and subcavity stacking must be guided towards the longitudinal axis of the magnet, posing a significant constraint in the subcavity height and the number of subcavities (total height limit of $L_{MRI} = 800$ mm). For solenoids, this condition is inefficient, comparable to the long multicavities stacked in length (see Figure 3.10e), since the maximal magnet height from the list of Table 3.1 is $L = 800$ mm, which can easily be attained with a single cavity. The remaining stacking orientations are more suited for this form of multicavity since they make use of both the bore length and diameter. Lastly, for the solenoid scenario employing tall subcavities with stacking in width (see Figure 3.15g), it has the same condition as tall multicavities with stacking in length. In case of necessity of using 1D multicavities with stacking in height, a multicavity based on not very tall subcavities (16 subcavities of $b = 50$ mm, for example) might be designed.

Using a value of $|k| = 0.025$ for the physical coupling and increasing the height b in a haloscope with $N = 2$, a research comparable to that of the preceding subsection was conducted for all the stacking directions (in length, in height, and in width). The performance of these sorts of stackings as a function of the total volume (which varies with the height b) is depicted in Figure 3.16.

The stacking in height with an inductive iris scenario has a limitation in the haloscope height with volume values approximately 50 mL providing the right $|k|$ value, as it is shown in Figure 3.16. The condition is comparable to that of the lengthy multicavities with an in length stacking orientation. There is no such limitation for the other alternatives, and the restriction is enforced by the mode separation. The in length and in width stackings with an inductive iris and the in height stacking with a capacitive iris are the greatest scenarios for the tall multicavities due to their large $Q_0 \times V \times C$ factor values as b (or V) grows, as depicted in Figure 3.16c.
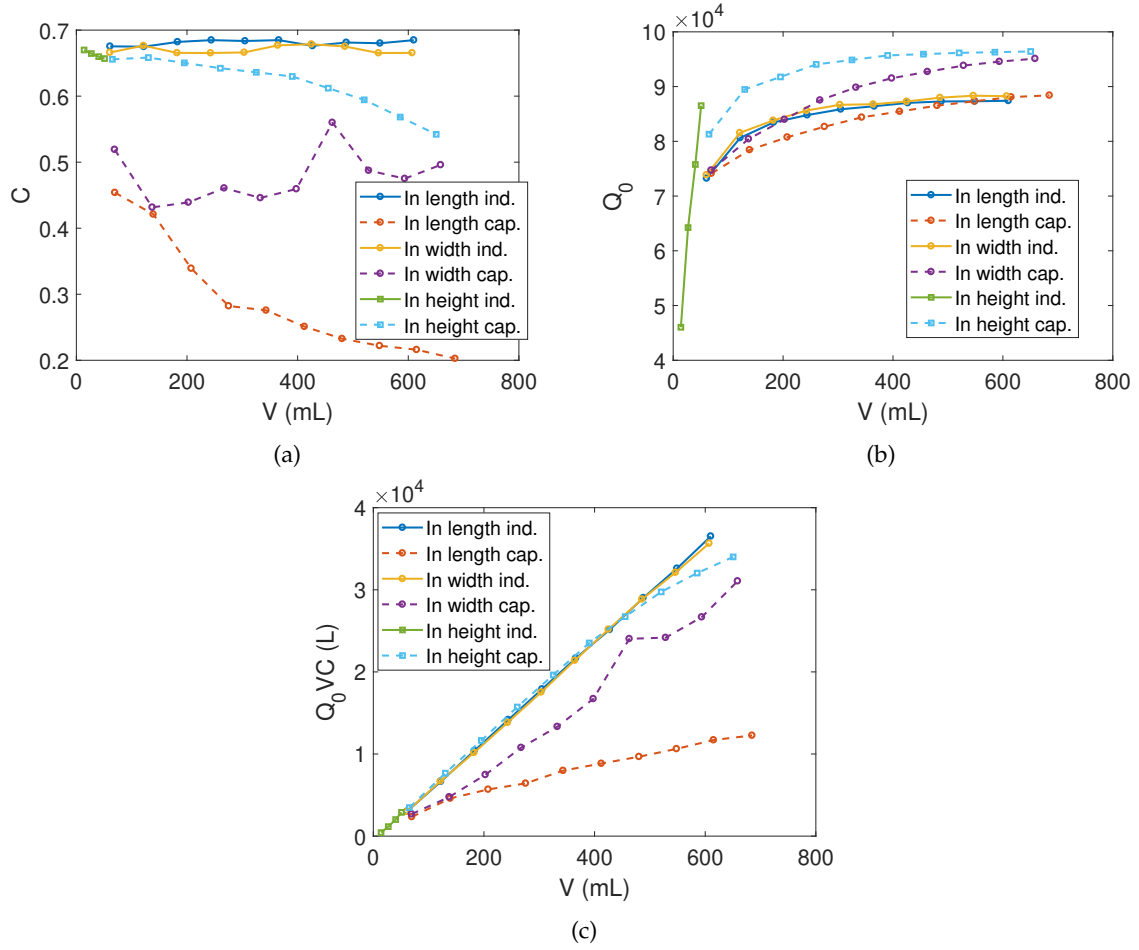
Figure 3.16: Behaviour of each type of iris window (inductive and capacitive) on the design parameters of a tall $N = 2$ multicavity employing the stacking in length, in height and in width: (a) form factor, (b) unloaded quality factor, and (c) $Q_0 \times V \times C$ factor. The volume value depends only on the subcavity height since N is fixed.

Regardless of magnet dimensions, the limit in the N and b values is enforced by the same principles as for single cavities (similarly to the long subcavities): the mode clustering detailed in section 3.1.1.1, but taking into account the outcomes shown in Figure 3.9b. Nonetheless, as previously indicated, the bore size of the magnets in an X-band haloscope employing the multicavity design is often significantly lower than the haloscope limitations for any type of stacking.

For validation, an all-inductive tall multicavity based on $N = 4$ subcavities with $b = 300$ mm was designed and manufactured with subcavities stacked in length (see Figure 3.17a). This haloscope would fit well in the magnets BabyIAXO (dipole) and MRI (solenoid), as it is shown in Figures 3.15b and 3.15e, respectively.
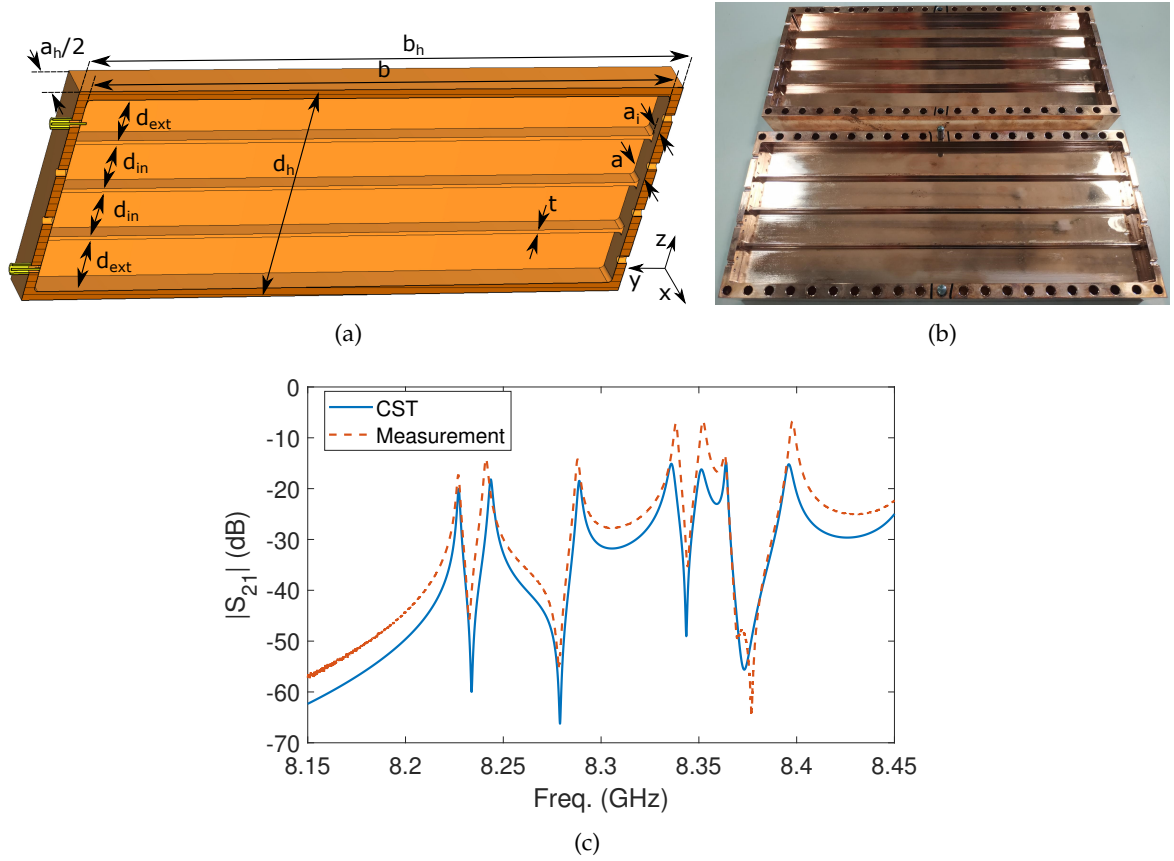
Figure 3.17: Produced prototype of the designed tall multicavity with $N = 4$ subcavities and three inductive irises making use of the in length stacking: (a) 3D structure of one of the two opposing symmetrical halves, (b) representation of the produced prototype disassembled, and (c) magnitude of the S_{21} parameter versus the frequency for both the simulation results and the measurements at $T = 300$ K. A good agreement is observed between experimental and theoretical results.

One more time, the $|k|$ value chosen for the iris couplings is 0.025, and the resulting coupling matrix is:

$$\mathbf{M} = \begin{pmatrix} 0.5 & -0.5 & 0 & 0 \\ -0.5 & 1 & -0.5 & 0 \\ 0 & -0.5 & 1 & -0.5 \\ 0 & 0 & -0.5 & 0.5 \end{pmatrix}. \tag{3.5}$$

Since the multicavity has all inductive irises, the signs of the M_{12}, M_{23} and M_{34} parameters (and their symmetrical pairings) are negative.

Figure 3.17b depicts a photograph of the produced structure. The technical drawings for the manufacturing of this prototype are depicted in Appendix I: Technical Drawings (see Figure A.6). Figure 3.17c shows the magnitude of the S_{21} parameter versus the frequency for both simulation results and measurements, which agree well. The VNA *ZVA67* with the *TOSM (Through - Open - Short - Match)* calibration has been used for the electromagnetic characterisation (measurement of the Scattering Parameters as a function of the frequency) of all the structures manufactured in this PhD thesis.

The prototype dimensions are as follows: subcavity heights $b = 300$ mm, subcavity widths $a = 22.86$ mm, external subcavity lengths $d_{ext} = 27$ mm, inner subcavity lengths $d_{in} = 26$ mm, inductive iris widths $a_i = 9$ mm. The thickness value of all the iris windows is $t = 2$ mm. The haloscope whole dimensions, including the copper housing thickness (with $t_{Cu} = 5$ mm), are: height $b_h = 310$ mm, width $a_h = 32.86$ mm, and length $d_h = 122$ mm.

Based on simulations using copper walls, the axion mode (at 8.227 GHz) has an unloaded quality factor of $Q_0^{2K} = 76000$ at $T = 2$ K and $Q_0^{300K} = 13200$ at $T = 300$ K. The prototype measurements gave a quality factor of $Q_0^{300K} = 7300$ (55.3 % of the simulation outcomes), which matches with a common drop in manufactured Q_0 when compared to previous RADES haloscopes [27]. The decrease in Q_0 can be attributed to a variety of factors, the most common of which are machining roughness and discontinuities of the RF surface current caused by fabrication cuts and assembling process.

In terms of form factor, a $C = 0.625$ has been found (through simulations), which can be enhanced further by optimisation. Table 3.6 lists the configuration modes of the resonances shown in Figure 3.17c.

Freq. (GHz)	Resonant mode	Configuration
8.227	TE_{101}	[+ + + +]
8.241	TE_{111}	[+ + + +]
8.288	TE_{121}	[+ + + +]
8.338	TE_{101}	[+ + − −]
8.352	TE_{111}	[+ + − −]
8.363	TE_{131}	[+ + + +]
8.398	TE_{121}	[+ + − −]

Table 3.6: Configurations modes shown in Figure 3.17c.

The mode clustering of this prototype is $\Delta f = 0.17$ % (14.3 MHz), which corresponds to the results from Figure 3.4b for the case $b/a = 300/22.86 = 13.12$. The closeness of the following configuration mode ([+ + − −]) is not a concern since it is frequency far (1.35 % or 111.4 MHz), which is to be expected given the small value of N ($N = 4$). The haloscope entire volume is $V = 743$ mL, and the $Q_0 \times V \times C$ factor value is 3.53×10^4 L, or 176.14 times that of a single cavity with the standard WR-90.

Tall multicavities have a further feature that helps to relieve mode clustering: the occurrence of transmission zeros. They are produced by the interaction of higher order modes when their frequencies are near. For instance, a transmission zero develops on the right side of the axion mode (TE_{101}) as a result of interaction with the TE_{111} mode. This can be explained with the phase cancellation between the mode signals. However, these transmission zeros can fade out and shift to the complex plane if the modes that create them have a low quality factor. In [107], more details can be found.

3.1.2.3 *Large subcavities*

Combining all of the preceding approaches is a great strategy for increasing the haloscope volume: 1D multicavity prototype with large (this is, long and tall) subcavities. It is expected that the ideal stacking orientation in a large multicavity will be fairly similar to that in multicavities with a long dimension and in multicavities with a tall dimension. Inspecting Figures 3.11 and 3.16, it is extracted that the stacking with the best $Q_0 \times V \times C$ results (taking into account only the limitation in the mode clustering) is the in height employing a capacitive iris for both dipoles and solenoids. Nevertheless, the ideal stacking orientation varies on the magnet used owing to its size, as it is seen in Figures 3.10 and 3.15.

In the dipole magnet of BabyIAXO, for instance, a large multicavity haloscope with stacking in width (as are the cases depicted in Figures 3.10d and 3.15d but with large subcavities) with $a = 17.85$ mm, $b = \frac{\phi_{BabyIAXO}}{2}\sqrt{2} - 2t_{Cu} = 414.26$ mm, and $d = 1600$ mm (restricted to prevent mode separation issues, as it is shown in Table 3.4) using a number of subcavities of $N = \lfloor \frac{b}{a+t} \rfloor = 20$ (being $t = 2$ mm the iris thickness) could be introduced. This haloscope dimensions would give a total volume of $V = 236.75$ L. In the solenoid magnet of MRI (ADMX-EFR), on the other hand, a multicavity employing the stacking in width (as it is the case in Figures 3.10g and 3.15g but using large subcavities) with $a = 17.85$ mm, $b = L_{MRI} = 800$ mm, and $d = \frac{\phi_{MRI}}{2}\sqrt{2} - 2t_{Cu} = 449.62$ mm, with a number of subcavities of $N = \lfloor \frac{d}{a+t} \rfloor = 22$ could be installed. This large haloscope would give a total volume of $V = 141.52$ L. When the multicavity volume in both magnets is compared the BabyIAXO scenario gives a better value. Despite the smaller value of the volume (141.52 L versus 236.75 L) and considering equation 2.10, the smaller value of the system temperature of the solenoid MRI bore (0.1 K versus 4.2 K, as it is described in Table 3.1) and its greater magnetic field (9 T versus 2.5 T) make it far more recommended.

As a introductory proof of concept, a large (employing $d = 100$ mm and $b = 100$ mm) all-inductive design with $N = 4$ subcavities stacked in width is carried out. A 3D model of this multicavity is depicted in Figure 3.18a. In this example, the physical coupling $|k|$ value is chosen (and its consequent coupling matrix) is that of the previous subsection with a tall design with four subcavities (see equation 3.5). The magnitude of the S_{21} parameter versus frequency is depicted in Figure 3.18b, which has been obtained from simulation. The structure dimensions are as follows: subcavity lengths $d = 100$ mm, subcavity heights $b = 100$ mm, external subcavity widths $a_{ext} = 17.85$ mm, inner subcavity widths $a_{in} = 17.6$ mm, iris widths $a_i = 8.9$ mm, and iris thicknesses $t = 2$ mm.

For the TE_{101} mode, the unloaded quality factor at $T = 2$ K is $Q_0 = 58327$, and the simulated form factor value is $C = 0.464$. For this example, the parameter C of the haloscope was not optimised (future line from this PhD thesis). Table 3.7 registers the configuration modes that are shown in Figure 3.18b.

(a)

(b)
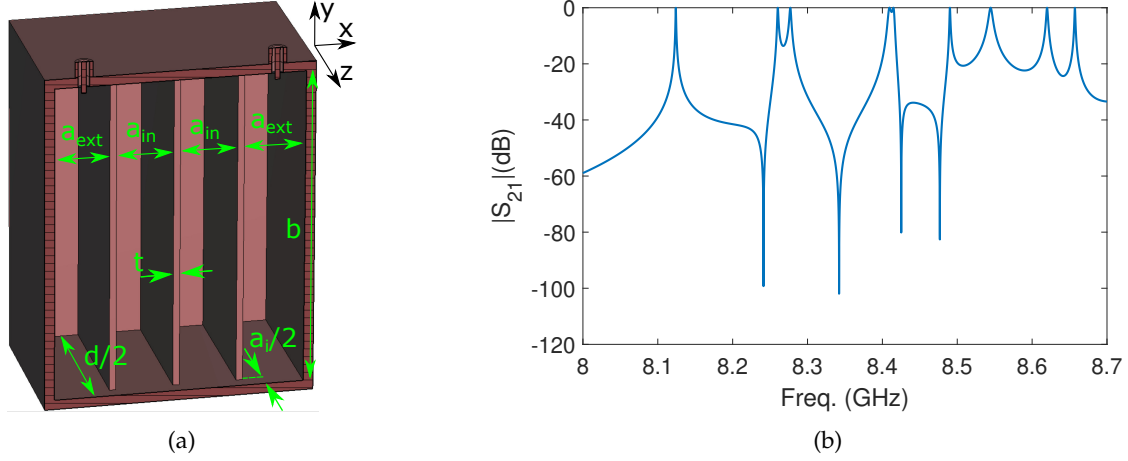
Figure 3.18: Multicavity design with three inductive couplings and four subcavities incorporating the long and tall cavity concepts (this is, a large structure): (a) 3D model of a symmetrical halve of the prototype, and (b) S_{21} parameter in magnitude versus the frequency at $T = 2$ K (obtained from simulation).

Freq. (GHz)	Resonant mode	Configuration
8.124	TE_{101}	$[+ + + +]$
8.26	TE_{111}	$[+ + + +]$
8.277	TE_{101}	$[+ + - -]$
8.409	TE_{101}	$[+ - - +]$
8.415	TE_{111}	$[+ + - -]$
8.49	TE_{101}	$[+ - + -]$
8.544	TE_{111}	$[+ - - +]$
8.62	TE_{111}	$[+ - + -]$
8.657	TE_{121}	$[+ + + +]$

Table 3.7: Configuration modes depicted in Figure 3.18b.

The relative mode clustering for this haloscope is $\Delta f = 1.67$ % (136 MHz), which is close to the value shown in Figure 3.4b for the case at $b/a = 100/17.7 = 5.65$ (1 %). Because the ports are located at the middle of the subcavities they prevent the TE_{102} mode excitation, which has a zero E-field at that location. If this mode occurred, it would meet the mode clustering described in Figure 3.2a with the case $d/a = 100/17.7 = 5.65$ (4.45 %). The distance of the following configuration mode ($[+ + - -]$) is not a concern since it is far apart in frequency (1.88 % or 153 MHz) because of the small N value utilised in this prototype. The S_{21} parameter of this haloscope, like the one in the preceding subsection (tall multicavities), reveals transmission zeros formed between resonant modes, assisting in their separation when they are near in frequency.

The total structure volume is $V = 714$ mL, giving a value in the $Q_0 \times V \times C$ factor of 1.9×10^4 L, or 96.44 times that of a single cavity with standard WR-90.

3.1.3 *2D and 3D multicavities*

From the 1D multicavity concept the development of 2D and 3D multicavities can be carried out, geometries that might be useful for fitting the available space in particular magnets. They can also give transmission zeros, which may be utilised to reject neighbouring modes to the axion one. These topologies use *cross-couplings*, a kind of interresonator coupling that are generated by irises that couple non-adjacent subcavities [74]. The easiest technique to achieve this aim is to fold the multicavity structure either vertically or horizontally, allowing for the introduction of coupling windows between subcavities that are not adjacent, and so generating a 2*D* multicavity. The resultant haloscope is a 3*D* multicavity if the initial topology (in-line) is folded along two distinct axes. Two examples of 2D multicavities (vertically and horizontally folded), and one example of 3D multicavity are shown in Figure 3.19. It should be noted

(a)

(b)   (c)
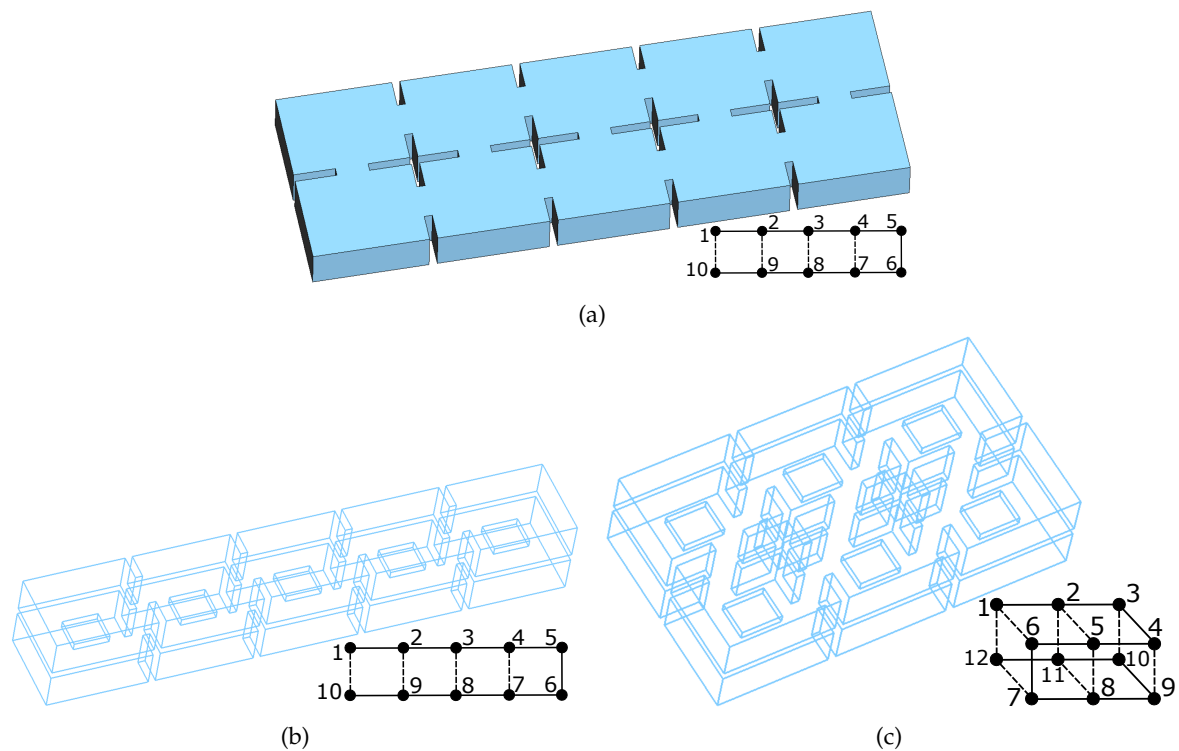
Figure 3.19: 2D and 3D multicavity examples employing cross-couplings: (a) 2D multicavity horizontally folded with $N = 10$ subcavities and four cross-coupling irises (a diagram of the topology is depicted at the corner), (b) 2D multicavity vertically folded with the same topology as in the (a) case, and (c) 3D multicavity (horizontally and vertically folded) with $N = 12$ subcavities and nine cross-coupling irises. In the diagram of the topologies, a solid line indicates the principal coupling path while a dashed line denotes a cross-coupling.

that diagonal cross-couplings might be included if necessary (for example, between the 1st and second last subcavities), however they are not included in these cases for simplicity.

For the 2D and 3D structures depicted in Figure 3.19, the corresponding coupling matrices to its topology diagrams are, respectively, as follows:

$$
M_{2D} = \begin{pmatrix}
\Omega_1 & M_{1,2} & 0 & 0 & 0 & 0 & 0 & 0 & 0 & M_{1,10} \\
M_{1,2} & \Omega_2 & M_{2,3} & 0 & 0 & 0 & 0 & 0 & M_{2,9} & 0 \\
0 & M_{2,3} & \Omega_3 & M_{3,4} & 0 & 0 & 0 & M_{3,8} & 0 & 0 \\
0 & 0 & M_{3,4} & \Omega_4 & M_{4,5} & 0 & M_{4,7} & 0 & 0 & 0 \\
0 & 0 & 0 & M_{4,5} & \Omega_5 & M_{5,6} & 0 & 0 & 0 & 0 \\
0 & 0 & 0 & 0 & M_{5,6} & \Omega_6 & M_{6,7} & 0 & 0 & 0 \\
0 & 0 & 0 & M_{4,7} & 0 & M_{6,7} & \Omega_7 & M_{7,8} & 0 & 0 \\
0 & 0 & M_{3,8} & 0 & 0 & 0 & M_{7,8} & \Omega_8 & M_{8,9} & 0 \\
0 & M_{2,9} & 0 & 0 & 0 & 0 & 0 & M_{8,9} & \Omega_9 & M_{9,10} \\
M_{1,10} & 0 & 0 & 0 & 0 & 0 & 0 & 0 & M_{9,10} & \Omega_{10}
\end{pmatrix} \tag{3.6}
$$

$$
M_{3D} = \begin{pmatrix}
\Omega_1 & M_{1,2} & 0 & 0 & 0 & M_{1,6} & 0 & 0 & 0 & 0 & 0 & M_{1,12} \\
M_{1,2} & \Omega_2 & M_{2,3} & 0 & M_{2,5} & 0 & 0 & 0 & 0 & 0 & M_{2,11} & 0 \\
0 & M_{2,3} & \Omega_3 & M_{3,4} & 0 & 0 & 0 & 0 & 0 & M_{3,10} & 0 & 0 \\
0 & 0 & M_{3,4} & \Omega_4 & M_{4,5} & 0 & 0 & 0 & M_{4,9} & 0 & 0 & 0 \\
0 & M_{2,5} & 0 & M_{4,5} & \Omega_5 & M_{5,6} & 0 & M_{5,8} & 0 & 0 & 0 & 0 \\
M_{1,6} & 0 & 0 & 0 & M_{5,6} & \Omega_6 & M_{6,7} & 0 & 0 & 0 & 0 & 0 \\
0 & 0 & 0 & 0 & 0 & M_{6,7} & \Omega_7 & M_{7,8} & 0 & 0 & 0 & M_{7,12} \\
0 & 0 & 0 & 0 & M_{5,8} & 0 & M_{7,8} & \Omega_8 & M_{8,9} & 0 & M_{8,11} & 0 \\
0 & 0 & 0 & M_{4,9} & 0 & 0 & 0 & M_{8,9} & \Omega_9 & M_{9,10} & 0 & 0 \\
0 & 0 & M_{3,10} & 0 & 0 & 0 & 0 & 0 & M_{9,10} & \Omega_{10} & M_{10,11} & 0 \\
0 & M_{2,11} & 0 & 0 & 0 & 0 & 0 & M_{8,11} & 0 & M_{10,11} & \Omega_{11} & M_{11,12} \\
M_{1,12} & 0 & 0 & 0 & 0 & 0 & M_{7,12} & 0 & 0 & 0 & M_{11,12} & \Omega_{12}
\end{pmatrix}. \tag{3.7}
$$

The three principal diagonals in both matrices behave similarly to the equation 3.2. Nevertheless, because of the novel cross-couplings, a non-zero anti-diagonal element arises for 2D and 3D multicavities. Furthermore, for 3D haloscopes extra cross-couplings might arise as a result of the folding created in the two axes (horizontally and vertically folded), as it can be seen in Figure 3.19c. This is the scenario for the parameters $M_{1,6}$, $M_{2,5}$, $M_{7,12}$ and $M_{8,11}$ (and its symmetrical pairs).

A thorough research was conducted as a preliminary proof of concept, in which numerous types of topologies were tried on an all-inductive 2D multicavity. The experiment was carried out on a $N = 6$ subcavities structure folded horizontally (with three subcavities in each row of the multicavity). All the subcavities possess the WR-90 standard dimensions. The primary goal of this research is to design a topology that rejects the axion next configuration mode to enhance the mode separation. This was accomplished with only one cross-coupling, which consisted of inserting an inductive window iris between the first and final (the 6th) subcavity. This multicavity was designed, optimised, and produced.

The next coupling matrix was used in the design of this haloscope to create the geometry dimensions:

$$
\mathbf{M} = \begin{pmatrix}
1 & -0.5 & 0 & 0 & 0 & -0.5 \\
-0.5 & 1 & -0.5 & 0 & 0 & 0 \\
0 & -0.5 & 1 & -0.5 & 0 & 0 \\
0 & 0 & -0.5 & 1 & -0.5 & 0 \\
0 & 0 & 0 & -0.5 & 1 & -0.5 \\
-0.5 & 0 & 0 & 0 & -0.5 & 1
\end{pmatrix}. \tag{3.8}
$$

Because of the employment of a cross-coupling window, a non zero value is picked for the parameters M_{16} and M_{61}, as it is shown in equation 3.8. Considering this coupling

matrix, it is clear that the sign is negative for all the interresonator couplings, which means $k < 0$. This implies that all the irises of the haloscope are set to inductive type, which is also applied to the cross-coupling one. A 3D model of the prototype is depicted in Figure 3.20.
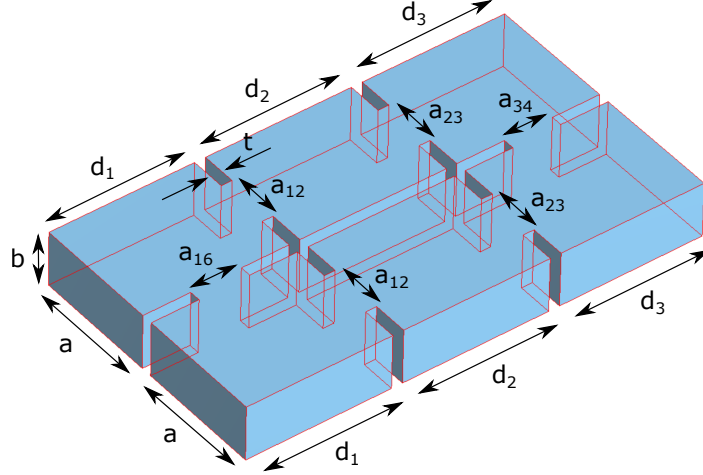
Figure 3.20: 3D model of an all-inductive 2D multicavity with $N = 6$ folded horizontally. The structure is based on two symmetrical rows of three subcavities. The physical folding in the horizontal plane gives the possibility of adding an inductive window between the 1st and 6th subcavities.

Figures 3.21a and 3.21b show two images of the constructed prototype. The technical drawings for the manufacturing of this prototype are depicted in Appendix I: Technical Drawings (see Figures A.7 and A.8). The optimisation procedure involved altering the frequency location of one of the transmission zeros in order to reject the nearest mode. This rejection of the nearest mode can be seen in Figure 3.21c, which shows the magnitude of the S_{21} parameter versus frequency for the design once it is optimised. Measurement results and the response of a structure with $N = 6$ (without cross-couplings) have been added for comparison.

The optimization of this structure provided the following dimensions (according to the Figure 3.20): $a = 22.86$ mm, $b = 10.16$ mm, $d_1 = 26.516$ mm, $d_2 = 26.845$ mm, $d_3 = 26.503$ mm, $a_{12} = a_{23} = 9.921$ mm, $a_{34} = 8.894$ mm, $a_{16} = 9.203$ mm, and $t = 2$ mm.

The mode clustering between the axion mode (which is located at 8.013 GHz) and the next configuration mode has been computed obtaining $\Delta f = 127$ MHz. The measurements provided a value of 111 MHz (being 34 MHz the mode separation without cross-couplings), so there is good agreement between both results. According to the studies using copper material, the axion mode has a $Q_0^{2K} = 40000$ at $T = 2$ K and a $Q_0^{300K} = 6800$ at $T = 300$ K. The measurements of the prototype at $T = 300$ K yield to a value of $Q_0 = 4000$ with the copper coating, which is a value that accounts for 60% of the simulation result. The form factor calculated for the axion mode is $C = 0.702$. It is worth noting that the C parameter value for this haloscope is greater than the theoretical

(a)

(b)

(c)
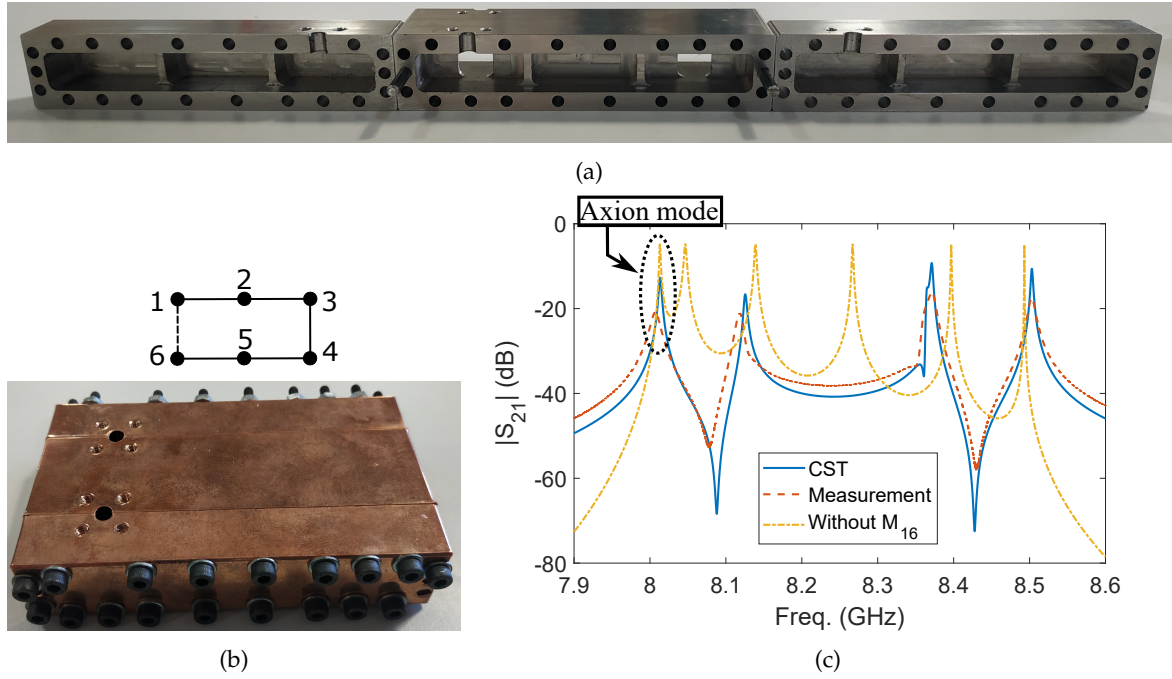
Figure 3.21: All-inductive 2D multicavity with $N = 6$ folded horizontally and a cross-coupling: (a) photo of the produced components (three sections), (b) topology diagram and picture of the mounted prototype with a copper coating, and (c) magnitude of the S_{21} parameter in magnitude versus frequency (simulation results and measurements at $T = 300$ K). To demonstrate the cancellation of the nearest mode using transmission zeros, the simulated response of a multicavity with $N = 6$ subcavities (but without cross-couplings) has been included.

one for a single rectangular cavity. This is caused by the employment of many subcavities coupled by irises, where one of the configuration modes is rejected by a transmission zero. As a result, the transmission zeros offer a fantastic opportunity not only to enhance the mode separation but also to slightly improve C. Even better results could be obtained when 2D and 3D geometries are employed at the same time with long, tall, or even large multicavities (or also the alternating iris idea) considering the main parameters studied in this work: the $Q_0 \times V \times C$ factor, the mode separation (Δf), the physical coupling between subcavities (k), the employment of transmission zeros generated by cross-coupling, and the magnet sizes for dipole and solenoid bores (see models from Figures 3.10 and 3.15).

The overall volume obtained in this structure is $V = 38$ mL, and the $Q_0 \times V \times C$ value is 1067 L, being 5.33 times that of a single cavity with the standard WR-90.

As a conclusion to this work, an intriguing 2D shape is now offered to make better use of the available bore footprint of the magnets. Because there are no cross-couplings in this case, and thus it does not include transmission zeros, the design is more straightforward than the prior one. The concept is based on the introduction of a meander shape in a multicavity, as it can be seen in Figure 3.22a. Figure 3.22b also depicts the magnitude of the S_{21} parameter versus frequency. Because the structure is designed with all inductive
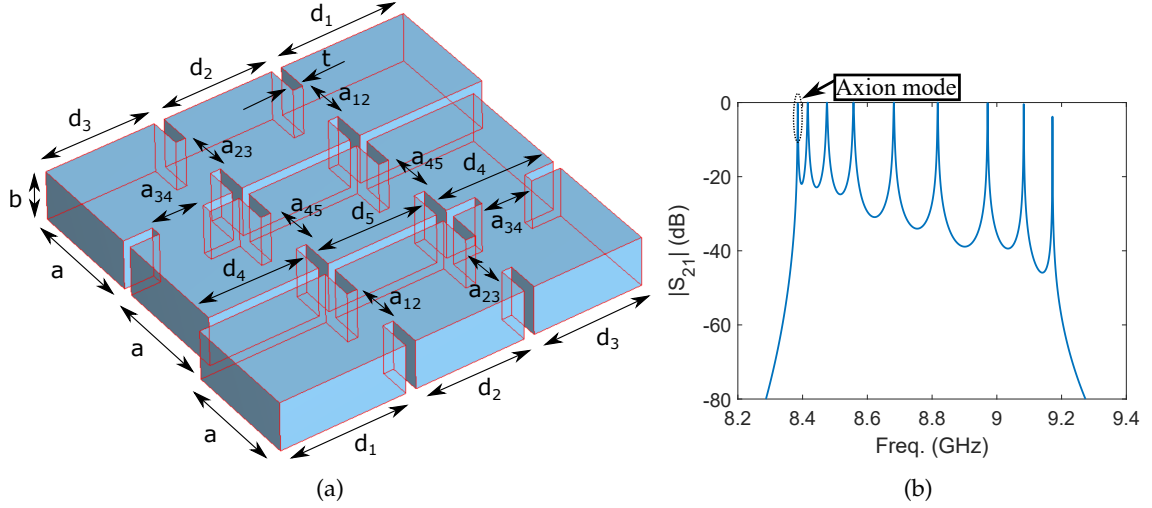
Figure 3.22: 2D multicavity design of $N = 9$ subcavities with a meander shape: (a) 3D model of the structure, (b) computing of the magnitude of the S_{21} parameter versus frequency.

irises, the axion mode is the initial resonance in the S_{21} response.

Despite the fact that the geometry of this haloscope is 2D, it is topologically 1D because it only employs irises from nearby resonators. This is seen in its coupling matrix:

$$\mathbf{M} = \begin{pmatrix} 0.5 & -0.5 & 0 & 0 & 0 & 0 & 0 & 0 & 0 \\ -0.5 & 1 & -0.5 & 0 & 0 & 0 & 0 & 0 & 0 \\ 0 & -0.5 & 1 & -0.5 & 0 & 0 & 0 & 0 & 0 \\ 0 & 0 & -0.5 & 1 & -0.5 & 0 & 0 & 0 & 0 \\ 0 & 0 & 0 & -0.5 & 1 & -0.5 & 0 & 0 & 0 \\ 0 & 0 & 0 & 0 & -0.5 & 1 & -0.5 & 0 & 0 \\ 0 & 0 & 0 & 0 & 0 & -0.5 & 1 & -0.5 & 0 \\ 0 & 0 & 0 & 0 & 0 & 0 & -0.5 & 1 & -0.5 \\ 0 & 0 & 0 & 0 & 0 & 0 & 0 & -0.5 & 0.5 \end{pmatrix}. \tag{3.9}$$

The resulting dimensions of this haloscope (see Figure 3.22a) are the following: $a = 22.86$ mm, $b = 10.16$ mm, $d_1 = 25.2$ mm, $d_2 = d_3 = d_4 = d_5 = 22$ mm, $a_{12} = a_{23} = a_{34} = a_{45} = 10.25$ mm, and $t = 2$ mm. This structure has a resonant frequency for the axion mode of $f_a = 8.385$ GHz, a form factor of $C = 0.684$, and an unloaded quality factor of $Q_0^{2K} = 41475$, which are extremely good results when compared to earlier RADES haloscopes and those given in the previous sections. According to Figure 3.9b, the mode separation Δf is 30.8 MHz (0.37%). The haloscope overall volume is $V = 49.14$ mL, and the value of the $Q_0 \times V \times C$ factor is 1394.05 L, or 6.96 times that of a single cavity with the standard WR-90.

The advantages of this multicavity geometry stem from its quasi-square form. In this example, the haloscope has a footprint of 72.58×76.4 mm^2 (along its width and its length), being 22.86×286.4 mm^2 (an elongated form) for the 1D multicavity scenario. This quasi-square area can be more suited in some circumstances where the bore of the magnet is restricted in all dimensions (as with some solenoid magnets, like the scenario from Figure 3.10g). In practise, several of the approaches presented in this PhD thesis can be merged to make better use of available room in the utilised magnet.

65

3.2 ANALYSIS OF THE QUALITY FACTOR IN HALOSCOPES

The quality factor of a haloscope cavity is one of the most important parameters to increase the axion-photon sensibility (see equation 2.10). Unfortunately, as it is previously stated, the Q_0 value is significantly reduced (usually by half) when the structure is fabricated. In the next section, the theory for the extraction of the loaded and unloaded quality factors, Q_l and Q_0, respectively, and the external coupling factor κ in a system based on a resonant circuit with two ports is presented. Thus, κ can be written in terms of the coupling coefficient β with the expression

$$\kappa = \frac{\beta}{1+\beta}. \tag{3.10}$$

Additionally, in the following sections, several RADES structures will be analysed for studying these parameters.

3.2.1 Q_l, Q_0 and β in microwave resonators

Filters, oscillators, frequency meters, and tuned amplifiers are just a few of the uses for microwave resonators. Because the functioning of microwave resonators can be modelled using classical circuit theory with lumped-element resonators, firstly, the examination of the fundamental properties of series and parallel *RLC* (Resistor + Inductor + Capacitor) resonant circuits is reviewed. Then, utilising distributed elements such as transmission lines and rectangular waveguides, several implementations of resonators at microwave frequencies are presented. The employment of coaxial probes and iris windows to excite resonators is also discussed.

A microwave resonator can generally be described at near-resonant frequencies by either a series or parallel *RLC* lumped-elements equivalent circuit, which fundamental features are presented as follows [69].

3.2.1.1 *Series resonant circuit*

Figure 3.23 depicts a series *RLC* resonant circuit, where it can be easily seen that the input impedance is:

$$Z_{in} = R + j\omega L - j\frac{1}{\omega C}. \tag{3.11}$$

On the other hand, the complex power delivered to the resonator is

$$P_{in} = \frac{1}{2}VI^* = \frac{1}{2}Z_{in}|I|^2 = \frac{1}{2}Z_{in}\left|\frac{V}{Z_{in}}\right|^2 = \frac{1}{2}|I|^2\left(R + j\omega L - j\frac{1}{\omega C}\right). \tag{3.12}$$

The resistor dissipated power is expressed as the real part of the complex power,

$$P_{loss} = \frac{1}{2}|I|^2 R. \tag{3.13}$$
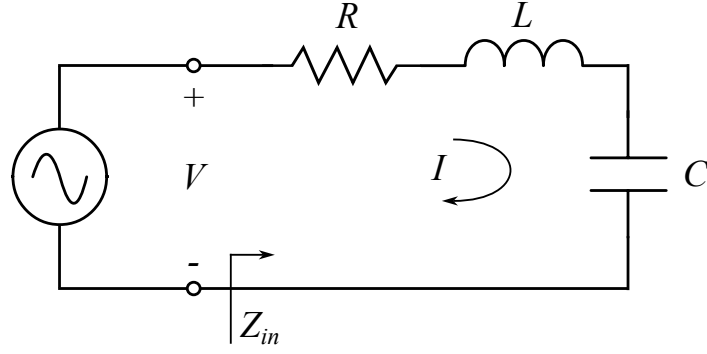
Figure 3.23: Series *RLC* resonant circuit.

Taking into account that V_c is the voltage across the capacitor, the average magnetic and electric energies stored in the inductor and capacitor, respectively, are:

$$W_m = \frac{1}{4} |I|^2 L, \tag{3.14}$$

$$W_e = \frac{1}{4} |V_c|^2 C = \frac{1}{4} |I|^2 \frac{1}{\omega^2 C}. \tag{3.15}$$

Thus, P_{in} and Z_{in} can be reformulated as

$$P_{in} = P_{loss} + 2j\omega (W_m - W_e), \tag{3.16}$$

$$Z_{in} = \frac{2P_{in}}{|I|^2} = \frac{P_{loss} + 2j\omega (W_m - W_e)}{\frac{1}{2} |I|^2}. \tag{3.17}$$

When the average stored magnetic and electric energies are equivalent, that is, $W_m = W_e$, resonance occurs. In this situation, equation 3.17 is rewritten, considering equation 3.13, as follows

$$Z_{in} = \frac{P_{loss}}{\frac{1}{2} |I|^2} = R. \tag{3.18}$$

Also, considering equations 3.14 and 3.15, the resonant frequency (ω_0) is defined as

$$\omega_0 = \frac{1}{\sqrt{LC}}. \tag{3.19}$$

The unloaded quality factor Q is a very important parameter in a resonant circuit and it is defined as follows [69]

$$Q = \omega \frac{\text{Average energy stored}}{\text{Energy loss/second (or Power loss)}} = \omega \frac{W_m + W_e}{P_{loss}}. \tag{3.20}$$

Therefore, the value of Q is an indicator of the resonant circuit losses (a smaller loss leads to a greater Q value). Resonator losses can be caused by the losses of the conductor, dielectric, or radiation, and are represented by the equivalent circuit resistor R. An external connected network might result in further losses. Each of these losses will result in a decrease in the quality factor. The unloaded Q, written as Q_0, is the quality factor of

the resonator itself, excluding external loading effects.

Employing equations 3.13, 3.14, 3.15 and 3.20, the unloaded quality factor of the circuit from Figure 3.23, in resonance, can be expressed as

$$Q_0 = \omega_0 \frac{2W_m}{P_{loss}} = \frac{\omega_0 L}{R} = \frac{1}{\omega_0 RC}. \tag{3.21}$$

On the other hand, making $\omega = \omega_0 + \Delta\omega$, being $\Delta\omega$ small, and considering a frequency close to the resonance, the input impedance from equation 3.11 may be rewritten as

$$Z_{in} = R + j\omega L \left(1 - \frac{1}{\omega^2 LC}\right) = R + j\omega L \left(\frac{\omega^2 - \omega_0^2}{\omega^2}\right), \tag{3.22}$$

with $\omega_0^2 = \frac{1}{LC}$. Due to the fact that $\omega^2 - \omega_0^2 = (\omega - \omega_0)(\omega + \omega_0) = \Delta\omega(2\omega - \Delta\omega) \simeq 2\omega\Delta\omega$ when $\Delta\omega$ is small, the previous impedance can be expressed as

$$Z_{in} \simeq R + j2L\Delta\omega \simeq R + j\frac{2RQ_0\Delta\omega}{\omega_0}, \tag{3.23}$$

which is useful for the identification of equivalent circuits in resonators with distributed elements.

A resonator with losses can also be characterised as a lossless resonator with the resonant frequency, ω_0, replaced with a complex effective resonant frequency [69]:

$$\omega_0 \to \omega_0 \left(1 + \frac{j}{2Q_0}\right), \tag{3.24}$$

which can be seen as the Z_{in} of a series resonator circuit without losses ($R = 0$):

$$Z_{in} = j2L(\omega - \omega_0). \tag{3.25}$$

This, employing equation 3.24, Z_{in} can be transformed into

$$Z_{in} = j2L\left(\omega - \omega_0 - j\frac{\omega_0}{2Q_0}\right) = \frac{\omega_0 L}{Q_0} + j2L(\omega - \omega_0) = R + j2L\Delta\omega, \tag{3.26}$$

which coincides with equation 3.23. Since the loss for most real resonators is relatively minimal, the quality factor may be calculated using the perturbation approach, starting with the lossless solution. Then, by substituting ω_0 with the complex resonant frequency (equation 3.24), the impact of losses may be applied to the input impedance.

In conclusion, examining the resonator half-power bandwidth depicted in Figure 3.24, which shows the magnitude of the input impedance as a function of the frequency, it can be seen that when the frequency is such that $|Z_{in}|^2 = 2R^2$, the average (real) power given to the circuit is one-half that delivered at resonance, as calculated by equation 3.12. BW is
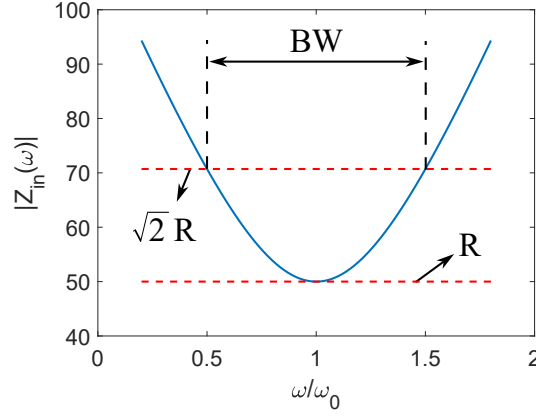
Figure 3.24: Magnitude of the input impedance (solid blue line) for the series RLC resonant circuit from Figure 3.23 in an example with $R = 50\ \Omega$ and $L = 10\ nH$. Computed employing equation 3.23.

the fractional bandwidth, and considering $\frac{\Delta\omega}{\omega_0} = \frac{BW}{2}$ at the upper band edge, equation 3.23 yields to

$$|R + jRQ_0(BW)|^2 = 2R^2 \rightarrow BW = \frac{1}{Q_0}. \tag{3.27}$$

3.2.1.2 *Parallel resonant circuit*

Figure 3.25 depicts a parallel RLC resonant circuit, the dual of the series RLC resonant circuit, where it can be seen that the input impedance is:

$$Z_{in} = \left(\frac{1}{R} + \frac{1}{j\omega L} + j\omega C \right)^{-1}. \tag{3.28}$$
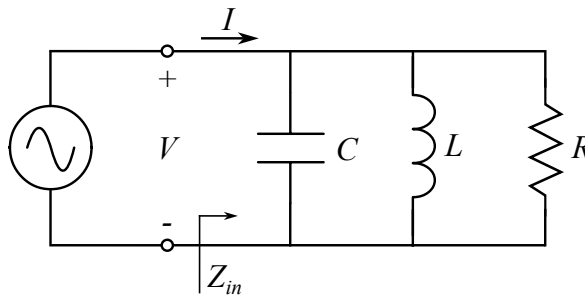
Figure 3.25: Parallel RLC resonant circuit.

The complex power delivered to the resonator is

$$P_{in} = \frac{1}{2}VI^* = \frac{1}{2}Z_{in}|I|^2 = \frac{1}{2}|V|^2\frac{1}{Z_{in}^*} = \frac{1}{2}|V|^2\left(\frac{1}{R} + \frac{j}{\omega L} - j\omega C \right). \tag{3.29}$$

On the other hand, the dissipated power of the resistor (R) is expressed as

$$P_{loss} = \frac{1}{2}\frac{|V|^2}{R}. \tag{3.30}$$

Taking into account that I_L is the current through the inductor, the average electric and magnetic energies stored in the capacitor and inductor, respectively, are:

$$W_e = \frac{1}{4}|V|^2 C, \tag{3.31}$$

$$W_m = \frac{1}{4}|I_L|^2 L = \frac{1}{4}|V|^2 \frac{1}{\omega^2 L}. \tag{3.32}$$

Thus, P_{in} and Z_{in} can be reformulated as

$$P_{in} = P_{loss} + 2j\omega\left(W_m - W_e\right), \tag{3.33}$$

$$Z_{in} = \frac{2P_{in}}{|I|^2} = \frac{P_{loss} + 2j\omega\left(W_m - W_e\right)}{\frac{1}{2}|I|^2}, \tag{3.34}$$

which are identical to its homologous in a series RLC circuit (equations 3.16 and 3.17, respectively).

The resonance condition occurs when, as in the case of the series circuit, $W_m = W_e$. In this situation, considering equations 3.30 and 3.34, the input impedance is converted into

$$Z_{in} = \frac{P_{loss}}{\frac{1}{2}|I|^2} = R, \tag{3.35}$$

which is also identical to its homologous in a series RLC circuit (equation 3.18). Thus, with equations 3.31 and 3.32, the resonant frequency can be expressed as

$$\omega_0 = \frac{1}{\sqrt{LC}}, \tag{3.36}$$

again identical to the series case (equation 3.19).

The unloaded quality factor (Q_0) of the parallel resonant circuit can be expressed using the definition of equation 3.20 and the results in equations 3.32, 3.31 and 3.30:

$$Q_0 = \omega_0\frac{2W_m}{P_{loss}} = \frac{R}{\omega_0 L} = \omega_0 RC. \tag{3.37}$$

In contrast to the series circuit, in a parallel RLC circuit the quality factor increases with the resistance R.

The series expansion can be used to simplify the input impedance of equation 3.28 near resonance. Then, assuming $\omega = \omega_0 + \Delta\omega$, being $\Delta\omega$ small, this input impedance can be converted into

$$Z_{in} \simeq \left(\frac{1}{R} + \frac{1 - \Delta\omega/\omega_0}{j\omega_0 L} + j\omega_0 C + j\Delta\omega C \right)^{-1} \simeq \left(\frac{1}{R} + j\frac{\Delta\omega}{\omega_0^2 L} + j\Delta\omega C \right)^{-1} \simeq$$

$$\simeq \left(\frac{1}{R} + 2j\Delta\omega C \right)^{-1} \simeq \frac{R}{1 + 2j\Delta\omega RC} = \frac{R}{1 + 2jQ_0\Delta\omega/\omega_0}, \tag{3.38}$$

with $\omega_0^2 = \frac{1}{LC}$. For $R = \infty$, this parameter is reduced to

$$Z_{in} = \frac{1}{2jC(\omega - \omega_0)}. \tag{3.39}$$

As with the series resonator, the impact of loss may be considered by substituting ω_0 with a complex effective resonant frequency (see equation 3.24).

Figure 3.26 depicts the magnitude of the input impedance versus frequency in an example. The edges of the half-power bandwidth lie at frequencies where $|Z_{in}|^2 = \frac{R^2}{2}$, this is
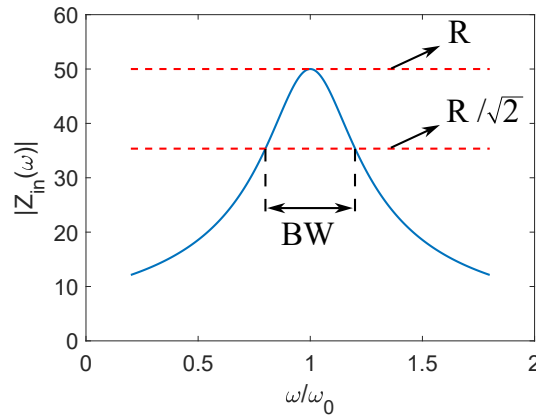
Figure 3.26: Magnitude of the input impedance (solid blue line) for the parallel RLC resonant circuit from Figure 3.25 in an example with $R = 50\ \Omega$ and $C = 10\ pF$. Computed employing equation 3.38.

$\frac{\Delta\omega}{\omega_0} = \frac{BW}{2}$, which yields (with equation 3.38) to

$$BW = \frac{1}{Q_0}, \tag{3.40}$$

as in the series resonant circuit (equation 3.27).

3.2.1.3 Loaded and Unloaded Q

The unloaded quality factor (Q_0) can be defined as the Q in the absence of any loading effects generated by external devices, and it is a property of the resonator itself. However,

in reality, a resonator is most of the times connected to other circuitry, which reduces its overall or loaded Q (Q_l). Figure 3.27 shows a resonator with an external load resistor R_L.
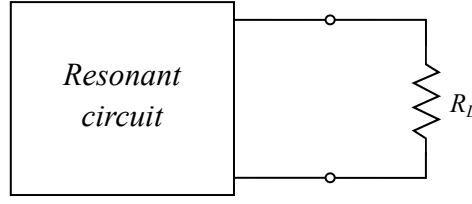
Figure 3.27: Resonator connected to a external load R_L.

If this resonator is a series RLC circuit, the external resistor R_L adds in series with R, resulting in $R + R_L$ as the total resistance in equation 3.21. Because the load resistor R_L combines in parallel with R in a parallel RLC circuit, in this case the total resistance in equation 3.37 is $\frac{RR_L}{(R+R_L)}$. Another type of quality factor can be defined for taking into account this effect: the external quality factor, which is expressed as

$$Q_e^{series} = \frac{\omega_0 L}{R_L},$$

(3.41)

for series RLC circuits, and

$$Q_e^{parallel} = \frac{R_L}{\omega_0 L},$$

(3.42)

for parallel RLC circuits. Thus, the loaded quality factor Q_l is defined as

$$\frac{1}{Q_l} = \frac{1}{Q_e} + \frac{1}{Q_0},$$

(3.43)

which is valid for both series and parallel RLC resonator circuits.

3.2.1.4 *The coupling coefficient and critical coupling in excited resonators*

Resonators are usually useless if they are not coupled to a external circuitry. Therefore, how they can be coupled to transmission lines and waveguides must be reviewed. The employed method depends on the type of resonator. Figure 3.28 shows various examples of resonator coupling procedures.

In this section, it is explained how some of the most common coupling techniques, such as coaxial probe and aperture coupling, work. Firstly, the critical coupling and the coupling coefficient for a resonator coupled to a feed line should be examined. A related practical subject is determining the unloaded quality factor of a resonator from the two-port response of a resonator coupled to a transmission line, which will be explained in the next section.

The amount of energy coupled required between a resonator and its connected devices is determined by the application. For example, in order to retain a high quality factor and acceptable accuracy, a waveguide cavity used as a frequency-metre is often loosely
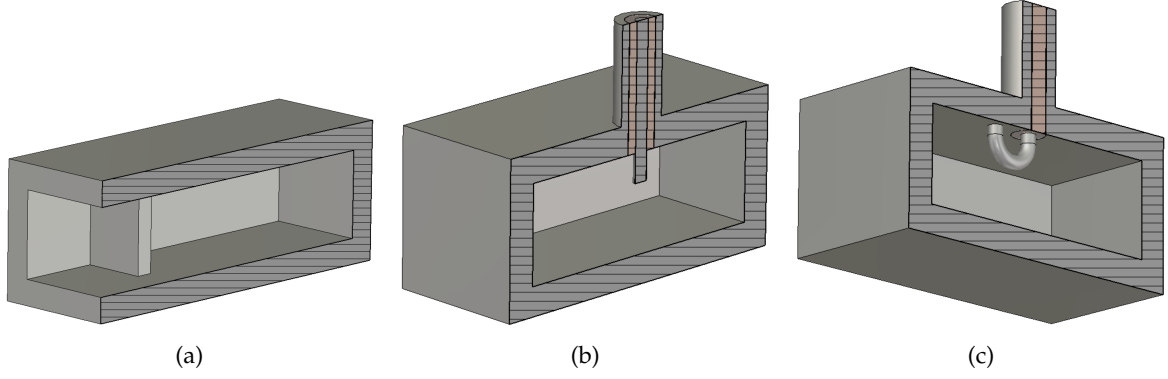
Figure 3.28: Examples of external couplings for exciting a rectangular waveguide resonator: (a) inductive iris window, (b) coaxial probe antenna, and (c) loop coaxial antenna. (a) and (b) show the symmetric half, being the dashed region the symmetry plane. In (c) the cutting plane is slightly shifted from the symmetrical plane to facilitate the visualization of the loop shape.

connected to its feed guide. A resonator employed in an oscillator or tuned amplifier, on the other hand, may be strongly coupled for optimum power transmission (maximum power transfer). The coupling coefficient (β) expresses the degree of coupling between a resonator and a feed. To achieve optimal power transmission between a resonant device and a feed line, the resonator should be matched to the line at the resonant frequency; this is referred to as *critical coupling*. In haloscopes, this is also an important condition that should be maintained when searching for axions in order to optimise its sensibility ($g_{a\gamma\gamma}$).

Considering the circuit from Figure 3.29 and equations 3.23 and 3.21, the input impedance and quality factor of a series resonant circuit close to the resonant frequency is

$$Z_{in} = R + j2L\Delta\omega = R + j\frac{2RQ_0\Delta\omega}{\omega_0}, \tag{3.44}$$

$$Q_0 = \frac{\omega_0 L}{R}. \tag{3.45}$$
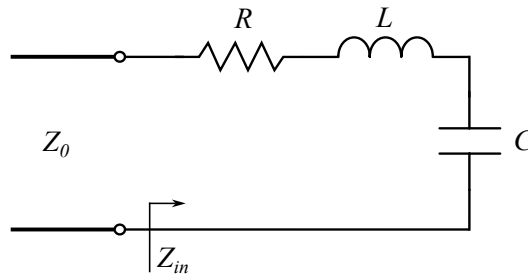
Figure 3.29: Series *RLC* resonant circuit connected to a feedline of characteristic impedance Z_0.

When $\omega = \omega_0$, $\Delta\omega = 0$, which leads to $Z_{in} = R$. On the other hand, for matching the resonant circuit with critical coupling the resistance must coincide with the characteristic impedance of the feedline ($R = Z_0$). Then, the unloaded quality factor can be expressed as

$$Q_0 = \frac{\omega_0 L}{R} = \frac{\omega_0 L}{Z_0}. \tag{3.46}$$

Therefore, the external quality factor, employing equation 3.41, can be expressed as

$$Q_e = \frac{\omega_0 L}{Z_0} = Q_0, \tag{3.47}$$

which illustrates that, under the condition of critical coupling, the external and unloaded Q's are equivalent. If the $Q_e = Q_0$ condition is applied to the equation 3.43, it can be extracted that the loaded quality factor is half of the unloaded one ($Q_l = Q_0/2$).

The coupling coefficient β can be expressed as [69]

$$\beta = \frac{Q_0}{Q_e}, \tag{3.48}$$

and when coupled to a transmission line with characteristic impedance Z_0, this parameter may be used in both series ($\beta = \frac{Z_0}{R}$, from equations 3.48, 3.47 and 3.45) and parallel ($\beta = \frac{R}{Z_0}$, from equation 3.48, $Q_0 = \omega_0 RC$ and $Q_e = \omega_0 Z_0 C$) resonant circuits. There are three distinct cases:

- $\beta < 1$, the *undercoupled* case

- $\beta = 1$, the *critically coupled* case

- $\beta > 1$, the *overcoupled* case

A very useful tool is commonly used by microwave engineers for analysing the coupling coefficient: the *Smith Chart*. P. Smith (Bell Telephone Laboratories) created a graphical tool for solving transmission line problems in 1939. Figure 3.30 depicts the Smith diagram or Smith chart with examples for the three previous cases, which is simply a representation of the reflection coefficient in the complex plane.

The Smith chart primary utility is the conversion of the reflection coefficient to normalised impedances (or admittances) and vice versa. The relationship between these two parameters is shown in [108].

3.2.1.5 *β extraction from one-port measurements*

There are many possibilities to extract the value of β from a measurement (experimental or simulation) [109]. In this PhD thesis, several of these methods are reviewed. The first of them is based on modifying the phase of the reflection parameter S_{11} from the measurement. The idea is to shift the S_{11} circle for being projected on the Smith chart

Smith Chart
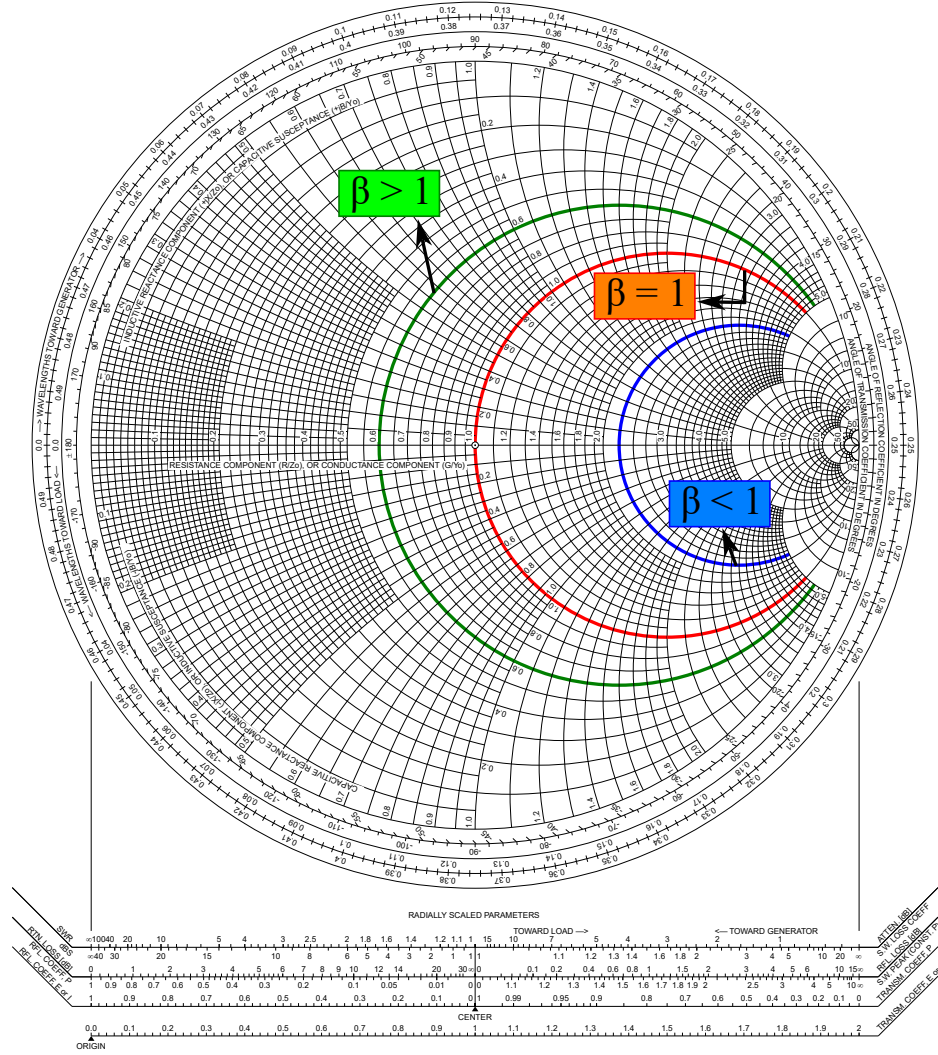
Figure 3.30: Smith chart sketching the impedance position for the series resonant circuit (equation 3.44 in the circuit from Figure 3.29) with three examples: undercoupled ($\beta < 1$ or $R > Z_0$, the blue line), critically coupled ($\beta = 1$ or $R = Z_0$, the red line), and overcoupled ($\beta > 1$ or $R < Z_0$, the green line). The characteristic impedance of the feedline (Z_0) is fixed, so the parameter that controls the β value, and therefore the diameter of the circle in the Smith chart, is the resistance R.

at the left (modelled by the parallel equivalent circuit) or right (modelled by the series equivalent circuit, as it is the case in the three examples from Figure 3.30) side. Once it is done, the next step is to check the point of intersection between the circle and the $x-$axis of the Smith chart (which represents the region with imaginary parts zero, $\Im\{z\} = 0$). If the circle is centered at the left side, β will take the value of the $\Re\{z\}$ Smith chart circle crossing such point. If it is centered at the right side, β will take the inverse of the $\Re\{z\}$ Smith chart circle value. In Figure 3.31 two measurement examples for both types are shown.

Smith Chart
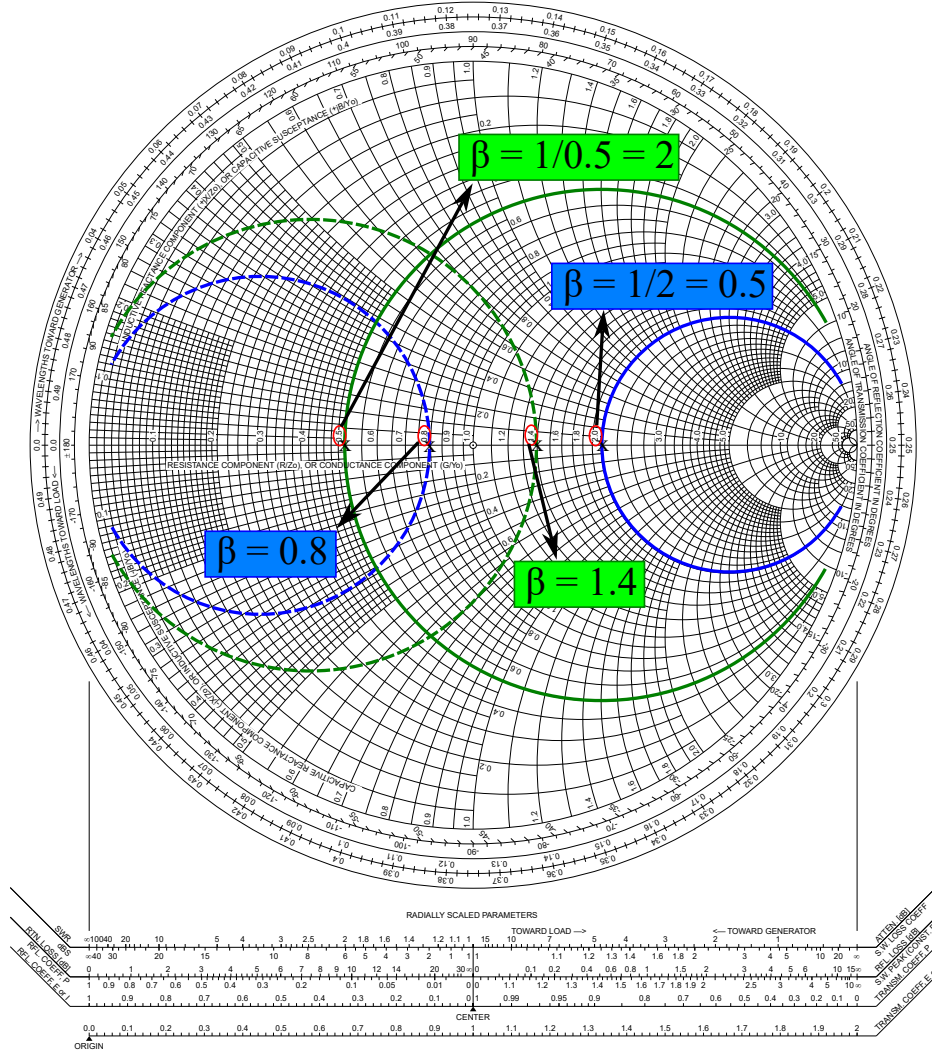
Figure 3.31: Smith chart showing four examples including undercoupled (blue lines) and over-coupled (green lines) measurements for two types of phase shifting: S_{11} circle at the left side (dashed lines) and at the right side (solid lines).

Thus, it can be seen how the diameter of the S_{11} circle projected on the Smith chart is directly proportional to the value of the reflection coefficient β, independently of the phase value (position of the circle). If this circle exceeds the center of the Smith chart, the cavity is overcoupled. If not, it is undercoupled (or critically coupled for the circle touching the center).

The second method studied in this PhD thesis is based on employing the following equations [109]:

$$\beta = \frac{1 - |S_{11}^{\omega_0}|}{1 + |S_{11}^{\omega_0}|},\tag{3.49}$$

for $\beta < 1$, and

$$\beta = \frac{1 + |S_{11}^{\omega_0}|}{1 - |S_{11}^{\omega_0}|},$$

(3.50)

for $\beta > 1$, where $|S_{11}^{\omega_0}|$ is the magnitude (in linear) of the reflection parameter at the resonant frequency. To identify whether the cavity is under or overcoupled, the circle of the S_{11} projected on the Smith chart is usually observed. Another procedure to identify whether a port is over or undercoupled, without the Smith chart, is based on varying its coupling (the depth of the antenna in the case of the coaxial probe, for example) and observing whether the resonance bell (of S_{11} or S_{21} parameter) widens or narrows. If the bell narrows when the coupling increases, the port is undercoupled, if not, it is overcoupled.

The previous methods can also be applied employing the complex plane instead of the Smith chart, which can be occasionally worth if the Smith chart tool is not available at the time of the β extraction. In this case, the diameter D of the S_{11} circle projected on the complex plane is the parameter employed for the β computing with the following equation [109]:

$$\beta = \frac{D}{2 - D}.$$

(3.51)

In Figure 3.32 two examples are shown to explain the behaviour of the parameter D in both undercoupled and overcoupled cases. For the undercoupled case, D takes the
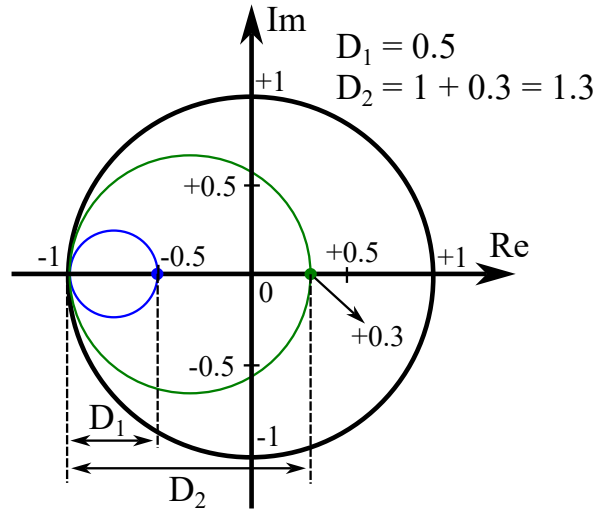
Figure 3.32: Complex plane depicting two measurement examples: undercoupled (blue line) and overcoupled (green line).

absolute value of the point of intersection between the circle and the $x-$axis. For the overcoupled case, the D parameter value is equal to the $x-$axis intersection point plus $+1$. The undercoupled example from Figure 3.32 has a coupling coefficient of $\beta = \frac{0.5}{2-0.5} = 0.33$ and the overcoupled case $\beta = \frac{1.3}{2-1.3} = 1.86$.

On the other hand, several methods are described in [109] for extracting the Q_0 value from the reflection parameter in one-port measurements. However, in general, the cavities studied in this PhD thesis are based on two-port measurements, although for haloscopes one of the ports is usually very undercoupled. In [109] is also described how to compute the unloaded quality factor in presence of coupling losses (which is typically represented as a S_{11} circle shifted towards the center of the Smith chart).

3.2.1.6 β and Q_0 extraction from two-port measurements

Figure 3.33 depicts a two-port network formed by a series RLC resonator installed in series between two transmission lines with characteristic impedances Z_{01} and Z_{02}, which act as ports (*Port* 1 and *Port* 2, respectively). In this situation, the loading effect is separated
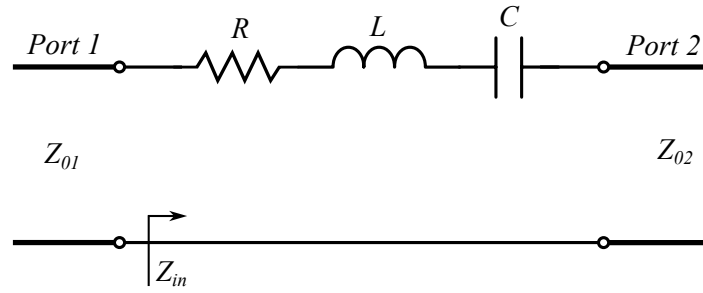
Figure 3.33: Series RLC resonant circuit with 2 ports.

into two external quality factors: Q_{e1}, referred to Port 1, and Q_{e2}, referred to Port 2. Thus, equation 3.43 becomes

$$\frac{1}{Q_l} = \frac{1}{Q_{e1}} + \frac{1}{Q_0} + \frac{1}{Q_{e2}}. \tag{3.52}$$

Multiplying by $Q_0 Q_l$ to this equation leads to

$$\frac{Q_0 Q_l}{Q_l} = \frac{Q_0 Q_l}{Q_{e1}} + \frac{Q_0 Q_l}{Q_0} + \frac{Q_0 Q_l}{Q_{e2}} \rightarrow Q_0 = Q_l \left(1 + \frac{Q_0}{Q_{e1}} + \frac{Q_0}{Q_{e2}} \right). \tag{3.53}$$

Therefore, considering equation 3.48, it can be extracted that

$$\beta_1 = \frac{Q_0}{Q_{e1}}, \tag{3.54}$$

for the coupling coefficient at Port 1, and

$$\beta_2 = \frac{Q_0}{Q_{e2}}, \tag{3.55}$$

at Port 2. Finally, equation 3.53 can be rewritten as

$$Q_0 = Q_l \left(1 + \beta_1 + \beta_2 \right). \tag{3.56}$$

In the case of centering the S_{11} and S_{22} circles at the left side of the Smith chart or complex plane, the extraction of the $1 + \beta_1 + \beta_2$ coefficient is realised with the following equations when using a two-port scattering matrix measurement [110, 111]:

$$S_{11}^{\omega_0} = -1 + \frac{2\beta_1}{1 + \beta_1 + \beta_2},$$

(3.57)

$$S_{22}^{\omega_0} = -1 + \frac{2\beta_2}{1 + \beta_1 + \beta_2},$$

(3.58)

where $S_{11}^{\omega_0}$ and $S_{22}^{\omega_0}$ are the complex values of the reflection parameters at the resonant frequency at Port 1 and Port 2, respectively. Operating, the following expression can be extracted:

$$1 + \beta_1 + \beta_2 = \frac{4}{(1 - S_{11}^{\omega_0})(1 - S_{22}^{\omega_0}) - (1 + S_{11}^{\omega_0})(1 + S_{22}^{\omega_0})}.$$

(3.59)

If the centering is applied to the right side, the sign of the $S_{11}^{\omega_0}$ and $S_{22}^{\omega_0}$ values has to be modified in equation 3.59.

Since the resistance value of the series resonator is minimum at resonance, maximum transmission occurs. When the resonator is not in resonance, the resonator impedance rises and the insertion loss rises. As a result, the network depicted in Figure 3.33 has a two-port transmission response (indicated by the transmission parameter $|S_{21}|$) of the form seen in Figure 3.34.
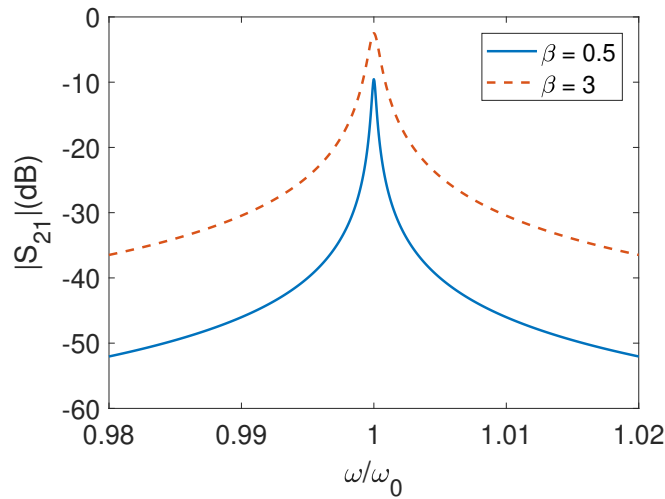
Figure 3.34: Magnitude of the transmission parameter versus frequency for two example ($\beta = 0.5$ and $\beta = 3$) in the series *RLC* resonant circuit with 2 ports from Figure 3.33 and $Q_0 = 5000$.

From equation 3.27 it can be extracted that $Q_L = \frac{f_0}{BW}$, where f_0 is the resonant frequency and BW is the half-power bandwidth (both in Hz) where the $|S_{21}|(dB)$ value is 3 dB lower than at resonance (the $-3\,dB\,method$). Finally, the Q_l and β values may be used to get the

unloaded Q with equation 3.56.

Two particular cases can be described for a two-port measurement: $\beta_1 = \beta_2$ (or $S_{11}^{\omega_0} = S_{22}^{\omega_0}$) and $\beta_2 \simeq 0$ (or $S_{22}^{\omega_0} \simeq -1$ for the case of centering the S_{11} and S_{22} circles at the left side of the Smith chart or complex plane, or $S_{22}^{\omega_0} \simeq 1$ for the right side). For the first case, where both ports are equally coupled to the resonator, employing equation 3.59 the expression of equation 3.56 can be reduced to

$$Q_0 = Q_l \left(1 + \beta_1 + \beta_2\right) = Q_l \left(\frac{4}{(1 - S_{11}^{\omega_0})^2 - (1 + S_{11}^{\omega_0})^2}\right) = Q_l \left(-\frac{1}{S_{11}^{\omega_0}}\right), \quad (3.60)$$

which is valid for the left centering of the circles. For the right centering, the sign of $S_{11}^{\omega_0}$ in equation 3.60 has to be modified.

For the other case, where Port 2 is very weakly coupled to the resonator (the case in axion haloscopes for data taking), equation 3.56 becomes

$$Q_0 = Q_l \left(1 + \beta_1\right), \quad (3.61)$$

where β_1 can be extracted with any method described in section 3.2.1.5. Alternatively, equation 3.59 can be employed and reduced and, applied to equation 3.56, the following expression can be extracted

$$Q_0 = Q_l \left(1 + \beta_1 + \beta_2\right) = Q_l \left(\frac{4}{2(1 - S_{11}^{\omega_0})}\right) = Q_l \left(\frac{2}{1 - S_{11}^{\omega_0}}\right), \quad (3.62)$$

which again is only valid for the left centering of the circles. For the right centering, the sign of $S_{11}^{\omega_0}$ in equation 3.62 has to be modified.

3.2.2 Q_0 in the all-inductive 5-subcavities haloscope

In the manufacture of a prototype using waveguide technology, the most important issue is the cutting plane of the metallic housing, which should be placed at a plane parallel to the E-field lines cutting regions with minimum surface current for preventing high Q_0 downgrades. In addition, other factor must be considered in production (like the manufacturing tolerances or the screw positioning).

In the earlier years, the RADES team employed the rectangular waveguide technology working with the fundamental TE_{101} mode for his first haloscope prototypes. In Figure 3.35 the TE_{101} electric field (at the three possible cutting planes) and the surface current of a rectangular cavity example are depicted. As it can be seen, the planes parallel to the electric field are the longitudinal and transverse ones. The first case has a lower surface current, so this is the best option for manufacturing the metallic housing in a rectangular waveguide cavity. For an all-inductive multicavity, the electric field lines and the surface
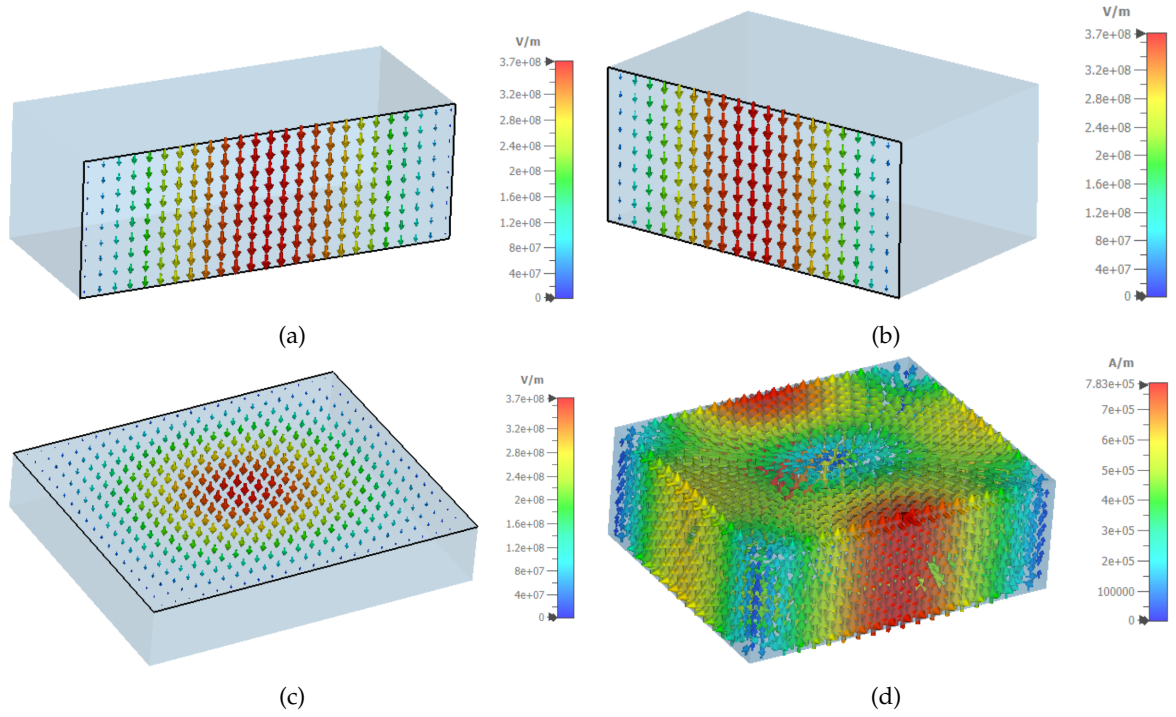
Figure 3.35: Example of a rectangular cavity with width $a = 22.86$ mm, height $b = 10.16$ mm and length $d = 28.55$ mm working at $f_{rTE_{101}} = 8.5$ GHz: TE_{101} electric field at (a) longitudinal plane, (b) transverse plane and (c) horizontal plane, and (d) surface current.

current are in the same direction of the single cavity since the inductive windows have a zero electric field level. In Figure 2.13 (Mode 1) the behaviour of the electric field for the TE_{101} mode for the first RADES structure, the all-inductive 5-subcavities multicavity, is shown. Thus, again, the best choice for a cutting plane is the longitudinal one just dividing the whole haloscope into two pieces (the left and the right pieces).

In 2017 the RADES team manufactured this cavity employing the most commonly used technique in the manufacture of RF filters based on rectangular waveguide technology: the horizontal cutting plane dividing the haloscope into two parts, the main body where the subcavities and the irises are located and the cover plate, as it is depicted in Figure 2.12b. Indeed, firstly, this structure was manufactured in the Universidad Politécnica de Valencia (UPV), Valencia, Spain, with stainless steel 316L material (with a post 30 μm copper coating layer, and a 5 μm nickel layer in between, at CERN coating laboratory for improving the electrical conductivity as well as the quality factor)[4]. However, after the installation in the CAST magnet at the end of such year, several magnetic problems were found. Also, resonance peak shifts were observed when the magnet ramp ups/downs occurred probably because the stainless steel 316L material is a slightly magnetic material.

---

4 Copper material for the manufacturing housing is not directly employed due to potential magnetic quenches that can suddenly occur in magnets (like CAST), due to the loss of superconductivity when its temperature is raised, that would deform severely the structure. For this reason, a more rigid material like the stainless steel is used. Furthermore, a silver coating was ruled out since it required a thicker nickel layer for the coating, which the experts advised against.

Then, a new fabrication (with the same cutting plane) was done at the CERN workshop employing a new material: the 316*LN*, a non-magnetic stainless steel that is used as a standard for the LHC magnets at CERN. This material is the one used to date for all RADES structures for axion data campaigns. Later, in 2018, the RADES team took into consideration the previous cutting plane studies and selected the longitudinal plane for a new manufacturing of the same multicavity prototype: the so-called *vertical cut* haloscope. The production of this structure (see Figure 3.36) provided the electrical response depicted in Figure 3.37 from a measurement at room temperature with the second port very weakly coupled ($\beta_2 \simeq 0$). From these parameters, all the information needed for calculating the
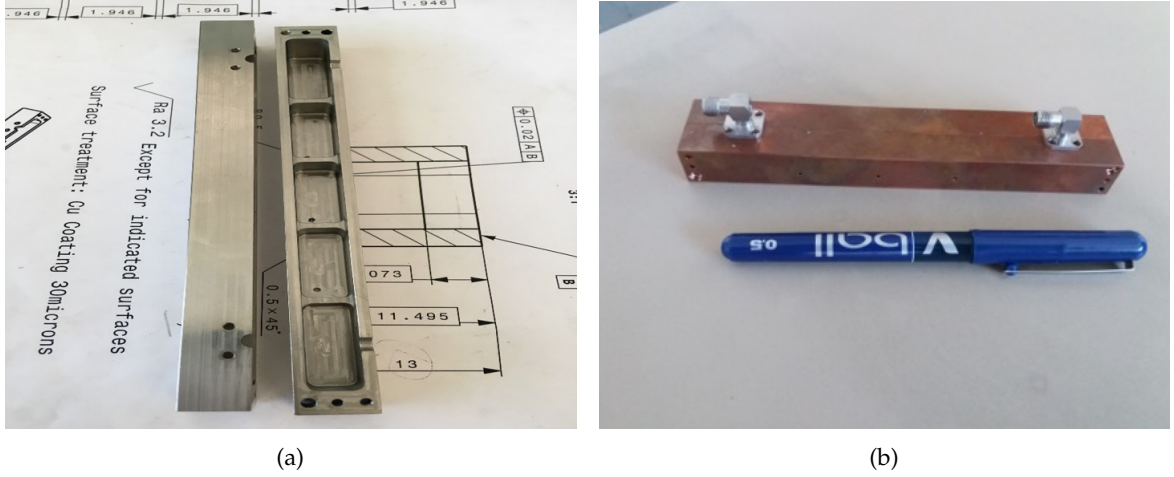
Figure 3.36: Manufactured prototype of the RADES vertical cut haloscope: (a) without and (b) with the 30 μm copper coating layer. The technical drawings for the manufacturing of this prototype are depicted in Appendix I: Technical Drawings (see Figure A.9).

unloaded quality factor can be extracted. Firstly, the loaded quality factor can be derived from the $|S_{21}|(dB)$ parameter (see Figure 3.37a) with the -3 dB method:

$$Q_l = \frac{f_0}{\Delta f_{-3dB}} = \frac{8.4167 \, GHz}{3.5 \, MHz} = 2338. \tag{3.63}$$

Because Port 2 is very weakly coupled, the methods described in the previous sections to extract the coupling coefficient of Port 1 from one-port measurements can be used. The value of β_1 can be calculated easily with the Smith chart once the S_{11} circle is centered at the left side, observing the resonant frequency point from Figure 3.37b, which gives $\beta_1 = 1.63$. Alternatively, employing the complex plane, the value of β_1 can also be extracted. From Figure 3.37c it can be stated that $D = 1 + 0.24$ and therefore

$$\beta_1 = \frac{D}{2 - D} = 1.63. \tag{3.64}$$

Then, employing equation 3.61 the unloaded quality factor is obtained:

$$Q_0 = Q_l(1 + \beta_1) = 2338(1 + 1.63) = 6149, \tag{3.65}$$
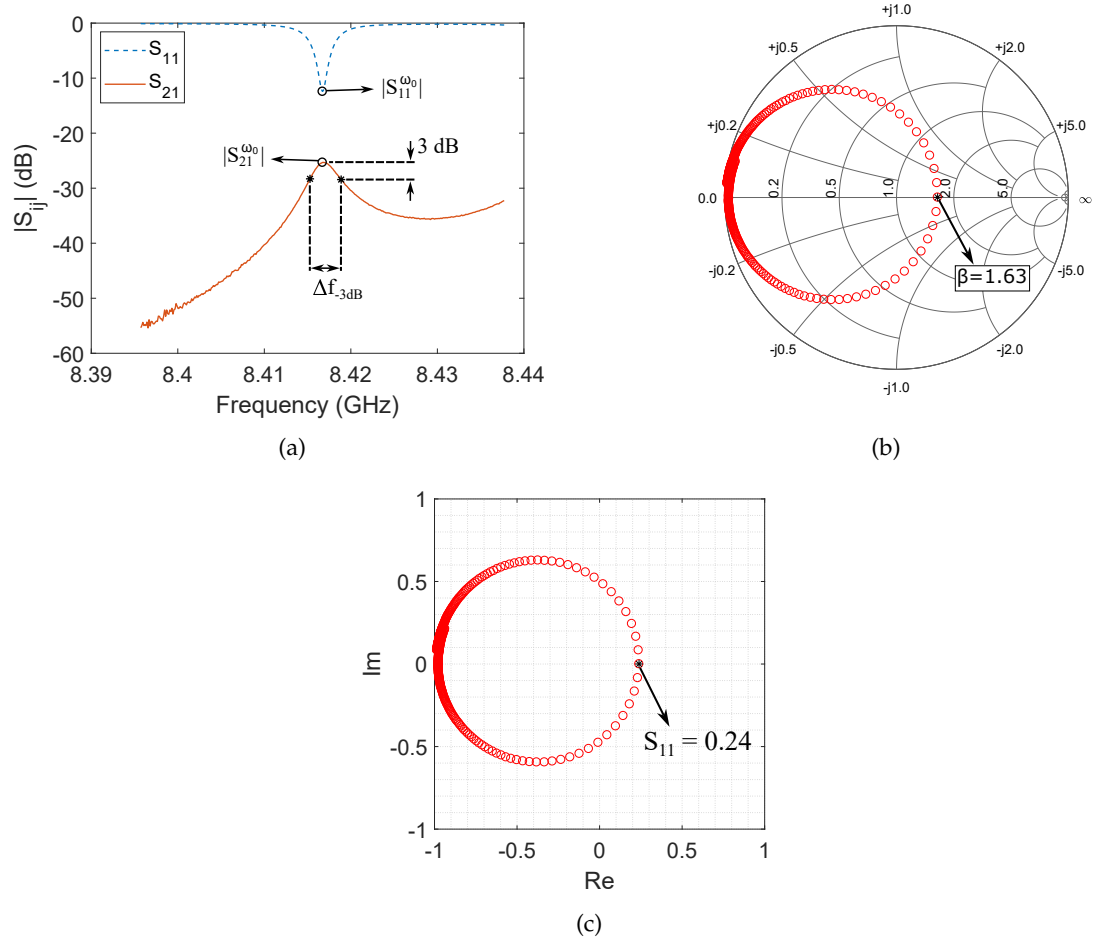
Figure 3.37: Vertical cut measurements at room temperature: (a) $|S_{21}|$ and $|S_{11}|$ parameters in dB, (b) S_{11} parameter at the Smith chart and (c) S_{11} parameter at the complex plane.

which corresponds with the 84 % of the theoretical result ($Q_0 = 7350$ in simulation), being a very good result in manufacturing. Later, several measurements were taken at cryogenic temperatures ($T \simeq 8$ K) that provided a $Q_0 \simeq 24000$, which is the 56 % of the simulation value ($Q_0 \simeq 43000$) [27]. These values are higher than the previous one due to the increasing of the copper conductivity at such cryogenic temperatures (from $\sigma_{Cu}^{T=300K} = 5.8 \times 10^7$ S/m to $\sigma_{Cu}^{T=8K} = 2 \times 10^9$ S/m [27]). On the other hand, the prototype with the horizontal cut has a manufactured Q_0 of ~ 16000 at $T = 2$ K cryogenic temperature (37 % from simulation), which confirms that the vertical cut is a good option for optimizing the manufacturing of rectangular all-inductive multicavity structures. Furthermore, it allows the possibility of tuning the structure by moving the two halves away from each other (as it will be explained in section 3.3).

3.2.3 Q_0 *in the alternating 6-subcavities haloscope*

In summer 2018, the modelling (at Universidad Politécnica de Cartagena (UPCT)), fabrication (at the *ITACA institute*, UPV), coating (at CERN) and testing (at UPCT + CERN) of an alternating iris multicavity based on six subcavities was realised by the RADES team. The

manufactured structure and its response at $T = 2$ K can be observed in Figures 2.17a and 2.19a, respectively. The resonance of this prototype that couples to the axion lies at a higher mode compared to an all-inductive (or all-capacitive) iris multicavity design. This was expected to facilitate the building of a longer cavity with more subcavities and avoid mode clustering at the working resonance frequency.

The manufacture of this prototype was performed with stainless steel 316LN material employing an horizontal cutting plane. In addition, small air gaps were added at both sizes of the top tooth of the capacitive irises in order to facilitate its fabrication, as it is shown in Figure 3.38. Similarly to the all-inductive prototype, a copper coating layer was
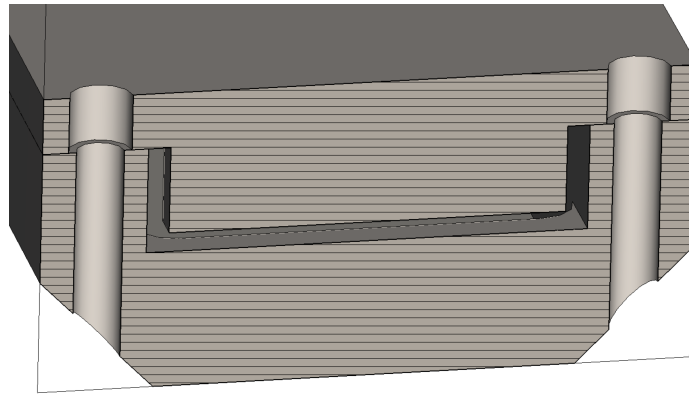
Figure 3.38: Transverse cut of the 3D model of the alternating 6-subcavities haloscope at the middle of one of its capacitive irises in order to observe the air gaps that are created at the top tooth when both the main body and the cover are jointed.

applied after the manufacturing. Once the structure was measured at room temperature, it provided a Q_0 value of 1200, 17 % from the simulation results that give a $Q_0 = 7000$. Additional research was conducted for a better understanding of this considerable disagreement. Following internal debate, it was determined that the contact between the cover and the main body of the cavity was insufficient. Then, the workshop engineers of CERN confirmed that the cover was a bit twisted. Furthermore, a minor slope between the exterior and inner sections of the main body structure at the joint section was found. All of this leads to a poor contact between both pieces. With the help of the CERN workshop, the cover was untwisted and the contact was improved, resulting in an unloaded Q of around 1600 (23 % from simulation). Then, different experimenting approaches to further improve and understand the contact between the two pieces were carried out:

- Conductive paint + thin indium foil

- Structure dimensions checking

- Study of the most sensitive contact region

- Addition of more screws + clamp pressure

- Soldering

The first approach was based on applying a small layer of conductive paint + indium foil (with the help of Dr. Sergio Arguedas and Jessica Golm) to ensure greater contact between the two parts of the structure, as depicted in Figure 3.39. Unfortunately, the
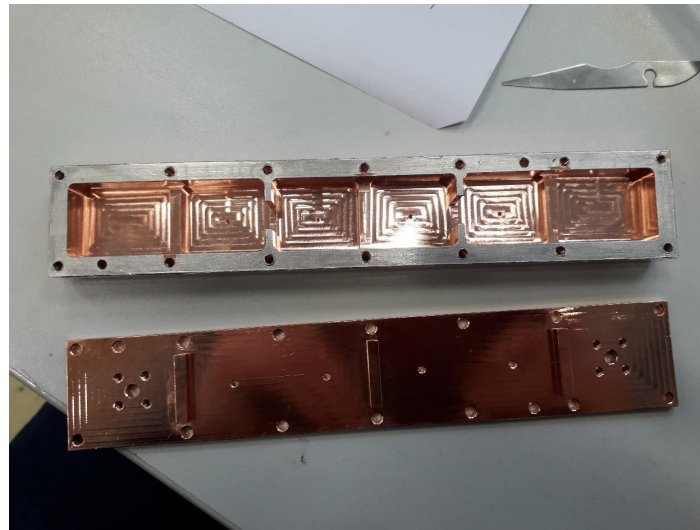
Figure 3.39: Alternating 6-subcavities prototype with conductive silver paint with an indium foil.

quality factor hardly improved with this method.

Secondly, the haloscope was sent in spring 2019 to a metrology laboratory (in *Mecanizados JJ Celdran S.L.U.*, Cartagena, Spain [112]) for computing the real dimensions and checking if the manufacture was done properly. Following these measurements, it was found that the only dimension without acceptable tolerances (< 100 microns) was the thickness of the lid, which was larger in the extreme regions of the longitudinal axis (~ 400 microns thicker). In any case, this difference can be easily solved if the tightening of the screw system is done properly.

The next step to understand the behaviour of the unloaded quality factor in this structure was to perform different simulations in order to identify the most sensitive sections to Q loss (regions with a high level of surface current) on the contact area of the two manufactured parts. A parametric study by varying the position of a small air gap in the junction region was carried out in the simulations. This gap has a width equivalent to the contact area thickness of the main body, a height of 0.5 mm, and length of 1 mm. A 3D model of this simulation is shown in Figure 3.40a. Furthermore, in Figure 3.40b the variation of the unloaded quality factor versus the position of the air gap along the contact length can be observed. Since the structure is symmetrical in the longitudinal and transverse planes, the contact gap parametric has been performed between the end of the first subcavity and the middle of the central capacitive iris. In this plot the Q_0 fluctuates over the longitudinal axis. At the capacitive and inductive windows, a clear quality factor reduction can be identified. Small quality factor reductions can be observed at the middle of the subcavities as well. At the remaining areas, the Q_0 value is maintained at high level.
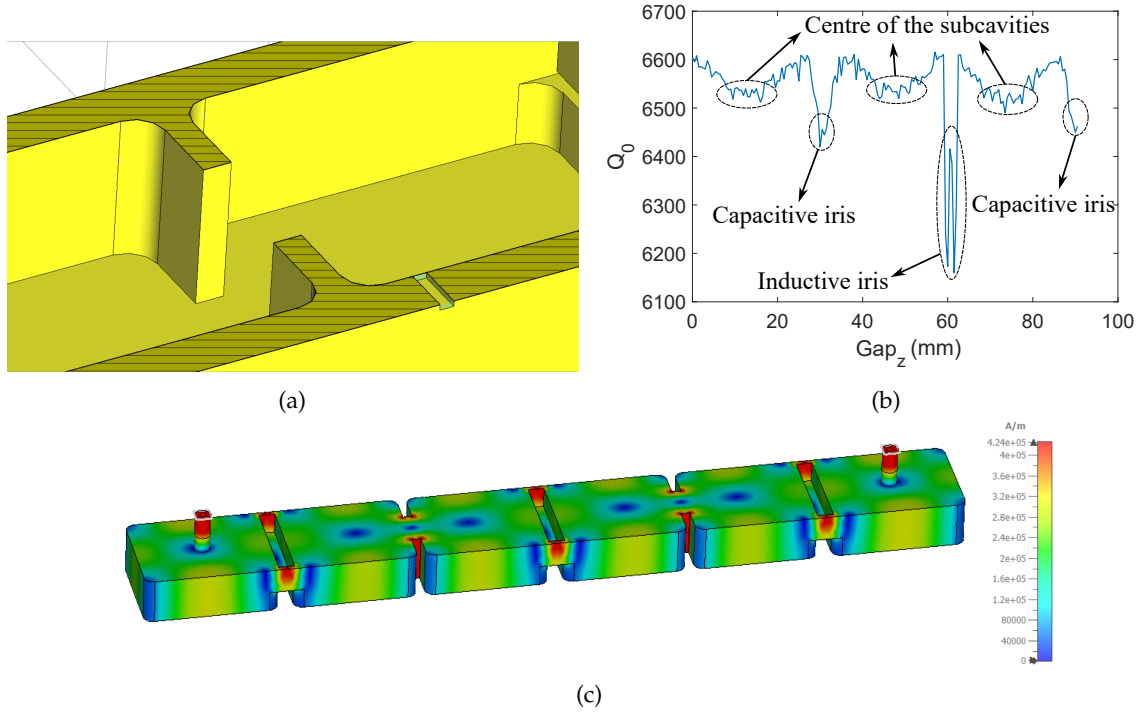
Figure 3.40: (a) 3D model of the alternating 6-subcavities haloscope with an air gap at the contact region of the manufactured prototype, (b) Q_0 versus the gap contact position along the longitudinal axis (Gap_z), and (c) absolute component of the surface current of the axion mode for this structure. Simulation results obtained from CST, an EM simulator [78].

Low oscillations along the curve are due to computational numerical errors in simulation. In addition, it should be noted that the reduction of Q_0 at the inductive iris is greater because the junction covers a larger area in the transverse axis (this can be easily observed in Figure 3.39 on the area covered with silver conductive paint, which looks greyish in colour). These results match with the surface current field for the axion mode, where maximums at the irises and at the middle of the cavities are present, as it is depicted in Figure 3.40c.

Later, the next stage was to increase the number of screw holes (from 14 to 50 screws) to tighten the cover plate and the cavity body more firmly. Figure 3.41a shows a picture of the alternating 6-subcavities haloscope with more screws. Also, clamps were added at the Q_0 measurement time (see Figure 3.41b) to observe if more pressure between both parts helps to improve this parameter. The position of the clamps was adjusted considering the critical regions from the previous results. As a result, the contact improved and the Q_0 value increased from 1600 to 2300 (33 % from simulation). As a consequence of these measurements, it was discovered that enhancing mechanical contact minimises the gaps between theoretical and observed results. The contact could not be improved much more applying extra pressure in such configuration because of the rigidity of the stainless steel material, however another method was employed as a final chance for improving the
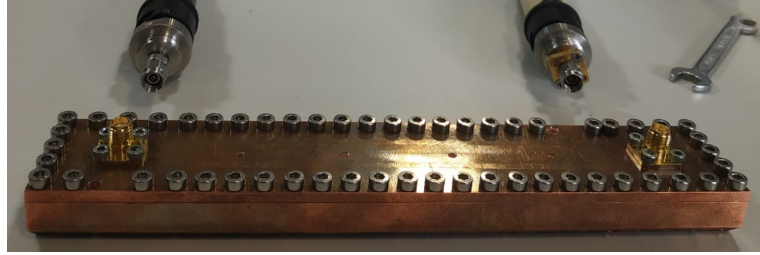
(a)

(b)

Figure 3.41: (a) Alternating 6-subcavities prototype with more screws. (b) High tightening of both parts of this prototype with clamps.

quality factor in this prototype: the soldering.

In summer 2021, a custom soldering process was carried out with the help of Dr. Fritz Caspers (at CERN) to joint both main body and cover of the alternating 6-subcavities haloscope and thus increasing the value of the Q_0 parameter. As Figure 3.42 depicts, a tin layer is applied on both pieces at the contact area for the soldering. Then, a 160 °C

Figure 3.42: Alternating 6-subcavities haloscope pieces with tin layers prepared for the soldering.

temperature is applied to this the structure on a heating station hot plate. This method conducted to a quality factor value of $Q_0 = 4500$ (64 % from simulation), which is a

very good value for a manufactured prototype. This result indicates that the difference between the theoretical and experimental quality factor comes indeed from the bad contact between the two parts.

Later, considering the good results from the 5-subcavities all-inductive vertical cut haloscope and the current surface of the 6-subcavities alternating structure (see Figure 3.40c), a new study applying the longitudinal plane as the manufacturing plane was carried out. Firstly, several simulations were done for comparing the Q_0 downgrade between the cases with the horizontal plane and with the vertical cut. For this purpose a thin ($\sim 100 \ \mu$m) air layer was applied in the simulations on the area of the jointing plane for each case. For the horizontal cut, this layer is deposited on the dashed region from Figure 3.40a. For the vertical cut, the air layer is positioned on the area dotted in red depicted in Figure 3.43. These simulations provided a Q_0 difference of 20 %, being the vertical cut
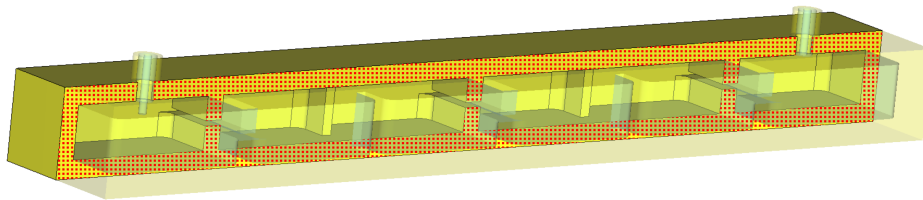
Figure 3.43: Alternating 6-subcavities model showing the area (dotted in red) where the air layer is deposited for the Q_0 downgrade simulations.

the best option for the manufacturing. Thus, the next step was to study this behaviour in the manufactured prototype. A longitudinal cut with the wire cut Electrical Discharge Machining (EDM) technique[5] (with a loss of 400 μm in the cut) was applied with the help of Eugenio Martín (Alta Precisión del Mecanizado S.L. (APM), Madrid, Spain [113]). For doing this, a previous desoldering was required for avoiding electrical problems from the tin layer. This desoldering was done heating the structure again to 160 °C temperature with the help of Dr. Fritz Caspers one week after the soldering process. The final appearance after the desoldering is shown in Figure 3.44a. Then, the remaining tin layer that lies on the jointing area had to be removed. In the first instance, an attempt was made to remove this layer of tin by means of a soldering iron. However, an extra milling process of 800 μm for the main body and 500 μm for the cover was necessary in order to completely remove this layer and flatten contact regions on both parts, the result of which can be seen in Figure 3.44b. Unfortunately, part of the 30 μm copper layer on this area has also been removed. In addition, the cavity walls have undergone a process of oxidation due to the soldering and desoldering treatments. For these reasons, the structure must be recoated once the vertical cut has been made.

An example of the wire EDM method is shown in Figure 3.45a. After this cutting process,

---

5 The wire cut EDM method is a manufacturing process that implements electrical sparks to form a metal shape. Because of these sparks, EDM is also known as *spark machining*. In this process, the desired shape is cut from the metal when current discharges, or sparks, are produced between two electrodes; where the sparks are produced, cuts are made in the metal, creating the desired shape and separating it from the sheet metal.

(a)

(b)

Figure 3.44: Aspect of the alternating 6-subcavities prototype after the desoldering process. (b) Appearance of this structure after the milling process for the tin removing.
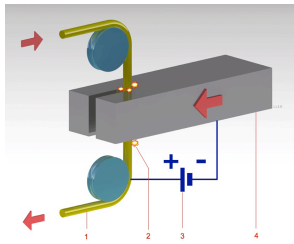
(a)   (b)

Figure 3.45: (a) Example of a wire cut EDM technique (by LaurensvanLieshout). (b) Aspect of the desoldered alternating 6-subcavities prototype after the vertical cut.

the structure is now divided into four pieces (because of the original horizontal cut and the new longitudinal cut). The final appearance of the structure with the top and bottom pieces bolted is shown in Figure 3.45b. With the vertical cut already made, as mentioned above, the next step was to re-apply a 30 micron copper layer. For an homogeneous copper coating, a pre-uncoating was necessary on this prototype. Also, two pins where added in the width axis for alignment purposes due to the new longitudinal cut. Since the structure was not originally prepared for this type of cut, the implementation of screw holes in the horizontal axis is not a simple task, so it has been left as future work. Two pictures of the prototype after these treatments can be observed in Figures 3.46a and 3.46b. In order to try to obtain the Q_0 of the fully closed structure while guaranteeing maximum contact in the vertical cut, clamps were again used to exert pressure at the time of measurement. The resulting quality factor value was 2400 (34 % from simulation), which is higher than the original value without vertical cut. The conclusions we can extract from this result are that the vertical cut in this type of structure does not affect practically and that the new copper layer has helped to eliminate the oxidation of the walls, which could be affecting

(a)

(b)
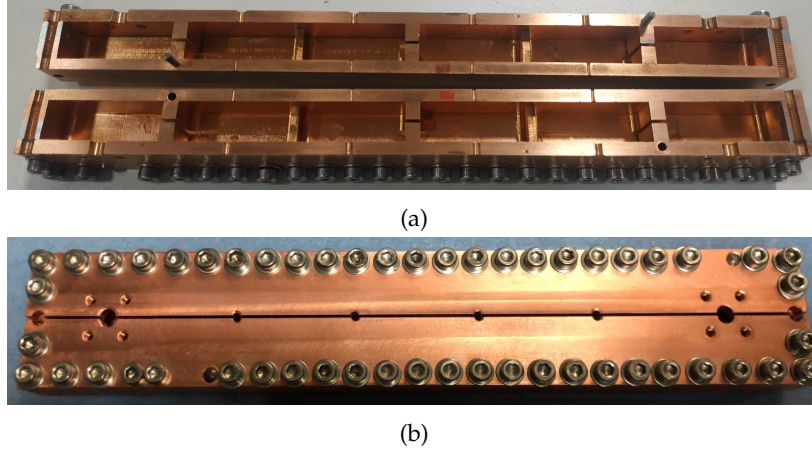
Figure 3.46: Appearance of the alternating 6-subcavities prototype after the copper coating: (a) Open structure to observe the inner Cu coating, and (b) aligned structure.

the electrical conductivity.

Finally, a last study was carried out to try to further increase the unloaded quality factor: a new soldering to join again the top and bottom parts together. To avoid oxidation resulting from soldering, it was decided to apply previously a very thin gold layer (0.2 microns). Thanks to the small thickness of this layer, the electrical conductivity associated with the electromagnetic fields on the walls of the haloscope remains at or very close to that of copper, which is more desirable as the conductivity of gold is lower ($\sigma_{Au}^{T=300K} = 4.11 \times 10^7$ S/m) in comparison with copper material. The soldering was realised by means of a tin layer at the jointing area and applying heat with the help of the APM workshop [113]. In addition, the amount of tin added has been done in a more moderate way compared to the previous soldering without vertical cut, showing special attention to ensure a good contact in the innermost section. With this, the resultant structure is now divided into two parts: left and right pieces. In Figure 3.47a a picture of the soldered structure is shown. On the other hand, as represented in Figure 3.47b, there are some regions where the soldering tin is spilled towards the inner part of the cavity in this treatment, leading to potential Q_0 downgrades due to the low value of the electrical conductivity of the tin ($\sigma_{Sn}^{T=300K} = 9.17 \times 10^6$ S/m). Once again, clamps were employed when measuring Q_0 (see Figure 3.47c) as this structure does not have any screw holes. As many clamps as possible were added. As a result, the obtained Q_0 value was 3700 (53 % from simulation), which is a good result compared with other manufactured prototypes tested previously. As a summary, Table 3.8 shows the Q_0 values that have been achieved over time in the alternating 6-subcavities prototype with respect to the treatments applied. As it can be seen, the Q_0 improvement achieved after all these treatments (3700) with respect to the prototype manufactured (1200) is 308 %. However, at the step where the structure was totally soldered ($Q_0 = 4500$), the enhancement in the unloaded quality factor was 375 %. We have left as a future research line the implementation of screw holes in the horizontal axis and a new soldering of the structure in order to continue studying the behaviour of the value of this parameter.
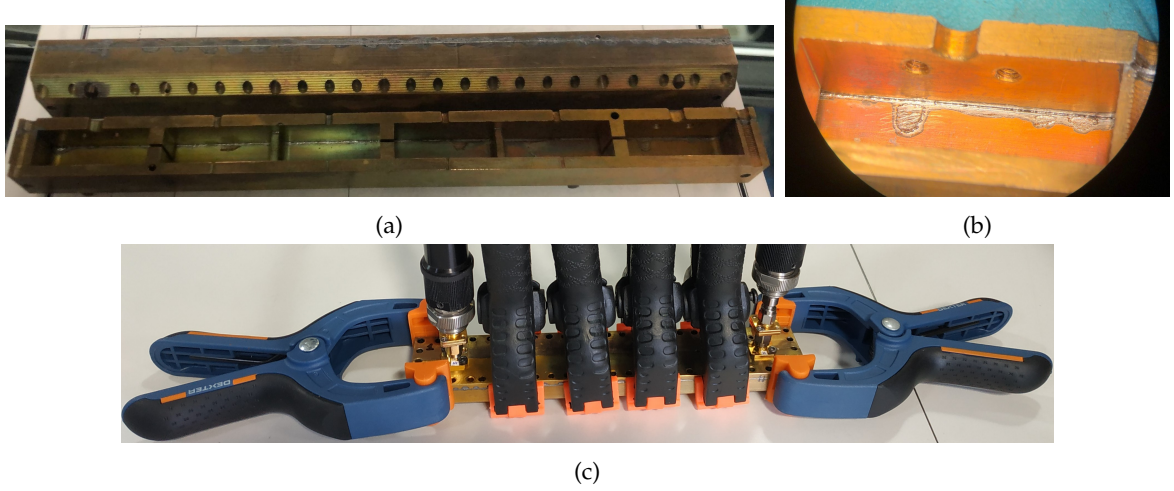
Figure 3.47: (a) Aspect of the alternating 6-subcavities prototype after the gold coating and the second soldering. The structure is now divided into two pieces. (b) Zoom in on a section where tin spillage can be observed. (c) High tightening of both parts with clamps to measure the Q_0.

Step process	Number of pieces	Q_0
Simulation	1	7000
Manufacturing	2 (HC)	1200
Untwisting	2 (HC)	1600
Conductive paint and indium foil	2 (HC)	1600
More screws and clamps	2 (HC)	2300
First soldering	1	4500
Desoldering, vertical cut, Cu uncoating and coating	4 (HC + VC)	2400
Au coating and second soldering	2 (VC)	3700

Table 3.8: Q_0 over the treatments applied in the alternating 6-subcavities prototype. HC means horizontal cut and VC vertical cut.

3.2.4 Q_0 in the alternating 30-subcavities haloscope

In 2019, the modelling (at UPCT), manufacturing, coating and testing (at CERN) of an alternating iris multicavity based on thirty subcavities (the evolution of the alternating 6-subcavities prototype) was realised by the RADES team, whose main purpose was to increase the volume compared to previous designs. In Figures 2.17b and 2.19b a picture of the manufactured structure and its response at cryogenic temperatures ($T = 2$ K) can be seen, respectively. In a similar way to its smaller version, the axion mode resides in the middle of the resonance band, at the 16-th resonant mode which corresponds with the 16-th peak in this case. Once again, this prototype was manufactured employing stainless steel 316LN material with a horizontal cutting plane. Also, as in the 6-subcavities version, small air gaps were added at both sizes of the top tooth of the capacitive irises to facilitate its production (see Figure 3.38). In addition, a 30 μm copper coating layer was applied after the manufacturing.

In summer 2019, this prototype was introduced into the bore of the CAST magnet (at CERN) for a data acquisition campaign with the help of Dr. Sergio Arguedas and Jessica Golm (from the RADES team). At the installation time the finding of the peak which couples to the axion and to determine the coaxial antenna length at the port to set a critical coupling (for a higher axion detection sensitivity) was needed. Due to various setbacks and a short time window between the production of the prototype and the deadline for the insertion of this structure in the CAST bore these parameters could not be measured in a simple way after the manufacturing. Although it is known that the axion mode is located at resonance number 16 of the 30 peaks band, this task was not so straight forward because the measurements did not show 30 peaks due to the losses and the mode clustering, especially at the extreme peaks of the band on both sides.

As it is shown in Figure 2.19b, the frequency response of this haloscope has a clear division into two sub-bands: the left sub-band with 16 peaks and the right sub-band with 14 peaks. The axion mode is in the last resonance of the first sub-band. Several theoretical studies were carried out to understand this behaviour, from which it was concluded that the sub-band division depends on three cases: $|k_{ind}| > |k_{cap}|$, $|k_{ind}| < |k_{cap}|$ and $|k_{ind}| = |k_{cap}|$, where $|k_{ind}|$ and $|k_{cap}|$ are the inductive and capacitive physical couplings in absolute value, respectively. In an alternating $N = 30$ haloscope, for $|k_{ind}| > |k_{cap}|$, the left sub-band of its response is composed by 16 peaks and the right sub-band of 14 peaks, and the axion mode is the last resonance of the first sub-band (our case). For $|k_{ind}| < |k_{cap}|$, the number of peaks is the same in both sub-bands (15 peaks), and the axion mode (the 16-th) is at the first resonance of the second sub-band. For $|k_{ind}| = |k_{cap}|$, there is not division into sub-bands, so the 30 peaks must be seen accurately in order to count up to the number 16, where the axion mode is located. Furthermore, it is worth mentioning that, for the $|k_{ind}| > |k_{cap}|$ and $|k_{ind}| < |k_{cap}|$ cases, the centre of the full 30-peak band is always in between the last resonance of the first sub-band and the first resonance of the second sub-band (valley region). This can be useful in case $|k_{ind}| \approx |k_{cap}|$, where it is difficult to identify the position of the valley separating the two sub-bands. For the $|k_{ind}| = |k_{cap}|$ case, this centre is located just at the resonance of the axion mode.

In the first instance, a design with $|k_{ind}| = |k_{cap}|$ was attempted, where the mode separation at the axion peak is larger as there are no sub-bands. Due to the large size of the structure and the large number of subcavities, $|k_{ind}|$ and $|k_{cap}|$ were very sensitive in all irises and the computing time in the design simulations was relatively high (about two weeks for the optimisation process). Therefore, when the structure was optimised in simulation to increase the quality and form factors, the response shown in the Figure 2.19b was accepted as a good result for manufacturing.

Before the installation, the first measurement showed a response where the left sub-band of resonances is not well defined, but the right sub-band is (see Figure 3.48a), being these the first instabilities found in this prototype. In this case the peak at ~ 8.33 GHz (marker
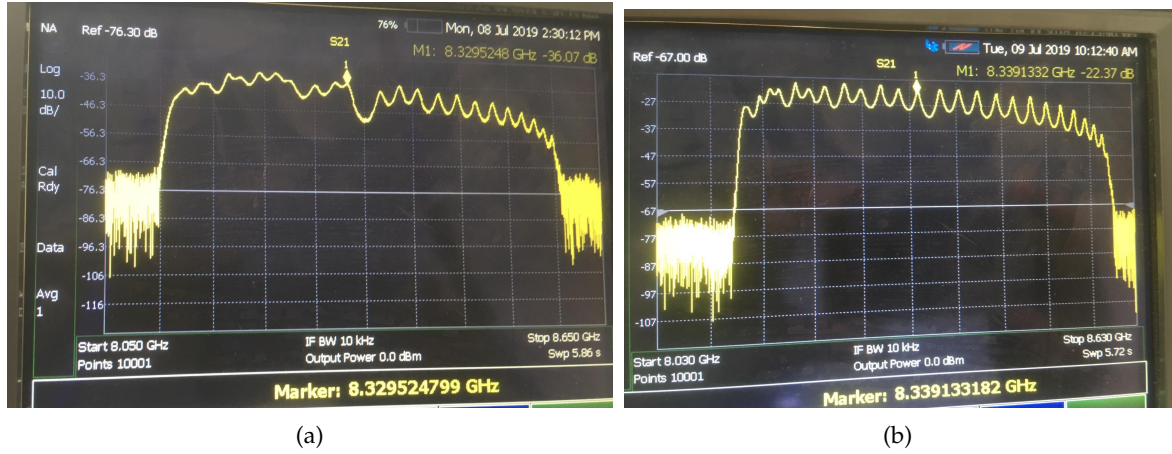
Figure 3.48: Pictures of the first VNA measurements of the magnitude of the transmission coefficient in the alternating 30-subcavities prototype with: (a) first orientation of the cover, and (b) cover turned 180°.

at Figure 3.48a) was identified as the axion mode due to be at the last resonance of what looks like a first sub-band, having on its right side a valley similar in shape to the response shown in the simulation results (see Figure 2.19b). The identification of this peak as the axion mode has been done assuming that the case $|k_{ind}| > |k_{cap}|$ holds from simulation to production. However, this may not be the case, but rather the case $|k_{ind}| < |k_{cap}|$, since the manufactured structure could have a different behaviour from the simulated one, resulting in the axion mode being the one to the right of the valley, as it is stated previously.

Then, we turned the cover 180° and screwed it again. For our surprise the definition of the left sub-band improved significantly (see Figure 3.48b). Unfortunately, the new prototype response showed a less clear band splitting (which is translated into the $|k_{ind}| \approx |k_{cap}|$ case according to the previous theoretical studies), leading again to possible confusion in the identification of the peak corresponding to the axion mode. This illustrates how the interresonator couplings are affected in a different way and its sensibility. Assuming a similar frequency position as in the previous case, the selected peak was the one found at the frequency of $\sim$ 8.339 GHz (marker at Figure 3.48b). The computed Q_0 value for this mode was $Q_0 = 1500$, 21 % from the simulation results that give a $Q_0 = 7000$, which confirms that the manufacturing tolerances and/or the contact between the main body and the cover were not the best.

On the other hand, an antenna length sweep was carried out before the haloscope installation in the CAST magnet and the higher value we got for β was 0.3, which is far from the critically coupled case $\beta = 1$. This behaviour was studied in simulation. Firstly, a parametric simulation was conducted to search the electrical conductivity of the housing material that gives a $Q_0 = 1500$ for the axion mode. Then, an antenna length sweep was realised in simulation achieving again a maximum β value of 0.3. This study was applied also for the alternating 6-subcavities haloscope, which finally provided the critically coupled case ($\beta = 1$) concluding that, indeed, the desirable port coupling situation is not

possible for low Q_0 values when the number of subcavities is high.

Another study was carried out for a better understanding of this behaviour, changing the position (subcavity) where is located the coaxial port. Figure 3.50 shows the 3D models of the three cases simulated for studying the possibility of achieving the critically coupled case at the 30-subcavities haloscope positioning the port at different subcavities. The results of these simulations showed that in the cases where the port

(a)   (b)

(c)
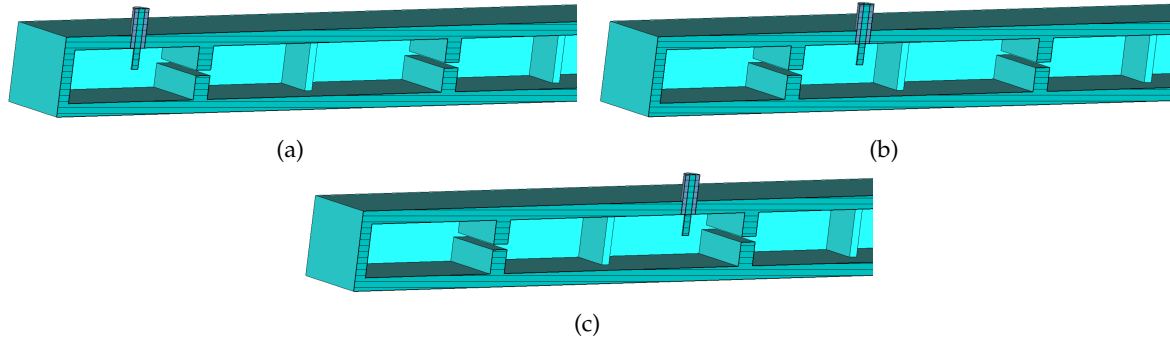
Figure 3.49: 3D models of the simulated 30-subcavities structure modifying the subcavity where the port is positioned for studying the port coupling level. The subcavities where the port has been tested was: (a) first, (b) second and (c) third. The 3D models show the symmetric half, being the dashed region the symmetry plane.

was positioned in the first or the third subcavity, the coupling failed to reach the value of $\beta = 1$. However, when the port was positioned in the second subcavity, it did. This led to the suspicion that the maximum electric field level in the vertical direction E_y for the working mode (mode 16-th, whose electric field can be found in Figure 2.18b) must be different in each subcavity. Therefore, a simulation was performed to extract the maximum level of E_y on each subcavity (which is located in the centre of the subcavities by the characteristic pattern of a TE_{101} mode), the result of which can be found in Figure 3.50. As it can be seen, in the first 10 subcavities, those in an odd position (1st,
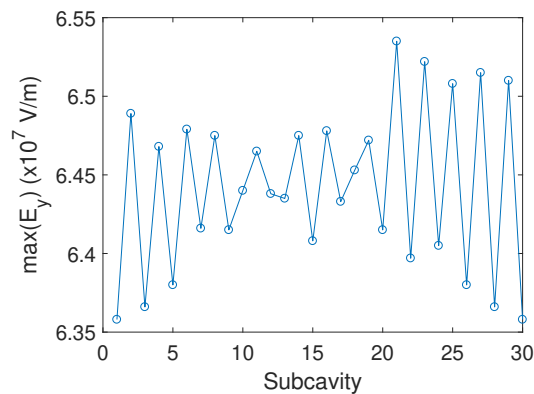
Figure 3.50: Maximum vertical electric field level in the 30-subcavities structure on each subcavity. An input RF power of 1 W is applied to the ports for these simulations.

3rd, 5th, ...) have a smaller maximum vertical electric field value than in the even ones

(2nd, 4th, 6th, ...), which explains why when the port is placed in the subcavity number 2 the value of TE_{101} is achieved, and it is expected to occur in the same way in the even subcavities. This behaviour also happens symmetrically at the other end of the multicavity.

Due to the fact that the structure was already fabricated and prepared to position the port in the first subcavity, the maximum achievable coupling (at room temperature at least) was assumed to be $\beta = 0.3$ for this data campaign. With this, we had to do a tricky estimation of the length for the antenna to obtain the same coupling value at cryogenic temperatures (since this haloscope did not have a port coupling adjustment system). This estimation method is based in the following steps:

1. The Q_0 value is computed with the best β value obtained ($\beta = 0.3$). This leads to a $Q_0 = 1500$.

2. There is a difference between the simulation or theoretical Q_0 and the real one that comes from the bad contact of the cover, this is an extra $Q_{external}$. It is called Q_{top} because it comes from the top part. So:

$$\frac{1}{Q_0^{real}} = \frac{1}{Q_0^{sim}} + \frac{1}{Q_{top}} \rightarrow \frac{1}{1500} = \frac{1}{7000} + \frac{1}{Q_{top}} \rightarrow Q_{top} = 2000. \qquad (3.66)$$

3. Now, from other RADES prototype measurements at the cryogenic laboratory it is known that the Q_0 improves ~ 4 times between room temperature and cryogenic temperatures. Furthermore it is assumed that the Q_{top} is not temperature dependent. So for cryogenics it can be estimated a Q_0 of:

$$\frac{1}{Q_0^{cryo}} = \frac{1}{4Q_0^{sim}} + \frac{1}{Q_{top}} \rightarrow Q_0^{cryo} = 1867. \qquad (3.67)$$

4. This Q_0^{cryo} value means the improvement for our Q_0 between room and cryo is around 1.195. This also means the β value at room has to decrease by 1.195 to be critically coupled at cryogenic temperatures:

$$\beta_{new} = \frac{\beta}{1.195} = \frac{0.3}{1.195} = 0.25, \qquad (3.68)$$

where β_{new} is the port coupling value to be set on Port 1 before the structure is entered into the CAST bore. From the port sweep it is known how to configure the antenna length to establish such value.

Then, once the length of the antenna was configured the introduction of this haloscope into the CAST bore was performed (see Figure 3.51a). Installation took place satisfactorily and on time, but the final response showed again a bad definition of the sub-bands, as depicts Figure 3.51b. Unfortunately, at the time of installation the 8.37 GHz peak (marker 1 at Figure 3.51b) was misidentified as the axion mode, whose correct position would later be identified as the one to its left.
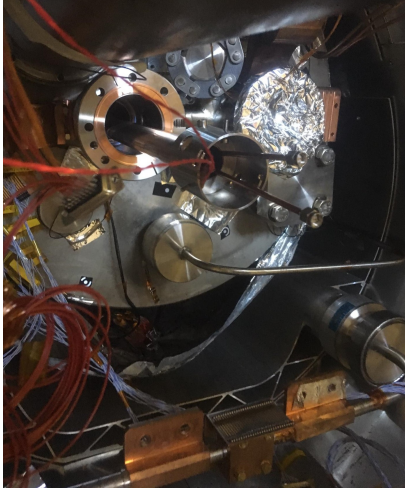
(a)
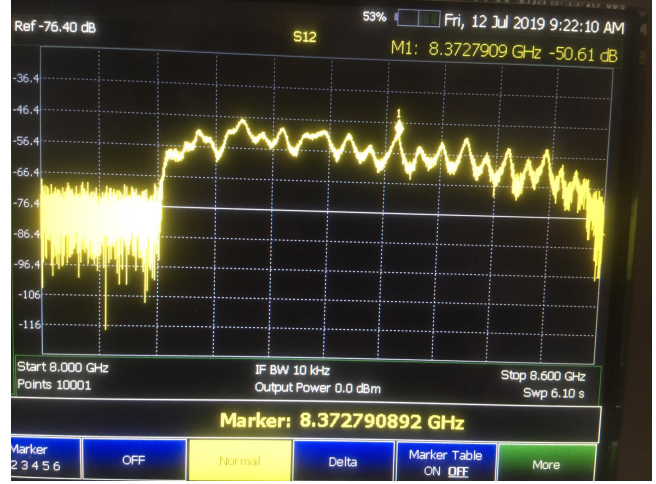
(b)

Figure 3.51: (a) Installation of the alternating 30-subcavities prototype at the CAST magnet. (b) Picture of the first measurement at CAST of the magnitude of the transmission coefficient in this prototype.

During the cool down of the CAST magnet the scattering parameters of the 30-subcavities prototype were measured. The response of the structure is illustrated for different temperatures in Figure 3.52. The peak that were identified at that moment as the axion mode
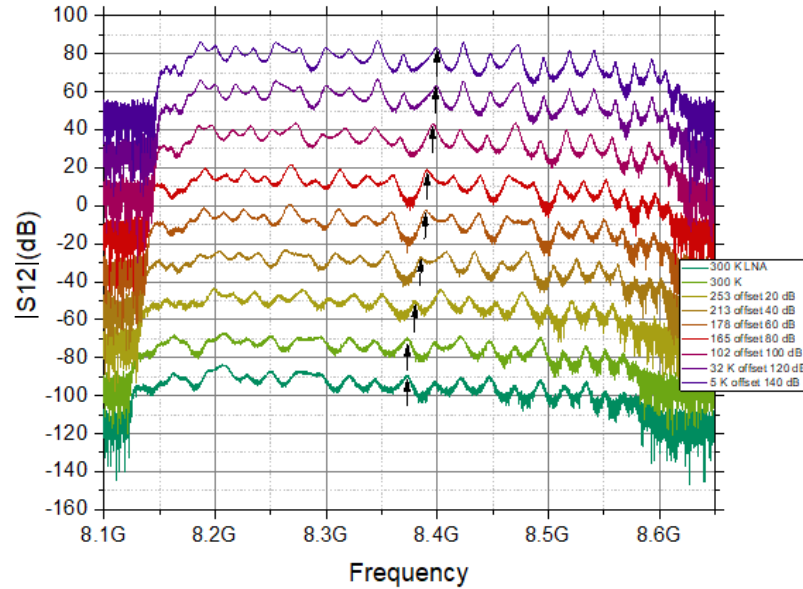
Figure 3.52: Recording of the transmission coefficient in the alternating 30-subcavities prototype during the cool down of the CAST magnet. Some curves have an offset in this plot in order to compare all of them easily.

is marked with a black arrow. The frequency increased $\sim$ 28 MHz for all the modes by cooling the cavity down from $T = 300$ K to $T = 5$ K. This was expected due to the geometry change of the cavity (thermal contraction).

After a large stop in the CAST magnet prior to data taking due to various reasons (including the COVID-19 pandemic starting in March 2020), an unwanted magnetic quench occurred in August 2020 and the response of the 30-subcavities structure deteriorated slightly. In Figure 3.53a are plotted the magnitude of the transmission parameter of three measurements (from different days) at cryogenic temperatures before the quench event and a measurement before it, where this behaviour can be observed. Observing the

(a)

(b)
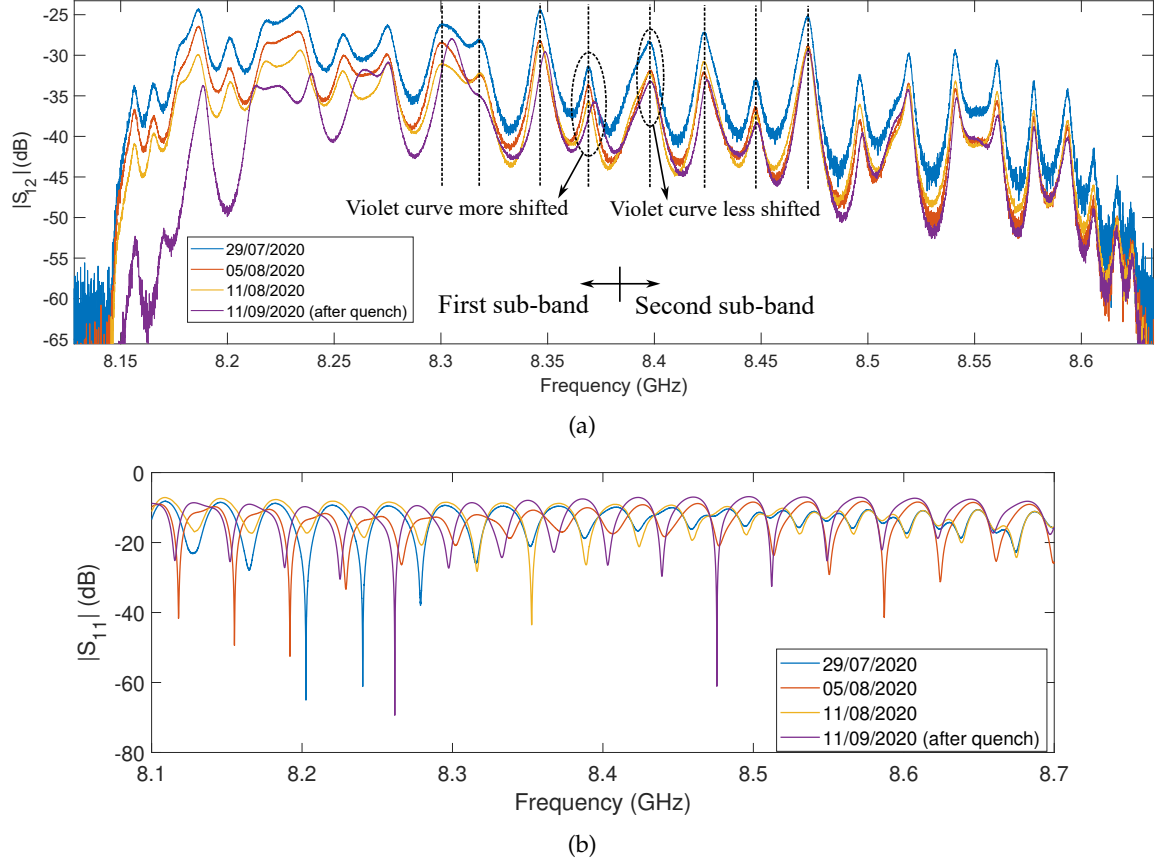
Figure 3.53: Hold on of four measurements at cryogenic temperatures: three measurements before a quench event and one after it. (a) Magnitude of the transmission parameter versus frequency. The plot depicts the point where the resonances of the measurement after the quench start to be more shifted leading to the identification of the sub-bands separation. (b) Magnitude of the reflection parameter versus frequency.

frequency range between 8.3 and 8.5 GHz where the axion mode could be located, it can be seen that there is a point where the peaks are more shifted for the measurement after the quench. Since it has been seen before that the first sub-band is more sensitive, we can state again here that the influence of the quench was greater at the first sub-band which lead to the identification of the sub-bands separation and therefore to the axion mode (assuming again the 16-th resonance as the last peak of the first sub-band). For some reason, the response of the 30-subcavities structure at CAST shows a complex behavior from one day to the next which makes it even more difficult to identify the axion peak. Anyway, these results again show that the axion mode is most likely to be found at the 8.37 GHz peak of the cryogenic temperature response.

Also, theoretical design studies in the MATLAB software (a numeric computing environment developed by *MathWorks* [114]) have shown that the first sub-band is associated with the coupling value provided by the capacitive irises, while the second sub-band is linked to the inductive irises. Seeing how the first sub-band deteriorates compared to the second sub-band can confirm that the capacitive windows in the manufacture of these haloscopes are more problematic than the inductive ones.

On the other hand, regarding with the reflection coefficient S_{11} it shows the response depicted in Figure 3.53b. Furthermore, it can be seen that the curve follows a quasi-periodic behavior even outside the region of the 30 resonance band (between 8.15 and 8.65 GHz). For this reason, the β value of this prototype installed at CAST could never be properly measured. The reason for this behavior is thought to be due to the high reflections and losses introduced by the cables and connectors.

The magnet ramp-up measurements (rise of the static magnetic field of the CAST magnet from 0 to 8.8 T) were analysed in order to check if the mode chosen for 2019 data taking was wrong. This ramp-up was applied to the magnet several times. In Figure 3.54 is shown one of these B_e ramp-ups. As it can be seen, there is a clear region of
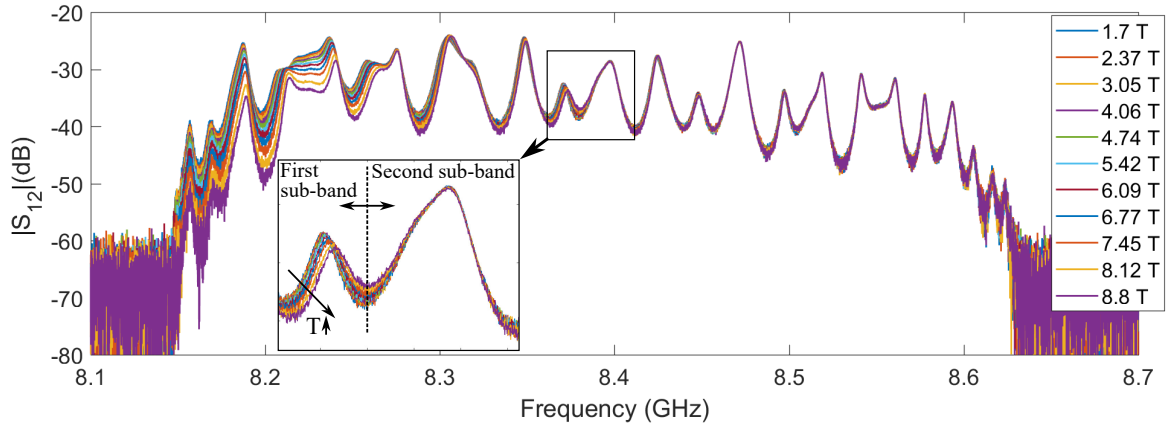
Figure 3.54: Recording of the transmission coefficient versus frequency in the alternating 30-subcavities prototype during a ramp-up of the CAST magnet.

resonances where the static magnetic field shifts the resonant frequencies differentiating the two sub-bands. With this, we can state again that the axion mode is located at 8.37 GHz.

Unfortunately, the cryogenic LNA of the RADES team was damaged in a period of quench testing, and the magnet was not reopened until 2020, therefore no data could be collected in 2019. The LNA was replaced in early 2020 with a Low Noise Factory *LNF-LNC6-20B* amplifier with a 36 dB gain working between 6 and 20 GHz. In 2020, around 15 days of magnet-on data were collected. Even if the port coupling value was extremely low ($\beta \simeq 0.1$) for this arrangement, the projected sensitivity for a 15-day integration period is better than the existing CAST limit at this mass [62]. Furthermore, the major concerns at that time have already been recognised, and it is clear that β can be much improved. The

current setup key problem is the construction of the cavity. With this prototype, it was discovered that the alternating irises must be manufactured differently. As it is shown in the next section, new designs have been investigated in which each subcavity and irises are machined independently and then screwed together.

During the data taking of this structure, when the axion mode was thought to be the one found at the frequency of 8.4 GHz in the cryogenic temperature response from Figures 3.52, 3.53 and 3.54, a study was carried out to extract the unloaded quality factor of this resonance with a method that takes into account a high mode-mixing. This issue impedes the extraction of the Q_l value from the resonance response with the -3 dB decay method due to the closeness with the low-Q_0 mode at its left side. The studied method is based on modelling the response of the structure analytically by means of the sum of two Lorentzian curves. This modelling is based on the resonance equation [105]:

$$S_{21} = \frac{2\sqrt{\beta_1\beta_2}}{1 + jQ_l\left(\frac{f}{f_0} - \frac{f_0}{f}\right)}, \tag{3.69}$$

where β_1 and β_2 are the port coupling factors and f_0 is the central frequency of the resonance. Then, by a linear sum of two Lorentzian curves ($S_{21}^{left} + S_{21}^{right}$, being S_{21}^{left} and S_{21}^{right} the Lorentzian curves of the left and right resonances, respectively) with a manual fitting process of the result to a measurement of the 30-subcavities structure (see Figure 3.55) and employing equation 3.56, a $Q_0 = 1500$ was extracted for the right mode and $Q_0 = 700$ for the left one. Although it is already known that the correct axion mode
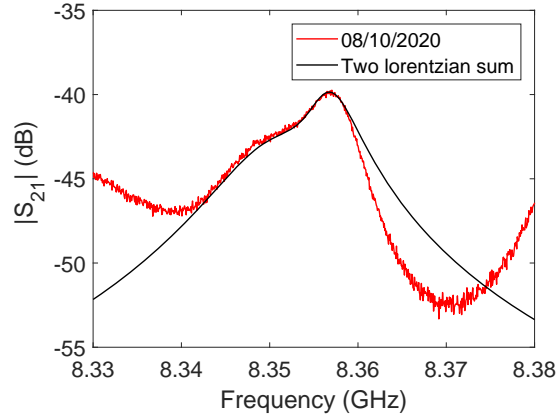
Figure 3.55: Fitting of a two Lorentzian curves sum ($S_{21} = S_{21}^{left} + S_{21}^{right}$) with a CAST measurement in the 30-subcavities structure response at a frequency region with a high mode-mixing behaviour.

of this structure is the 8.37 GHz one (in the responses from Figures 3.52 and 3.53), which does not have a high mode-mixing and therefore its Q_l can be easily extracted, this study could be very interesting for other large structures where this behaviour is much more significant.

Once the data collection process was completed, the CAST magnet was opened in the summer of 2021 and the 30-subcavities prototype could be extracted. Due to the good results obtained in the soldering process for the alternating 6-subcavities prototype, it was decided to apply this soldering again on the large structure (with the help of Dr. Fritz Caspers, at CERN) (see Figure 3.56a) in order to increase the unloaded quality factor and also make it possible to obtain a critical coupling for the axion mode. This resulted in the response shown by the yellow curve in Figure 3.56b, which is based on a room temperature measurement. As it can be seen, thanks to the improvement of the contact

(a)

(b)

(c)

(d)
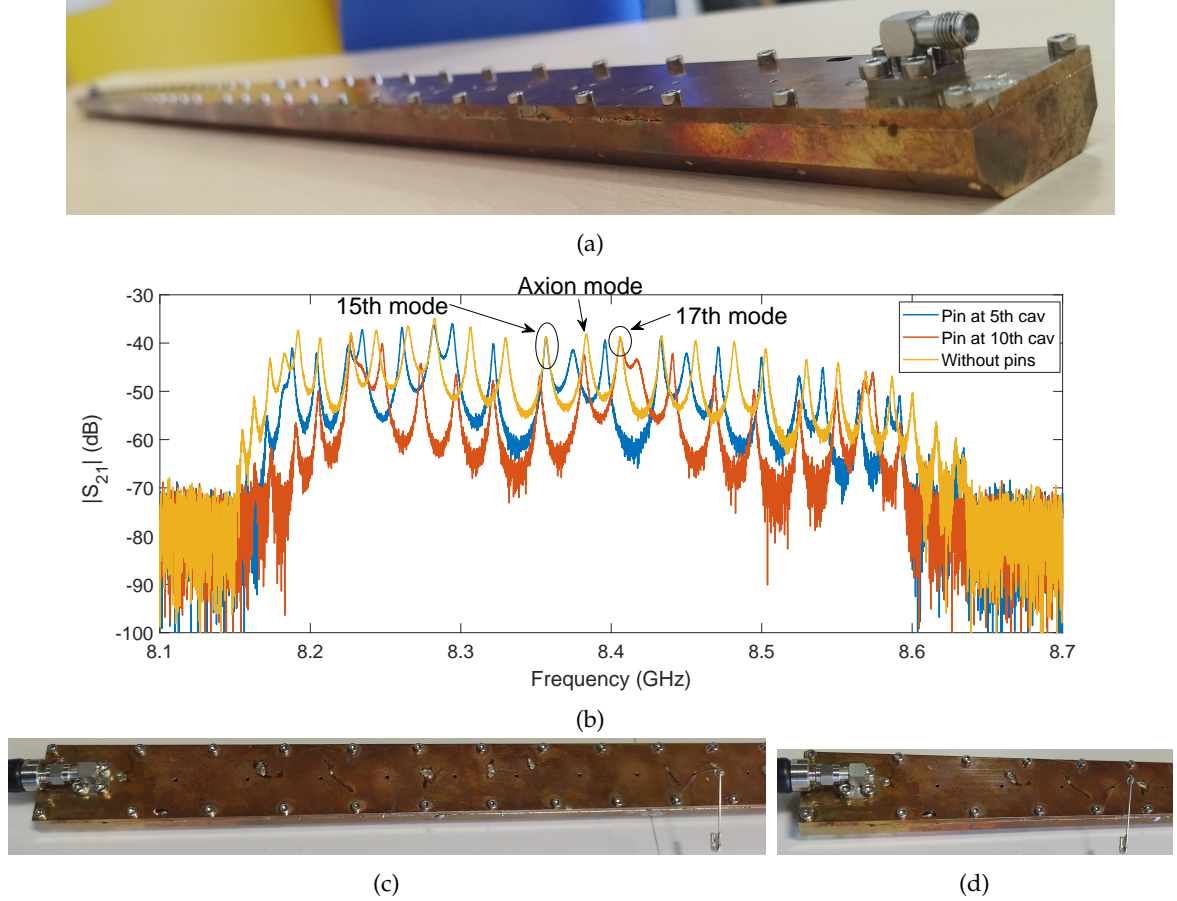
Figure 3.56: (a) Picture of the alternating 30-subcavities prototype after the soldering process. (b) Transmission coefficient versus frequency in this structure for three cases: no metallic pins (yellow), metallic pin introduced through the vacuum hole of the subcavity number 10 (red), and through the vacuum hole of the subcavity number 5 (blue). (c) Picture of this prototype with a metallic pin at the 10-th subcavity, and (d) at the 5-th subcavity.

and therefore of the Q_0, new peaks have appeared although the first and last resonances are still not visible due to the high mode-mixing in those regions, so it can still give rise to doubt as to which is the axion mode counting from the first mode to the 16-th mode. Because of this, a novel and definitive method of axion mode identification was devised that validates all previous methods: the use of metallic pins. This method is based on the electric field patterns of the modes immediately above and below to the axion mode, i.e. in the 15-th and 17-th modes of the alternating 30-subcavities structure (see Figure 2.18b). As it can be seen, unlike the axion mode (16-th), the 15-th and 17-th modes have a zero

electric field value in some of their subcavities. For the 15-th mode these zeros are found in subcavities number 10 and 21. For the 17-th mode they occur in subcavities number 5 and 26. This means that if a metallic perturbation is introduced in these zero-value subcavities (by the introduction of a metallic pin through the vacuum hole in this case), the resonant frequency of such mode should remain unaltered.

Figure 3.56b shows the results when the metallic pin is introduced around 1 cm through the vacuum hole of the subcavity number 10 (red curve) (see Figure 3.56c) and 5 (blue curve) (see Figure 3.56d). For the first case, it can be seen that the resonance at 8.357 GHz remains unaltered with respect to the case without pins, while for the second case this mode is shifted, so it can be associated with the 15-th mode. Similarly, for the first case the resonance at 8.406 GHz is shifted with respect to the case without pins, while for the second case this mode remains unaltered, which confirms that this mode is the 17-th mode. With this, the 16-th mode (the axion mode) can be now easily identified as the peak at 8.383 GHz, which is shifted for both cases as expected. If we apply the method of identifying the valley region of sub-band separation by the centre frequency of the resonance band,it can be seen that this valley is between the 16-th and 17-th mode resonances, which also confirms that we are in the case $|k_{ind}| > |k_{cap}|$ (first sub-band with 16 resonances and second sub-band with 14).

On the other hand, by comparing the new response with the previous case where the structure was not soldered (Figure 3.48b), it can be observed that the resonance band has been shifted ~ 40 MHz, which is also the case for the axion mode frequency (from 8.339 to 8.383 GHz at room temperature).

In July 2021, before soldering, the unloaded quality factor was again measured giving a value of $Q_0 = 700$. The difference from the previous result of 1500 is thought to be due to the oxidation of the copper layer in the structure, the effect of which is greater over time. The quality factor value of the axion mode after the soldering was $Q_0 = 3500$ (50 % from simulation), which represents a 500 % increase in this value. This improvement is a very good result compared to the gain obtained in the case of soldering on the 6-subcavities prototype (308 %). In June 2022 and January 2023 this parameter was recalculated, giving $Q_0 = 1300$ and $Q_0 = 941$, respectively, which confirms that the effect that reduces the quality factor so much is the copper oxidation.

In September 2021, with the help of Dr. Babette Döbrich and Jessica Golm (from the RADES team, at CERN) a proper antenna length was set to be critically coupled at cryogenic temperatures for the axion mode with the estimation method described previously. Then, with the help of Dr. Marios Maroudas and Dr. Theodoros Vafeiadis (from the CAST collaboration, at CERN) the re-installation of the 30-subcavities prototype at the CAST magnet was carried out. Unfortunately, due to the low budget and the lack of physical data from all research groups within the CAST collaboration, in December 2021 CERN took the decision

to cancel the CAST project definitively, leaving the magnet as a museum object. In summer 2022, the structure was deinstalled and sent to the UPCT for further research. The same reprocessing carried out on the 6-subcavities haloscope (desoldering, vertical cutting, re-coating and soldering) is expected to be applied to this prototype, which is left as future line of this PhD thesis.

3.2.5 *Modularity solution*

This PhD thesis has also developed a novel idea that combines efficient manufacturing for avoiding Q_0 degradation, reduction of the production price and time, better tolerances for a design with a high number of subcavities and scalability, by means of a modular subcavity system: the *modularity* idea. Although it has been demonstrated that vertical cutting can help to reduce the manufacturing impact on the value of the quality factor Q_0, this concept is based on using the transverse plane as the cutting plane (see Figure 3.35b) since it also helps in preventing this parameter degradation (as it has been explained in section 3.2.2), and allows to introduce the mentioned improvements. Figure 3.57 depicts an example of a multicavity module employing the transverse plane for the cutting plane.
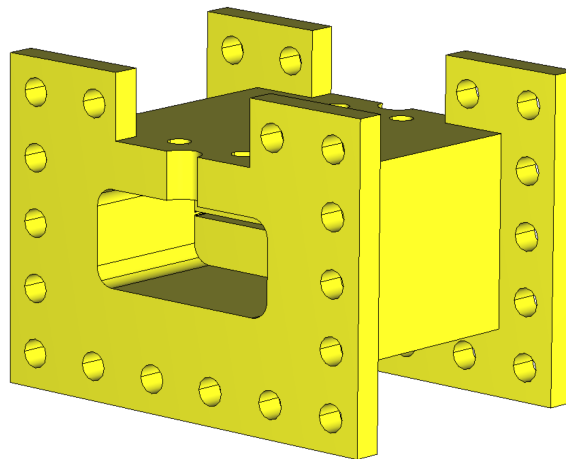
Figure 3.57: 3D model of a multicavity module example based on the modularity idea. In this case, the structure is based on two half subcavities and a capacitive iris.

Unlike a haloscope manufactured with a horizontal or vertical cut, this new way allows the concatenation in the longitudinal axis of as many modules as needed, so this type of structure has the benefit of scalability. Once a structure has been manufactured with this type of cut, if more subcavities (greater volume) are desired, as many modules as necessary can be added. Similarly, the number of subcavities could be reduced if desired by simply removing subcavities from the system. On the other hand, the production of the individual modules that are afterwards joined provides better tolerances and reduces the machining time and price compared to the manufacturing of the whole body which could be problematic for a haloscope with a high number of subcavities (as it is the case for the alternating 30-subcavities prototype), previously described in subsection 3.2.4. This could

lead to the possibility of manufacturing, for example, a structure based on 300 subcavities.

Although this transverse plane is parallel to the electric field lines in a TE_{101} mode (as in the vertical plane and contrary to a horizontal plane), this cutting plane cannot be used for tuning as the opening would produce a high radiation in the direction of propagation of the electromagnetic wave, which goes from the port 1 (positioned at the first subcavity) to the port 2 (located at the last subcavity). In case of need a mechanical tuning with the opening procedure in such structures, a vertical cut should also be added.

If this vertical cut is not added, the idea of modularity also brings the advantage of not cutting either the inductive or capacitive irises, which could be of great interest to reduce the impact on the quality factor in the manufacturing process. This aspect is quite attractive especially for structures that include capacitive windows which, as it can be seen in the previous sections, are often a problem in production. Another advantage of this type of structure is that the capacitive windows do not require gaps (see Figure 3.38), which reduces the complexity of the experiment.

In order to examine the position of the cross section that reduces the quality factor the least, a simulation study has been carried out testing the 3 possibilities that can be realised in production: cutting plane at each of the centres of the subcavities, at the ends of the inductive irises, and at the ends of the capacitive irises. This has been tested with the alternating 6-subcavities haloscope as depicted in the 3D models from Figure 3.58[6]. Simulation results at these positions, applying a 500 microns cut and the electrical conductivity of copper at room temperature for the housing, have resulted in a different quality factor reduction. For the case of the cuts at the centres of the subcavities a $Q_0 = 4361$ value was obtained (62.3 % from the ideal case), $Q_0 = 3841$ for the case of the cuts at the ends of the inductive windows (54.9 % from the ideal case) and $Q_0 = 2053$ for the case of the cuts at the ends of the capacitive windows (29.3 % from the ideal case). Thanks to these results and those obtained from the study of the air gap in this haloscope with horizontal cut (see Figure 3.40) it can be concluded that the best solution is to position the transverse cuts at the centres of the subcavities.

Then, for testing this concept in manufacturing, where a more realistic effect of using the idea of modularity can be studied, two prototypes have been designed, produced (in stainless steel 316L for the first one and in aluminum for the second one), copper coated (only for the first one) and measured: a small version and a larger evolution of this one. The first prototype is based on 2 subcavities with 1 capacitive iris, the so-called *2cav-Cap*. A 3D model of this structure and its electrical response in simulation (after its design) can be found in Figure 3.59a[7], and in Figures 3.59b and 3.59c (dotted blue and yellow lines),

---

6 In the case of production of the idea with the cuts at the ends of the inductive irises (see Figure 3.58b), two extra cuts would be needed at the centre of each end subcavity. These cuts have not been added in simulation since its effect is negligible if the number of subcavities is high (our goal).

7 It is relevant to note that for the production of haloscopes using cross-cutting planes there are rounded chamfers (about 2 mm radius typically) on the edges of the subcavities in the longitudinal axis due to the
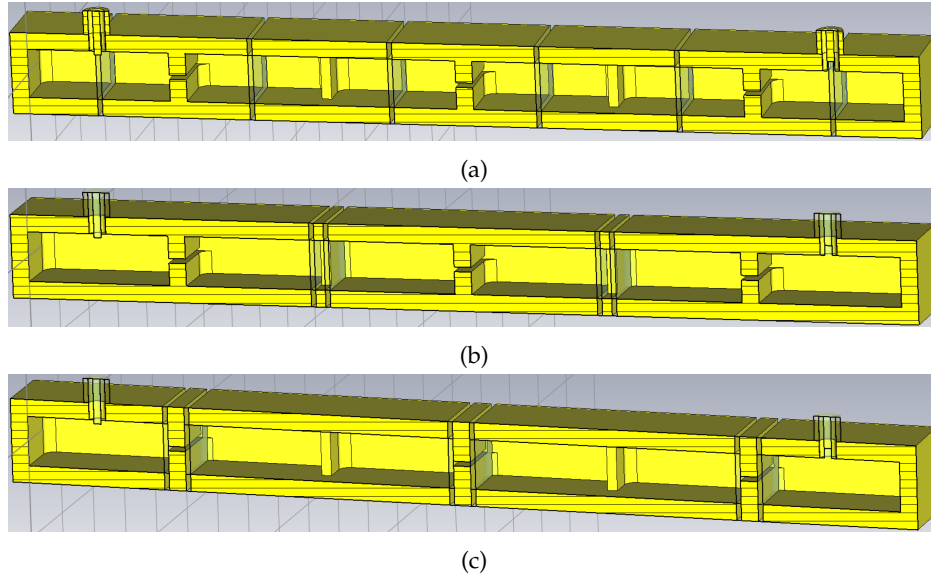
Figure 3.58: 3D model of the alternating 6-subcavities haloscope simulated with different transverse cutting planes for studying its electromagnetic radiation. The position of the cutting planes are: (a) subcavity centres, (b) ends of the inductive irises, and (c) ends of the capacitive irises. The 3D models show the symmetric half, being the dashed region the symmetry plane.

respectively. The axion mode is now located at the last resonance because it is based on an all-capacitive design (contrary to the all-inductive structures where the axion mode is at the first peak). Applying a stainless steel 316L and annealed copper electrical conductivity at room temperature at the simulated housing, an unloaded quality factor value of 770 and 5200 is obtained, respectively, for this mode.

As mentioned above, to manufacture this structure applying modularity, the production cuts are only 2 and they are located at the centres of the subcavities, dividing the haloscope into three modules: two identical modules based on a half-end subcavity (the *2cav-Cap-ModuleEnd* module), and a module containing the halves of the two end sub-cavities plus the capacitive iris (the *2cav-Cap-ModuleCap* module). In addition, protruding panels or flanges are added at the cutting plane sections for the screwing of the modules since, contrary to the horizontal or vertical cut structures, the housing thickness cannot be used now for this purpose (the screws should be extremely large, which is not practicable). In order to be able to correctly position the coaxial SMA ports, these flanges have been designed eliminating the section in the upper central area. The technical drawings for the manufacturing of both types of modules (generated in this PhD thesis) are depicted in Appendix I: Technical Drawings (see Figures A.10 and A.11). These technical drawings contain the final prototype dimensions of the simulated design and all the production considerations for the machining company (screw holes, tolerances, alignment, etc.) that

---

orientation of the machining drill. For the case of using horizontal cutting, these chamfers of the subcavities are on the edges in the height direction (see Figure 2.17), whereas for vertical cutting they are in width (see Figure 3.36a).

(a)

(b)   (c)
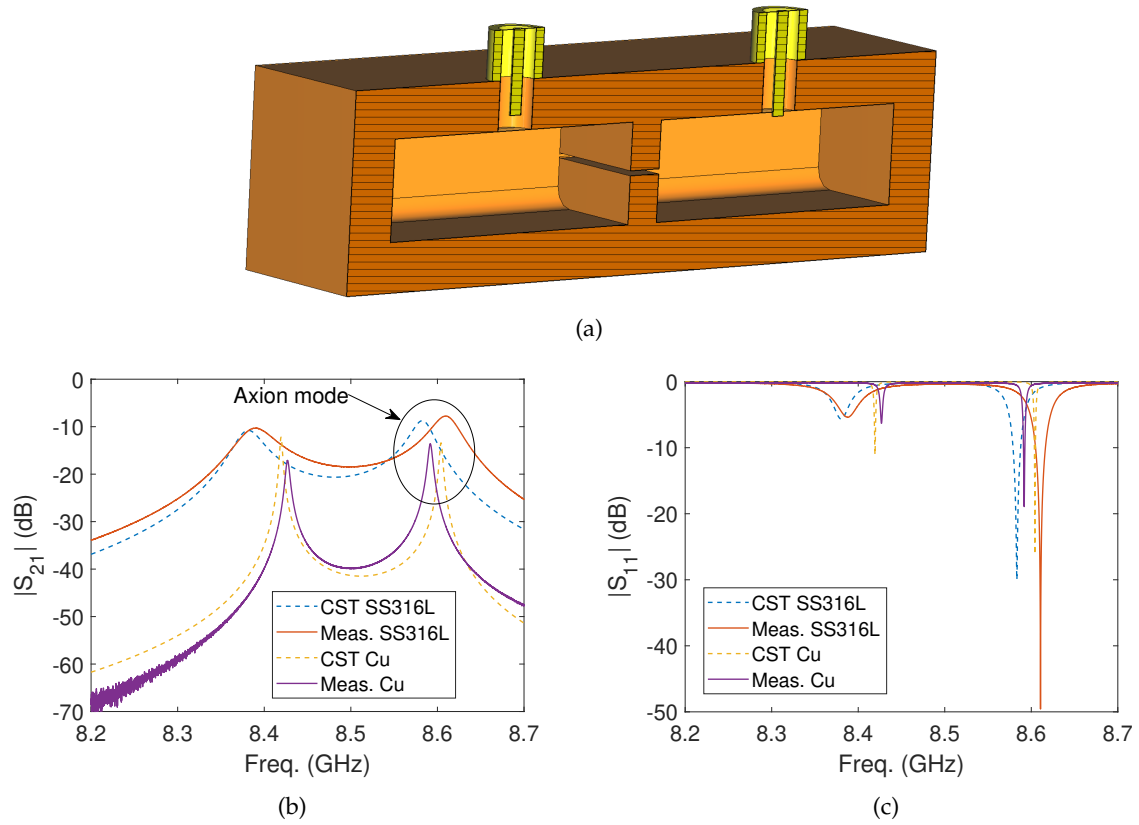
Figure 3.59: 2cav-Cap haloscope: (a) 3D model, and (b) and (c) magnitude of the transmission and reflection parameters, respectively, versus frequency in simulation after its designing process (dotted blue and yellow lines for SS316L and copper materials, respectively) comparing with a VNA measurement (solid red and violet lines for SS316L and copper materials, respectively). The 3D model shows the symmetric half, being the dashed region the symmetry plane. All the responses are configured for providing a critically coupled case at port 1 with a very undercoupled condition at port 2 (the target at the data taking time).

carried out the manufacturing.

Unfortunately, we encountered two difficulties in the production of the *2cav-Cap-ModuleCap* module. Firstly, due to the small size (0.5 mm) of the capacitive iris (necessary to properly acquire the interresonator coupling value imposed in the design process), several machining companies reported that it is not easy to drill such a window due to the length of 14.5 mm between the transversal plane of the cut and the iris, as the drill would have to be very thin and long (which is not practicable as it would produce instabilities in the machining). Secondly, the copper coating companies consulted reported that it would probably be very difficult to cover the inner walls of this capacitive iris with the requested 30 μm copper layer due to its small size and position. In the first instance and in order to try to solve the first problem, the following possible solutions were analysed for this module:

- Adding a transverse cut at the middle of the capacitive iris length (or at the ends, idea from Figure 3.58c). This was rapidly rejected because of the high Q_0 degradation obtained in the simulation studies.

- To add a vertical cut at the capacitive modules. This would be already implemented if a vertical cut tuning is desired. However, if other tuning systems are applied for avoiding such a cut, this solution would be also not be accepted.

- Machining the waveguide body and then soldering the capacitive iris walls (top and bottom capacitive teeth). This idea would raise the price and complexity of production and is therefore also rejected.

- Adding a horizontal cut at half height and then solder the top and bottom pieces of the module. Although soldering has already shown to be a good solution for horizontal cuts (as it can be seen for the 6-subcavities and 30-subcavities prototypes), this solution is still somewhat complex.

- Using EDM technique. Although it is a high-priced fabrication, it was thought that this may be the best solution due to its low complexity.

Finally, the last proposed solution was employed. On the other hand, although the third and fourth solutions were the best solutions for the coating problem, initially the first issue was given higher priority. It was therefore decided to go ahead with the EDM solution and attempt copper coating. Fortunately, a simulation study has shown that if only the inner walls of the capacitive iris in the 2cav-Cap structure have the electrical conductivity of stainless steel (and copper for the rest of the walls), the decrease in Q_0 is only 5 %, which is more than acceptable.

In this scenario, the three modules (two *2cav-Cap-ModuleEnd* modules and one *2cav-Cap-ModuleCap* module) were produced in *Alge S. Coop.* (Murcia, Spain) [115] using stainless steel 316L. The wire EDM technique was later applied for the capacitive iris creation for which it has been necessary to make a previous perforation for the threading (see Figure 3.60a). Unfortunately, the drill for the creation of the threading hole broke due
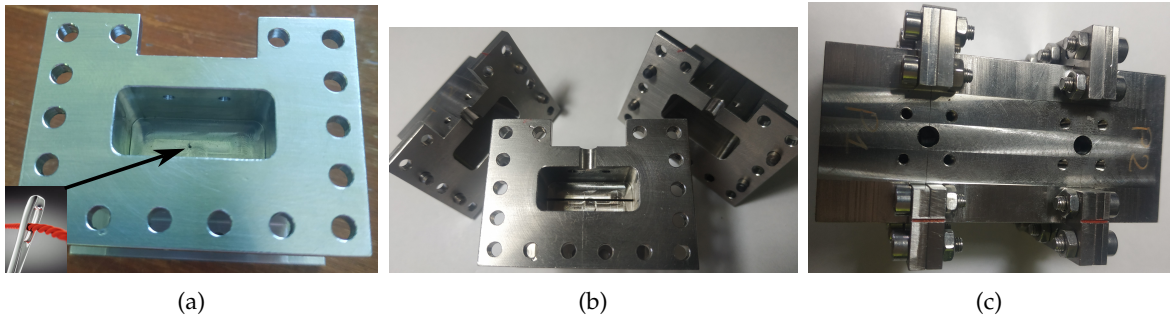
Figure 3.60: 2cav-Cap modules manufacturing: (a) appearance of the *2cav-Cap-ModuleCap* module after trying to drill the threading hole, (b) final aspect of the three modules, and (c) assembling of all the modules.

to the high hardness of the material (without damaging the haloscope). Therefore, this capacitive window was finally realised by die sinking EDM at APM (Madrid, Spain) [113]. Figures 3.60b and 3.60c depict the final appearance of the three modules that compose the prototype. The response measurement of this stainless steel structure can be observed

in Figures 3.59b and 3.59c (solid red lines), which provided an unloaded quality factor Q_0 of 630 (82 % from simulation). This is a very good result compared to other RADES structures manufactured, where values in the order of 50 % simulation were obtained for this parameter.

After consulting many copper plating companies and considering different methods for applying the copper layer (among which it was considered to replace it with a silver layer, whose conductivity is slightly higher, $\sigma_{Ag} = 6.3 \times 10^7$ S/m, with three previous layers of Nickel, Alkaline Copper and Acid Copper), the coating was carried out in the company *Finitec Electrolisis S.L.* (Madrid, Spain) [116]. There, a previous layer of bright Nickel of 2 microns thick was deposited on the structure (for housing adherence purposes) and finally the copper layer (Acid Copper) of about 30 microns, which is the method that has always been used for all RADES haloscopes. The final result is shown in Figures 3.61a and 3.61b, and its response is plotted in Figures 3.59b and 3.59c (solid violet lines). This

(a)   (b)
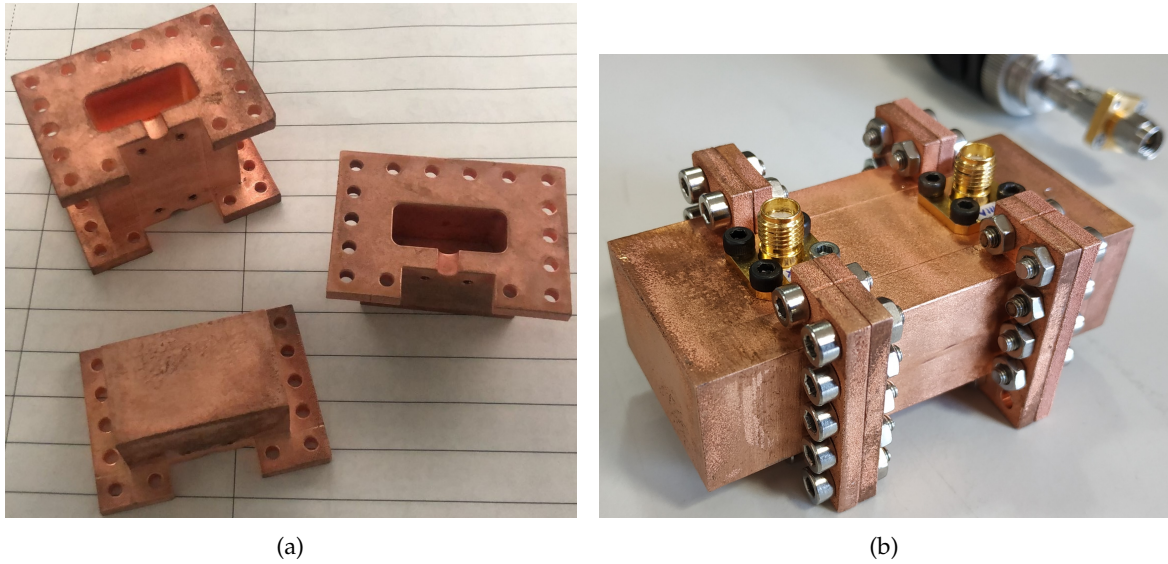
Figure 3.61: Aspect of the 2cav-Cap prototype after the Cu coating process: (a) modules disassembled, and (b) assembled.

Cu coating has provided a large rise in Q_0, up to a value of 4400 (85 % from simulation). This is an even greater improvement than in previous configurations. We can therefore conclude that this kind production and coating, and the idea of modularity itself, have proved to be a real success.

As an additional investigation, the behaviour of the response of this structure has been studied when the screws that join the modules are eliminated and openings are applied in the longitudinal axis. The change in frequency and quality factor values have been monitored. Figure 3.62a shows the results for four cases: closed case (assembled) and openings of 1, 2 and 3 mm. The study has been adjusted so that the gaps in both cuts are the same at each time. As it can be seen, the axion mode has undergone a frequency shift of 277 MHz with an aperture of 3 mm. The longer the length of the subcavities, the
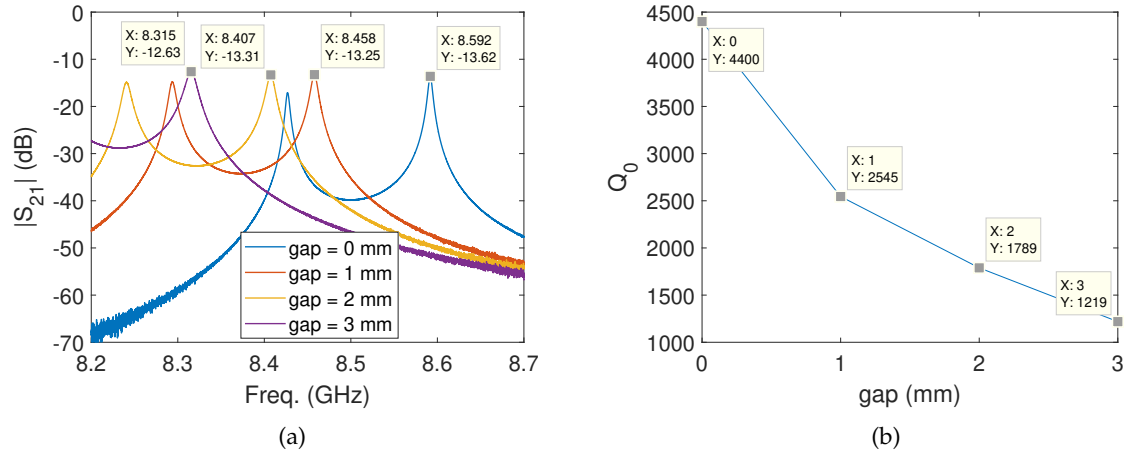
Figure 3.62: Results for different opening gaps at the 2cav-Cap prototype: (a) magnitude of the transmission parameter versus frequency, and (b) unloaded quality factor for the axion mode.

lower their resonant frequency. Unfortunately, and as previously predicted, the unloaded quality factor (see Figure 3.62b) for this mode drops rapidly at relatively small apertures, obtaining a $Q_0 = 1219$ for a gap of 3 mm that corresponds to 28 % of the value with the prototype assembled.

Due to the good results obtained previously, it was decided to design, manufacture and measure a new prototype based on the idea of modularity, an evolution of the first one. As mentioned above, in order to produce a haloscope with more subcavities using this type of structures, it will only be necessary to produce as many *2cav-Cap-ModuleCap* modules as subcavities desired. However, as in this case it is simply required to test the behaviour with more subcavities (and not the copper coating, which is already known that works correctly) it was decided to design and manufacture a prototype based on $N = 5$ subcavities with 4 capacitive irises (i.e. an all-capacitive haloscope) in aluminium *AW-5083 (28.5 IACS%)*, an easier and cheaper material compared to the stainless steel 316L one (avoid manufacturing deformations), without applying a copper layer for now. Therefore, the end modules (*2cav-Cap-ModuleEnd*) have also been manufactured again for reasons of incompatibility with the previous prototype. The 3D model and the simulated results after its design can be found in Figures 3.63a and 3.63b (blue line). On the other hand, because in a multicavity haloscope the external subcavity lengths are different from the internal ones (as the resonance frequencies are different to achieve the axion mode condition [27]), there are two different types of intermediate modules[8]. In this case, these types are the modules *5cav-AllCap-IntermediatePiece1*, based on half external and half internal subcavity length, and the *5cav-AllCap-IntermediatePiece2*, based on two internal subcavity lengths.

---

8 For $N = 3$ only one type of intermediate module will be needed, based on half external and half internal subcavity length.

(a)

(b)

(c)

(d)
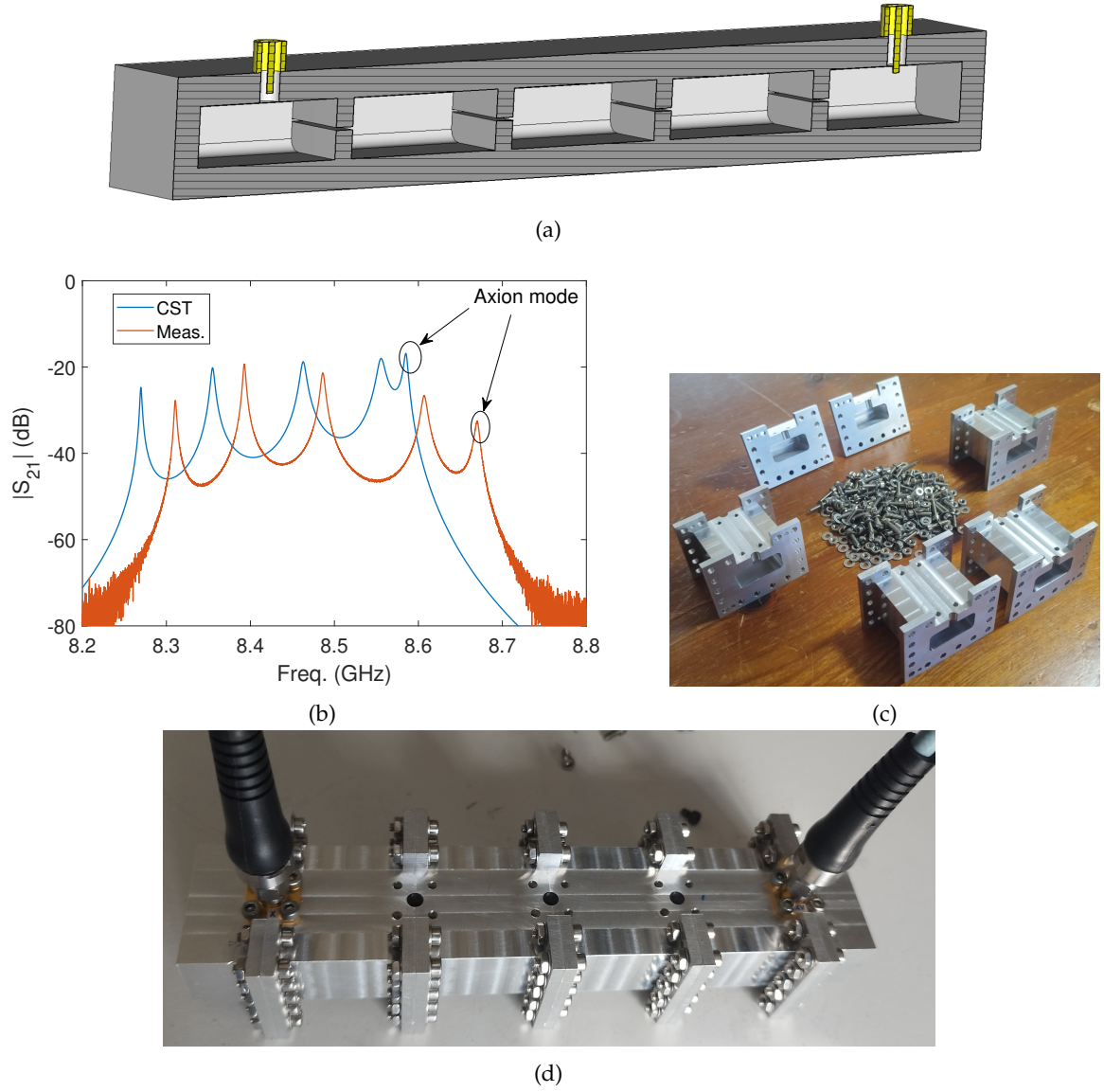
Figure 3.63: 5cav-AllCap haloscope: (a) 3D model, (b) magnitude of the transmission parameter versus frequency in simulation after its designing (blue line) comparing with a VNA measurement (solid red line), (c) final aspect after the manufacturing of this structure, and (d) prototype assembled. The 3D model shows the symmetric half, being the dashed region the symmetry plane.

With this, for the construction of a all-capacitive 5-subcavities multicavity, two *2cav-Cap-ModuleEnd*, two *5cav-AllCap-IntermediatePiece1* and two *5cav-AllCap-IntermediatePiece2* modules were manufactured. For the *2cav-Cap-ModuleEnd* modules the technical drawings are exactly the same as the ones shown in Figure A.10. For the *5cav-AllCap-IntermediatePiece1* modules the technical drawings are the same as the ones shown in Figure A.11 but replacing the half-subcavity length dimension of 14.5 mm by 15.345 mm. For the *5cav-AllCap-IntermediatePiece2* modules the technical drawings are the same as the ones shown in Figure A.11 but replacing the two half-subcavity length dimensions of 14.5 mm by 15.345 mm. The response and the final aspect of the manufactured prototype are shown in Figures 3.63b (red line), and in Figures 3.63c and 3.63d, respectively.

Again, since it is a multicavity with all capacitive irises, the axion mode is the last peak of the 5-resonance band. As it can be seen, the response is frequency shifted by about 86 MHz with respect to the structure designed in simulation, from $f_{axion} = 8.585$ to $f_{axion} = 8.671$ GHz, due to manufacturing inaccuracies. On the other hand, the designed or theoretical Q_0 is 2589, while the manufactured prototype gives a $Q_0 = 1600$ value (62 % from simulation), which is a correct value in production. Then, we state that the modularity gives also good results for a haloscope with a higher number of subcavities.

3.3 TUNING SYSTEMS

Another important feature of a haloscope is the tunability of the operation frequency since the axion mass (or frequency) is unknown, and a portion of the spectrum must be swept in any data taking. One of the works of this PhD thesis focuses on the development of different mechanisms for scanning a specific axion mass area utilising mechanical systems, ferromagnetic elements, and ferroelectric mediums, with special emphasis on the latter.

As it can be seen in equations 2.15, 2.16, 2.17, and 2.18, the resonant frequency of a cylindrical or rectangular cavity for any mode depends on the cavity dimensions and on the permittivity and permeability values. Frequency tuning systems for haloscopes can therefore be divided into mechanical tuning (based on modifying the dimensions of the resonant cavity) and electronic tuning (the principle of which is to modify the permittivity and/or permeability of the cavity medium). Also, although these equations show that the parameters a, b, d, ε_r, and μ_r affect to the resonant frequency of the haloscope maintaining the relative mode separation when tuning, there may be cases where this behaviour is not always met when systems become more complex. An example of this is the insertion of a dielectric material into the cavity that does not completely fill its volume, which will be discussed later in this chapter. Changing the mode clustering with frequency tuning can become a problem for high volume haloscopes where the closeness of the frequencies is already at the limit for a single frequency (see section 3.1). This condition establishes one of the criteria when designing a tuning system.

3.3.1 Mechanical tuning: the sliding wall

So far, all tuning methods used in the axion community for haloscopes have been mechanical. Cylindrical cavities containing one or more rods are used in the ADMX [117], HAYSTAC [118], and Institute for Basic Science (IBS)/CAPP [97] collaborations. Tuning is achieved by rotating these metallic rods within the cavities, which affects to the electromagnetic field distribution of the resonance within the cavity, hence changing the resonant frequency of the desired mode. A set of gears attached to a step motor or piezoelectric actuators provide rotational movement to the rod system. In the QUAX experiment [119], movable sapphire shells are employed to adjust the resonance frequency of the cavity. On the other hand, the CAST-CAPP/IBS group [120] uses two movable dielectric sapphire plates

110

arranged parallel and symmetrically to the cavity sidewalls.

The sliding wall system is one of the most basic methods for modifying a cavity. However, like with any tuning system, the ohmic losses caused by the geometry change must be considered. Figure 3.64 shows two types of sliding walls: movable sliding short and vertical cut tuning. The sliding short is put into the cavity using a stick, narrowing it and
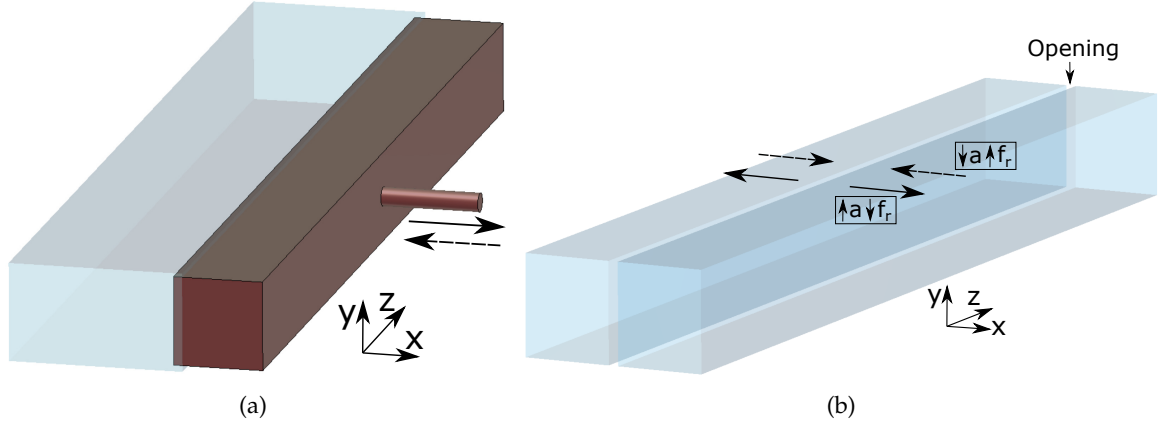
Figure 3.64: Two types of sliding walls in a long cavity: (a) movable sliding short and (b) vertical cut tuning. The arrows with dotted lines in the $x-$axis indicate a decrease in width (and an increase in the resonant frequency f_r), and vice versa for arrows with a solid line.

raising its resonant frequency. In the case of the vertical cut the cavity is divided into two pieces and one of them is moved to regulate the total width, which yields to a frequency shift. Generally, the losses and the Q_0 factor reduction as a result of the vertical cut opening are low since our working mode (TE_{101}) has a minimum value of current surface crossing that region, as it is demonstrated in previous sections. Concerning the sliding wall system, a choke section is usually applied to avoid high losses due to radiation [121]. The use of gasket fingers is an alternative that is also under study.

3.3.1.1 *Vertical cut tuning in the all-inductive 5-subcavities haloscope*

In the case of the RADES group, one of our first tuning investigations were based on a mechanical tuning method employing the vertical cut haloscope (see subsection 3.2.2), which is divided into two similar parts that can be adjusted symmetrically to alter the effective width dimension of the cavities, hence changing the axion frequency search range [106]. A mechanical lateral motion system for width control in this haloscope was designed and fabricated by Jessica Golm (more details can be found in her PhD thesis). In this doctoral thesis, supporting work has been carried out to follow up this system. This work has mainly consisted of the study and simulation of theoretical designs and radiation of the structure, as well as the calculation of the quality factor from several measurements of the manufactured prototype.

Three alternatives for this mechanical tuning concept were considered. A piezoactuator was used in the first two proposals to move the two cavity components. The third

approach is to move one section of the cavity from the outside using gears. The third variant has the benefit of allowing a motor to be placed outside of the magnet at room temperature. This allows to access to the motor during the data taking time and to replace it if something goes wrong. A motor that does not need to function at ultra high vacuum and cryogenic temperatures is also cheaper. As a result, the gears version was produced and tested at the CERN main workshop and at the CERN Central Cryogenic Laboratory (commonly known as the *Cryolab*), respectively.

In Figures 3.65a and 3.65b several pictures of the 3D model and the manufactured prototype of this width motion system are observed. It is based on a casing where the

(a)   (b)
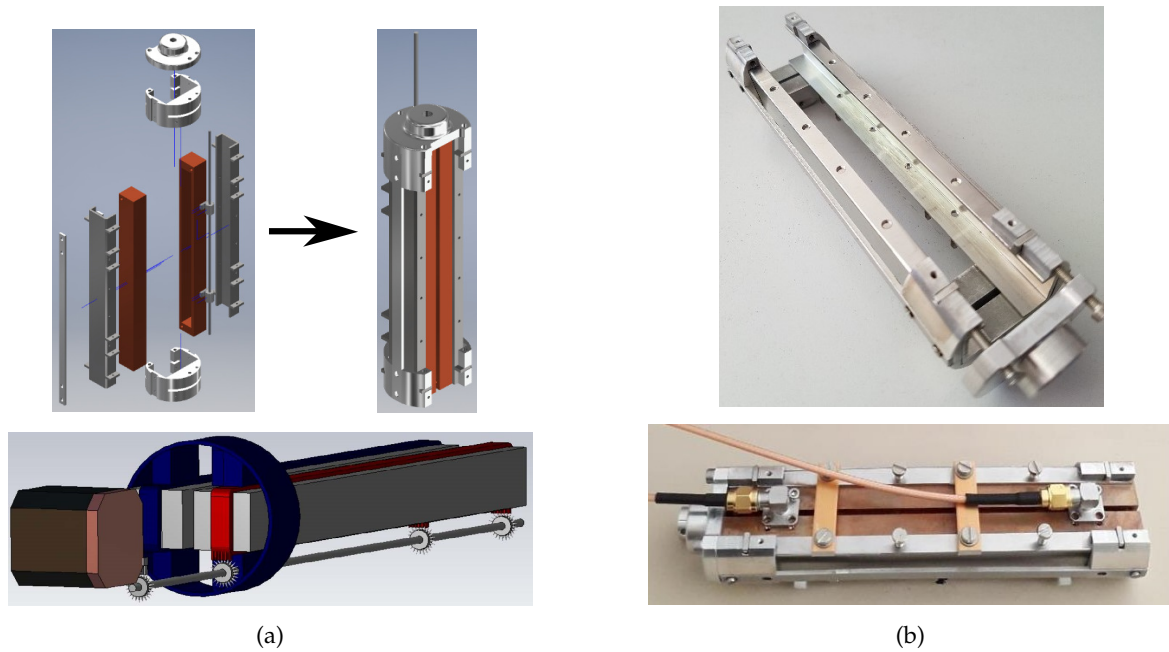
Figure 3.65: Tuning control system for the vertical cut haloscope: (a) 3D models of the structure, and (b) manufactured housing made of aluminium and stainless steel (because of their low friction coefficient) without and with the vertical cut haloscope (top and bottom pictures, respectively). At the bottom picture of (a) the object on the left is a cryogenic piezoelectric motor, which drives a gear that moves the casing that can separate the cavity halves. Pictures from Jessica Golm.

haloscope is inserted with several gears plus a stick that can be connected to a motor for the movement control. This design is prepared to be used in a dipole magnet because of its orientation. An alternative design of this system for working in solenoid magnets is under study.

Figures 3.66a and 3.66b show the frequency shift of the response and the unloaded quality factor variation with the opening gap at room temperature, respectively, in this structure. As it can be seen, a frequency tuning range of 750 MHz ($7.668 - 8.419$ GHz) is obtained with a range of gaps of 2.75 mm in this vertical cut haloscope, maintaining a maximum Q_0 decrease of 14 %, which are considered as competitive results in the axion community [97, 117–120]. The simulations show very similar results, obtaining also a
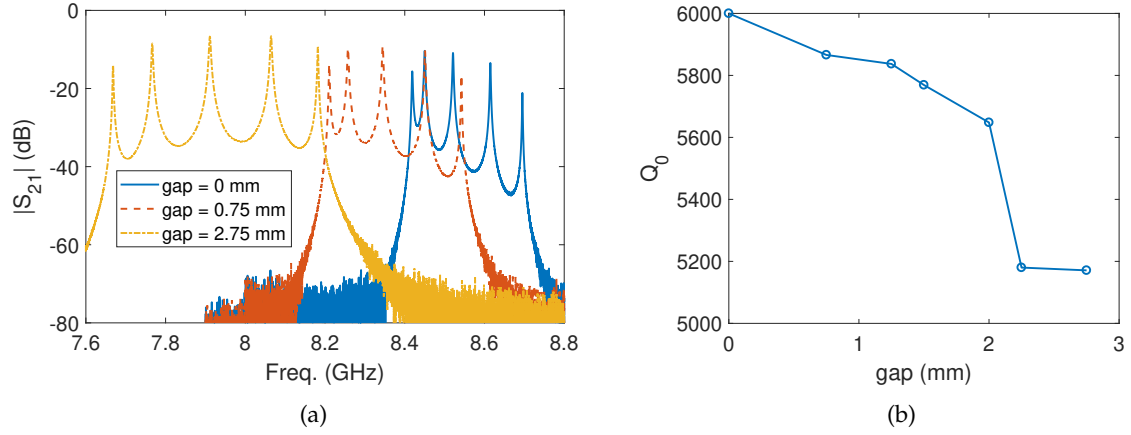
Figure 3.66: Measurements of the vertical cut haloscope at room temperature with several gaps employing the mechanical tuning system: (a) magnitude of the transmission coefficient for 3 opening gaps, and (b) variation of the unloaded quality factor versus the opening gap.

range of variation in the form factor of $C \in [0.57, 0.65]$, which are more than acceptable values. The decreasing behaviour of the unloaded quality factor from Figure 3.66b is due to the radiation produced when opening. On the other hand, it is important to note the difference between the two values of Q_0 from equation 3.65 and the one obtained with the case $gap = 0$ mm in Figure 3.66b. Although in both cases the structure is closed, in the first one a higher contact has been ensured by exerting more pressure with the screws (which cannot be used when tuning).

From Figure 3.66a it can also be extracted that the bandwidth of the group of 5 resonances becomes larger, the larger the aperture gap (or the lower the resonant frequency of the axion mode) which in turn helps to improve (or increase) the separation between modes. This is because the inductive irises widths, which provide the couplings between the subcavities, are also increased significantly with the opening, giving therefore a larger coupling. More theoretical details of why the bandwidth increases with coupling are shown in [27] and [80].

Measurements at cryogenic temperatures were taken for two gap cases (0 and 1.25 mm) with the vertical cut haloscope at the Cryolab. The system setup before the installation is shown in Figure 3.67a. Figure 3.67b depicts the frequency change of the axion mode versus the temperature for the measurements with the cavity closed (left) and 1.25 mm open (right). The resonant frequency varies by roughly 25 MHz during the entire cool down process. At cryogenic temperatures, the axion frequency of the 1.25 mm open cavity is 338 MHz lower than that of the cavity in closed position ($8.112 - 8.449$ GHz). This is in agreement with the results obtained from measurements at room temperature. The unloaded quality factor rises with decreasing temperature and reaches saturation around $T \approx 40$ K. At cryogenic temperatures this quality factor is around 24000 (for both tested gaps), corresponding to the 56 % of the theoretical value ($Q_0 = 43000$). Then, greater gaps
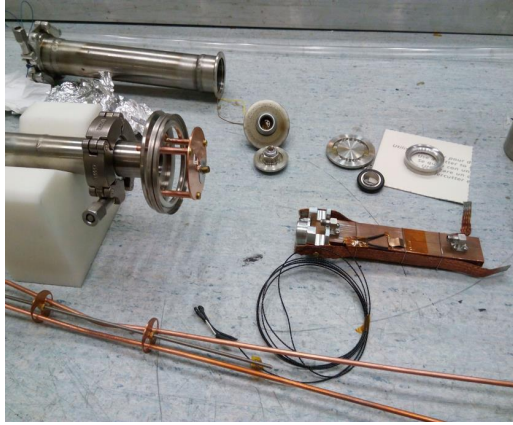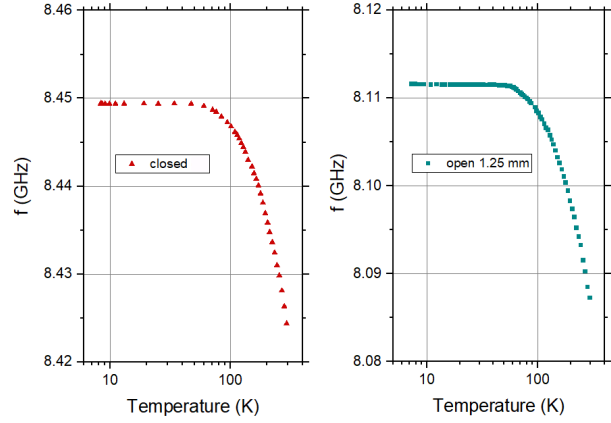
Figure 3.67: Cryolab measurements: (a) Vertically cut cavity before installation at Cryolab. The cold finger is visible on the left hand side. The vertical cut haloscope on the right hand side is fitted with heat conducting wire to allow the cavity to take on the temperature of the cryostate. (b) Frequency shifting versus temperature (in K) obtained in the measurements. Pictures from Jessica Golm.

could be applied to increase the tuning range in order to test the limit where the unloaded quality factor is maintained at high values.

Research is still ongoing to adapt the movable system (see Figure 3.65) for frequency tuning in the Cryolab and dipole magnets.

3.3.1.2 *Vertical cut tuning in the alternating 6-subcavities haloscope*

As it can be seen in subsection 3.2.3, the alternating 6-subcavity structure underwent various treatments in order to increase its unloaded quality factor. In the penultimate process carried out (see Table 3.8) this haloscope had a vertical cut (plus a horizontal cut, where the screw system is located). During the period that this structure was in this state, measurements were taken at room temperature to check the frequency tuning range and the consequent reduction of the Q_0 parameter due to electromagnetic radiation losses.

A picture of the haloscope during the tuning measurements, the tuning frequency range and the fluctuation of the unloaded quality factor with the tested opening gaps are depicted in Figure 3.68. As it can be seen, for apertures smaller than 5.5 mm a relatively high Q_0 is maintained. For the range $0 < gap < 5.5$ mm, the frequency tuning range obtained is 925 MHz ($7.567 - 8.494$ GHz), which is more than enough for a spectrum sweep in a data campaign at this frequency.

The the energy stored in a resonant cavity is directly proportional to the size of the cavity, and hence to the Q_0 parameter (see equation 3.20). On the other hand, the power loss in this case can be caused by the radiation and the conductive walls (inner surfaces of the cavity). Then, it has been concluded that the reason for achieving a high Q_0
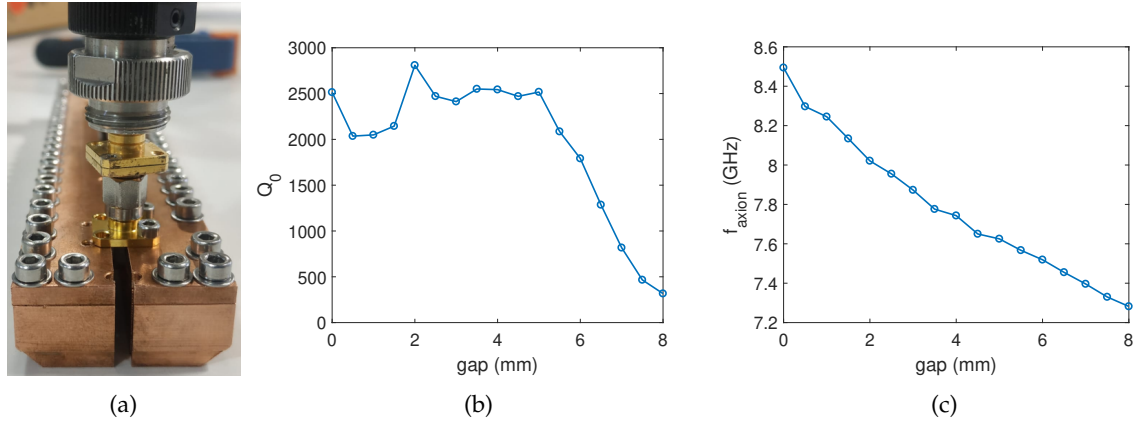
Figure 3.68: Measurements of the alternating 6-subcavities haloscope with vertical cut at room temperature with several gaps: (a) picture of the structure at the tuning measurement process, (b) axion mode frequency versus gap, and (c) variation of the unloaded quality factor versus the opening gap.

over a long range of gaps is because the volume V gained (by making the width a of the haloscope larger) compensates for the radiation losses. The area of the cavity walls remains unaltered. For $gap > 5.5$ mm the radiation losses become very high and the unloaded quality falls rapidly.

At this point, it has been demonstrated that the vertical cut tuning in alternating structures is also possible. In addition, the tuning control system shown in Figure 3.65 could be adapted for this prototype, just modifying slightly its longitudinal dimension.

The study of this tuning in the current state of the structure (last row of Table 3.8) has been left as a future line of this PhD thesis. It is also intended to perform a vertical cut to the 30-subcavities haloscope to perform these tuning investigations, where more mode crossings are expected due to the existing mode clustering.

3.3.1.3 *Vertical cut tuning in the tall 4-subcavities haloscope*

The tall prototype with 4 subcavities and 3 inductive irises was another of the designed structures, manufactured and measured, with which frequency tuning studies were also carried out. This process is depicted in Figure 3.69, where an image of this structure during the measurement time and the displacement of the response for different apertures can be observed. As it can be seen in Figure 3.69b, a lot of resonances appear in the frequency range scanned due to the high value of the height dimension ($b = 300$ mm). For all the cases, the axion mode is located at the first resonance of the response. In this structure, the tuning frequency range achieved for a 3 mm gap variation is 815 MHz ($7.357 - 8.173$ GHz), which could be increased by making larger openings. This corresponds with a good value compared with previous haloscopes.

Regarding the unloaded quality factor, as it is shown in Figure 3.69b, its value suffers an increase from $gap = 0$ to 2 mm, and a slight detriment for the case $gap = 3$ mm. This
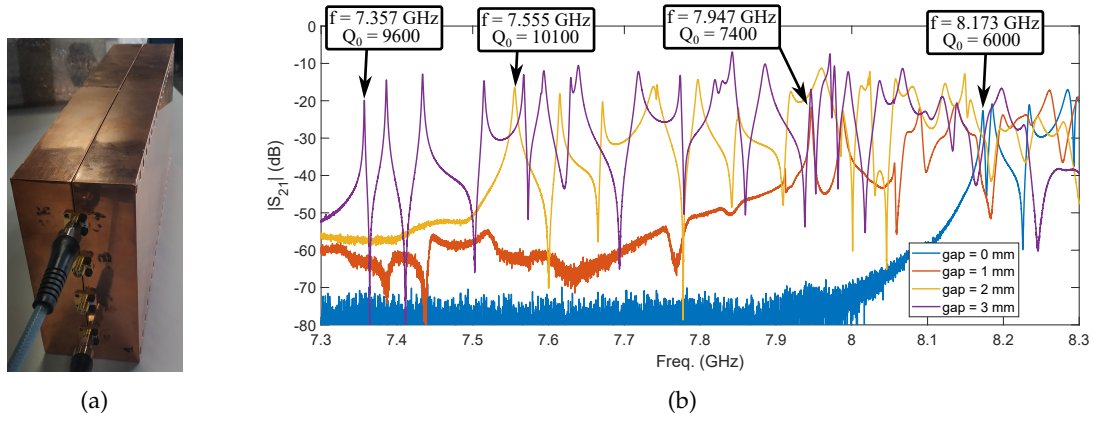
Figure 3.69: Measurements of the tall 4-subcavities haloscope with vertical cut at room temperature with several gaps: (a) illustration of the structure at the procedure of the tuning measurements, and (b) magnitude of the transmission coefficient versus frequency for four gap cases. In (b) the axion mode frequency and unloaded quality factor values are depicted for each gap.

fits with the conclusion drawn from the tuning study of the 6-subcavities alternating structure, where the radiation effect is compensated by the volume gained enhancing the quality factor as the aperture gap is increased up to a certain limit.

Again, the movable control system from Figure 3.65 could be used for this prototype, but this time with major modifications as the volume and weight are greater than those of the vertical cut haloscope.

3.3.1.4 *Vertical cut tuning in the 2D 6-subcavities haloscope*

The prototype based on an all-inductive 6 subcavities structure with an interresonator cross-coupling was also used to study the possibility of employing the vertical cut as a tuning medium. The concept for this structure is a bit different from the other studied prototypes, as this time the vertical cut has been performed in manufacturing twice due to the arrangement of the subcavities (2D design). Therefore, the tuning in this case was based on modifying the opening gap of both cuts simultaneously. For this reason, washers were employed for ensuring the same gaps, as it is depicted in Figure 3.70a. These measurements were taken before the cooper coating, being the prototype manufacturing based on the stainless steel 316L material. In Figure 3.70b it can be seen how a frequency tuning range of 615 MHz (7.391 − 8.007 GHz) is achieved for a gap range of $0 < gap < 2.5$ mm, which again it is considered as a good result for a RADES haloscope. In addition, as it is shown, the value of the unloaded quality factor is maintained relatively high for all the cases (633 − 708).

The mode separation from the axion one to the next resonance is $\Delta f = 110$ MHz with the $gap = 0$ mm case. However, for a gap of 2.5 mm this parameter decreased to $\Delta f = 73$ MHz since the transmission zero that operates for rejecting the second eigenmode of the structure is very sensitive with the haloscope dimensions. Anyway, it is still better

|S_{21}| (dB) vs Freq. (GHz)

f = 7.391 GHz, $Q_0 = 633$ | f = 7.656 GHz, $Q_0 = 648$ | f = 8.007 GHz, $Q_0 = 708$

gap = 0 mm
gap = 1.5 mm
gap = 2.5 mm

(a) (b)
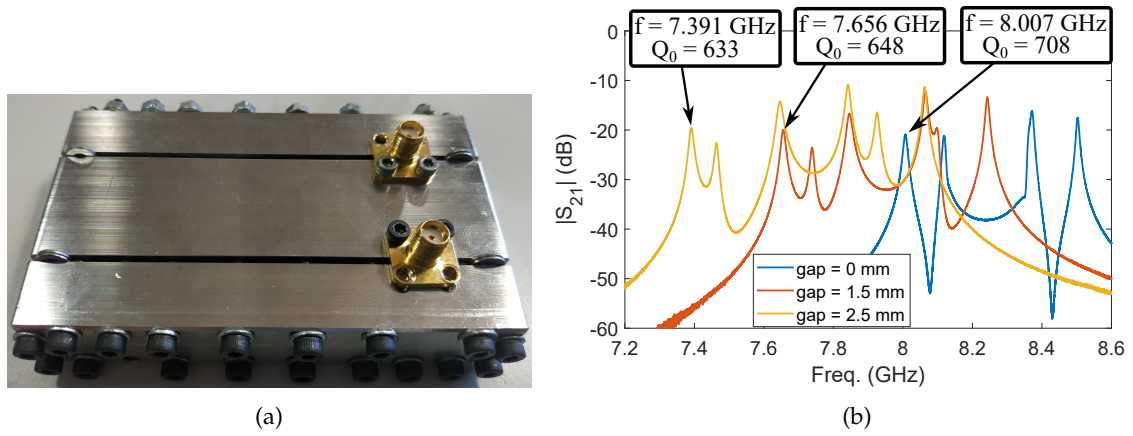
Figure 3.70: Tuning study with the all-inductive 6-subcavities haloscope with a cross-coupling: (a) picture of the structure with washers (warranting the same opening gap at both vertical cuts), and (b) magnitude of the transmission coefficient versus frequency for three gap cases. In (b) the axion mode frequency and unloaded quality factor values are depicted for each gap.

than the case without cross-coupling: $\Delta f = 34$ MHz. Then, tuning is possible deteriorating slightly this mode separation.

In 2D structures the system for controlling the haloscope width could be adapted if it divided into 3 pieces, where only the lateral modules are moved while the central one in fixed.

3.3.1.5 *Mechanical tuning in high-volume haloscopes*

More investigations have been carried out for applying mechanical tuning in haloscopes with a high volume, where the mode mixing could be a problem since the resonant frequencies of the modes are very close.

Observing equation 2.17, the frequency tuning range for an specific *a* range can be extracted. X-band examples for both long and tall structures when the width dimension is employed for the haloscope tuning are shown in Figure 3.71. Also, Figures 3.71b and 3.71d depicts how the differences in the mode clustering here are negligible preserving a high tuning range (see Figures 3.71a and 3.71c). These results could be applied for both sliding wall methods, sliding short and vertical cut tuning.

3.3.2 *Electrical tuning*

Unlike mechanical tuning, electrical tuning can create a system that is less prone to mechanical failures (for example, by avoiding movable components in a cryogenic environment) and so complements and enhances current procedures. Another advantage of this type of tuning for multicavity systems is the ability to alter the multiple cavity frequencies and interresonator coupling values independently to preserve the right modal
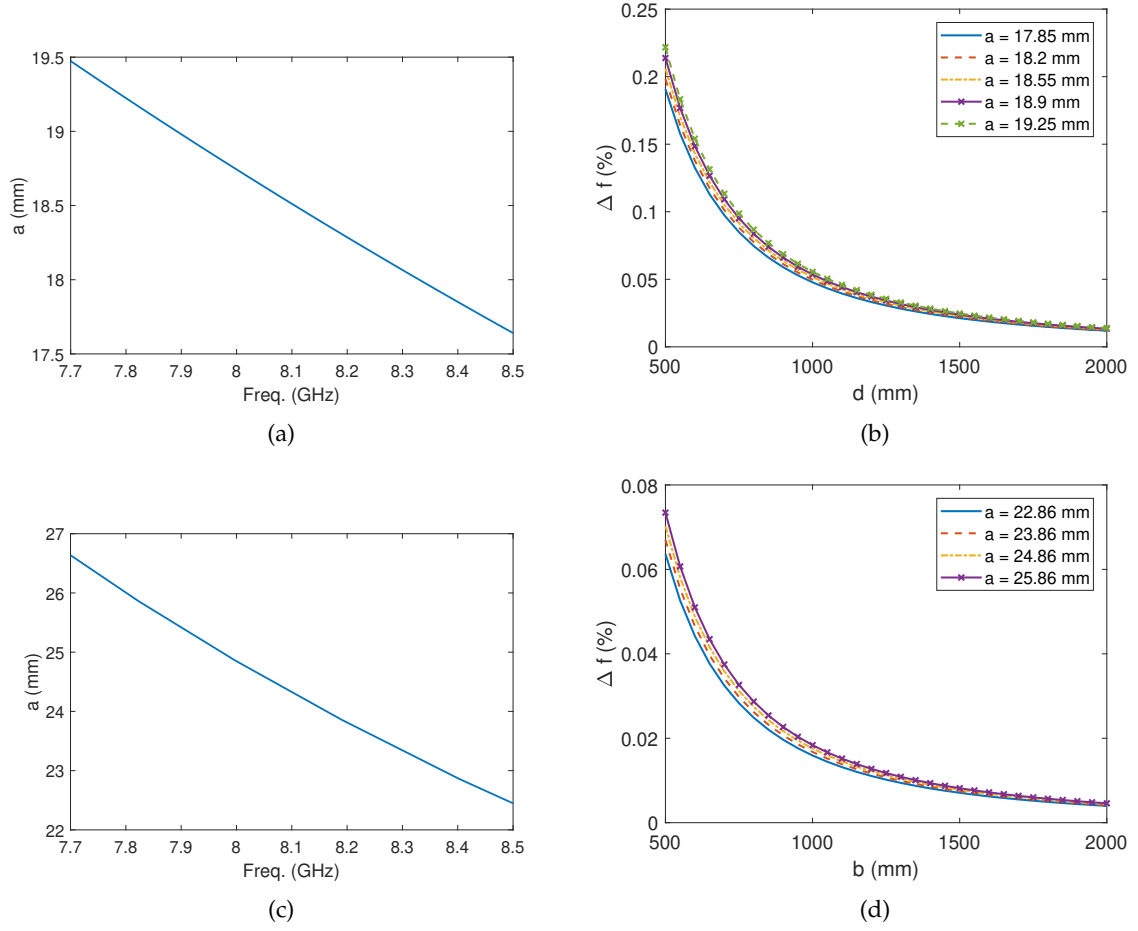
Figure 3.71: Tuning characteristics for both long and tall structures varying the *a* dimension of the cavity: (a) Tuning (varying *a*) for a long structure with $b = 10.16$ mm and $d = 1400$ mm, (b) mode clustering for different *a* values versus the length dimension (with $b = 10.16$ mm), (c) tuning (varying *a*) for a tall structure with $d = 28.55$ mm and $b = 1500$ mm, and (d) mode clustering for different *a* values versus the height dimension (with $d = 28.55$ mm).

structure and electromagnetic field pattern (which could improve also the form factor). Furthermore, when these haloscopes are constructed at higher frequencies, the mechanical tuning does not scale properly (for example from X-band to Ku-band). The electrical tuning mechanisms presented in this PhD thesis may be able to overcome this problem.

In this work, several tuning technologies has been investigated in order to implement an electrical tuning system in our haloscopes: liquid crystals, dielectrics, ferromagnetics, ferroelectrics, piezoelectrics, MEMS, composite ceramics based on mixtures of ferroelectrics and semiconductors (varactors), and so on. However, due to the environment imposed on an axion detection system (cryogenic temperatures, high static magnetic field level, minimal losses and, in some magnets, ultra high vacuum), the ferroelectric and ferromagnetic technologies, which might work in this environment, are the most promising ones. Because these type of dielectric materials change permittivity with temperature or bias Direct Current (DC) voltage, the idea is to load the haloscope with one of them and then vary its

relative electric permittivity ε_r (for ferroelectrics) or its relative magnetic permeability μ_r (for ferromagnetics) to induce a frequency shift.

3.3.2.1 *Ferroelectric tuning*

Ferroelectrics are non-linear dielectrics with high relative permittivity values that are commonly used in commercial decoupling capacitors, acoustic-electronic transducers, and MEMS [122]. Its permittivity may be changed by applying an external static electric field (or by changing the temperature), which is the most essential property of some perovskites that makes them appealing for agile microwave components (such as varactors, tunable RF filters, and phase shifters).

There are about 300 ferroelectric materials available, but the most common is Barium Strontium Titanate or $Ba_xSr_{1-x}TiO_3$ (BST), which operates in the paraelectric phase at room temperatures ($\sim$ 297 K) [123, 124]. The Strontium Titanate or $SrTiO_3$ (STO) was previously employed at cryogenic temperatures by the ADMX-Fermilab axion research group, which researched ferroelectrics as a tuning element for the ADMX project [71]. However, the frequency shifts and accompanying dielectric permittivity changes were not as large as projected [125, 126]. Furthermore, the losses in these studies resulted in a decrease in the unloaded quality factor of more than 90 %. In this sense, this PhD thesis proposes a novel technique of utilising electronic tuning systems based on ferroelectric elements.

One of the main works carried out in this PhD thesis is the design of a novel concept for using the ferroelectric Potassium Tantalate or $KTaO_3$ (KTO) material as a tuning element in haloscopes, a ferroelectric crystal with good tuning parameters and a very low loss tangent ($\tan\delta \simeq 10^{-5}$ at X-band, whereas for the conventional STO material it is $\sim 10^{-3}$) in the cryogenic temperature range $0.1 - 10$ K [127].

The developed tuning methods are based on thin ferroelectric films near the side walls whose relative permittivity value is modified with a temperature or applying a DC voltage biasing. The cavity is not completely filled with the ferroelectric material since the form factor would be drastically reduced (see factor ε_r in equation 2.6). In section 4.1 the theoretical details for the use of ferroelectric films as tuning are described.

It is important to note that in the ferroelectric tuning system unlike the sliding walls method, it does not decrease the cavity volume when the frequency changes since the tuning is done by a electric permittivity change and not by a mechanical movement (or geometrical change). In addition, the ferroelectric method (electrical tuning) can be combined with the vertical cut (mechanical tuning) for more versatility in frequency adjustment.

3.3.2.2 *Ferromagnetic tuning*

Once the ferroelectric tuning system was developed, another of the studies carried out in this work was the possibility of using ferromagnetic crystals as electronic tuning (instead of ferroelectric media). From equations 2.15, 2.16, 2.17, and 2.18, it can be extracted that the ε_r and μ_r affect to the resonant frequency of a cylindrical or rectangular cavity for any mode equally. However, the great advantage is that these crystals would be tuned with the same static magnetic field already provided by the magnet (both dipole and solenoid type) where the axion data campaign is to be carried out, avoiding the need to introduce electrodes for the DC voltage inside the cavity, which has been a hard challenge at a technological level point of view. Of course, it should be avoided varying the magnetic field to zero, as this would result in no detected RF signal as the inverse Primakoff effect would not be fulfilled (see section 2.2).

The axion experimental group QUAX performed in 2018 some tuning studies with haloscopes using ferromagnetic materials. According to [128], this group discussed that a tuning of a few MHz (with axion operating frequency at 14 GHz) could be obtained by varying the static magnetic field. However, this experiment is not exactly equivalent to RADES since what is sought is the interaction of the axion directly with the spins inside the crystal (via axion-electron coupling).

Following an internal discussion in the RADES collaboration, it was decided to investigate the Yttrium Iron Garnet (YIG) [129] and *Gadolinium Vanadate* or *GdVO$_4$* [130] ferromagnetic crystals (recommended by Dr. Takis Kontos, from the *French National Centre for Scientific Research*) to find out whether they are capable of working at cryogenic temperatures, what is the range of μ_r through which these crystals move against a magnetic field of a few Teslas, and their commercial availability (price, sizes and geometries).

The first step in developing an electronic tuning system based on ferromagnetic materials was to search the literature for an approximate range of values of relative permeabilities versus the static magnetic field. This search was not easy, but we managed to extract some approximate values from the paper [131] for the YIG material, which have been chosen as a reference for our studies even if they do not correspond to the final values of the magnetic field to be used in a measurement. The selected range is $1 < \mu_r < 100$ (assuming a relative permittivity value of $\varepsilon_r = 1$ and a magnetic tangent loss value of $\tan \delta_m = 0$ for these preliminary studies). The reason for choosing this strategy is that we can also play with the crystal orientation since the μ_r sensitivity depends on the parallelism between the ferromagnetic crystallographic axis and the magnetic field direction. In this way, if the range that gives the greatest variability is, for example, around 1 T, then the crystal can be rotated so that the 8 T (in the CAST magnet) or 2.5 T (in the BabyIAXO magnet; see Table 3.1) could correspond to 1 T on that orientation.

In this way, we have made a preliminary design that allows us to see this effect by making a static magnetic field sweep with which, once characterised in manufacture, the orientation and geometry are adjusted, if necessary, for the definitive design. The first study carried out was the tuning effect investigation for one of our single (non multicavity) haloscopes: the HTS prototype. A cylindrical YIG piece of diameter $d = 5$ mm and height $h = 10$ mm was provided by Dr. Takis Kontos. As it can be seen in the 3D models from Figure 3.72, the idea is to load (glueing with PolyMethyl MethAcrylate (PMMA) resist) at one side of the HTS haloscope, with its longitudinal orientation parallel to the electric field and then, parallel to the magnetic field lines of a Helmholtz coil (similarly to the solenoid magnet case), where the experiment has been carried out. In Figure 3.72b several

(a)	(b)
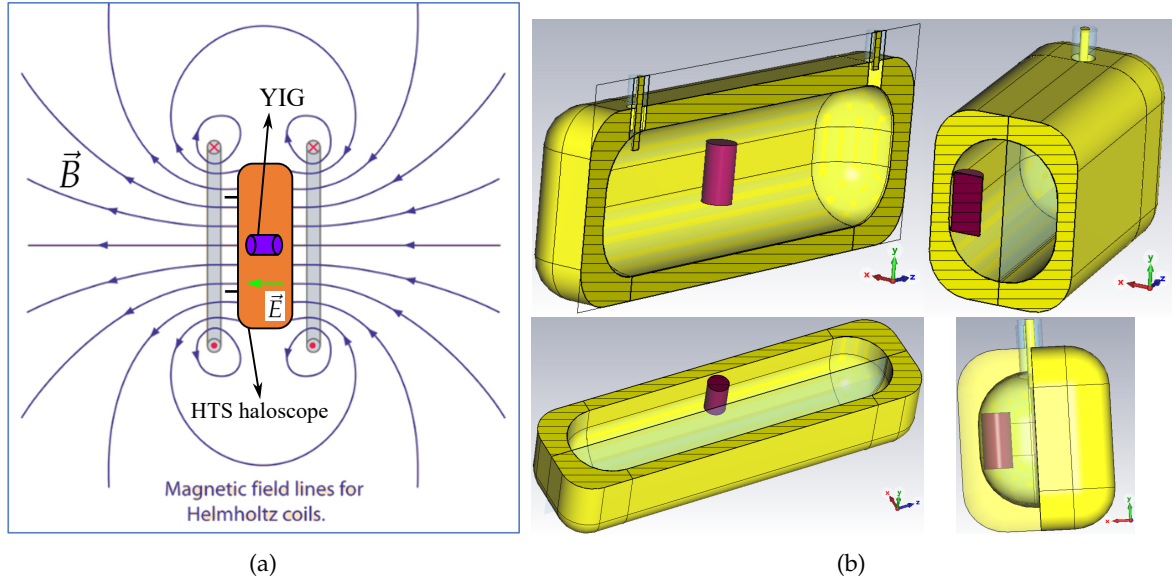
Figure 3.72: HTS prototype loaded with a YIG cylinder for the ferromagnetic studies: (a) magnetic field lines in a Helmholtz magnet with the HTS structure, and (b) 3D models of the HTS structure with the loaded YIG material. The ferromagnetic cylinder is positioned at the middle in the height and longitudinal axis, and attached to one side.

3D models are depicted for a more detailed demonstration of the YIG position inside the HTS prototype.

A tuning range of 246 MHz ($8.805 - 9.051$ GHz) has been obtained in simulation with a permeability range of $1 < \mu_r < 10$, giving an increase of the quality factor from $Q_0 = 42063$ ($\mu_r = 1$) to $Q_0 = 45554$ ($\mu_r = 10$).

By rotating 90° degree the YIG piece in the width axis, a greater tuning range has been obtained for the same μ_r change: 640 MHz ($8.411 - 9.051$ GHz), this is 2.6 times higher. In this case, the unloaded quality factor goes from $Q_0 = 42063$ ($\mu_r = 1$) to $Q_0 = 52212$ ($\mu_r = 10$). However, with this orientation the YIG is not anymore parallel to the magnetic field. Thus, an intermediate orientation is under study to increase both the YIG sensitivity and the tuning range.

Experimental measurements have been carried out in the *Laboratoire de Physique de l'Ecole Normale Supérieure* (by Dr. Takis Kontos and Arnaud Thery) with this setup, the results of which are still under analysis.

In addition, using the same configuration used for the ferroelectric tuning designs (which will be explained in the next chapter), a setup has been found in simulation with a $1 < \mu_r < 10$ range that provides a 1 GHz tuning range with good quality factor ($Q_0 > 50000$). The ferromagnetic films employed here have a rectangular shape with dimensions 0.3 mm $\times$ 10.16 mm $\times$ 22.86 mm. The implementation of this setup in a real experiment has been reserved as future work.

3.4 MOVABLE COAXIAL PORT

As it has been seen throughout this PhD thesis, the port coupling β (see equation 3.48) in a haloscope is an essential parameter to ensure good axion detection sensitivity in any data campaign, and its value should be as close to 1 as possible (the critically coupled regime). When an axion detector is installed in a magnet and cooled to cryogenic temperatures, this coupling value may vary and not be as expected, even when using the prediction methods discussed in subsection 3.2.4. Once the magnet is driven to these conditions, the extraction of the cavity for port correction is not straightforward, so the use of a β coupling readjustment system is almost mandatory in a realistic experiment. On the other hand, this coupling tuning system will also be necessary if in an axion data taking a portion of the electromagnetic spectrum (instead of a single frequency) is swept with a frequency tuning system since the value of the coupling with the axion mode varies according to the operation frequency.

There are several types of external coupling mechanisms, like waveguide irises (usually employed in W-band structures) or coaxial probes. The most commonly used in X-band and UHF-band structures are the latter because they can control the external coupling easily by varying the depth of the coaxial pin inserted into the cavity. As it was studied in previous sections, the optimum length of the coaxial pin is the one which establishes the critically coupled regime. A sweep of several pin lengths has to be carried out to find the optimum value. For a coaxial port, the pin movement depends on the type of magnet and port position due to space constraints. Assuming a straight coaxial pin positioned at the top of the first subcavity in a multicavity structure, for a solenoid magnet the movement will be straight (up and down). Most coupling tuning systems for adjusting the depth of antennas on SMA coaxial ports have been designed to be used in these types of magnets, such as those used by HAYSTAC [72] whose linear motion control system is based on a tuning vernier and springs, or the employed by ADMX [132] whose system based on gears are frequently run into mechanical problems at cryogenic temperatures.

However, the RADES team has made use of dipole magnets (such as CAST) until today, so the motion needs to convert a longitudinal movement (due to limited available space) into a vertical one. In the case of solenoid magnets the external access comes from the upper part of the bore ($z-$axis in Figure 2.10a), and in dipole magnets it comes from one side ($z-$axis in Figure 2.10b). Thus, the concept differs depending on the magnet since there is a 90° angle between the direction of the bore access and the orientation of the coaxial port for dipoles. Therefore, preliminary investigations have been carried out in this work in which a first coupling tuning system adapted to dipole type bores has been designed, manufactured and measured.

3.4.1 *The first adjustable coaxial system*

The first system developed in this PhD thesis for the external coupling control was based on the use of wedges and a pushing element, with a sophisticated arrangement of square panels, screws, and springs at a SMA port device allowing to transform a longitudinal motion into a vertical displacement for the variation of the antenna penetration into the subcavity where the port is positioned. A picture of this manufactured system in stainless steel 316 is shown in Figure 3.73a, where its behaviour is being tested in a single cavity that operates around $f_{TE_{101}} = 8.53$ GHz. Also, in Figures 3.73b and 3.73c the lower (more antenna inside the cavity) and upper (less antenna) limits of the system path can be visualised. Figure 3.73d shows a sketch of the system providing more details of the system modules. The solid arrows in Figure 3.73a indicate an upward movement (extraction of the pin from the cavity) when the left-hand piece push the wedges of the port system. The dotted arrows denote a downward motion (introduction of the pin) when the left-hand piece moves to the left side alleviating the pressure (here the springs push down the whole system). The two screws with springs at the panels are screwed (immovable) to the cavity for fixing the upper position of the springs (allowing the compression and the reversible motion). On the other hand, the two screws without springs are used for attaching the system panels with the SMA one. In addition, all of them provide alignment.

In Figure 3.74a the reflection coefficient of the system (S_{11}) is measured for three different penetration depths of the pin into the testing cavity. Figure 3.74b shows the Smith chart of the measurements, revealing more information to extract the behaviour of the external coupling. Port 2 is very weakly coupled. As explained in the subsection 3.2.1.4, if the centre of the Smith chart is inside the S_{11} circumference the port is overcoupled, and vice versa for the undercoupled situation. For the case where the circle is on the centre the port is critically coupled, which is the target in axion data taking. In the example of Figure 3.74, the black lines correspond with the case from Figure 3.73b, while the blue lines represent the Figure 3.73c case. The critically coupled case (red lines) is achieved in an intermediate step between these two limits.
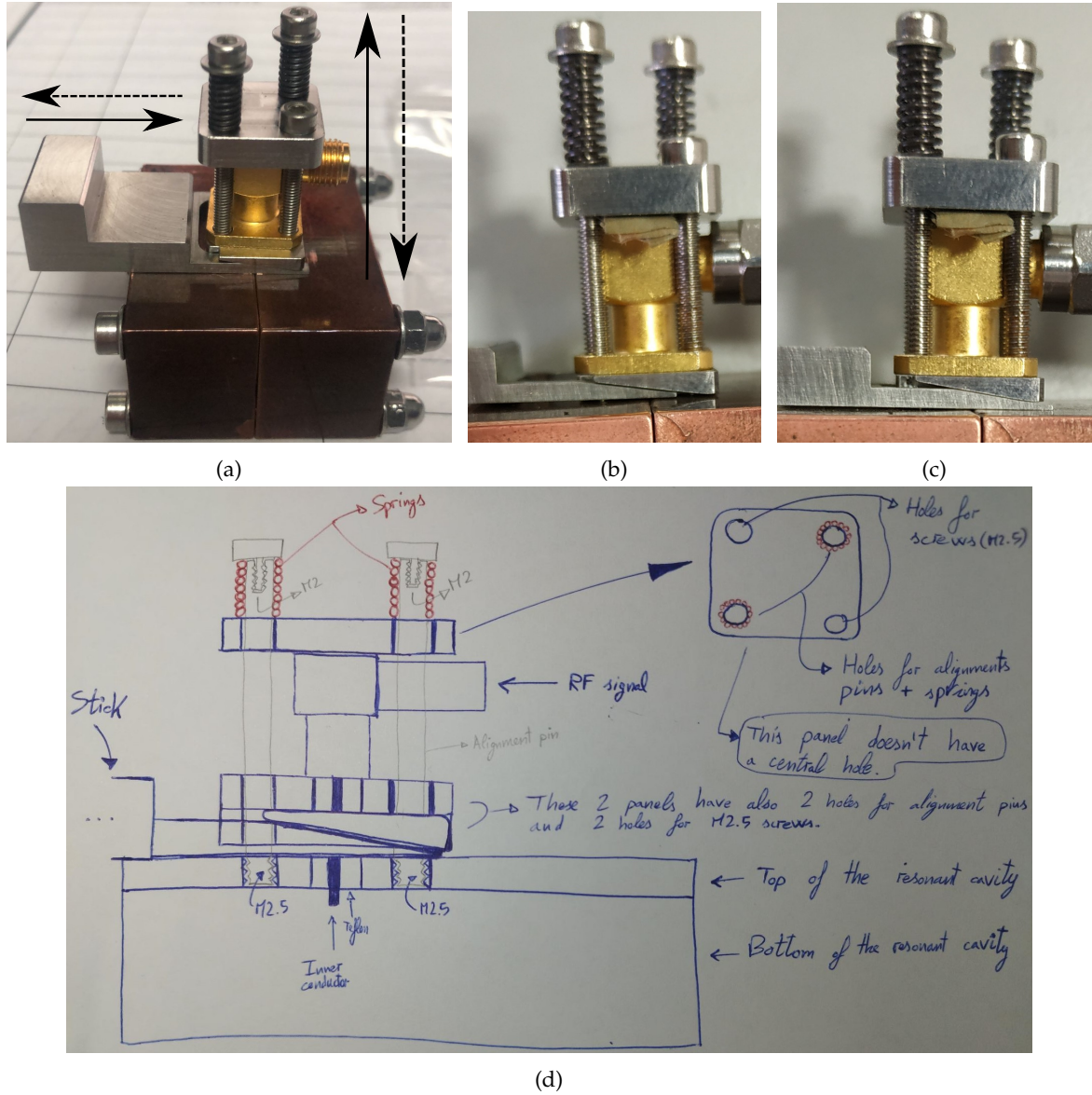
Figure 3.73: First adjustable external coupling system: (a) manufactured prototype, (b) lower limit case, (c) upper limit case, and (d) sketch with more information about the device components. The solid arrows in (a) denote an upward movement (extraction of the antenna pin from the cavity) when the left-hand piece push the wedges of the port system. The dotted arrows represent a downward motion (introduction of the pin) when the left-hand piece shifts to the left side alleviating the pressure (here the springs push down the whole system).

An evolution of this prototype with longer stick wedges providing a higher range of movement is under study (see Figure 3.75a). This will be almost mandatory since the sensitivity of the S_{11} magnitude level with the coaxial pin movement depends on the quality factor of the haloscope. If the cavity manufacturing yields to a worse Q_0 than expected ($< 50\%$ of the simulation value), the system will have to deal with greater antenna movement ranges than expected when the frequency is shifted (tuning). This behaviour has been tested with some of the low-Q_0 haloscopes manufactured by RADES, such as the alternating 6-subcavities and 30-subcavities multicavities, where less sensitivity is found in the S_{11} parameter at the axion frequency when the coaxial antenna is swept compared
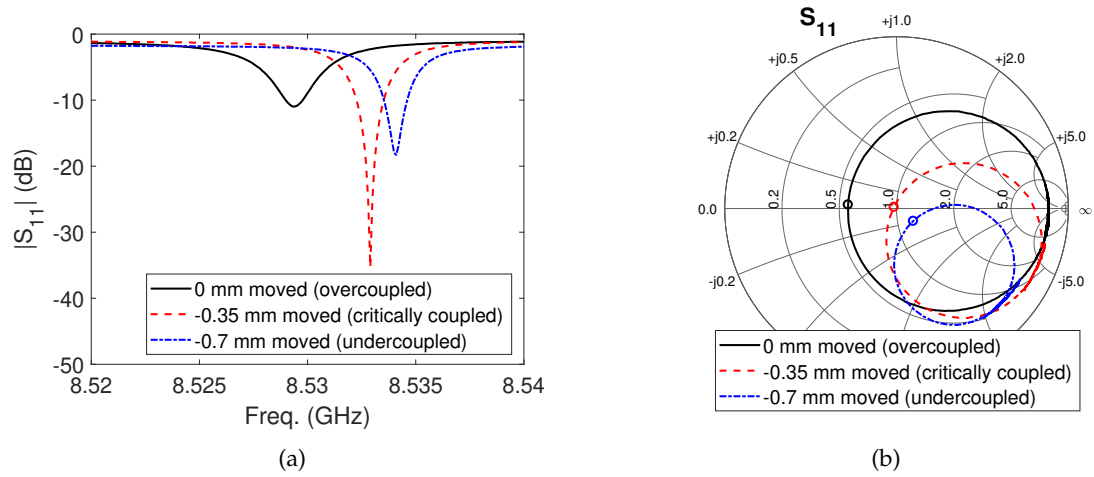
Figure 3.74: Test measurements of the first adjustable external coupling system: (a) S_{11} scattering parameter magnitude as a function of the frequency for three different penetration depths (the negative sign denotes an opposite vertical direction to the inner of the cavity), and (b) measured reflection coefficient in Smith chart format.
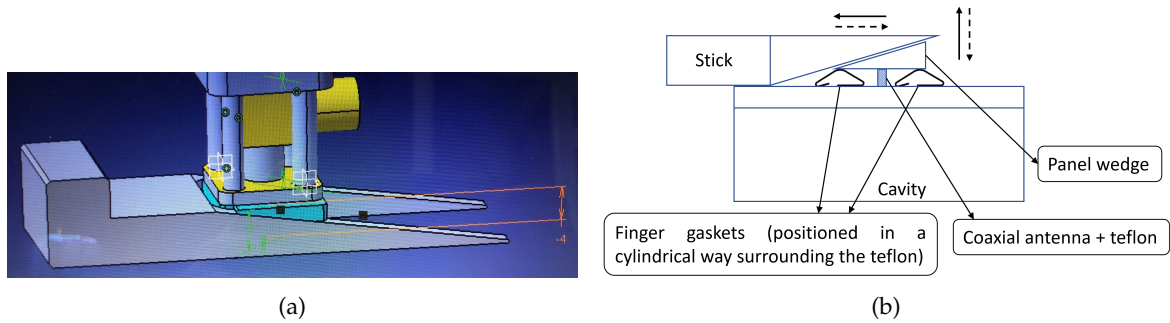
Figure 3.75: Sketches of the investigations carried out to evolve the first coupling tuning system: (a) longer stick wedges for a higher antenna sweep range, and (b) re-designing of the system with finger gaskets and inverted wedges.

with other structures with a higher quality factor.

On the other hand, after the optimization of this adjustable port system prototype, the idea was to attach the left-hand piece (stick) to a step motor / piezoelectric to make possible its control from the outside of the dipole magnet test-bed once it is installed for data taking, although this will depends on the inner geometry of the employed magnet bore (cryostat, thermal plates, elbows, bore length,...). A stepping motor (the *HT23-595 - NEMA 23 High Torque Step Motor*) and its controller (the *STR2 - DC Powered Advanced Microstep Drive*) have been already acquired with which performance tests will be carried out with our coupling tuning systems in the near future. After that, the next step will be to buy a nanopositioner (similar to the Cryo Linear Actuator *CLA2603* device) for making further tests. For the moment, push and pull force studies of the manufactured prototype have been carried out, obtaining results (6 and 2 N, respectively) within the limits imposed by the commercial motor devices considered (< 30 N).

One of the main problems with this prototype is that it does not correctly guarantee the contact between the port and the cavity, since when sliding the stick and raising the system, the inner section of the coaxial (teflon + inner antenna) is exposed to a high electromagnetic radiation. This translates directly into losses increasing rapidly as the antenna goes up (less depth into the haloscope, or less coupling). Looking at Figure 3.74a, it can be seen how this phenomenon is fulfilled as the off-resonance offset level decreases (from −1.15 to −1.78 dB), the value of which indicates the level of coupling losses. This means that a higher range of movement would lead to higher losses in this prototype. Therefore, the redesign of this system through the use of finger gaskets must be carried out in order to ensure greater contact between the SMA coaxial port and the top of the haloscope housing. Figure 3.75b shows a simple diagram of the use of finger gaskets, where the orientation of the wedges in the panels and in the stick have been inverted. With this design, the use of springs would not be necessary, reducing at the same time the total height of the system to solve possible space incompatibilities within the bore of the magnet. However, as we have not yet found commercial finger gaskets that meet our needs, we have left the manufacturing of this structure as future line.

3.4.2 *The second adjustable coaxial system*

A study was carried out to contemplate the possibility of implementing a different prototype based on the readjustment of the coaxial antenna by means of a perpendicular gear. This prototype was provided by Pedro Plaza (from the *ITACA institute*, UPV, Valencia). Figure 3.76a shows the tested cavity (an HTS haloscope prototype, see section 5.2.3 for more details) adapted with this antenna movement system for several experiments. Figures 3.76b, 3.76c and 3.76d depict the modules of the system once it is disassembled. The horizontal cylinder that can be observed in the intermediate module (see Figure 3.76c) is employed for friction/contact purposes.

The inset in Figure 3.76a expose the possibility to adapt the gear with a complementary gear that could allow the transformation of a rotary motion in the longitudinal axis into another revolving movement in the vertical axis (antenna axis). This would be very interesting for dipole magnets, as previously discussed. For solenoid magnets, the solution would be even simpler: to add a parallel spur gear attached to a cylinder stick that could be extended to the solenoid outside, allowing the transformation of a rotary motion from it to the gear of the antenna tuning system, both in the vertical axis.

Once the HTS cavity was assembled, and with the port 2 set to have a very weak coupling, it has been found that it is possible to go from an undercoupled to an overcoupled state, passing through the critically coupled case, at the port 1 due to this coupling tuning system, similarly to the studies carried out to obtain the results from the Figure 3.74. In addition, in order to check the behaviour of this system in a tuning situation at the data campaigns, and taking advantage of the fact that this haloscope is prepared to be tuned easily by means
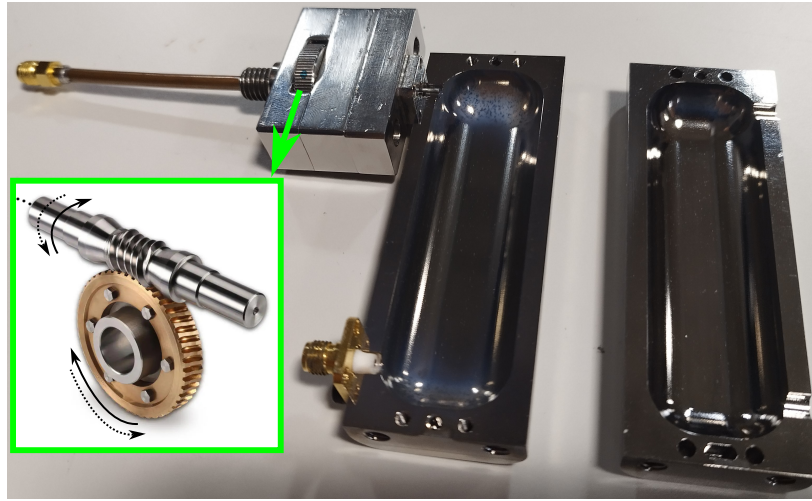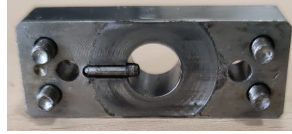
Figure 3.76: Coupling tuning system based on a gear: (a) picture of the test realised with an HTS haloscope prototype which is based on a vertical cut in manufacturing, (b) pieces of the top module, (c) intermediate module, and (d) bottom module. The inset in (a) shows another gear concept that could be adapted in the current prototype. The cavity is disassembled for the visualisation of the coaxial antennas.

of its vertical cut, a study was carried out to maintain the critical coupling for any tuned frequency by a manual adjustment of the gear when the cavity is opened (also manually for these tests) with several gaps (from 0 to 2 mm). In Figure 3.77 the transmission and reflection parameters of this cavity when is tuned and adjusted to be critically coupled are shown. As it can be observed, the frequency range is 800 MHz for an opening range of 2 mm. Also, these results show how the critically coupled case can be achieved in the axion mode for all the tuned frequencies ($|S_{11}| < -20$ dB), verifying that this system could be appropriate for a future data taking. For the cases with two resonances on the frequency range shown in Figure 3.77 (pink and black lines) the axion mode corresponds with the left one, being the right peak a higher mode resonance. On the other hand, more research is being carried out to study the losses produced by this system.

3.5 CONCLUSIONS

The volume limitations of rectangular microwave cavities working as haloscopes were investigated in this chapter. This parameter enhances the axion detection sensitivity, which is a primary incentive in the recent years studies. Several techniques for rising up the volume are provided in the first section of this chapter, considering restrictions such
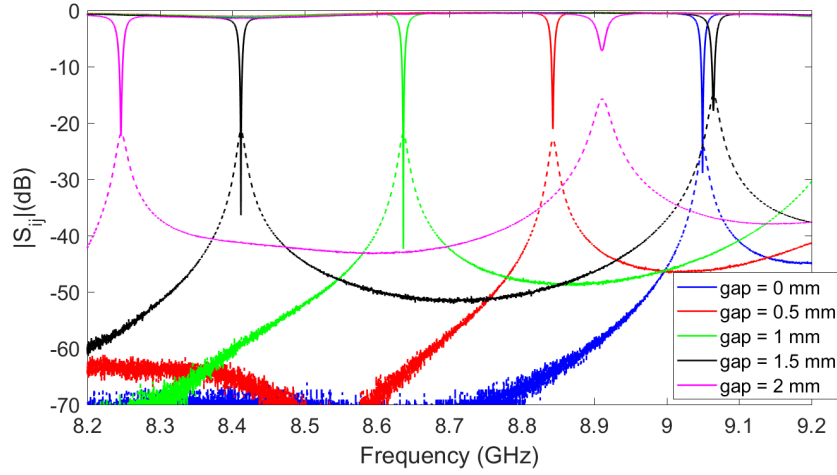
Figure 3.77: Transmission and reflection parameters (S_{21} and S_{11}, respectively) of the measurement tests carried out with the HTS haloscope prototype. These tests are based on adjusting the antenna depth with the coupling tuning system to be critically coupled with 5 different vertical cut openings. The dotted lines represent the S_{21} parameter, while the solid lines correspond with the S_{11} parameter.

as the mode separation or mode clustering, and the modification of the form factor and the unloaded quality factor parameters. This study also includes extensive investigations with single cavities and 1D multicavities, as well as, in a more basic manner, 2D and 3D multicavities that achieve outstanding $Q_0 \times V \times C$ factor values. These haloscopes have been shown to be compatible with the biggest dipole and solenoid in the axion community. Several prototypes were produced and tested, yielding favorable results in unloaded quality factor and mode separation, demonstrating the possibilities of several of these investigations while also acting as validation.

Large cavities have been discovered to have the best $Q_0 \times V \times C$ factor among single cavities. Furthermore, despite their additional complexity in the design stem, the usage of multicavities can lead to an enhancement of this parameter. When looking for the axion in a range of frequencies or masses, however, the rise in volume is restricted by the number of tolerated mode crossings. The emergence of transmission zeros in several haloscope designs, on the other hand, permits to shift or reject modes nearby to the axion mode, reducing both mode separation and potential mode crossings across a range of frequencies. These approaches are meant to serve as a guide for any experimental axion team looking for volume restrictions in the construction of a haloscope based on rectangular cavities (or multicavities) to be installed at dipole or solenoid magnets. However, same techniques and analyses are also applicable to any application in which rising up the volume of a waveguide cavity for a given resonant frequency is a target.

Depending on the kind and configuration of the magnet for axion data taking, this study brings up a wide variety of interesting options. The solutions outlined in this work allow for the most efficient use of bore space with the goal of increasing the sensitivity of

axion search detectors. In this respect, studying the geometry limitations using numerous concepts given in this work, such as alternating coupling in 1D multicavities or long, tall, and large multicavities in 2D / 3D geometries, is a worthwhile challenge for the construction of a high competitive haloscope within the axion community. The extrapolating of all these research and testing to cylindrical cavities and multicavities has been left as future research work.

In the second section of this chapter, there is analysed the quality factor in several haloscopes developed by the RADES team, proposing new solutions, like the modularity, for the improvement of this parameter. The modularity idea is a novel concept developed in this PhD thesis and it is based on applying manufacturing cuts at efficient areas in order to lessen the influence on the surface currents (and consequently on the quality factor) in the resonant waveguide cavities. Experimental results from several manufactured prototypes employing this method has resulted in good agreement with the simulation outcomes. Also, a new technique for an indirect identification of the axion mode has been created utilising metallic pins that perturb the EM fields and shifts the frequency of the some configuration mode resonances.

Finally, the last two sections show the studies carried out in the RADES team for the implementation of various tuning systems (both mechanical and electrical) and input / output coupling readjustment arrangement. In the case of the coupling system, a first prototype based on wedge and spring mechanisms has been developed, firstly in simulation and later in fabrication, obtaining a preliminary module for the adjustment of the coaxial antenna depth and, therefore, accomplishing the $\beta = 1$ or critically coupled condition in any haloscope.

<div style="text-align: right; font-size: 4em; color: gray;">4</div>

FERROELECTRIC ELEMENTS IN AXION DETECTORS

As explained in previous sections, during this PhD thesis ferroelectric elements have been used to improve the RADES team axion detectors. In 2018, Euclid Techlabs [133] suggested using a ferroelectric tuning system for axion searches in the RADES, and ADMX groups. Euclid proposed using $KTaO_3$ as a tuning component, a ferroelectric crystal with exceptional tuning parameters and a very low loss tangent ($\tan\delta \simeq 10^{-5}$ at X-band frequencies), compared to other alternatives at cryogenic temperatures, like the standard $SrTiO_3$ element [127]. Euclid Techlabs used electromagnetic simulations to investigate the KTO permittivity value and its fluctuation within a 8 GHz test cavity. Euclid is currently working on producing a first structure of the test cavity loaded with ferroelectric materials, as well as characterising a small test cavity in the $2 - 10$ K range, for experimentally verifying the expected value of the permittivity, the tuning range, and loss tangent.

The ferroelectric elements are dielectrics with a non-linear behaviour and a great ε_r value. They are commonly used in electroacoustic transducers, decoupling capacitors, and microelectromechanical systems [122]. The relative permittivity of these ferroelectrics is modified with a DC voltage or by a the temperature change, a key feature that makes them good options for microwave components (like varactors, RF filters with tuning, phase shifters, and so on).

Firstly, novel electrical tuning mechanisms for axion dark matter detection addressed in the RADES project are offered in this PhD thesis. Unlike mechanical tuning, the tuning systems based on electrical elements can create a design that is not as vulnerable to mechanical failures (for instance, by avoiding moveable components, which could be a problem at cryogenic temperatures) and so complements and enhances current procedures. For multicavities, these systems have also the ability to rectify the resonant frequency of the subcavities and, at the same time, the window iris coupling (k) value. This is very important since it allows the preservation of a right modal structure and its associated E-field pattern (improving also the form factor C). Moreover, for haloscope designs working at different frequency bands (for instance, from X-band to Ku-band), the tuning systems based on mechanical movements do not scale well due to the manufacturing tolerances. This problem might be overcome by the electrical tuning systems presented. If metallic rods are employed for tuning, for example, they must be larger or smaller

depending on the cavity size (or resonant frequency), and the motors / piezoactuators that provide mechanical motion must deal with several weight levels. Furthermore, these mechanical systems become significantly tiny at very high frequencies, requiring smaller manufacturing tolerances. This work is simplified by the method suggested in this PhD thesis, which requires simply films, which may be bigger or smaller depending on the cavity dimensions, and a variable DC biasing or temperature. In addition, ferroelectric tuning systems may provide a simple and reliable supplementary way of fine tuning to mechanical tuning systems for future multicavities operating at high frequencies.

For the implementation of an electrical tuning system in the RADES haloscopes, as it is introduced in subsection 3.3.2, various tuning technologies, including dielectrics, ferromagnetics, ferroelectrics, liquid crystals, piezoelectrics, and so on [74], have been explored. The ADMX team has also been investigating superfluid helium injection into a cavity as a tuning technique [134]. As it is the case of the ferroelectric elements, this method is based on altering the permittivity of the cavity medium and therefore adjusting the frequency of the axion mode. This approach has been demonstrated to be effective at cryogenic temperatures [135]. Yet, due to the extreme conditions imposed on an axion detection system (temperatures around mK, high B_e value, minimal losses, etcetera), the ferroelectric materials, which might work in this environment, appeared to be the most promising. The first idea was to take advantage of the permittivity dependence with the bias DC voltage or temperature, developing a system where the haloscope cavity or multicavity is loaded with ferroelectric films to cause a frequency shift.

As a first order approximation, the equation 2.17 (TE_{101} mode resonant frequency) may be used for a scenario where a rectangular cavity is completely filled with a dielectric element. As can be observed, this frequency is inversely proportional to the relative permittivity with the square root ($f_{mnl} \propto \frac{1}{\sqrt{\varepsilon_r}}$), therefore for a smaller frequency of the haloscope, a greater ε_r is required. This fluctuation in permittivity affects the distribution of the EM fields inside the cavity, which is the event used in this study for tuning. This impact is investigated in section 4.1.

Because of the great variation in permittivity given by ferroelectric films, the second notion investigated in this study is their application as interresonator coupling components in multicavity haloscopes. As it has been seen in previous chapters, rectangular waveguide multicavities employing iris window couplings have been utilised in the past for the designing of haloscopes in the RADES team [68]. Inductive or capacitive windows can be used to obtain an interresonator coupling between subcavities (see Figure 2.11), as it is explained in section 2.4.2. This also defines the sign of the coupling k [74, 136].

Consequently, the degree of coupling between neighbouring subcavities is controlled by the iris dimensions. Because this interresonator coupling is primarily employed to improve mode clustering at axion mode frequency, a suitable coupling component should

be capable of successfully controlling the value and sign of k.

The iris windows are prone to fabrication issues, particularly when both kinds (inductive and capacitive) are used in a multicavity of $N > 3$ subcavities [80]. In this scenario, the manufacturing necessitates 3D machining procedures with more than one cutting plan. Due to the low values in the Q_0 parameter of the manufactured structures it was deduced in prior RADES investigations that there are poor contacts between metallic surfaces at these prototypes, and hence a significant decrease in the flow of surface currents because of these cutting planes. The employment of ferroelectric materials provides an excellent solution to eliminate these limitations, since positive and negative coupling values may be readily produced using KTO films. This can be accomplished by loading these elements within the constructed rectangular housing avoiding the structure cutting at areas with high levels of surface current.

These novel interresonator couplings, on the other hand, allow precise adjustment of k, which could be interesting for the fixing of errors induced by production discrepancies (tolerances) and film misalignment within the rectangular cavity, due to the capability to modify the permittivity. This gives a competent adjustment system for the mode separation.

In section 4.1, the fundamental features of ferroelectrics are firstly discussed. Later, the innovative methods to employ these films as tuning components in single cavities or multicavities, to address concerns such as the restricted tuning range mentioned in [125, 126], are reviewed. The use of ferroelectrics as interresonator coupling elements is investigated in section 4.2 for the creation of reconfigurable single cavities and multicavities, regulating the mode separation. In section 4.3, some practical aspects for accurate ferroelectric biasing are commented. In section 4.4, different methods for the characterization of the future acquired KTO crystals are examined. Lastly, in section 4.5, the PhD thesis findings about the ferroelectric topics and its future lines are exposed.

4.1 THE KTO FERROELECTRIC AS A TUNING ELEMENT

As mentioned in section 3.3.2.1, there are a multitude of ferroelectric materials, but the most employed, working at room temperature, is the BST element [123, 124]. The ADMX-Fermilab team studied the ferroelectric STO previously for tuning purposes at cryogenic temperatures [71]. The Fermilab project [125, 126] centred on harnessing the new electrical features of nonlinear dielectric materials (using the STO) to create electronically adjustable detectors for axion dark matter studies. Many thick-film STO elements were created and evaluated on quartz and sapphire substrates employing various film deposition processes by this collaboration. The frequency tuning (and the ε_r variation) was not as good as foreseen, according to [125, 126]. ADMX obtained a tuning range lower than 0.1% (much smaller than the ones in haloscope utilising mechanical tuning systems, $> 1\%$ [97, 117,

118]), and the losses resulted in a decrease of more than 90 % in Q_0. In this sense, this PhD thesis proposes a new technique of employing electronic tuning systems by the use of ferroelectric elements.

According to [137], the KTO crystal is an emerging ferroelectric device with features comparable to STO and Calcium Titanate or $CaTiO_3$ (CTO). Although KTO and STO have many affinities, the first one retains its cubic shape at extremely low temperatures by simply lowering its losses ($\tan \delta$) between $T = 300$ and 5 K, but the STO crystal does not [127, 137]. Because of the smaller losses, KTO single crystals are appealing for the design of microwave tuning devices working at cryogenic temperatures.

It is worth noting that KTOs have not been well investigated below 4 K [127]. The microwave dielectric characteristics of KTO materials with high purity were evaluated in [127] at $T = 4$ K using a cylindrical film acting as dielectric resonator and working with the TE_{0n1} and quasi-TE_{011} modes. At cryogenic temperatures, the $KTaO_3$ does not experience a phase change like the $SrTiO_3$ ferroelectric. KTO stays with a paraelectric behaviour down to 5.4 K, confirming theoretical expectations. A decrease of the $\tan \delta$ parameter was demonstrated in [127] at temperatures from 300 to 4 K throughout the frequency range of 1 to 10 GHz. In [127], the characteristics (loss tangent and dielectric constant) of the ferroelectric KTO, composed by the materials Ta_2O_5 (99.993 % pure) and K_2CO_3 (99.999 % pure), were calculated at 5 GHz and at cryogenic temperatures. These analysis gave values around $\tan \delta \approx 10^{-4}$ and $\varepsilon_r \approx 4500$. In addition, a study of the KTO tuning range is described [138]. At temperatures between 4 and ~ 10 K, the ε_r value grows to roughly 4500 at zero bias, but saturates for $T < 4$ K, according to [127].

In conclusion, at cryogenic temperatures, the KTO ferroelectrics may enable the construction of an electrical tuning system based on extremely low losses. Commercially accessible KTO elements of 99.99 % purity can be found in [139].

4.1.1 *Rectangular haloscope tuning with ferroelectrics*

The approaches for using KTO materials as tuning elements in resonant cavities (for rectangular geometries) are now explained, considering the characteristics of these dielectrics, described in the previous section. The initial stage in this process is to determine the appropriate position of KTO films (with specific shape) within the resonant cavity for giving a reasonable frequency tuning range while minimising the influence on other parameters (form and unloaded quality factors). To avoid a significant density of EM field within and around the KTO, the ideal ferroelectric position must be searched. This work is extremely difficult because of the enormous value of the KTO dielectric constant, particularly at cryogenic temperatures. If a dielectric pill with a high ε_r value is placed at the bottom centre of a single cavity (as depicts Figure 4.1a), for instance, the E-field lines are curved and acquire a tendency to be centralized in the surroundings of the dielectric

for great relative permittivity values ($\varepsilon_r = 50$, for this example), as shown in Figures 4.1b and 4.1c. This is represented as a dielectric resonator, and it has been widely explored in

(a)

(b)

(c)
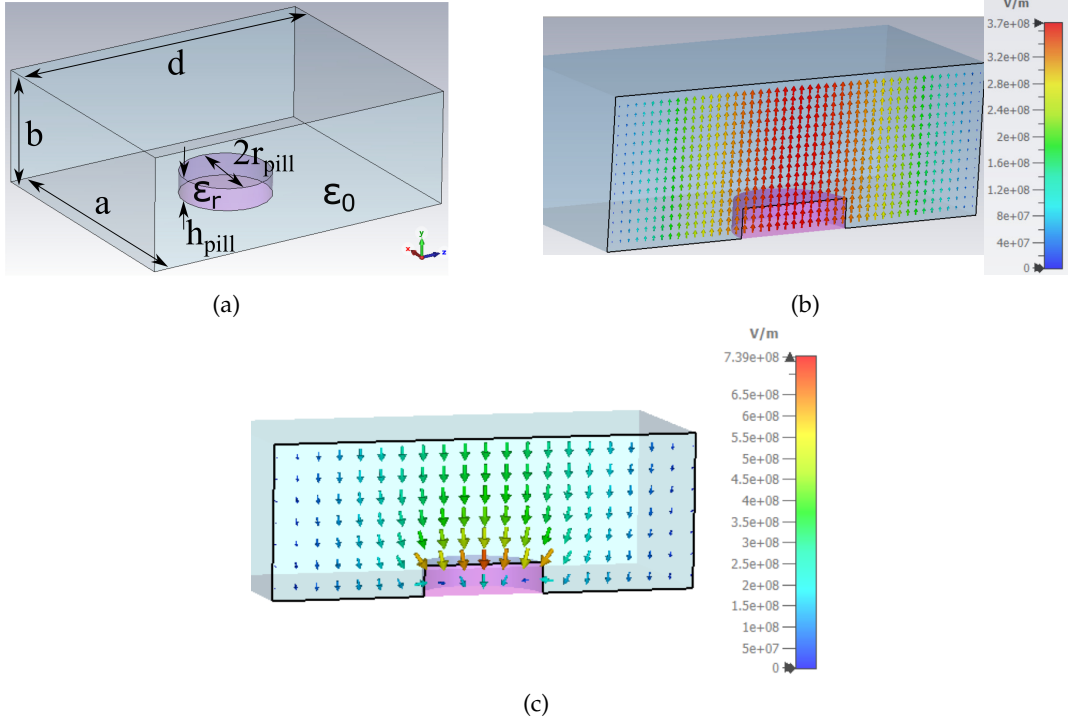
Figure 4.1: Rectangular single cavity with a high permittivity dielectric pill at the bottom centre: (a) 3D model, (b) vertical cutting plane for the visualisation of the E-field at the middle of the cavity for $\varepsilon_r = 1$, and (c) for $\varepsilon_r = 50$. The dielectric pill acts as a dielectric resonator.

the literature of microwave engineering [140, 141]. The resonant frequency, and the Q_0 and C parameters, are provided in Table 4.1 for some ε_r values in this scheme. For $\varepsilon_r = 1$,

ε_r	f_r (GHz)	Q_0	C
1	8.406	4.5×10^4	0.657
2	8.249	4.5×10^4	0.624
5	8.070	4.5×10^4	0.589
10	7.972	4.5×10^4	0.573
20	7.903	4.4×10^4	0.554
30	7.865	4.3×10^4	0.540
40	7.819	4×10^4	0.509
50	7.710	3×10^4	0.386

Table 4.1: Properties of a single cavity (based on the dimensions $a = 22.86$ mm, $b = 10.16$ mm and $d = 28.5$ mm) with a high permittivity dielectric pill (based on the dimensions $r_{pill} = 4$ mm and $h_{pill} = 2$ mm) placed at the center bottom for several ε_r values. This dielectric pill is lossless. For the metallic housing of the cavity, it is assumed an electric conductivity of copper at cryogenic temperatures (this is, $\sigma_{Cu}^{2K} = 2 \times 10^9$ S/m).

the form factor is equivalent to the $C_{TE_{101}}$ value for the unloaded cavity (this is, $C = 0.657$), which may be calculated from 2.6. Regardless of the good frequency tuning obtained for $\varepsilon_r = 50$, the unloaded quality factor and the form factor values are drastically reduced. These outcomes unequivocally show that this dielectric location and form must be ruled

out for the KTO case, since it has remarkably high ε_r values in practise (near $\varepsilon_r = 4500$).

After multitude of manual optimizations simulating different dielectric forms and locations within the resonant cavity (see some of these cases in Figure 4.2), it was obtained a tuning system concept based on thin ($l_d \simeq 500$ μm, where l_d is the KTO thickness) ferroelectric materials positioned near the housing walls (see Figure 4.3a) that gave excellent outcomes in the Q_0 and C parameters, and in the frequency tuning range.
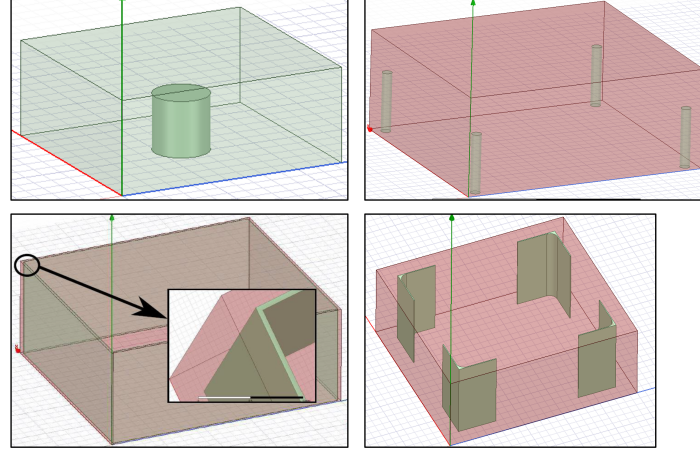
Figure 4.2: Geometrical forms and placements investigated for the KTO as tuning system. These designs produce sub-optimal results in the unloaded quality and form factors, plus low tuning ranges, and have been ruled out as feasible options for tuning in haloscopes.

(a)   (b)
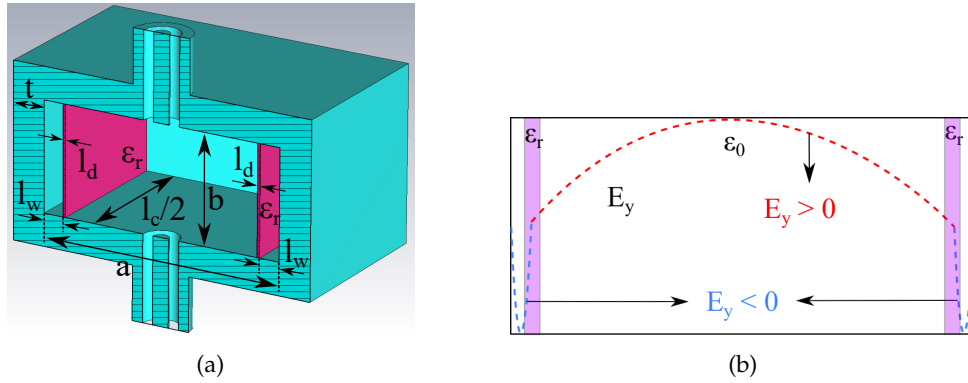
Figure 4.3: (a) 3D model of a KTO-loaded single cavity employing two ports (input and output coupling) of SMA coaxial type. The image depicts the symmetric half, where the dashed area is the plane of symmetry. The ferroelectric films (KTOs) are shown in pink colour. l_c is the cavity length, which can be adapted for working at the desired frequency. l_w is the length of the space between the KTOs and the cavity walls. t is the housing thickness. (b) Transverse plane picture of the E-field (vertical component, E_y) for the *modified-TE$_{301}$* mode at f_0 (the resonant frequency of the cavity for such mode). The E-field end lobes (blue dashed lines) are within the ferroelectrics. The E_y value is positive at the inner area (red dashed lines) and negative at the KTO (and beyond them). Because of the high narrowing of lateral lobes at the ferroelectric films, the *modified-TE$_{301}$* mode is quite similar to the initial TE_{101} mode for an unloaded cavity with rectangular geometry.

Because a numerical determination of a transverse resonance equation is required to analyse a structure comprising a rectangular waveguide section partly loaded [69], the

analytical computation in this cavity is not simple. Alternatively, it was realised the design on the frequency domain employing CST [78]. Another concern encountered in the structure design is the great cost of computation required for the simulations because of the existence of models with extremely high ε_r values, which necessitates the use of a large number of mesh tetrahedrons for obtaining a right numerical precision. This limitation was overcome by employing adaptive meshing in the EM simulations and making use of electrically extremely thin ferroelectric sheets. The structure was also simulated using *FEST3D* [78], a software that applies an integral equation methodology that is competently solved using the Method of Moments (MoM) and BI-RME. Then, the numerical findings achieved in the various haloscope designs with the ferroelectric system are validated by employing these two full-wave EM simulators.

The basic concept for designing this type of system is to begin with the TE_{301} mode, which is disturbed by the high dielectric constant value of the KTO to resemble the TE_{101} mode, so rising up the form factor value. This principle is depicted in Figure 4.3b. The novel mode obtained by this method is known as the *modified-TE$_{301}$* mode. In this mode, two of the three E-field lobes along the cross section of the cavity are quite confined because of the great dielectric constant value of the ferroelectrics (depicted by the blue dashed curves in Figure 4.3b), while the E-field variation at the center is expanded in the vacuum area (shown by red dashed curves in Figure 4.3b). To do this, the KTO thickness should be similar the half of the guided wavelength, which is the distance between two zeros of the pattern of a transverse standing wave, computed as [69]:

$$l_d = \frac{\lambda_g^{KTO}}{2} = \frac{\lambda_0}{2\sqrt{\varepsilon_r}\sqrt{1 - (f_c^{KTO}/f_0)^2}} = \frac{c}{2f_0\sqrt{\varepsilon_r}\sqrt{1 - (f_c^{KTO}/f_0)^2}}, \qquad (4.1)$$

being λ_g^{KTO} the KTO guided wavelength, λ_0 the wavelength at vacuum (which can be calculated as $\lambda_0 = c/f_0$), f_c^{KTO} the KTO TE_{10} cut-off frequency (which can be calculated as $f_c^{KTO} = c/(2l_c\sqrt{\varepsilon_r})$), and f_0 the working frequency. In general, the width of the cavity (a) is in the f_c denominator. In this example, nevertheless, it is utilised l_c (the length of the cavity) since an analysis of the transverse resonance expression is carried out for setting the $x-$axis as the propagation orientation of the EM TE_{10} wave (and hence model the pattern of the standing wave).

As it will be demonstrated in the following subsection, changing the ε_r of the ferroelectric KTO efficiently changes the location of the *modified-TE$_{301}$* lateral lobes, offering a decent frequency tuning range. In the meanwhile, it prevents the form factor from decreasing because of the small area of the negative lobes in the E_y (blue dashed curve in Figure 4.3b).

In this PhD thesis, it is assumed a permittivity in the range $\varepsilon_r \in [3000, 5000]$. This technique, nevertheless, is adaptable to any other condition that may be advantageous if production tolerances of the ferroelectric films result in a distinct practical range. Additionally, as it is stated previously in this chapter, the losses of the KTO are $\tan \delta = 10^{-5}$;

however, in the simulations for the ferroelectric investigations, $\tan \delta = 10^{-4}$ is chosen to be more cautious and considering potential extra losses in manufactured structures. A value of $\sigma = 2 \times 10^9$ S/m is used for the cavity conductivity (copper at cryogenic temperatures). It yields a Q_0 value of about 4×10^4 for a single cavity (as it was presented in the previous chapter, in Table 3.2).

4.1.2 *Results for a single cavity with KTO at sides*

It has been optimised, as an example, at the operation frequency $f_0 = 8.5$ GHz the model from Figure 4.3a. Employing equation 4.1, this results in a KTO thickness ranging from $l_d = 250\,\mu$m (with $\varepsilon_r = 5000$) to $l_d = 322\,\mu$m (with $\varepsilon_r = 3000$), as preliminary values. l_c, on the other hand, is adjusted to resonate at 8.5 GHz (for the TE_{101} mode), in a cavity without ferroelectrics, which gives the dimensions $l_c = 26.97$ mm, $a = 22.86$ mm and $b = 10.16$ mm.

To pick the optimal film thickness (this is l_d) and KTO separation from the cavity walls (this is l_w), an optimization technique is used, which involves gently altering the values of l_d and l_w (observe Figure 4.3) to obtain the maximum range of frequency tuning with good values in the Q_0 and C parameters. The examined parameters for the design of a haloscope are β, V, C, and Q_0, as mentioned previously. With equation 2.14 and assuming that β and V remain constant throughout the design, a handy figure of merit is $FM = Q_0\,C^2$. After an optimization procedure maximising FM (similarly to the cases in [80]) and frequency tuning range, an ideal design with $l_d = 235\,\mu$m, and $l_w = 1.88$ mm is achieved. The frequency tuning range, Q_0 parameter, C parameter, and FM parameter for this setup are presented in Figure 4.4. With these settings, a frequency tuning range of 700 MHz (7.2 %) is accomplished with an essentially constant $C = 0.52$ value for the whole tuning range and $Q_0 \in [10^4, 5.5 \times 10^4]$ (observe Figure 4.4).

From the outcomes shown in Figures 4.4a and 4.4b, the plot shown in Figure 4.5 can be derived, which illustrates the frequency dependence of Q_0 (lower unloaded quality factor values at higher frequencies).

If the Q_0 decrease is unacceptable, the structure may be designed with a lower ε_r range: $\varepsilon_r \in [3000, 4200]$, for example, which presents a tuning of 2.23 % (216 MHz) and $Q_0 > 2.1 \times 10^4$ (good results for an efficient axion detection at these frequencies [80]).

4.1.3 *Results for a multicavity with KTO at sides*

Using this ferroelectric approach, a haloscope consisted of four subcavities connected by inductive windows was designed using the standard WR-90 (observe Figure 4.6a). In this example, it was used a ferroelectric film thickness of $l_d = 250\,\mu$m and a KTO separation from the cavity walls of $l_w = 1.5$ mm, at all the subcavities. These values were acquired using an optimization approach based on increasing FM and the tuning range, similarly
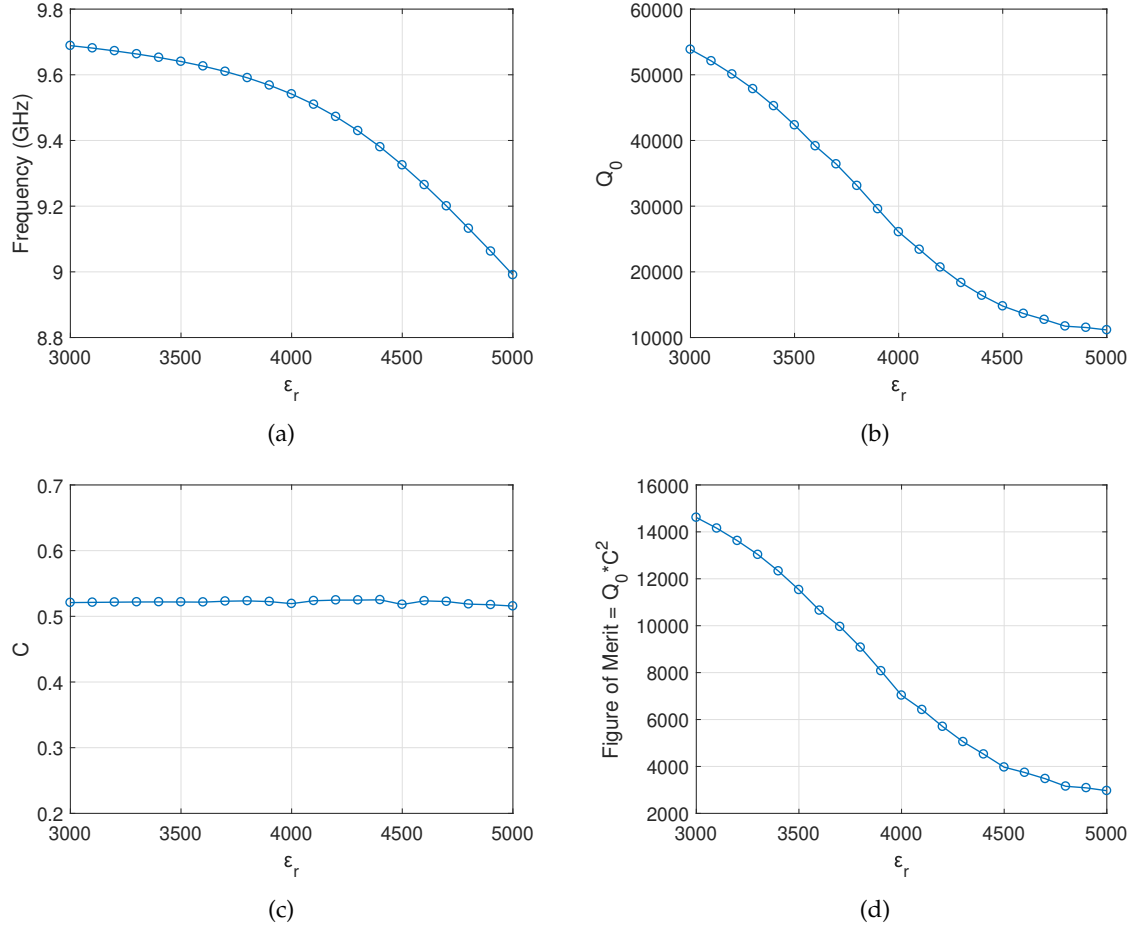
Figure 4.4: Characteristics of the design from Figure 4.3 versus ε_r with $\tan\delta = 10^{-4}$. (a) Tuning frequency range. (b) Quality factor parameter. (c) Form factor parameter. (d) *FM* parameter.

to the previous case with a single cavity. The responses achieved for two distinct levels of ε_r (3000 and 3600) are depicted in Figure 4.6b. Our findings reveal that the resonance frequency has been shifted by 37 MHz (0.4 %), laying the groundwork for demonstrating that this method may be utilised to create efficient tunable haloscopes employing the multicavity concept.

It was found parameter ranges $Q_0 \in [3.8 \times 10^4, 4.6 \times 10^4]$ and $C \in [0.49, 0.509]$ for the permittivity range $\varepsilon_r \in [3000, 3600]$. It should be noted that these values offer a *FM* of the same order of magnitude in the single cavity, as demonstrated in the previous subsection. Moreover, because of the limited volume of the ferroelectric films, expanding the ε_r value has no effect on the form factor.

Lastly, the patterns of the E-field with $\varepsilon_r = 3000$ for both the single cavity and multicavity cases are depicted in Figures 4.7a and 4.7b, respectively. A significant colour scale has been used in these pictures to properly comprehend the negative E-field in the ferroelectric region. Small values of E-field would be noticed at the surroundings of the inductive window irises if this scaling was not there, suggesting that this is the right mode. As can
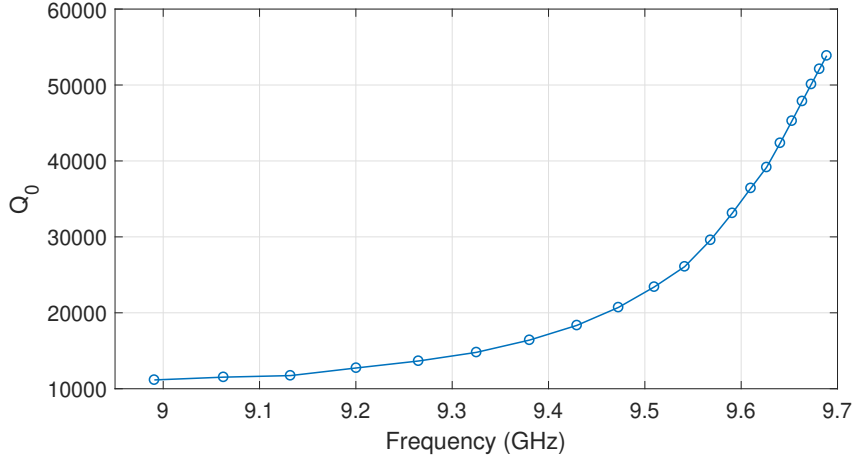
Figure 4.5: Unloaded quality factor versus frequency for the structure from Figure 4.3.

(a)

(b)
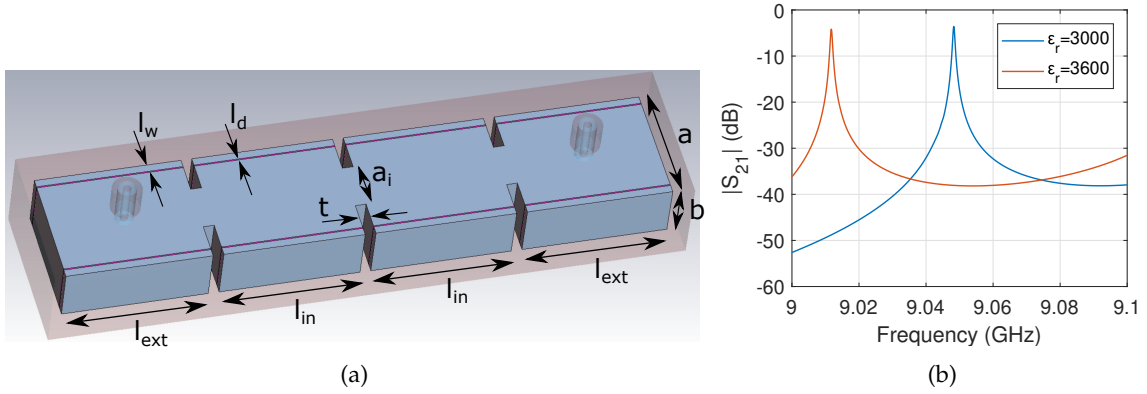
Figure 4.6: (a) All-inductive multicavity with $N = 4$ subcavities loaded with KTO ferroelectric films at the subcavity sides. (b) magnitude of the S_{21} parameter versus frequency for $\varepsilon_r = 3000$ and 3600. The dimensions of the multicavity are $a = 22.86$ mm and $b = 10.16$ mm, $l_{ext} = 26.97$ mm, $l_{in} = 26$ mm, $t = 2$ mm, and $a_i = 9$ mm.

be observed, the axion corresponds in both situations with the *modified-TE$_{301}$* mode. The primary E-field variation (the positive E_y value or red color in Figure 4.7c) is more condensed at the KTO films at higher ε_r values. This minor modification in the E-field causes the desired frequency shift, resulting in a tuning in the search frequency for the axion.

4.2 THE KTO FERROELECTRIC AS AN INTERRESONATOR COUPLING ELEMENT

At the present subsection, it will be seen how KTO films may be employed as interresonator coupling components in a multicavity, replacing the iris windows (see Figure 2.11). As it was previously explained in the previous chapter in section 3.2.1, iris windows frequently generate quality challenges in production because of manufacturing tolerances and cuts on planes with high values of the surface current in the axion mode. This results in misalignment problems and low Q_0's in some circumstances. With the usage of KTO films, just a single cut (on a low surface current plane) is required for producing the multicavity
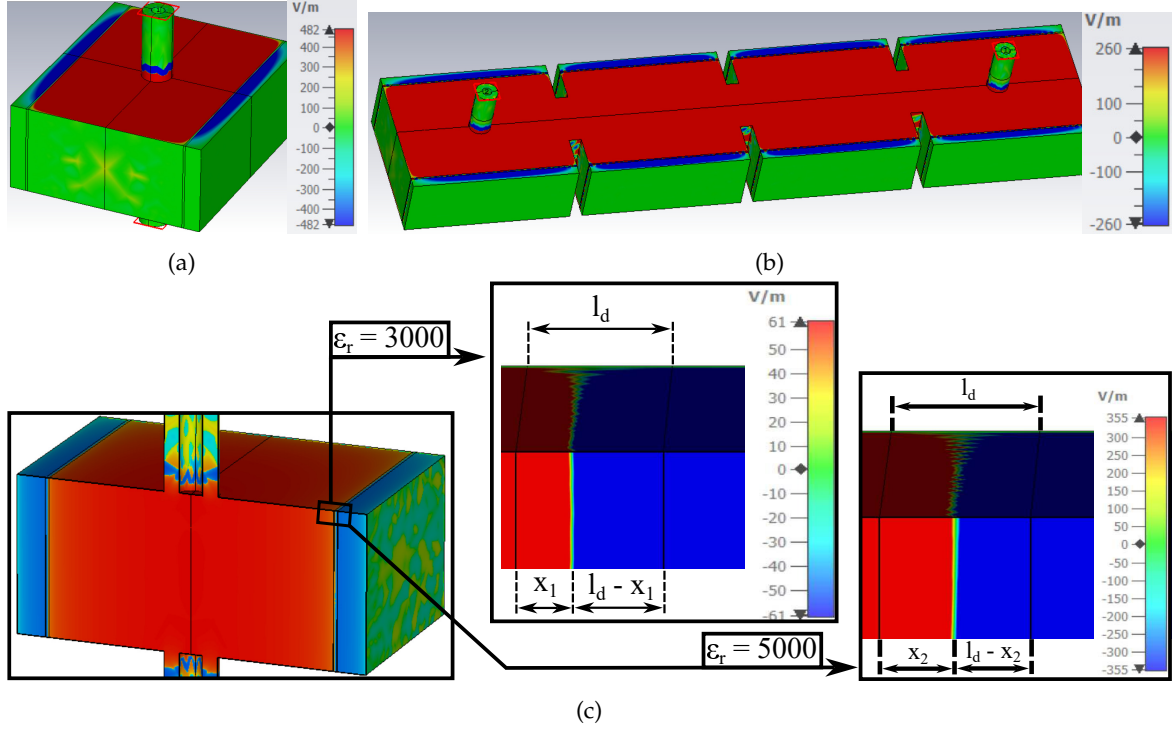
Figure 4.7: Vertical component of the E-field with $\varepsilon_r = 3000$ at designs of (a) single cavity, and (b) multicavity. (c) Zoom of the KTO region to see the zero transition of the *modified-TE$_{301}$* E-field inside the single cavity design (a) employing a transversal cut at the middle of the resonant cavity for the cases $\varepsilon_r = 3000$ and $\varepsilon_r = 5000$. It is satisfied that $x_1 < x_2$, being x_1 and x_2 the widths of the positive regions of the electric field within the ferroelectrics with $\varepsilon_r = 3000$ and $\varepsilon_r = 5000$, respectively.

housing. Therefore, with this setup, the idea would be to introduce thin slits to position the ferroelectric films within this housing.

4.2.1 *Modelling*

The setup utilised to investigate the impact of KTO films as interresonator couplings in cavities with rectangular geometry is depicted in Figure 4.8. It is made up of two types of waveguide sections: two sections of vacuum at the ends with l_{port} (the distance from the port reference plane to the KTO location) and one section of KTO at the middle with l_d. In this case, for analysing this model more easily, ports of waveguide type are utilised (instead of coaxial type).

To evaluate this setup, a basic transmission line representation based on single-mode (observe the first circuit from Figure 4.9) may be created. The transmission lines *(1)* and *(3)* represent the vacuum section from Figure 4.8, and the transmission line *(2)* the ferroelectric. For all the transmission lines, the characteristic impedance (Z_0 for the vacuum section and
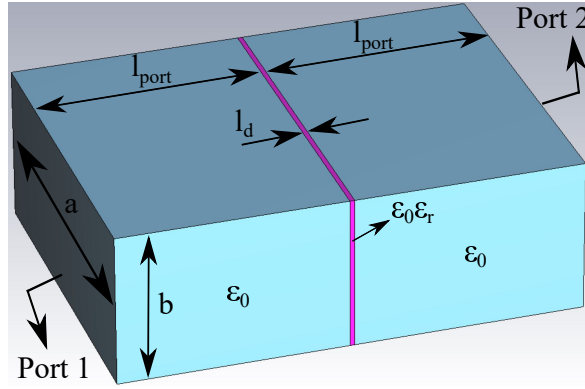
Figure 4.8: Modelling of a KTO film as an interresonator coupling component. This setup is composed by three sections: a first section of vacuum (this is $\varepsilon = \varepsilon_0$), a second section filled with the ferroelectric film (this is $\varepsilon = \varepsilon_0\,\varepsilon_r$), and a third section of vacuum. The waveguide is based on the standard WR-90. l_d, the KTO length, and ε_r, the permittivity of the KTO, control the coupling level. On the other hand, l_{port} is the length from the port reference plane to the ferroelectric.

Z_d for the KTO section) is the fundamental mode (TE_{10}) impedance, which depends on the permittivity medium, computed as [69]:

$$Z_i = Z_{i,TE_{10}} = \frac{2\,\pi\,f\,\mu_0}{\beta_i} = \frac{\eta/\sqrt{\varepsilon_{ri}}}{\sqrt{1 - (f_{ci}/f_0)^2}}, \tag{4.2}$$

being β_i the fundamental mode propagation constant at each section (i), $f_{ci} = c/(2\,a\sqrt{\varepsilon_{ri}})$ the cut-off frequency of the fundamental mode (the TE_{10} mode) at each section (i), $\eta = \sqrt{\mu_0/\varepsilon_0} \simeq 120\pi\,\Omega$ the impedance at free space, and ε_{ri} the relative permittivity at each section (i). β_i can be represented as $\beta_i = (2\pi)/\lambda_{gi}$, where $i = d$ for the transmission line *(2)*, and $i = 0$ for the transmission lines *(1)* and *(3)*.

A significant impedance step between the KTO and vacuum sections emerges because of the great ε_r deviation between both mediums. When the length of the transmission line *(2)* is near to $l_d = \lambda_{gKTO}/2$, it functions as a resonator [69]. This condition may be modelled by a parallel resonator with lumped LC elements, as illustrated in the second scheme from Figure 4.9. This parallel LC system resonates at $f_{KTO} = \frac{1}{2\pi\sqrt{LC}}$, being L the inductance value and C the capacitance value.

For frequencies with $f < f_{KTO}$, the inductor admittance ($Y_L = \frac{1}{j2\pi fL}$) is greater than the capacitor one ($Y_C = j2\pi fC$), resulting in inductive behaviour. The admittance is the inverse of the impedance (this is, $Y = 1/Z$) and it is commonly used in parallel circuit analysis. In reality, at these frequency values, the current flows mostly through the L element. As a result, the ferroelectric functions as an inductive coupling, as seen in the third scheme from Figure 4.9. On the other hand, at $f > f_{KTO}$, the KTO operates as a capacitive coupling (observe fourth scheme from Figure 4.9). Yet, the ε_r value of the ferroelectric film may be exploited to simply adjust f_{KTO}, the KTO resonant frequency. This allows to easily modify the frequency ranges where the KTO functions as inductive or
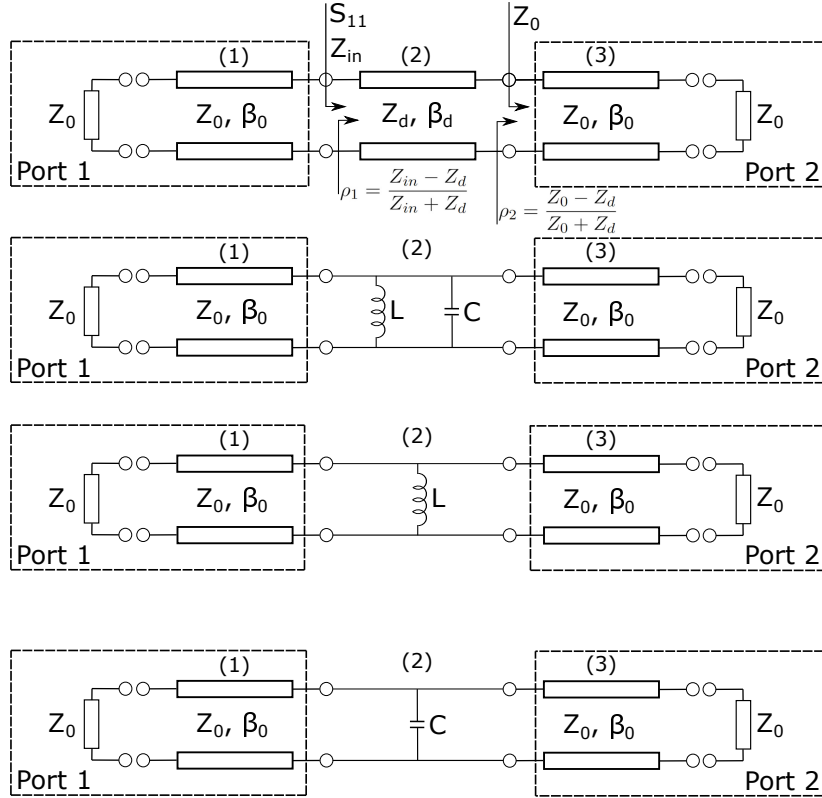
Figure 4.9: Single-mode transmission line model for analysing the structure from Figure 4.8. Circuit from top to bottom: three transmission lines, replacing the central transmission line with a LC resonator, replacing the central transmission line with an inductor (KTO acting as inductive coupling), and replacing the central transmission line with a capacitor (KTO acting as capacitive coupling).

capacitive coupling. More details will be exposed in the next subsection, designing a KTO film to work as a coupling component.

It has been defined the behaviour of the model of Figure 4.8 by examining the first scheme from Figure 4.9. In this circuit, the scattering parameters may be computed by:

$$S_{11} = \frac{Z_{in} - Z_0}{Z_{in} + Z_0},$$ (4.3)

$$S_{21} = \frac{(1 + S_{11})(1 + \rho_2)e^{-j\beta_d l_d}}{1 + \rho_1},$$ (4.4)

being S_{11} the reflection scattering parameter, S_{21} the transmission scattering parameter, Z_{in} the impedance at the input, Z_0 the characteristic impedance of the transmission lines *(1)* and *(3)* (the vacuum sections), ρ_2 the reflection coefficient of the transmission line *(3)* referred to the transmission line *(2)* (the ferroelectric section), $j \equiv \sqrt{-1}$ the imaginary unit, β_d the propagation vector (longitudinal part) in the transmission line *(2)*, and ρ_1 the input reflection coefficient referred to the transmission line *(2)*. The propagation vector can be

defined as $\beta_d = (2\pi)/\lambda_{gd}$. λ_{gd} can be calculated with 4.1 employing the ferroelectric cut-off frequency as $f_c^{KTO} = c/(2a\sqrt{\varepsilon_r})$. The theory of transmission lines can be employed to compute Z_{in} by:

$$Z_{in} = Z_d \frac{Z_0 + j Z_d \tan(\beta_d l_d)}{Z_d + j Z_0 \tan(\beta_d l_d)}. \tag{4.5}$$

4.2.2 *Results for a multicavity with KTO as an interresonator coupling element*

Applying the equations from the previous subsection and using $\varepsilon_r = 4000$ and $l_d = \lambda_g/2 = 279\,\mu m$ for obtaining $f_{KTO} = 8.5$ GHz, for instance, the findings presented in Figure 4.10 are achieved. As previously mentioned, for $f < f_{KTO} = 8.5$ GHz, the KTO
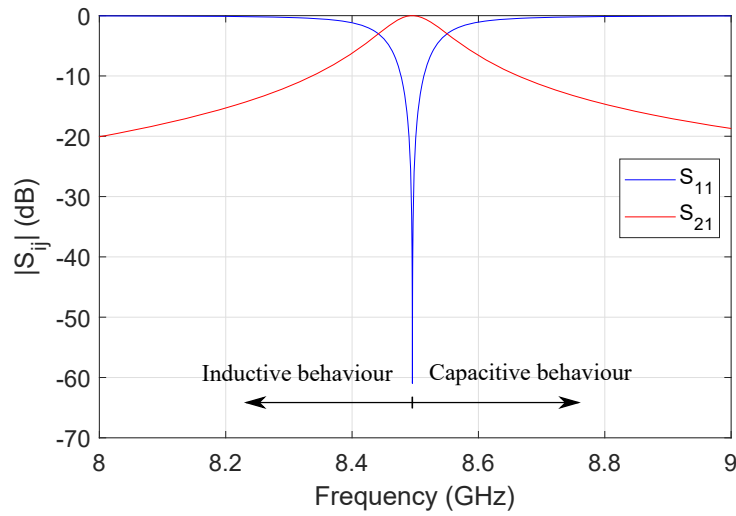
Figure 4.10: $|S_{11}|$ and $|S_{21}|$ versus frequency for the model from Figure 4.8, obtained employing 4.3 and 4.4. For $f < f_{KTO}$, the ferroelectric acts as inductive coupling, and for $f > f_{KTO}$ it behaves as capacitive coupling.

coupling is of inductive type, while for $f > f_{KTO} = 8.5$ GHz, it is capacitive. The frequency ranges where the KTO functions as inductive or capacitive coupling may be modified without difficulty by tuning f_{KTO}, which may be readily adjusted by l_d or ε_r.

The physical coupling k value is determined using a model consisting of two subcavities coupled by a single interresonator coupling. In this work, this coupling is provided by the KTO film. The 3D model from Figure 4.11 has been used for this purpose, where the port couplings has been implemented with inductive irises. With this model, k may be calculated as follows [74] (section 14.2.2):

$$k = \frac{f_{even}^2 - f_{odd}^2}{f_{even}^2 + f_{odd}^2}, \tag{4.6}$$

being f_{even} the even (or magnetic) frequency and f_{odd} the odd (or electric) frequency [74].
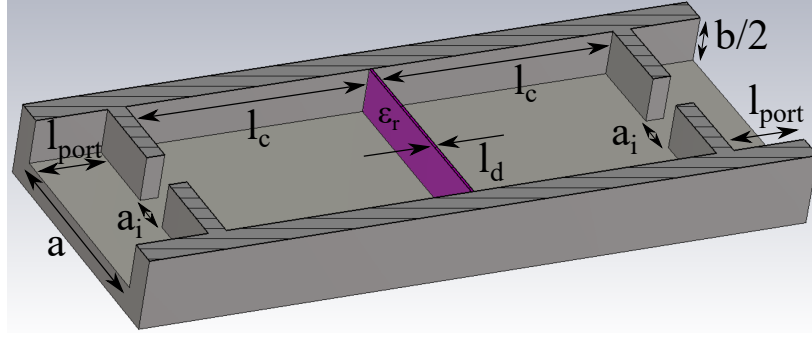
Figure 4.11: 3D model of a $N = 2$ multicavity employing a ferroelectric film KTO as interresonator coupling element. The port coupling sections are conducted by inductive irises. The image depicts the symmetric half, where the dashed area denotes the plane of symmetry. For this prototype, the dimensions are identical to the structure from Figure 4.8, with $l_{port} = 8$ mm. l_c is establish for obtaining $f_0 = 8.42$ GHz, and l_d is adapted to position f_{KTO} above or below f_0 to enforce either inductive or capacitive coupling. a_i is set to 5 mm in order to lower the load effect.

After this, the KTO must be characterised as a coupling component with an operation frequency of $f_0 = 8.42$ GHz. In the first instance, it is calculated the inductive coupling for the KTO. In this scenario, the KTO resonance is set at a frequency greater than 8.42 GHz. A $f_{KTO} = 9.5$ GHz is chosen for this experiment, which translates to a $l_d = 250\,\mu$m with $\varepsilon_r = 4000$. It is supposed that the ferroelectric permittivity takes values between 3000 and 5000. Secondly, $l_d = 316\,\mu$m is chosen for the capacitive coupling case, resulting in a $f_{KTO} = 7.5$ GHz with $\varepsilon_r = 4000$, which is smaller than f_0. Figure 4.12 illustrates the computed coupling values versus ε_r for both types of coupling: inductive and capacitive. The outcomes show that a KTO sheet may operate as a coupling element, with coupling values ranging from near zero to values over $|k| = 0.04$, including the possibility of change the sign. As Figure 4.12 depicts, for the case of the ferroelectric film acting as an inductive coupling the value of $|k|$ increases with permittivity, while for the capacitive case it decreases with ε_r.

For window irises, a common feasible $|k|$ value is 0.02 [80]. To demonstrate the efficiency of the KTO ferroelectric as a coupling element for the this interresonator coupling value, it has been carried out investigations with dielectric films. $|k| = 0.02$ is reached at $\varepsilon_r = 4806$ for the inductive coupling scenario, and at $\varepsilon_r = 3295$ for the capacitive coupling scenario, as shown in Figure 4.12.

With the alternation of high and low ε_r values, the alternating 6-subcavities haloscope from the RADES team (see Figure 2.17a) may be created replacing the window irises with the KTO films. Alternating interresonator couplings, as stated in the previous chapter, promotes mode separation. Furthermore, in the scenario of manufacturing inaccuracies or if an adjustment of the response is necessary for whatever motive, this system can offer a final correction in the ferroelectrics. This is easily accomplished by altering the ε_r of the films employing the DC voltage mentioned in the following section.
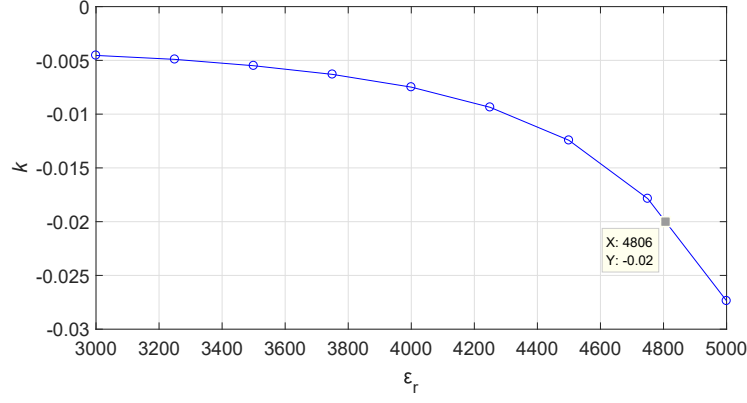
(a)
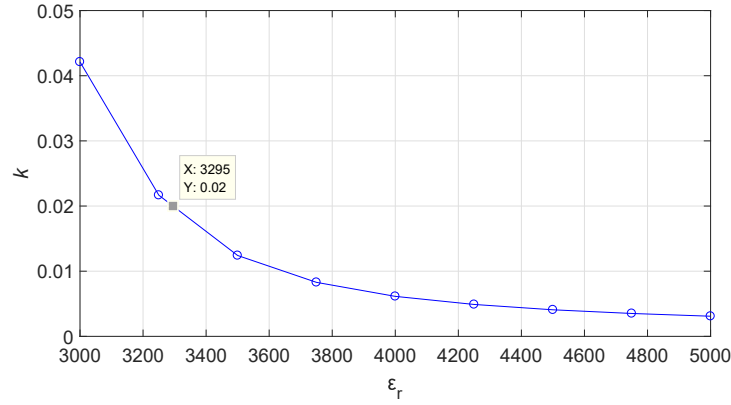
(b)

Figure 4.12: Value of the physical interresonator coupling as a function of the KTO ε_r in the multicavity from Figure 4.11, working at $f_0 = 8.42$ GHz, for two cases: (a) inductive coupling (utilising $l_d = 250\,\mu$m), and (b) capacitive coupling (with $l_d = 316\,\mu$m).

As demonstrated in Figure 4.13a, the preceding case may be utilised to create a more realistic haloscope based on an alternating multicavity with $N = 4$ subcavities and three ferroelectric interresonator couplings (two capacitive and one inductive), making use of ports with coaxial couplings. This strategy improves the mode clustering when compared to an all-inductive or all-capacitive haloscope, as it has been seen in the previous chapter. It must be utilised the acquired KTO thickness and permittivity values, this is $l_d = 316\,\mu$m and $\varepsilon_r = 3295$ for the capacitive case (films with pink color in Figure 4.13a), and $l_d = 250\,\mu$m and $\varepsilon_r = 4806$ for the inductive scenario (film with brown color in Figure 4.13a), for obtaining the mentioned $|k| = 0.02$ value in all the interresonator couplings. In this case, the coaxial antennas are designed to have a low port coupling. The transmission parameter extracted with these ferroelectric films is depicted in Figure 4.13b. Since this prototype is based on alternating couplings, the axion mode is located at the second resonance [80]. In addition, Figure 4.13c displays the axion E-field, being the negative E-field value (depicted in blue color) within the ferroelectric films. It is worth noting that this model has shown to be extremely successful since the E-field is synchronous in all the subcavities, which is essential to optimise the form factor [80]. The resultant mode separation (63 MHz or 0.75 %) and the unloaded quality and form factor

145
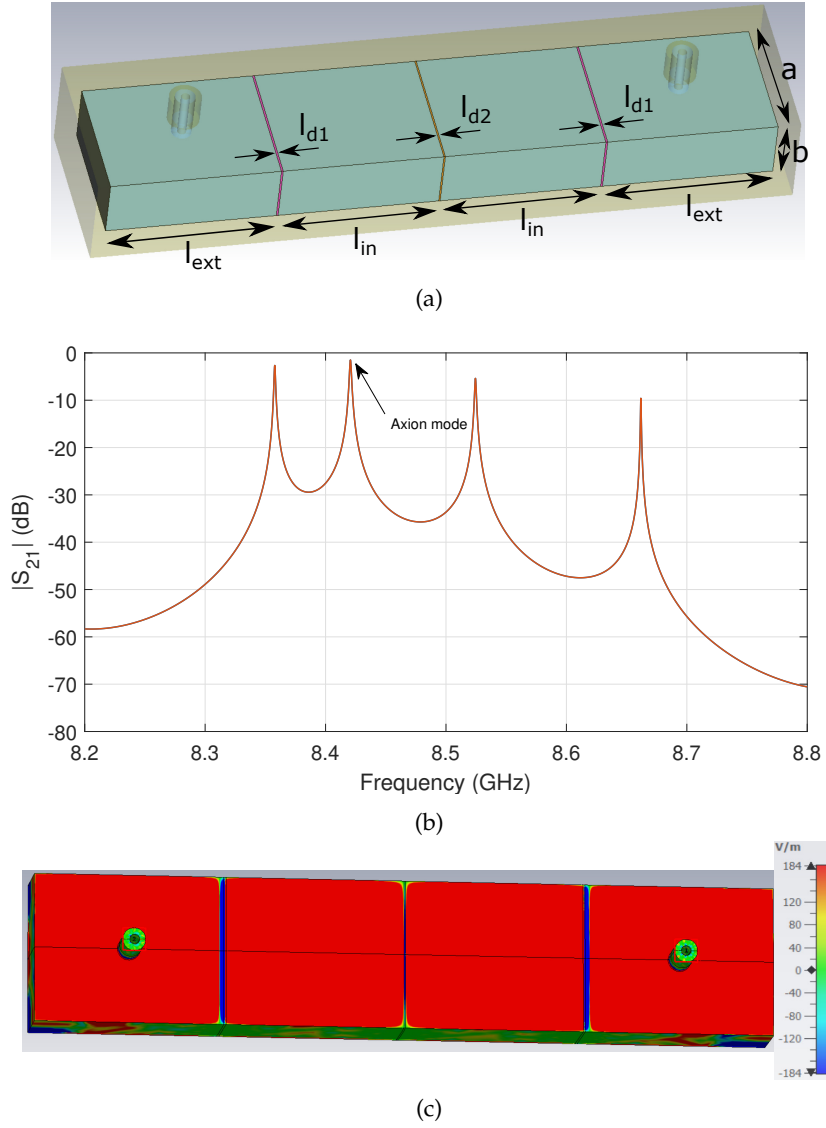
Figure 4.13: Haloscope based on a $N = 4$ multicavity with three KTO couplings (2 capacitive and 1 inductive) and port couplings of coaxial type: (a) 3D model with $a = 22.86$ mm, $b = 10.16$ mm, $l_{ext} = 29.05$ mm, $l_{in} = 27.34$ mm, $l_{d1} = 316\,\mu$m, and $l_{d2} = 250\,\mu$m. (b) Magnitude of the S_{21} parameter. (c) Vertical component of the axion mode E-field (working at the frequency $f_0 = 8.42$ GHz). As it is the case in Figure 4.7b, a high colour scaling has been implemented to appropriately understand the behaviour of the E-field.

values ($Q_0 = 3.2 \times 10^4$ and $C = 0.586$, respectively) are quite excellent (see Figure 4.13b), proving that this idea may be utilised for the construction of haloscopes with the extra flexibility of permitting a simple mix of inductive and capacitive interresonator couplings.

Lastly, using of KTOs as coupling elements eliminates the necessity to fabricate window irises, which induced many quality factor issues in the RADES haloscopes.

146

By providing a DC voltage or changing the temperature, the permittivity of a ferroelectric may be altered. For the voltage case, an asynchronous structure with independent tuning of each KTO film can be constructed. With the temperature choice, however, the entire axion detector will be cooled/warmed, thus all KTO films will have the same permittivity value. For the latter case, various aspects must be considered when designing an alternating multicavity with an electronic tuning based on ferroelectric elements. The most important is to use an appropriate ferroelectric thickness. A longer l_d for the capacitive couplings should be employed, establishing f_{KTO} below the working frequency (observe Figure 4.10). If ε_r diminishes, k will fluctuate, but it will always work within the capacitive zone. In a similar way, for KTO films acting as inductive couplings, l_d should be lower to guarantee that f_{KTO} is considerably high to ensure that k varies within the inductive zone (observe Figure 4.10). If the permittivity of the ferroelectric films is changed by voltage, l_d of all the KTO films may be the same, and the coupling sign could be altered by implementing various voltages to each ferroelectric element.

Because haloscopes must work at the lowest possible temperature, increasing the its value to regulate the ferroelectric permittivity could reduce the performance (the axion-photon conversion sensitivity in this case) of the experiment due to the effect in T_{sys} and Q_0. As a result, the DC voltage appears to be the best approach for changing ε_r.

When applying a DC voltage to these KTO slabs, the location of the electrodes must be cautiously evaluated. To give access to the interior of the cavity for the wires of DC biasing, small perforations in the walls of the haloscope are required. Furthermore, an appropriate notch filter must be developed at the DC voltage stage to minimise significant losses caused by parasitic components implemented by non-desirable frequencies. The electrodes would be placed at the two nearest surfaces evenly over it. Moreover, the cables of the biasing (and its access holes) are placed around the cavity corners, as it is illustrated in Figure 4.14, because the TE_{101} surface current level is minimum on this area.

According to [133], the contacts for the DC voltage biasing and deposition technologies are heavily reliant on the design of the haloscope. For a mode that does not include any E-field components parallel to the ferroelectric film surfaces, the biasing contacts can be formed of either high conductivity or superconducting elements. High conductivity elements can be put on electrodes, and adhesion and thermal expansion matching sheets can be used to assure minimal losses at the biasing stage. As it has been stated, the deposition of a superconducting layer of the electrodes is another option. A resonator was built on 0.5 mm × 10 mm KTO pills with an epitaxially polishing in [122]. Also, the co-evaporation method was employed to deposit superconducting Yttrium Barium Copper Oxide (YBCO) layers [122].
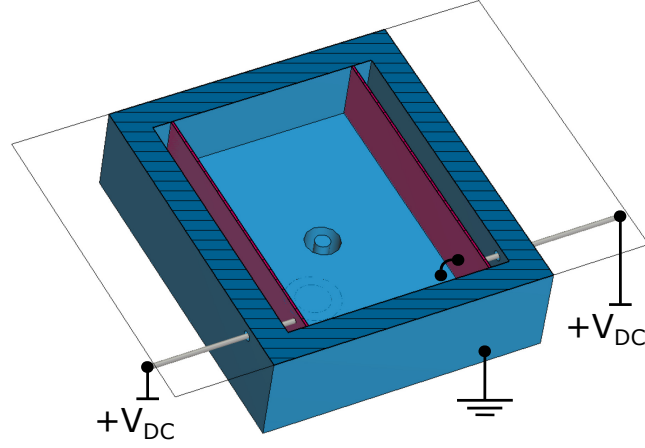
Figure 4.14: Single cavity loaded with two KTO films (pink color) with an horizontal cut for depicting the place of the biasing electrodes. V_{DC} symbolizes the DC voltage implemented to these electrodes. One of the two biasing electrodes in each ferroelectric slab is attached to the housing of the cavity (blue color), operating as ground.

As it has been seen previously, the TE_{101} mode has its field lines parallel to the surface of the biasing contacts. With this, high resistivity contacts can be employed for the biasing to avoid a high Q_0 deterioration. The biasing connections must be placed on the crystal surface in this circumstance. To prevent shorting the cavity, preliminary simulation studies of bias electrodes with high resistivity levels in a cavity without ferroelectric elements have been carried out. The results gave acceptable quality and form factor values using $R_s > 2 \times 10^6 \ \Omega/Sq$, where R_s is the sheet resistance. Although it is difficult to create such a scenario with metallic electrodes, [142] reports several materials that might produce R_s values of 10^9 to $10^{17} \ \Omega/Sq$ with a thickness of 100 nm. These materials would be analysed in a future work.

Lastly, to prevent the insertion of an extra noise source, the DC voltage supply must not emit noise in the frequency range of the haloscope. With proper design and a filter of low-pass type, this noise source may be minimised. It is also critical to ensure that the wires of the DC voltage are properly shielded to bypass the origination of pick-up noise.

4.4 CHARACTERIZATION OF FERROELECTRIC FILMS

Once the KTO material to be used in the designed tuning system has been purchased, it is mandatory to characterise the ferroelectric material, as the characteristics provided by the vendor may vary from one crystal to another, and even more so if the film shapes are modified to obtain the appropriate geometry. Normally, vendors provide pill-shaped KTOs (like the case from Figure 4.1), but the desired geometries in this work are rectangular (see Figure 4.3, for example). Therefore, cuts must be applied in the crystal, which can change its dielectric properties.

To characterize the electrical permittivity of the KTO (this is, its dielectric constant ε_r and loss factor $\tan\delta$ as a function of the biasing) in this PhD thesis it has been developed a setup that could be used to apply a DC voltage at the ferroelectric, measuring its behavior. After investigating a multitude of geometries for the KTO crystal, a novel setup has been proposed providing good characteristics in terms of mode crowding (which is an issue due to high permittivity). This system is based on a coaxial port connected to two parallel metallic plates, being the KTO film attached between them (see Figure 4.15 (left)), like a capacitor. The external conductor of the coaxial is electrically connected to the top metallic
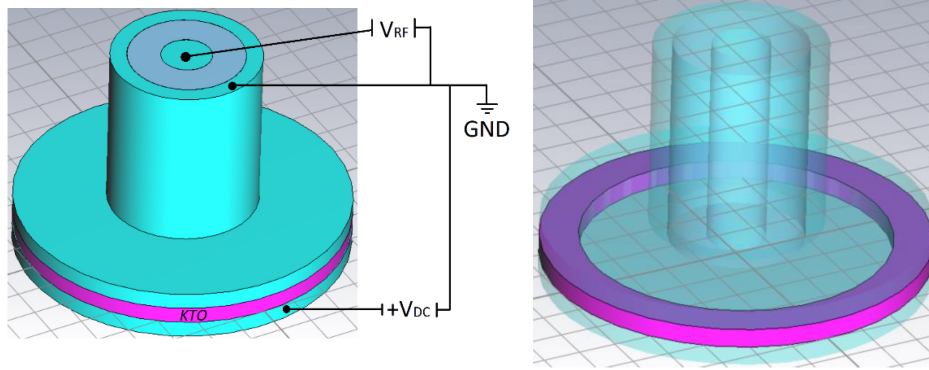
Figure 4.15: Left: Scheme of the KTO characterization setup based on a coaxial port and two metallic plates forming a sandwich with the KTO in the middle. V_{RF} and V_{DC} are the voltages at RF frequencies (operation frequency at which the KTO will be characterize, at X-bands for our case) and at DC frequencies ($f = 0$ Hz, the biasing frequency of the contacts), respectively. As it can be seen, the external conductor of the coaxial port acts as common GrouND (GND) for both RF and DC signals. Right: Highlighting of the KTO material in the 3D model to observe its geometry (ring shape).

plate, which carries the 0-voltage level (GND), while the inner conductor is only connected to the V_{RF} signal. The bottom plate will carry the positive DC voltage. A classical analysis consists in comparing the S_{11} parameter (the reflection coefficient) at the coaxial port with and without ferroelectric, measuring the resonant frequency shift and the increase in the bandwidth (or decrease of the quality factor) for a mode close to the frequency of interest. Nevertheless, it will be necessary in order to obtain accurate results to develop an optimization technique which fits the setup simulation results (by means of numerical methods) with those of the measurement. Therefore, the concept is based on extracting the permittivity value from the frequency shift and the losses from the S_{11} level.

The KTO shape must be based on a ring (see Figure 4.15 (right)), to apply a uniform DC voltage along its top/bottom walls. A circular shape would lead to a non-uniform DC distribution due to the lack of GND signal at the inner conductor and at the dielectric of the coaxial. If the ring production is found difficult, a solid KTO disk as alternative could be also feasible, assuming a lower accuracy due to the previous reasons. In the example of the 3D model shown in Figure 4.15 (right), the ring thickness (radial axis) is 1 mm, but it could be higher (3 mm, for example) if it solves manufacturing incompatibilities. On the other hand, the high step from KTO permittivity to air permittivity (~ 1) allows to assume

a boundary condition of perfect magnetic wall in that zone.

The setup relying on the concept of huddling several E-field variations (lobes) of TM_{0x0} modes, being x and entire number, at the KTO ring thanks to its high permittivity value, similarly to the *modified-TE*$_{301}$ mode concept described in section 4.1.1. Figure 4.16 shows the obtained results from the simulations carried out varying the ε_r value from 3000 to 5000 (the expected permittivity range for the ferroelectric KTO). As it can be seen,

(a)

(b)
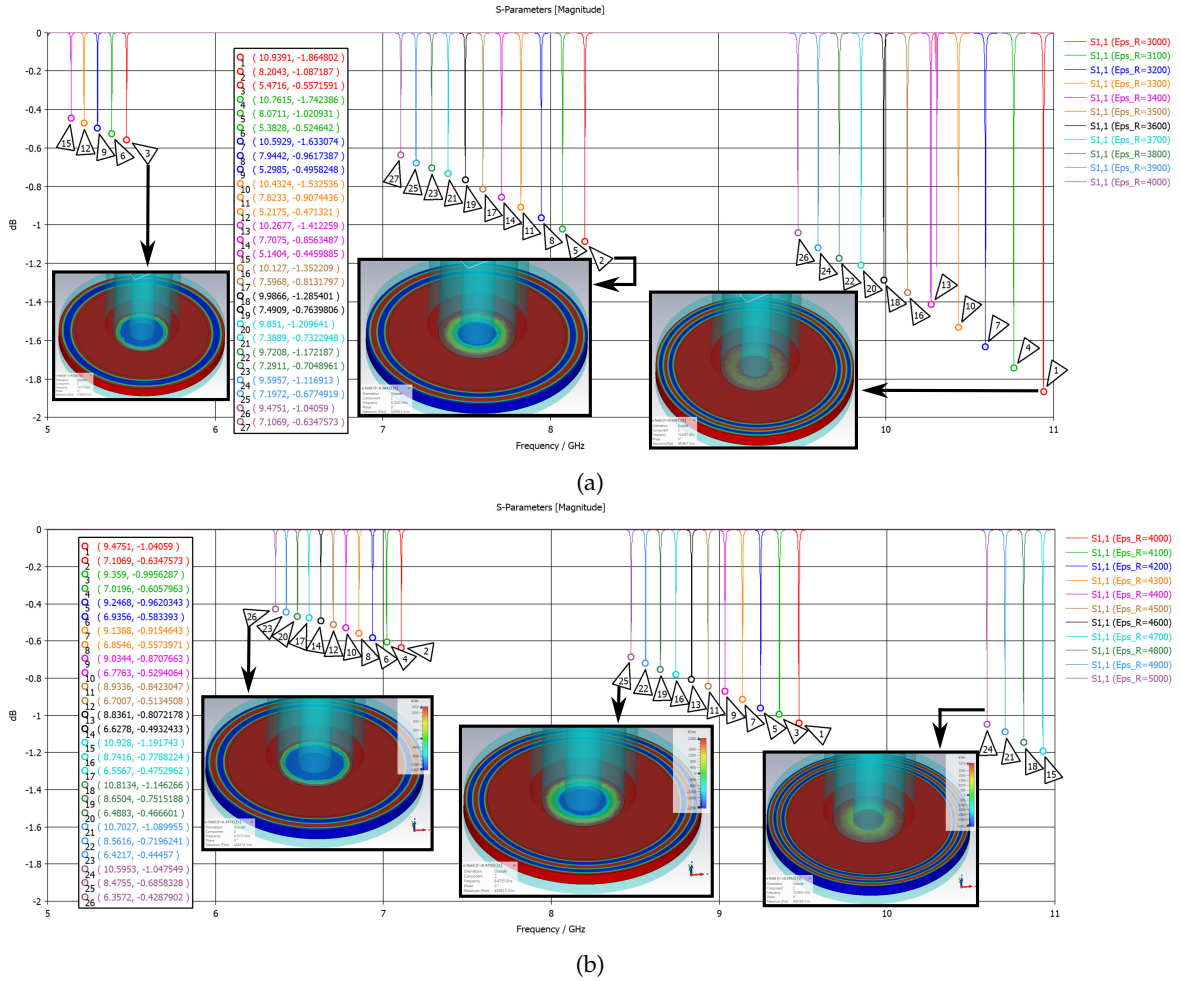
Figure 4.16: Simulation results of the $|S_{11}|$ parameter as a function of the frequency for several permittivity values with the setup from Figure 4.15 employing $\tan \delta = 10^{-4}$: (a) from $\varepsilon_r = 3000$ to 4000, and (b) from $\varepsilon_r = 4000$ to 5000. At the insets of both figures there is depicted the vertical component of the E-field for several TM_{0x0} modes: (a) $\varepsilon_r = 3000$ with $x = 2$, 3 and 4, and (b) $\varepsilon_r = 5000$ with $x = 3$, 4 and 5.

depending on the frequency at which the KTO is to be characterised, a mode with a specific x value must be used. For example, if it is desired to characterise the ferroelectric in the range $f \in [8.5, 9.5]$ GHz, the TM_{040} mode (this is, $x = 4$) should be studied since it covers the whole spectrum. It is worth noting that for the permittivity range between 4000 and 5000 (see Figure 4.16b), the TM_{020} mode has been left out of the simulated frequency span (below).

Finally, in this setup one has to take care that no electrical discharge from the V_{DC} part to the V_{RF} part takes place, because this could damage the VNA seriously. A low-pass filter should be implemented in this stage between the RF output to ground. That filter would prevent in case of a failure that the high anode voltage is applied to the RF output. In any case, these concepts are still under development and have been reserved as a future line of research for this PhD thesis.

4.5 CONCLUSIONS

The ferroelectric research in this work provides a new technique of using electronic tuning systems with KTO elements. Design instructions and simulation data for haloscopes scanning a large spectrum area of axion masses are offered in this chapter. A $N = 4$ multicavity with three iris windows of inductive type providing a reasonable tuning range and good outcomes in Q_0 and C has been created.

In addition, the usage of KTO slabs to create any sort of interresonator coupling is illustrated in this study. An alternating $N = 4$ multicavity with acceptable form factor and quality factor outcomes was created using three KTO films. To promote the mode separation at the axion frequency, the structure incorporates the mentioned alternating behaviour: two KTO films operating as capacitive coupling elements and one as inductive. This work indicates that the approach permits the relatively easy combination of inductive and capacitive interresonator couplings within the same multicavity. In addition, the KTOs suppress the requirement to produce iris windows and may increase the haloscope quality factor.

Also, this type of ferroelectric tuning in multicavities allows the alteration of the multiple frequencies of the subcavities and, at the same time, the k value at each interresonator coupling independently to preserve the right modal behaviour and the pattern of the EM field in the mode. This concept could enhance the form factor parameter.

To exemplify the suggested principles, two multicavities with ferroelectric slabs have been studied. The primary future line of this work will be the experimental testing of these ferroelectric films (the KTO) in several prototypes while establishing an appropriate DC voltage mechanism with the least influence on the Q_0 and C parameters. In addition, the merging of both approaches (KTO elements for tuning and interresonator coupling) in the same structure is being examined.

Finally, a simple setup for the characterization of the acquired KTO crystals has been presented. Several simulation outcomes are provided showing good results, demonstrating the feasibility of this system against the mode crowding, a typical issue in structures with dielectrics of high permittivity values.

5

OTHER HALOSCOPE STUDIES

As discussed in Chapter 3, there are many ways to improve a dark matter axion detector. Some of these enhancements (such as increasing the volume, improving the form factor and the quality factor, and implementing a more efficient tuning system) have been discussed in the previous two chapters. In this chapter, other studies carried out in this PhD thesis within the framework of the RADES team will be presented, with the aim of contributing to the axion community with investigations and developments in the design of haloscopes.

Firstly, section 5.1 shows the studies carried out to implement a port summation system in single cavities and multicavities to aid mode separation and assisting in the identification of the axion mode resonance. Secondly, in section 5.2 there are presented additional studies with haloscopes. Section 5.2.1 shows the investigations conducted for the implementation of QuBit devices, whose main advantage is based on the lowering of the system temperature thanks to the thermal noise improvement. In section 5.2.2, the results of other prototype designs working at UHF-band and W-band frequencies to search the axion at different spectrum areas are presented. In section 5.2.3, the HTS concept and the developed structures are exposed, which allows the increasing of the unloaded quality factor beyond the limits exposed in section 3.1.1. Finally, in section 5.2.4 the efficient full-wave modal technique BI-RME 3D is presented, which helps with the analysis of the EM coupling axion-photon in a haloscope.

5.1 MULTI-PORT COMBINATION FOR MODE REJECTING

As explained in section 3.1, the increase of volume (or dimensions) in a single cavity or multicavity is limited by the frequency approximation of unwanted modes to the axion mode resonance. In the case of single cavities, it was shown that these limiting modes are the higher order resonant modes. In particular, for rectangular single cavities, it has been studied that the modes TE_{111} and TE_{102} are the ones that limit this increase in volume. On the other hand, in multicavities of N subcavities, with N number of configuration modes for each resonant mode, it was shown that the ones imposing this constraint can be either one of these configuration modes for the operation resonant mode (TE_{101} in our case), or a configuration mode of a higher order resonant mode (TE_{111} or TE_{102}), depending

on the height (*b*) and the length (*d*) of the subcavities and on the number of subcavities (*N*).

Furthermore, as it can be seen in the above-mentioned section, there is the possibility to implement transmission zeros in the response of a haloscope based on the concept of multicavity for the exceeding of the discussed limits. These zeros are created either by the approximation of resonant modes with a relatively high quality factor or by the implementation of a cross-coupling in the design topology. Thanks to them, it was demonstrated with a simple and preliminary 2D multicavity prototype that the mode separation can be increased by more than three times (see Figure 3.21c). In this sense, this PhD thesis shows that there is a wide range of possibilities to combine the studied geometries and topologies for the further increasing of the mode separation.

In order to rise up the mode separation (or continue increasing this parameter if transmission zeros are employed) in haloscopes, another new idea has also been developed in this work, which allows different modes to be rejected in single cavities and multicavities: coherent combination of port signals with *phase matching*.

Unfortunately, although this technique allows the rejection of different modes, as it will be seen below, being a post-processing (after the expected axion detection), these modes will still disturb the electromagnetic field of the axion mode if they are very close to it in frequency. Therefore, phase-matched rejected modes will still affect the form factor value (*C*) if the frequency separation is excessively low, as it can be seen in section 3.1, where the limits in which *C* was considered a good value were established, depending on the quality factor of a single cavity or 1D multicavity. However, even if these limits are maintained this method of summing port signals to reject modes can be useful in two ways: mode identification and quality factor calculation.

As discussed in section 3.2.4, in this PhD thesis it was invented a new technique for the identification of configuration modes in multicavities with vacuum holes on the top (or bottom) walls of its subcavities by using metal pins and observing the displacement of the modes in the response (see Figure 3.56). This method was employed in the 30-subcavities RADES multicavity demonstrating its usefulness. However, this technique may not be easily implementable in many situations (especially in the data campaigns). Moreover, it does not allow the identification of different resonant modes (it identifies only different configurations for a particular resonant mode). The proposed phase matching method, on the other hand, facilitate these tasks, as it will be shown.

In section 3.2.4, a method for the extraction of the Q_l value in a structure with low unloaded quality factor, where its computation is quite tricky, was also presented. This technique is based on the fitting of a two Lorentzian curves sum (see Figure 3.55). In this sense, the phase matching can be employed as a replacement or auxiliary technique of the

previous method, as it will be demonstrated.

The use of the phase matching concept has been investigated and employed previously by some experimental axion teams, like CAST-CAPP [143], for searching axion particles by multiple single cavities in order to take advantage of the spare space in the magnets [32]. This is accomplished by the combination of the cavity outputs (with only one port in each haloscope), guaranteeing a phase matching of the axion coherent signal [32].

In the case of this work, the idea proposed consists of the implementation and coherent combination of several ports matching their signal phases for the same haloscope (single cavity or multicavity). The first structure analysed is the one from Figure 5.1, an example based on the destructive interference of several ports in a tall ($b = 300$ mm) single multicavity haloscope of $N = 2$ subcavities with an inductive coupling iris and 4 ports. The ports are positioned at the centres of the subcavities at top and bottom walls. In
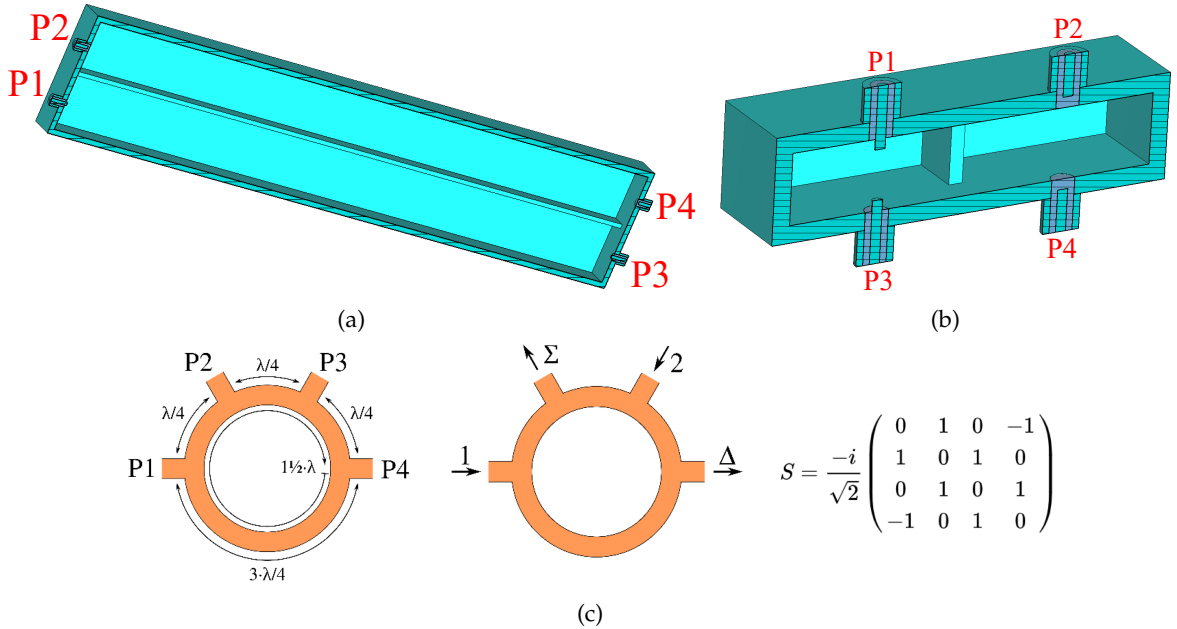
Figure 5.1: Phase matching example based on a tall multicavity with $N = 2$ subcavities, one inductive iris window and 4 ports: (a) 3D model of the structure employed for the phase matching example, (b) non-tall model for an easy visualisation of the coaxial antenna lengths, and (c) Rat-Race devices (scheme with the port numeration and lengths, scheme depicting its functionality as adder (Σ, in phase) and differencer (Δ, 180° out of phase), and its associated Scattering Parameters). The structures from (a) and (b) show the symmetry half of the haloscope (being the dashed region the symmetry plane), and *P1*, *P2*, *P3* and *P4* depict its port numeration. The characteristic impedance of all the sections in the Rat-Race device are $Z_0\sqrt{2} \approx 70.71$ Ω, being $Z_0 = 50$ Ω.

Figure 5.1b it is depicted a non-tall ($b = 10.16$ mm) version for showing the antenna lengths (which is not correctly appreciated with the tall dimension in Figure 5.1a). As it can be seen, the antenna lengths of the first subcavity are equally configured (for the critically coupled condition), and the antenna ports of the second subcavities the same (for a very undercoupled scenario). In this case, the phase matching is done to sum with a destructive interference of the top ports with the bottom ports, this is *P1 + P3* and *P2 + P4*

of the structure from Figure 5.1a, employing the differencer option (Δ) of the a Rat-Race device (see scheme at the middle of Figure 5.1c), which are usually utilised for the implementation of this technique [144]. With this, after the destructive interference sum, the final response would show a 2-port structure, being the first port critically coupled and the second one very undercoupled, which is the situation pursued for data taking.

The method followed consisted of, firstly, extracting the Scattering Parameters from the haloscope. For the phase matching, work has been carried out in this PhD thesis with 3 types of haloscopes according to their number of ports: 2 ports, 4 ports and 8 ports, which generate (in CST simulations or VNA measurements) the .s2p, .s4p and .s8p files, respectively. Secondly, these files are loaded into the ADS software [145], where the data is post-processed to perform the summation. The schematic shown in Figure 5.2 has been implemented using Rat-Races, and it is composed by the following elements:
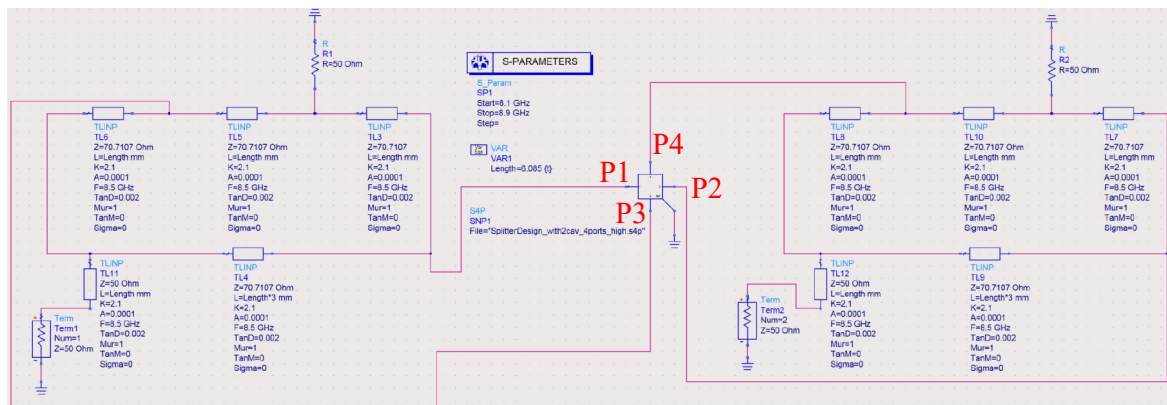
Figure 5.2: Schematic in ADS for the phase matching of the two top ports with the two bottom ports of a tall 4-port multicavity based on $N = 2$ subcavities with an inductive iris as interresonator coupling (see structure in Figure 5.1a).

- *TLINP*, a 2-Terminal Physical Transmission Line where, for our case, only the operation frequency (f), characteristic impedance (Z) and length (L) parameters are employed. For our example, $f = 8.5$ GHz and $Z = 70.71$ Ω. In addition, L is optimized with the variable *Length* for a correct rejection of the unwanted modes. In any case, the value of the length of the lower transmission line in each Rat-Race shall be three times that of the three upper transmission lines.

- *Term*, a Port Termination for S-Parameter, used to define the impedance ($Z = 50$ Ω in our case) and location of the ports. In this case, the final ports are two: *P1* and *P2*, as depicted in Figure 5.2.

- *R*, a Resistor with a resistance value of *R* employed here to model a matched load of $R = 50$ Ω.

- *S4P*, a module for importing the Touchstone .sNp[1] files. In this case, it is utilised for .s4p files, this is, for 4-port responses (containing a 4×4 Scattering Parameter matrix). In this example, the .s4p file is imported from CST.

- *VAR*, a component for defining and handling the variables and equations. It this case, it it employed for the optimization of the transmission line lengths with the variable *Length*.

- *S-PARAMETERS*, an element for the S-Parameter and frequency sweep configuration.

The two lines from the *S4P* device to the left carry the signals from ports 1 and 3 (coaxial antennas in the subcavity 1 at the top and bottom, respectively), and are summed (with destructive interference) by the Rat-Rice on the left. On the other hand, the two lines from the *S4P* device to the right carry the signals from ports 2 and 4 (coaxial antennas in the subcavity 2 at the top and bottom, respectively), and are summed thanks to the Rat-Rice on the right. Both final signals already summed are connected to terminals *Term1* and *Term2*. This simulation will therefore provide a 2×2 Scattering Parameter matrix. The ADS simulation results after optimising the *Length* variable are shown in Figure 5.3. Also,

Response before the sum:

m10 freq=8.866GHz dB(S(1,1))=-10.503
m11 freq=8.892GHz dB(S(1,1))=-11.426

m1 freq=8.509GHz dB(S(1,2))=-9.446
m2 freq=8.523GHz dB(S(1,2))=-8.823
m3 freq=8.566GHz dB(S(1,2))=-8.900
m4 freq=8.639GHz dB(S(1,1))=-11.777
m5 freq=8.665GHz dB(S(1,1))=-9.954
m6 freq=8.679GHz dB(S(1,1))=-10.974
m7 freq=8.722GHz dB(S(1,1))=-13.041
m8 freq=8.740GHz dB(S(1,1))=-9.526
m9 freq=8.793GHz dB(S(1,1))=-11.842

Freq(m2) − Freq(m1) = 14 MHz

Response after the sum:

m10 freq=8.866GHz dB(S(1,1))=-0.051
m11 freq=8.892GHz dB(S(1,1))=-6.688

m1 freq=8.509GHz dB(S(1,2))=-3.527
m2 freq=8.523GHz dB(S(1,2))=-40.824
m3 freq=8.566GHz dB(S(1,2))=-2.921
m4 freq=8.639GHz dB(S(1,1))=-0.085
m5 freq=8.665GHz dB(S(1,1))=-8.484
m6 freq=8.679GHz dB(S(1,1))=-0.044
m7 freq=8.722GHz dB(S(1,1))=-5.159
m8 freq=8.740GHz dB(S(1,1))=-9.265
m9 freq=8.793GHz dB(S(1,1))=-0.086

Freq(m3) − Freq(m1) = 57 MHz

Figure 5.3: Phase matching results from ADS with the schematic from Figure 5.2. The top picture depicts the response before the port combination, while the bottom picture represents the outcomes after the sum.

in Table 5.1 there are listed the configuration modes that appear at the plot of the top

---

1 This *N* should not be confused with the number of subcavities. In this PhD thesis, *N* has been defined as the number of subcavities in a multicavity. The .sNp files, on the other hand, use this *N* as the number of ports employed in a measurement.

picture from Figure 5.3.

#	Freq. (GHz)	Resonant mode	Configuration	Eliminated ?
1	8.509	TE_{101}	[+ +]	Not
2	8.523	TE_{111}	[+ +]	Yes
3	8.566	TE_{121}	[+ +]	Not
4	8.639	TE_{131}	[+ +]	Yes
5	8.665	TE_{101}	[+ −]	Not
6	8.679	TE_{111}	[+ −]	Yes
7	8.722	TE_{121}	[+ −]	Not
8	8.74	TE_{141}	[+ +]	Not
9	8.793	TE_{131}	[+ −]	Yes
10	8.866	TE_{151}	[+ +]	Yes
11	8.892	TE_{141}	[+ −]	Not

Table 5.1: Configuration modes shown in the first plot of Figure 5.3. The configuration modes that are rejected thanks to the phase matching are detailed.

As it can be seen in the plot of the bottom picture from Figure 5.3, the second, fourth, sixth, ninth and tenth resonances have been eliminated. From Table 5.1, it can be concluded that these eliminated resonances correspond to the resonant modes with odd variation in height (i.e. TE_{mnp} modes with n odd) for both configurations: [+ +] and [+ −]. To explain this phenomenon, the orientation of the ports in the structure from Figure 5.1a and the fact that the Rat-Races are working in its differentiating mode must be taken into account. Indeed, top and bottom ports are oriented 180° opposite each other, so the electric field collected by the bottom ports, for any resonant mode, will be phase shifted by 180° with respect to the top ports. For TE_{mnp} modes with n even (TE_{101}, TE_{121}, ...), the electric field lines in the top port section have the same orientation as the coaxial antenna, but the bottom ports are oriented 180° (180° phase shift of the signal collected by these ports). However, for TE_{mnp} modes with n odd (TE_{111}, TE_{131}, ...), both ports pick up the signals without phase shift, since the E-field orientation will be the same as that of the ports. With this, considering the Δ operation of the Rat-Races (180° phase shift to top or bottom ports), the total phase shifts between top and bottom port signals are 0° (in phase or constructive interference) and 180° (destructive interference) in TE_{mnp} modes with n even and odd, respectively.

The axion mode is located at the first resonance ($f = 8.509$ GHz) since the structure is based on an all-inductive multicavity design. Then, with the phase matching technique it has been demonstrated that the mode separation parameter rises from $\Delta f = 14$ MHz to 57 MHz, as it is indicated in Figure 5.3. This mode separation enhancement ($\times 4$ factor) is similar to the one obtained with transmission zeros in the 2D structures detailed in section 3.1.3 ($\times 3.3$ factor). A way to eliminate the next resonance (the TE_{121} resonant mode), and further increasing the mode separation, would be to position the ports in the region with 0-level electric field for that mode. To achieve this, the ports should be positioned at 1/3 and 2/3 of the total height along the sidewall. On the other hand, in

order to obtain a good coupling with the axion mode (TE_{101} resonant mode), loops (see Figure 3.28c) should be used instead of straight coaxial ports. Several investigations are being carried out in this line, obtaining good preliminary results. The development and analysis of this research is reserved as a future line of this work.

Another of the studies developed in this PhD thesis was to reject configuration modes in a multicavity, which must be done by summing ports from different subcavities. To carry out this study, the structure of Figure 5.1b has been used adding the ports of the subcavity 1 with those of the subcavity 2. In order to perform a destructive interference of the signals, the phase matching *P1 + P4* and *P2 + P3* has been performed. Adjusting the phases, the summations *P1 + P2* and *P3 + P4* could also be performed. Wilkinson power divider devices operating as combiners [146] could also be employed for this phase matching. The ADS results before and after the phase matching with this configuration are depicted in Figure 5.4. As it can be seen, the second mode ([+ −] configuration mode of the TE_{101} reson-
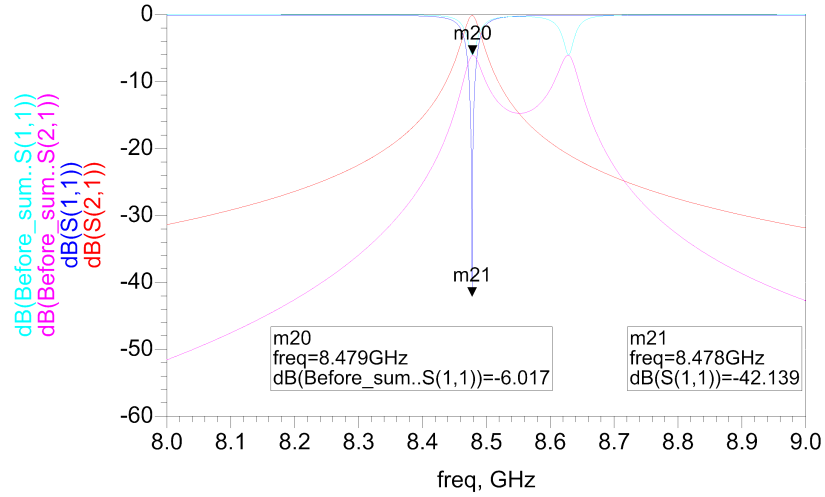
Figure 5.4: ADS results for the *P1 + P4* and *P2 + P3* phase matching of the structure from Figure 5.1b. The light blue and pink lines show the S_{11} and S_{21} parameters before the phase matching, respectively, while the dark blue and red lines depict the S_{11} and S_{21} results after it.

ant mode) has been eliminated from the response, leaving alone the axion mode resonance.

The following study consisted of the elimination of three of the four configuration modes (to isolate the axion mode) of a non-tall all-inductive multicavity based on $N = 4$ subcavities, with one coaxial port positioned in each of the subcavities top walls. The topology of the phase matching for this scenario is depicted in Figure 5.5a. The configurations for the TE_{101} resonant mode of this multicavity are: [+ + + +], [+ + − −], [+ − − +] and [+ − + −]. Conducting a first simulation in ADS with a similar schematic used previously with Rat-Races (see Figure 5.2), but combining now *[P1 + P2] + [P3 + P4]* with a third Rat-Race, it was obtained that only the second and fourth configuration modes (which are the ones with odd symmetry) were eliminated. It was concluded that the third eigenmode was not canceled due to the presence of the k_{23} coupling, this is, the
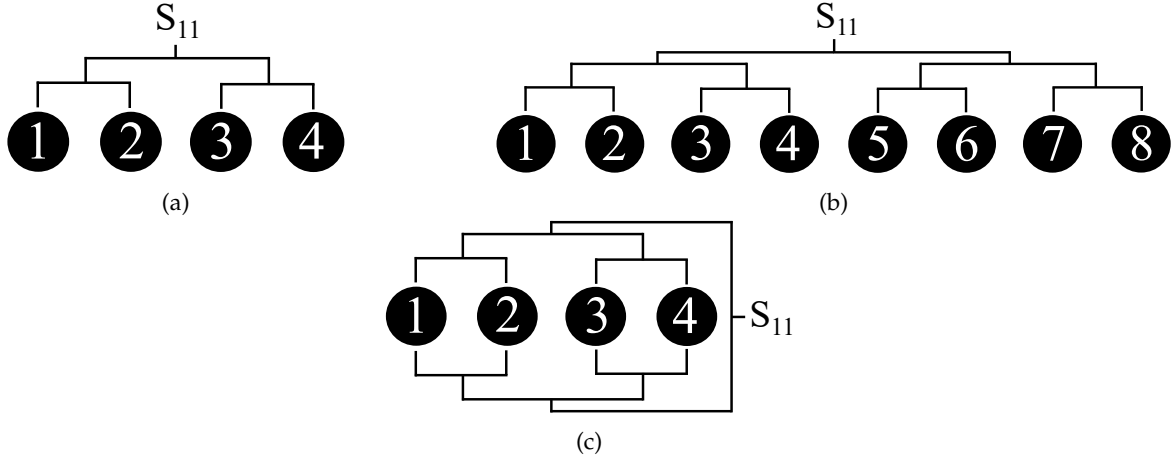
Figure 5.5: Topologies of different phase matching examples: (a) 4 ports of a 4-subcavities multicavity with ports at top walls, (b) 8 ports of a 8-subcavities multicavity with ports at top walls, and (c) 8 ports of a 4-subcavities multicavity with ports at top and bottom walls. The black dots with the numbers depict the subcavities.

interresonator coupling between subcavities number 2 and 3. To reject also this resonance, an extra transmission line was implemented to the cables carrying the signal of the first and last subcavity ports, whose length was used as an optimisation parameter. This resulted in a clean band with only the axion mode. It is important to note that, after adding up all the ports, only one Scattering Parameter is present, the S_{11} (as it is shown in all the examples from Figure 5.5), with which both the β and the loaded quality factor Q_l can be extracted, as it was explained in the subsection 3.2.1.5.

To perform phase matching in order to eliminate all the configuration modes but the axion one ([+ + + ... +]) in a $N > 4$ subcavity multicavity, with all ports on each of its top walls, more than one optimisation transmission line must be used. For example, in a $N = 8$ subcavities multicavity with 8 ports on the top walls (see topology in Figure 5.5b), 7 Rat-Races (for the port combination *[[P1 + P2] + [P3 + P4]] + [[P5 + P6] + [P7 + P8]]*) and 3 different optimisers (one in the signals of the subcavities 2 and 7, one in the subcavities 3 and 6, and one in the subcavities 4 and 5) must be implemented[2]. As it can be seen, the complexity of the port combination system increases rapidly with the number of subcavities N. However, in a practical application, it will not be necessary to eliminate all configuration modes, but only those that are closer to the axion mode, which will facilitate the implementation of this technique. Further studies are being carried out in this direction to implement other topologies of interest.

As a proof of concept on a real haloscope, a high ($b = 300$ mm) all-inductive structure based on 4 subcavities with 8 ports (4 top and 4 bottom) has been designed, simulated, fabricated and measured in this PhD thesis. This prototype was previously analysed in section 3.1.2.2 (see Figure 3.17), where it was demonstrated the possibility of increasing

---

2 In this case, an 8-way power divider operating as combiner could be employed for the direct combination of the 8 ports (without Rat-Races). However, a phase shifter would be necessary at each port signal for the optimization of the phase matching process.

the height of a multicavity (in order to increase the volume parameter, which is very important for a good axion detection sensitivity), obtaining excellent results in terms of form factor, quality factor and mode separation. In this section it is analysed its other great feature: the use of its ports to perform phase matching increasing the parameter Δf. In this case, the idea to be tested is the sum of all the port signals (as depicted in the topology shown in Figure 5.5c) for the rejection of the unwanted configuration modes of the resonant modes TE_{mnp} with any n. This is possible thanks to the position of the coaxial antennas (at all the subcavities and at top / bottom walls).

Since our laboratory did not have an 8-port VNA (for the production of a .s8p file), a collection of measurements had to be made with the available VNAs to generate the 8×8 Scattering Parameter matrix of this 8-port structure. To build this matrix with a 2-port VNA (.s2p files), 28 measurements had to be made combining the ports in the following way: (1, 2), (1, 3), (1, 4), (1, 5), (1, 6), (1, 7), (1, 8), (2, 3), (2, 4), (2, 5), (2, 6), (2, 7), (2, 8), (3, 4), (3, 5), (3, 6), (3, 7), (3, 8), (4, 5), (4, 6), (4, 7), (4, 8), (5, 6), (5, 7), (5, 8), (6, 7), (6, 8), and (7, 8). Also, as a cross-check validation, it was employed a 4-port VNA (.s4p files) with which only 6 measurements are necessary for the construction of the 8×8 matrix, using the following port combinations: (1, 2, 3, 4), (1, 2, 5, 6), (1, 2, 7, 8), (3, 4, 5, 6), (3, 4, 7, 8), and (5, 6, 7, 8). It is important to note that ports that are not used in the 8×8 matrix construction measurements must be matched with a 50 Ω load. For this purpose, seven *ANNE-50+* loads (from *Minicircuits* [147]) were bought and employed. In Figure 5.6 it is shown one of the measurements with the 4-port VNA. Once
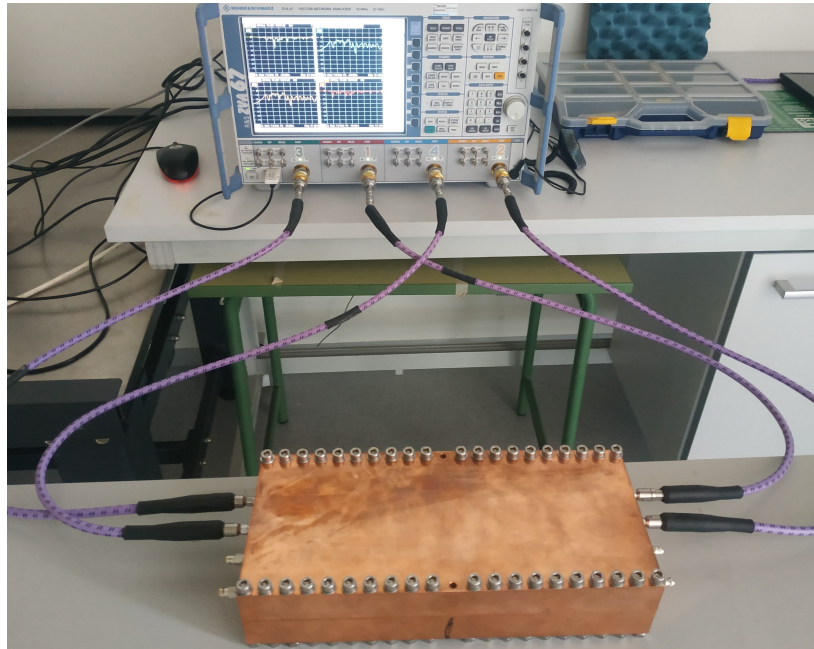
Figure 5.6: One of the measurements (the (1, 2, 5, 6) port combination) with the 4-port VNA of the all-inductive tall multicavity of 4 subcavities for the construction of the 8×8 Scattering Parameter matrix.

these measurements were taken (.s2p files with the 2-port VNA and .s4p files with the 4-port VNA), they were imported to MATLAB for the appropriate combination and fi-

nal production of the .s8p file. It was checked that both VNA measurements agree very well.

This .s8p file was then imported into ADS in a schematic similar to Figure 5.2, but adapted for 8-port phase combination by incorporating various optimisation sections, as discussed above. In Figure 5.7, the results from simulations (in CST), measurements (using the VNA) and post-processing (in ADS) with phase matching are shown. As it can be seen,
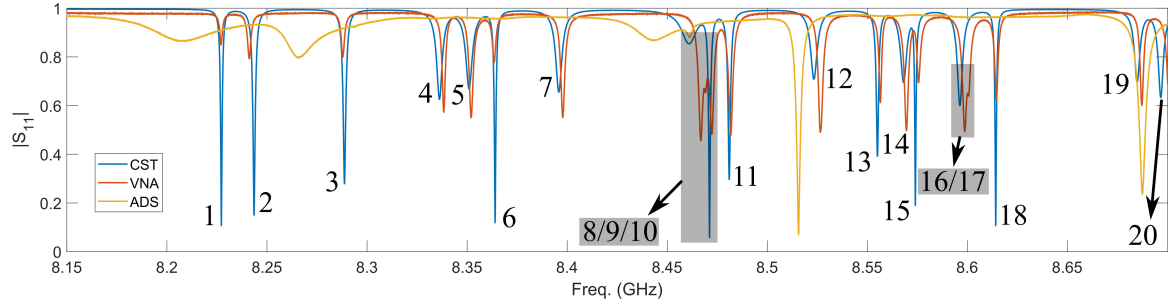
Figure 5.7: Results of the tall multicavity based on 4 subcavities and 3 inductive irises before and after the phase matching. The blue, red and yellow lines represent the CST simulation, VNA measurements and ADS phase matching results from measurements, respectively. The numbers on the plot depict the resonance numeration in order of appearance. The dark rectangles represent a high mode mixing region, where resonances are difficult to distinguish due to its frequency proximity.

the similarity between the simulation (blue line) and measurement (red line) results is high.

Analysing with simulations the electric field pattern of the enumerated resonances, it has been extracted the Table 5.2, where they are identified with each configuration mode of the structure. The results of phase matching in ADS show that most resonances have been successfully rejected. Thus, the mode separation parameter is significantly increased. Even more modes could be eliminated if necessary by fine tuning the optimisation section implemented in the schematic, as depicted in Table 5.2. It is important to note that the response shown in Figure 5.7 (yellow line) has a level of S_{11} not appropriate for an axion data taking, as this parameter must be minimal to obtain the critically coupled case. This poor parameter level also explains why the plot of this figure is represented in linear (instead of in dB) for an easy visualisation of the mode positions. A good S_{11} level could be achieved with a fine tuning by means of a length sweep on the coaxial antennas used by the fabricated prototype. Several investigations are being carried out in these directions, reserved as future lines of this work. In any case, the results shown in this work serve as a preliminary validation of the phase matching technique in large volume multicavities.

As it has been shown, even if complex phase matching systems are used, the resonance that will always establish the mode separation in a tall multicavity, if no mode crossing tuning systems or mode cancelling loops are implemented, will be that of the configuration mode type in the third row of Table 5.2, i.e. the configuration [+ + + ... +] of the TE_{121} resonant mode. Therefore, in a practical application for this case, it would in principle only be necessary to cancel the resonance of the second row of this table, i.e. the [+ +

#	Freq. (GHz)	Resonant mode	Configuration	Eliminated ?
1	8.2271	TE_{101}	[+ + + +]	Not
2	8.2411	TE_{111}	[+ + + +]	Yes
3	8.2879	TE_{121}	[+ + + +]	Not
4	8.3385	TE_{101}	[+ + − −]	Yes
5	8.352	TE_{111}	[+ + − −]	Yes
6	8.3635	TE_{131}	[+ + + +]	Yes
7	8.3978	TE_{121}	[+ + − −]	Yes
8/9/10	∼8.466	TE_{141}	[+ + + +]	Not
8/9/10	∼8.466	TE_{131}	[+ + − −]	Yes
8/9/10	∼8.466	TE_{101}	[+ − − +]	Not (Opt)
11	8.4817	TE_{111}	[+ − − +]	Yes
12	8.5265	TE_{121}	[+ − − +]	Not (Opt)
13	8.5565	TE_{101}	[+ − + −]	Yes
14	8.5695	TE_{111}	[+ − + −]	Yes
15	8.5756	TE_{141}	[+ + − −]	Yes
16/17	∼8.6	TE_{151}	[+ + + +]	Yes
16/17	∼8.6	TE_{131}	[+ − − +]	Yes
18	8.6144	TE_{121}	[+ − + −]	Yes
19	8.6871	TE_{131}	[+ − + −]	Yes
20	8.701	TE_{141}	[+ − − +]	Not (Opt)

Table 5.2: Configuration modes shown in Figure 5.7. There are detailed the configuration modes that are rejected thanks to the phase matching. "*(Opt)*" represents that the rejection of that configuration mode is possible with an extra optimization.

+ +] configuration of the TE_{111} mode. For such purpose, it would only be necessary to combine, for example, the top port with the bottom port of the first subcavity. This has been carried out in practice obtaining the results shown in Figure 5.8, where this time much more appropriate reflection levels for the search of axion dark matter particles have been obtained. This external coupling value (S_{11} level) has been obtained following the
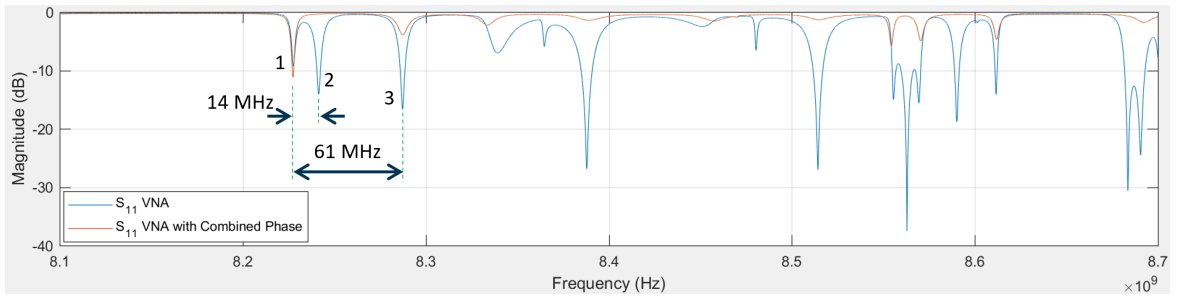
Figure 5.8: Results of the tall multicavity before and after the phase matching combining the top and bottom ports of the first subcavity. The blue and red lines represent the VNA measurement and ADS phase matching results, respectively.

procedure described in Appendix II: Critical coupling combining 2 ports. As this plot demonstrates, the mode separation has been increased from $\Delta f = 14$ to 61 MHz, which is an enhancement (×4.4 factor) similar to the one obtained in the phase combination from Figure 5.3 with a tall 2-subcavities multicavity.

Another future line that has emerged from this PhD thesis is to apply the studies presented in this section in a prototype with more and higher subcavities (e.g. a multicavity design with $N = 40$ subcavities and a height of $b = 600$ mm, which could fit in the bore of the BabyIAXO magnet).

Finally, this work has led to the study of a new design technique, which is still under development, based on the use of pyramidal waveguide transitions (with a geometry similar to that of horn antennas) in order not to excite resonant modes in height in tall haloscopes (see example in Figure 5.9). With this method, the responses of our axion detectors would
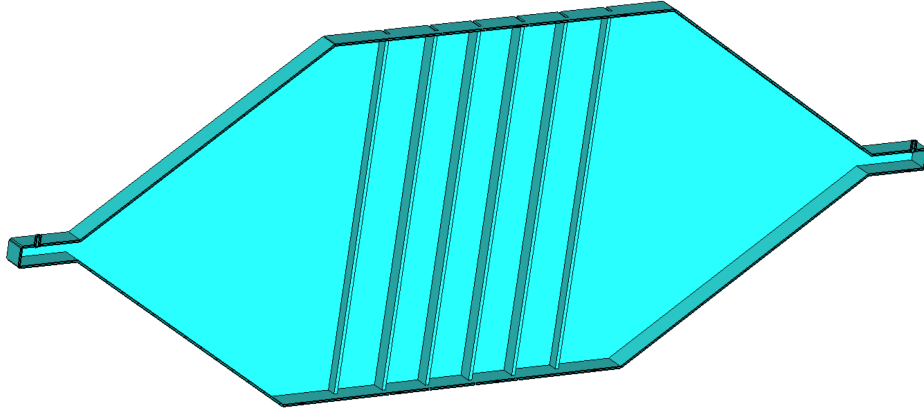
Figure 5.9: Example of a horn waveguide transition employed in an all-inductive 5-subcavities multicavity. There is depicted only the half of the structure housing.

only show TE_{m0p} resonant modes, so that the height could be increased, ideally (since there may be inaccuracies, due to machining tolerances, for example) as much as desired. This technique has been explored in [148]. Also, the use of ferroelectric KTO elements as interresonator couplings (instead of iris windows) with these pyramidal transitions is understudy. Unlike inductive irises, KTOs could serve to excite only TE_{10p} modes in addition to adjust the interresonator coupling by changing their permittivity values with voltage or temperature. This is in theory possible because they would be embedded inside the housing of the haloscope in a homogeneous way on the cross section.

5.2 ADDITIONAL HALOSCOPE INVESTIGATIONS

Although to a lesser extent, this PhD thesis has analysed some secondary aspects for the advancement of RADES haloscopes in various topics, which are described below.

5.2.1 *Qubits*

In the framework of the RADES group, studies have also been carried out on the implementation of QuBits devices in haloscopes to reduce the noise temperature of the system. As equation 2.10 shows, this is a key parameter for increasing the detection sensitivity of

the axion.

A QuBit or quantum bit is a quantum system with two possible states that can be arbitrarily manipulated [149]. It can only be correctly described by quantum mechanics, and only has two states that are well distinguishable by physical measurements. Modern dark matter detectors operating at microwave frequencies employ a resonant cavity to coherently collect the field generated by dark matter and a linear amplifier close to the standard quantum limit to read out the cavity signal. Reducing the detection level below these standard quantum limits, the boosting of the sensitivity to the dark matter signal is possible. In reference [91] the creation of a revolutionary microwave photon counting technology is presented, where more details of the operation of these devices can be found. In order to apply these methods to haloscope designs, the RADES team is conducting some research along these lines.

As a preliminary investigation the RADES group is studying how to couple a QuBit with resonant cavities in a setup of 2 subcavities coupled in height using a QuBit chip within a small iris window, which operates at 8.5 GHz. The first idea was to characterise several parameters (resistance, frequency, relaxation time, and so on), observing the effect of the QuBit in the cavity system. The final purpose is to read the photon content of the bottom cavity with the upper one through the QuBit. The design and fabrication of this setup was realised in this PhD thesis. Figure 5.10a shows the 3D model of this structure. As it

(a) (b)
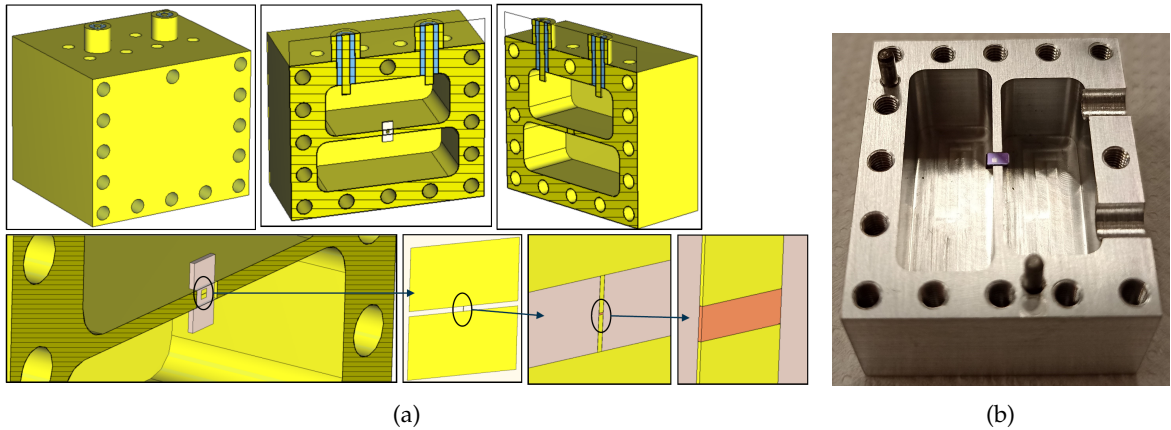
Figure 5.10: Setup based on 2 resonant cavities coupled by a QuBit to test its behaviour: (a) 3D model, and (b) prototype manufactured in aluminum. The upper cavity, where the coaxial ports are located, is used as readout and control. In (a) several zooms are applied to show more details. (b) taken from RADES.

is depicted, the QuBit device is based on two rectangular aluminum plates orientated on the chip (Silicon substrate) side by side united in the middle by a Josephson junction (two small metallic plates), which acts as a non-linear LC resonator (with the inductor being the non-linear component) [150]. It is positioned in the centres of the cavities, maximizing the coupling between the QuBit and the upper cavity, employed for readout and control. The resonant frequency of the TE_{101} mode (the operational resonant mode) for the bottom cavity is $f_r = 8.5$ GHz, which should be far away enough ($\Delta = |f_r - f_q|$), from the QuBit

$|0\rangle$ to $|1\rangle$ transition frequency (f_q). It is desired that these detuning values Δ because the goal is to run the system in the dispersive limit ($\Delta \gg g/2\pi$), being g the QuBit coupling to the cavity [150, 151]. The QuBit introduces a state-dependent shift on the cavity in this dispersive limit, which is the foundation of the readout process [150, 152]. In Figure 5.10b a picture of the manufactured prototype (in aluminum material) for the designed setup is shown. Also, alternative setup versions employing copper material have been manufactured for further investigations. At the time of publication of this PhD thesis, various measurements are being taken to analyse their electrical behaviour.

5.2.2 *Haloscope designs at other frequency bands*

As it is shown in section 2.2, there is a wide frequency spectrum still unexplored by the axion community (see Figure 2.5). In this line, the RADES group, whose haloscopes work mostly at frequencies within the X-band, has carried out diverse research to design detectors to search for axions in the UHF and W frequency bands. The accessibility to other magnets (apart from the CAST magnet, used during the first stage of this experimental group) with different geometries and volumes, like the BabyIAXO [59] and Canfranc [96] magnets, has allowed the development of this type of haloscopes.

5.2.2.1 *UHF-band*

As mentioned in previous chapters, the BabyIAXO dipole magnet design has relatively large dimensions, 600 mm in diameter and 10 m in length. Furthermore, from the equation 2.17 it can be easily extracted that the larger the cavity, the lower the resonance frequency. With these two premises, the design of a haloscope of 5 m total length based on the concept of the multicavity with twelve cylindrical subcavities coupled by eleven elliptical inductive irises, operating at $\sim$ 347 MHz (UHF-band), has been carried out. It makes great use of the volume of the BabyIAXO magnet. Figure 5.11 shows a 3D model of this structure.
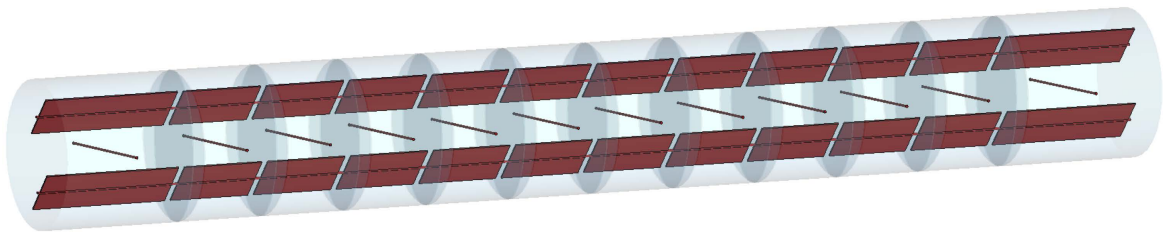
Figure 5.11: 3D model of the UHF-band haloscope design based on twelve subcavities connected by eleven elliptical window irises, employing a frequency tuning system with mechanical rotation of inner plates in longitudinal axis. Horizontal rods are positioned at the middle in length at each subcavity for rejecting a unwanted mode.

The resonant mode used to search for axions with this haloscope is the TE_{111}, since it is the one that is most similar to the static magnetic field profile produced by this magnet [59]. The results obtained in this design are: volume of $V = 1296$ L, unloaded

quality factor of $Q_0 = 3.16 \times 10^5$, and form factor of $C = 0.69$. As it can be seen in Figure 5.11, a frequency tuning system has been applied based on the mechanical rotation of inner plates in longitudinal axis. A frequency tuning range of $[324 - 347]$ MHz has been achieved with this system. The variation in the form factor and quality factor throughout the tuning range are: $[0.21 - 0.69]$ and $[1.8 \times 10^5 - 3.16 \times 10^5]$, respectively. On the other hand, studies applying a loop coaxial port (see Figure 3.28c) to this haloscope has been realised. Because the coupling via a loop antenna is dependent on the magnetic flux through the loop, rotating the loop allows for modification of that input / output coupling. As a result, whether the tuning process results in overcoupled or undercoupled circumstances, it has a degree of freedom to achieve critical coupling again.

Other designs are being investigated for the development of UHF structures with more subcavities and the application of 2D and 3D topologies.

5.2.2.2 *W-band*

As discussed in Chapter 3, solenoid magnets create a static magnetic field that is constant and parallel to the magnet axis. To optimise C, an electromagnetic mode with an electric field parallel to the magnetic field must be used. For this reason, the haloscope should be orientated in the appropriate axis for high axion detection sensitivity. As it can be seen in section 3.1, solenoids tend to have a higher magnetic field but significantly smaller dimensions. Therefore, the design of structures working at high frequencies such as 90 GHz (W-band) will be a good choice for these magnets as the dimensions of the cavities are much smaller (see equation 2.17). Furthermore, as it is shown in Figure 2.5, this frequency band is much less explored, so the development of haloscopes at these frequencies will be of great interest to the axion community. Along these lines, the structures shown in Figure 5.12 are under studied to be designed and to be used in the Canfranc solenoid (at the *Laboratorio Subterráneo de Canfranc* [96]), which is based on a bore of diameter $\phi = 130$ mm, and length $L = 150$ mm with a static magnetic field of $B_e = 10$ T (see Table 3.1).

The main disadvantage of working at high frequencies is the low volume achieved by the cavities and the reduction of the quality factor. Smaller manufacturing tolerances are as well necessary and critical. In addition, the input / output coupling at W-band should be realised thru waveguide irises (not straight or loop coaxials) due to size incompatibilities. On the other hand, 2D shapes could be applied to these structures in order to apply transmission zeros by cross-coupling, also increasing the volume.

5.2.3 *HTS structures*

Because the figure of merit of our detector is linearly related to the quality factor of the cavity, the RADES group has investigated the feasibility of coating the haloscope structures with superconducting materials instead of copper. With this purpose, the unloaded

(a)

(b)

(c)
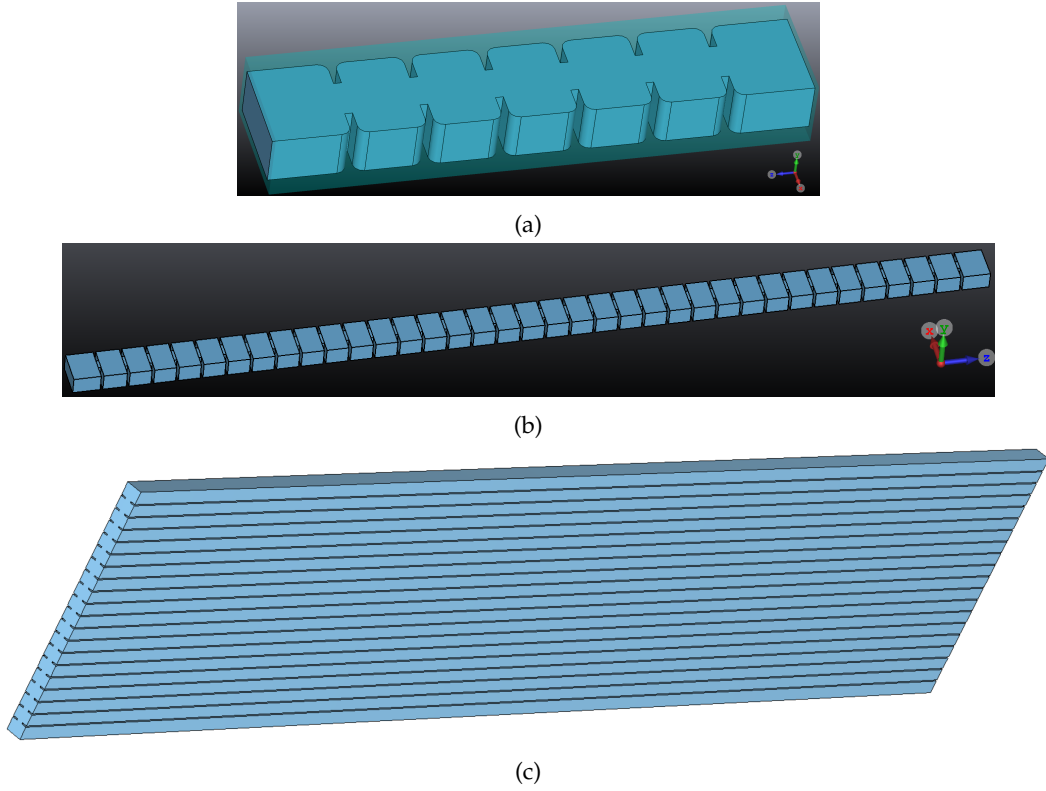
Figure 5.12: 3D models of the W-band haloscopes under study for its design. All the designs are based on the multicavity concept employing an all-inductive topology: two multicavities with the standard WR-10 ($a = 2.54$ mm and $b = 1.27$ mm) using (a) $N = 5$ subcavities and (b) $N = 35$ subcavities, and (c) tall $N = 20$ subcavities with width $a = 2.54$ mm and height $b = 150$ mm.

quality factor would raise thanks to the detriment of the surface resistance (or increase of the electrical conductivity at the cavity walls). In this line, the RADES team has designed and manufactured four test single cavities (without the multicavity concept) based on the quasi-cylindrical model depicted in Figure 5.13.

These resonant cavities has been coated with two different superconducting materials: $REBa_2Cu_3O_7$ (or REBCO) [153], and Nb_3Sn [154], obtaining higher quality factor values compared to the case with copper coating. These materials have been selected because the experiment will runs in magnetic fields of 11 T or higher, so superconductors with high critical magnetic fields are required. The designed microwave cavities resonate at roughly 9 GHz with a shape optimised for superconducting coating and to fit within the bore of the SM18 magnet [90]. These structures were tested under high magnetic fields at 4.2 K. More details about these designs can be found in [90] and in the PhD thesis of Jessica Golm. In addition, a data taking has been carried out recently with a HTS haloscope by the RADES team in the SM18 magnet, whose physics results are being analysed (on going activity).
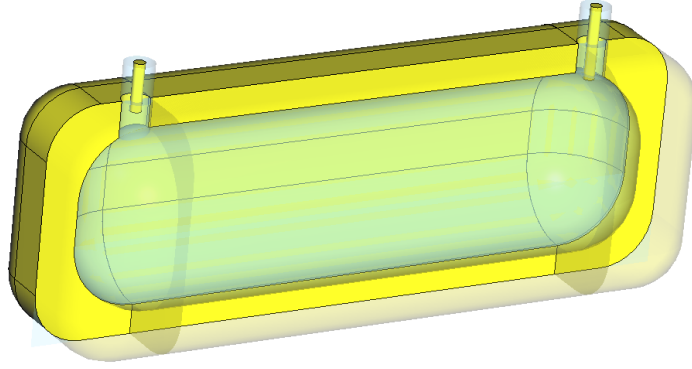
Figure 5.13: 3D model of the HTS haloscope design based on a quasi-cylindrical single cavity operating at 9 GHz. The technical drawings for the manufacturing of this prototype are depicted in Appendix I: Technical Drawings (see Figures A.12 and A.13).

5.2.4 *BI-RME 3D*

Also, the RADES team has been making an effort to implement the Boundary Integral-Resonant Mode Expansion (BI-RME) 3D method to the study of dark matter axions. With this technique, the EM coupling axion-photon in a microwave resonant cavity has been revisited. This full-wave modal approach was used for a thorough examination of the axion field excitation inside a microwave cavity. The EM field created by the axion-photon interaction may be expected to be driven by electrical charge and current axion densities in this case. These current densities have been included into the expressions of the BI-RME 3D method, representing the RF EM field within a cavity as an integral incorporating the cavity Dyadic Green's functions (under Coulomb gauge) and such densities. Any arbitrary spatial and temporal variation in the magnitude and phase field of the axion may be accounted by this approach.

Then, a basic network driven by the source of the axion current has been achieved. This current illustrates the coupling between the field of the axion and the modes of the resonant cavity. Employing this technique, the extracted and dissipated RF power can be computed as a function of frequency over a wide frequency range without using the Cauchy-Lorentz approximation. With this, it has been accomplished the spectrum of the EM field generated in the cavity, considering modes close to the axion one. Therefore, a comprehensive information of the cavity signal (in amplitude and in phase) is obtained using this approach. This might be an interesting subject for future research if the axion phase is a key parameter.

One of the most significant advantages of this approach is that it provides a precise frequency response throughout a broader frequency range rather than simply at the resonant frequency. To replicate the frequency response near the resonance it is not necessary to apply the Cauchy-Lorentz approximation (like for the traditional method). In addition, it permits the derivation of an expression indicating that the response to each resonance is influenced not only by that resonance but also by the others: there is a coupling between

all the resonances. This indicates that the axion might excite more than one resonance because they are all interconnected. When resonances are sufficiently apart, overlapping is minor; nevertheless, it is critical when the resonances are close (mode mixing issue). The traditional technique does not take resonance couplings into consideration. More details about the BI-RME 3D method can be found in [81] and in the PhD thesis of Pablo Navarro Martínez. The present formulation can be extended to the analysis of arbitrary shape dielectric and magnetic elements in the axion-photon coupling domain, which is under study.

5.3 CONCLUSIONS

Other investigations for enhancing the haloscope designs of the RADES group have been explored in this chapter. In the first section, a comprehensive novel technique for rejecting unwanted modes developed in this PhD thesis, has been presented. This method, which is based on the combination of several ports in a single haloscope by phase-matching, has been tested with simulations and with experimental prototypes, giving satisfactory results. The study of this approach has opened up several lines of research to develop this concept further.

Additionally, in the second section of this chapter, additional investigations carried out by the RADES team and this PhD thesis has been shown. Firstly, it has been mentioned the possibility of implementing QuBits elements in the haloscopes developed by this group in order to reduce the temperature of the system (thus increasing the figure of merit of detection). Then, some of the haloscope designs being developed at frequencies different from those used in this work (UHF and W bands) are shown. Next, the studies that are being carried out to improve the unloaded quality factor of dark matter detectors through the implementation of superconducting materials have been described. These materials substantially increase the electrical conductivity of the cavities, and thus the detector performance. Finally, an efficient analysis has been presented to analytically characterise the axion field behaviour inside a resonant cavity by means of the BI-RME 3D method.

6

RF BANDPASS FILTERS FOR SATELLITE COMMUNICATIONS

As it is introduced in 2.5, the development of RF waveguide filters for applications related with the satellite communication field has emerged as a spin-off of the multicavity haloscope designs, which are originally employed for the detection of dark matter axion particles in the fields of the cosmology and astroparticle physics. The investigations of the filters from this section has been carried out in order to contribute to the scientific community with new radio frequency components that can be used to improve the RF payloads of future communication satellites.

In section 6.1, this PhD thesis adds to the scientific field of AM waveguide filter production by demonstrating how evanescent mode filter designs may be fabricated utilising 3D printing methods. The main target of this work is to complement and expand the studies carried out in [155] about 3D printed evanescent mode filters produced from dielectric materials (usually employed in AM techniques) that can be produced quickly and cheaply. Improvements have been applied to these prototypes through the use of *tuning screws*, which are commonly used in in the tuning process of waveguide filters [74].

On the other hand, in section 6.2, it is presented the studies carried out to apply the ideas of the alternating (see Figure 2.17) [80] and 2D (see section 3.1.3) topologies of haloscope designs in the design of RF bandpass filters for satellite communication applications. The objective of this work is to optimize the final volume, weight and footprint of the filters, thus reducing the total cost of the launch where they can be embarked.

6.1 EVANESCENT FILTER WITH AIR HOLES

6.1.1 *Introduction*

One of the most significant efforts in the microwave engineering sector is the creation of filters in waveguide technology [156]. In reality, waveguide filters are utilised in the input / output stages of many systems, both in space and on the ground, where the use of low loss materials and high power handling are key criteria [74]. Moreover, several physical limitations such as low volume and tiny footprint in the structures are also necessary. Additionally, the most prevalent method of manufacturing microwave filters in waveguide

technology is by Computer Numerical Control (CNC) machining, which has also been employed in the production of the haloscopes studied in this PhD thesis. Regrettably, CNC machining processes have constraints when it comes to producing some complicated geometries [157].

Therefore, developing AM methods are becoming highly appealing for producing innovative passive filters with complex geometries [158, 159], and other RF devices [160, 161]. Complex structures may, indeed, be made fairly quickly using AM methods [162]. Utilizing thermoplastic elements, for example, and then metallizing (like the copper coating technique employed for the haloscopes studied in previous chapters) the components, the filter structure mass may drastically be lowered [163]. The walls of the structures studied in [164] are metallized employing an automated deposition procedure of silver ink for a high conductivity. In [165] authors employ a more sophisticated approach, in which air passages are incorporated into the plastic walls, which are subsequently loaded with a liquid metal. It is also worth noting that [164] utilised a similar technique to develop a waveguide switch, whose performance is accomplished by pumping liquid metal in and out of tubes based on plastic materials. Moreover, careful adjustment of the geometry of conventional implementations can greatly minimise the Insertion Loss (IL) parameter of the filter devices [166]. Some scientists have attempted direct geometrical alterations on the cavities, employing rounded forms, resulting in novel resonators with much improved unloaded quality factors. The spherical resonators proposed in [167, 168], or the utilisation of sophisticated rounded forms described in [169] are also interesting studies in this approach.

The use of dielectric resonators in the context of AM has also been investigated in the past few years. Several Fused Deposition Modeling (FDM) or StereoLithogrAphy (SLA) AM printers available on the market employ some thermoplastics and ceramic elements with good dielectric performances (such as low loss tangent) [170, 171]. Many ways for incorporating 3D printed dielectrics into a waveguide filter prototype have also been considered. The work [172] provides an intriguing study, in which a dielectric resonator based on alumina with $\tan\delta < 2 \times 10^{-3}$ and $\epsilon_r \approx 10$ operating with a TM mode is utilised to directly print a multicavity filter with $N = 2$ subcavities. After the housing manufacturing by AM techniques, the exterior sides are metallized to form the structure lateral sections. The structure provides low losses, but with modest frequency deviations due to the tolerances of the 3D printing. Another option is to make the dielectric resonators out of a single plastic piece and fix them into the housing with the metallic elements of the coupling irises. This method is shown in [173], where plastic bars are employed for the printing of the dielectric resonators using an in-line topology, and in [174], with more sophisticated techniques for interresonator couplings.

In this regard, in this work it has been addressed the design of the evanescent mode filter designs shown in Figure 6.1: a straight version and an horizontal folding version.

The latter reduces the footprint in the longitudinal direction (z−axis) and uses a more rectangular surface than the straight filter. In addition, it has been studied how to enhance the response of these filters (fabricated utilising 3D printing methods in [155]) by the use of *tuning screws*. In [141, 175], a comparable collection of evanescent filter topologies is
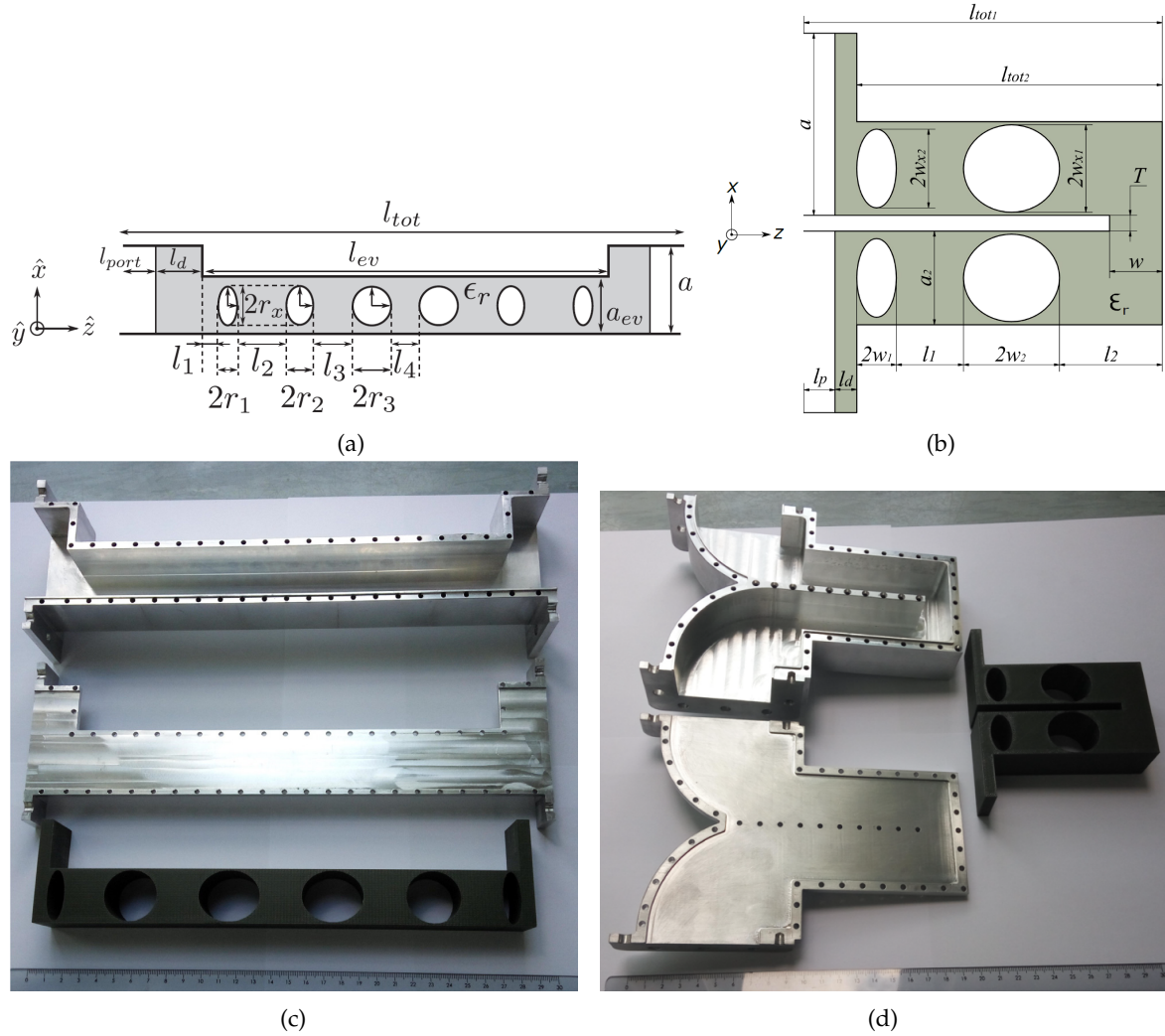
Figure 6.1: 2D sketches ((a) and (b)) and manufactured pictures ((c) and (d)) of the investigated evanescent mode filters based on two different multicavity topologies: straight with $N = 5$ subcavities ((a) and (c)), and horizontally folded (2D) with $N = 4$ subcavities ((b) and (d)). The technical drawings for the manufacturing of these prototype are depicted in Appendix I: Technical Drawings (see Figures A.14, A.15, A.16 and A.17 for the straight filter, and Figures A.18, A.19, A.20 and A.21 for the folded filter).

investigated in Substrate Integrated Waveguide (SIW) technology. The prototypes studied in this PhD thesis are based on commercial AM dielectric materials for an inexpensively production. The filter designs of this study integrate AM components for the dielectric elements with traditional aluminium CNC machining for the housing, resulting in an hybrid production technique. Using this method, the metallic sections of the structures are kept basic, while complicated shapes for the dielectric elements may be easily fabricated.

The dielectric components described in this study are realised with a cheap plastic commercially available in [176], the *ABSplus* material from *Stratasys*, which has a permittivity value of $\varepsilon_r = 2.55$. This material is nowadays accessible in low-cost 3D printers. The first structure presented (see Figures 6.1a and 6.1c) is a rectangular multicavity filter of $N = 5$ subcavities with a decreased width section (compared to the standard WR-229, which employs $a = 58.166$ mm) filled with the ABSplus dielectric, with interresonator and input / output couplings made of elliptical air holes. The second filter (see Figures 6.1b and 6.1d) is based on the same concept but folded horizontally and employing $N = 4$ subcavities.

It should be noted that the suggested structures are referred to as *evanescent mode waveguide filters* since the frequency of the operating mode, the TE_{10}, would be under its cut-off frequency at the waveguide section with reduced width (a_{ev}) if the ABSplus were not introduced. This mode can be propagated when the dielectric material is placed inside this section thanks to the higher permittivity value and its influence on the cut-off frequency. As a result, the structure resonators are generated by dielectric-filled patches within this waveguide section of decreased width. The TE_{10} mode, on the other hand, cannot propagated at the air holes contained inside this evanescent section. As a result, such air areas are utilised as coupling elements.

The 3D printed plastic elements were created employing a Fused Deposition Modeling (FDM) 3D printer in the UPCT. In contrast, the aluminium cases were created utilising CNC machining at *Mecanizados JJ Celdran S.L.U.*, Cartagena, Spain [112]. This technique provides a quick and low-cost filter production, albeit the combination of AM for plastic and CNC for the housing provides a penalty of slightly increased insertion losses. This research also demonstrates another advantage of this hybrid production technique. Specifically, using the same exterior aluminium housing, various filters with varying transfer functions may be simply implemented. All that is required is the 3D printing of new dielectric pieces. Using this strategy, just one common metallic case is produced using CNC machining processes, resulting in significant flexibility by making various low cost plastic components to obtain diverse transfer functions.

6.1.2 *Bandpass filters design*

Two Chebyshev filters (composed of 4 and 5 resonators) with a Return Loss (RL) of $RL = 21$ dB were utilised in this study to show the hybrid production technique. The filters were constructed in the C-band, operating at $f_c = 3.68$ GHz, being f_c the central frequency, and utilising a bandwidth of $BW = 120$ MHz (this is, a fractional bandwidth of $FBW \approx 3.2\%$). For simplicity, the filters are constructed using an in-line topology, as no interresonator cross-couplings are implemented. It should be noted, nevertheless, that this type of coupling could be added at the folded design just by opening (with CNC machining, for example) an iris window between the first and last subcavities, similarly to the

2D haloscope manufactured in this PhD thesis (see Figures 3.20 and 3.21). As mentioned in previous chapters, the use of the coupling matrix is very common in waveguide filter design. In this case, the coupling matrices used for the straight and folded structures are as follows:

$$M_{N+2}^{Straight} = \begin{pmatrix} 0 & 1.0137 & 0 & 0 & 0 & 0 & 0 \\ 1.0137 & 0 & 0.8653 & 0 & 0 & 0 & 0 \\ 0 & 0.8653 & 0 & 0.6357 & 0 & 0 & 0 \\ 0 & 0 & 0.6357 & 0 & 0.6357 & 0 & 0 \\ 0 & 0 & 0 & 0.6357 & 0 & 0.8653 & 0 \\ 0 & 0 & 0 & 0 & 0.8653 & 0 & 1.0137 \\ 0 & 0 & 0 & 0 & 0 & 1.0137 & 0 \end{pmatrix} \tag{6.1}$$

$$M_{N+2}^{Folded} = \begin{pmatrix} 0 & 1.0587 & 0 & 0 & 0 & 0 \\ 1.0587 & 0 & 0.9348 & 0 & 0 & 0 \\ 0 & 0.9348 & 0 & 0.7131 & 0 & 0 \\ 0 & 0 & 0.7131 & 0 & 0.9348 & 0 \\ 0 & 0 & 0 & 0.9348 & 0 & 1.0587 \\ 0 & 0 & 0 & 0 & 1.0587 & 0 \end{pmatrix}. \tag{6.2}$$

It is important to note here that, unlike the coupling matrices used for the design of multicavity haloscopes, in the study of communications filters the coupling matrices are usually based on sizes $(N + 2) \times (N + 2)$ in order to take into account the coupling between the input port with resonator 1, and the output port with the last resonator (the input and output couplings). This is because such couplings are used as a design parameter (in this case, for the bandwidth specification of the filter response). In axion multicavities, these couplings were directly parameterised by the variable β which, as seen in previous chapters, should be as close to unity as possible. On the other hand, it should be noted that in the design of haloscopes, capacitive couplings were said to give positive signs, whereas inductive couplings were said to give negative signs. However, as can be seen in equations 6.1 and 6.2, in the design of bandpass filters for communication applications the capacitive and inductive couplings give negative and positive signs, respectively, and this is the way in which these couplings are typically used in the microwave community [74].

Figure 6.1 shows 2D drawings of the suggested filters. For the input / output ports a standard WR-229 was employed, which is based on a waveguide cross section of width and height $a = 58.166$ mm and $b = 29.083$ mm, respectively. Both filters are made out of a dielectric component inserted inside an evanescent waveguide section with a sequence of elliptical air holes. The TE_{10} mode, which can propagate in the evanescent section once the dielectric is introduced, is employed in these filters. The elliptical air sections, where the cut-off frequency of this mode is above the operation frequency, are utilised as interresonator coupling components. Then, higher order modes are not propagated close to the operating frequency thanks to the reduce width section where the dielectric elements are located. The dielectric areas between between air holes (see l_i in Figures 6.1a and 6.1b) determine each subcavity resonant frequency. The shape of the air holes are based on elliptical cylinders, and their size (see r_i and w_i in Figures 6.1a and 6.1b) is employed to adjust the interresonator and input / output couplings. As a result, six air holes are necessary for the design of the first filter with $N = 5$ subcavities. For the second filter, with $N = 4$ subcavities, only 4 air holes are needed since an iris window is utilised

to couple resonators 2 and 3, at the folding section. The size of the first and last air holes controls the input / output couplings in these configurations. The step discontinuity required to create the evanescent waveguide section of width a_{ev}, on the other hand, have an impact on this coupling.

The dielectric component in both filters is longer than the waveguide section (l_{ev} in the straight structure), as seen in Figure 6.1. The supplementary length (l_d) helps the dielectric component to align with the aluminum housing. It was also confirmed that the additional dielectric portion aids in increasing the filter input / output coupling value. The additional length l_d value cannot, however, be extremely high since this section may become resonant owing to the establishment of an air / dielectric discontinuity (a trade-off is imposed here).

It should be noted that the cylinders in both constructions illustrated in Fig. 6.1 are elliptical in form, and the radius along the $x-$axis has been set to $r_x = 14$ mm. With an evanescent waveguide width of $a_{av} = 30$ mm, this ensures a gap of 1 mm between the side walls of the waveguide and each hole. On the other hand, the folded filter implements 90° waveguide bends added to its input / output ports (see Figure 6.1d). These newly added sections are air filled. The reason for adding these waveguide bends is that they avoid the space problem in the fitting of the flanges with the manufactured filter.

A variant of the conventional even / odd analysis approach, as described in [177], was utilised for the design process. Using this technique, the interresonator coupling is given as a function of the semi axis of the elliptical cylinders (r_i and w_i for the first and second filters, respectively), while the length (l_i) is employed for the subcavity resonant frequency. The external quality factor Q_{ext} is utilised to adjust the input / output coupling value, as defined in [74, 178]. This technique, which employs the semi axis of the first / last air holes for the input / output coupling design, respectively, is based on the *Doubly Terminated Resonator* approach [74]. After the design and optimisation of these two filters, whose details can be found in [155], the extracted final dimensions are shown in Tables 6.1 and 6.2.

Variable	Value (mm)	Variable	Value (mm)	Variable	Value (mm)
l_{port}	10	l_1	0	r_1	4.859
l_d	7	l_2	22.11	r_2	14.54
l_{ev}	258.847	l_3	23.23	r_3	16.86
l_{tot}	292.847	l_4	23.13	r_x	14

Table 6.1: Final dimensions for the straight filter. The dimensions are referred to the sketch from Figure 6.1a.

Figure 6.2 depicts the broad band responses of both bandpass filters. The exhibited findings were obtained using the electromagnetic simulator HFSS, from ANSYS [179]. From the first filter response it can be seen that the obtained results are: a centre frequency of $f_c = 3.678$ GHz, a bandwidth of $BW = 120$ MHz ($FBW \approx 3.2\%$), a Return Loss of

Variable	Value (mm)	Variable	Value (mm)	Variable	Value (mm)
l_p	10	l_1	21.55	w_1	6.343
l_d	7	l_2	32.98	w_2	15.4
l_{tot1}	115.016	T	5	w_{x1}	14
l_{tot2}	98.016	w	16.9	w_{x2}	12.6

Table 6.2: Final dimensions for the folded filter. The dimensions are referred to the sketch from Figure 6.1b.

(a)

(b)
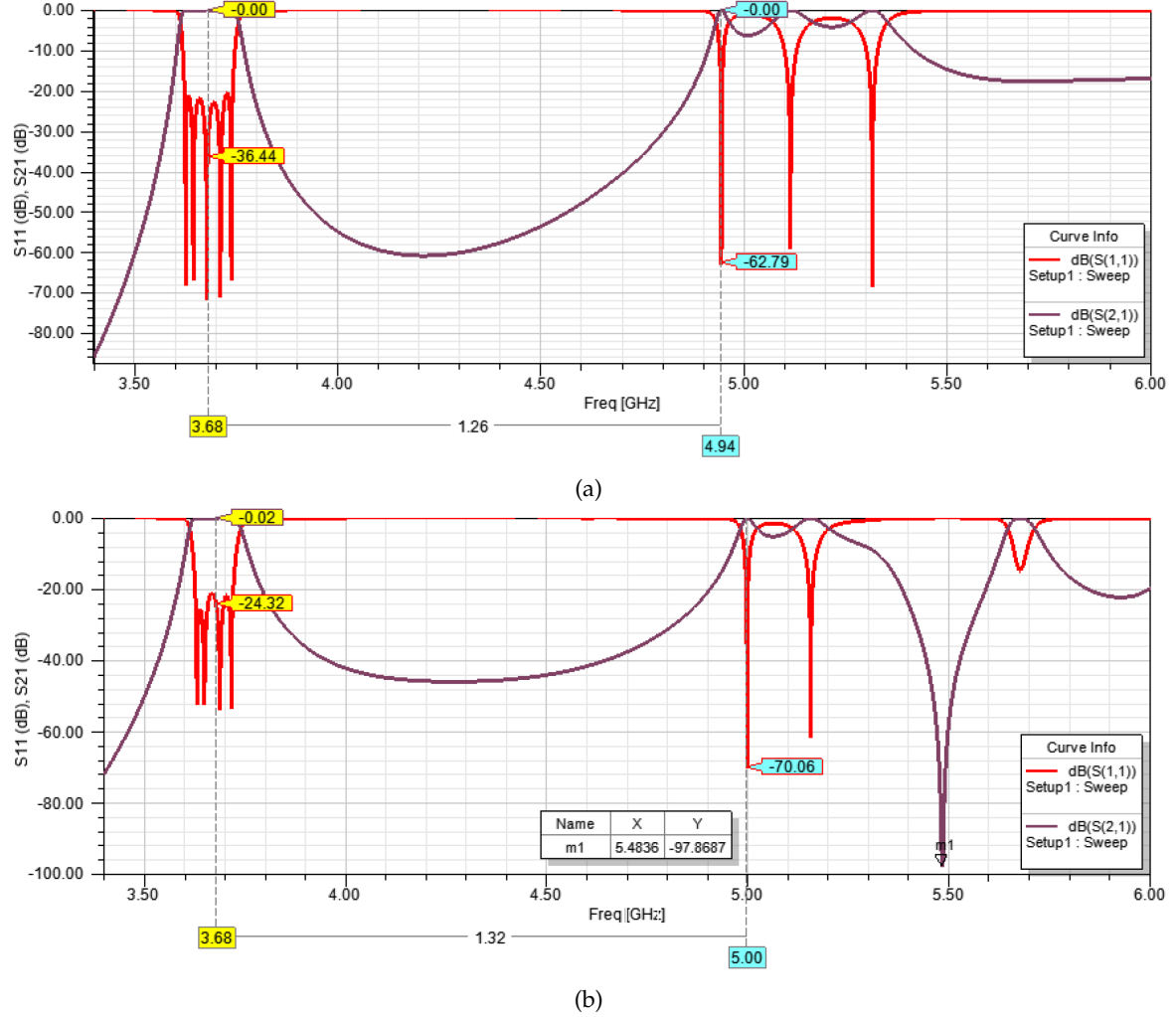
Figure 6.2: Scattering Parameters (S_{11} and S_{21}) of the designed evanescent mode filters in wide band: (a) straight structure, and horizontally folded multicavity.

$RL = 20.31$ dB and a Spurious Free Range (SFR) of $SFR = 1.26$ GHz. For the second one: $f_c = 3.668$ GHz, $BW = 95$ MHz ($FBW \approx 3.2\%$), $RL = 20.1$ dB and $SFR = 1.32$ GHz. Unfortunately, due to the remarkable geometrical modification in the ports in the second filter, the input and output couplings are more sensitive to changes, which has led to a difficult bandwidth optimisation, resulting in a value 25 MHz below the synthesis target. Nevertheless, it can be considered a reasonable value for sending the filter to the manufacturing stage.

6.1.3 *Experimental results*

As mentioned in the previous sections, an hybrid production strategy was employed to execute the two proposed filters. The dielectric pieces were created via AM, whereas the metallic housings were made using CNC machining. The metallic portions were made of aluminium, while the dielectric sections were produced with ABSplus on a 3D-printer (Dimension 1200-bst model [180]).

The elements produced for the straight and folded versions are depicted in Figures 6.1c and 6.1d, respectively. For each filter, the housing is constructed in two components, the main body and the top cover. Because the design is so basic, a normal CNC milling method may be employed. The dielectric components are 3D printed in a single structure, for both filters, that includes all resonators and couplings. As a consequence, aligning the dielectric components inside the metallic bodies is straightforward. The usage of two expanded portions of length $l_d = 7$ mm at both ends of the ABSplus parts also helps with alignment.

6.1.3.1 *Evanescent straight filter*

The measured findings of the first filter, acquired directly from the constructed prototype, are depicted in Figure 6.3a (blue and red lines with circle symbols). These measurements
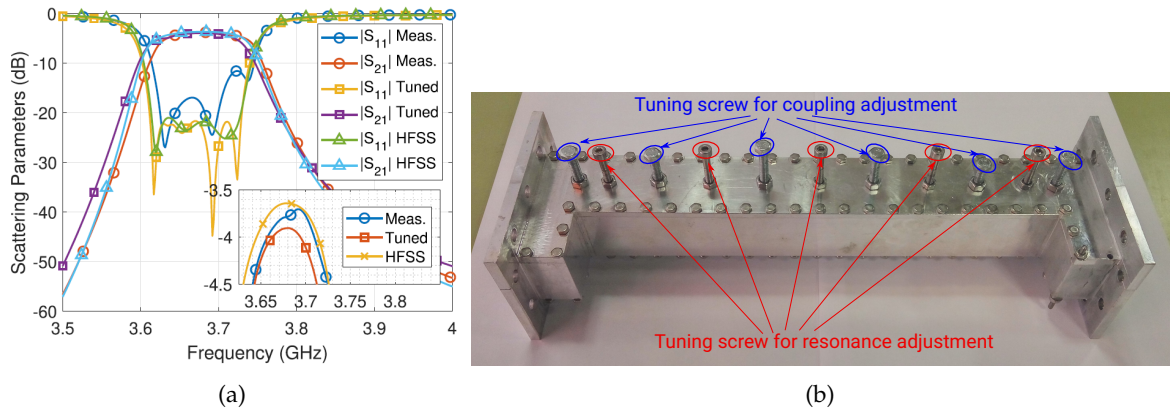
Figure 6.3: Straight evanescent RF filter: (a) Scattering Parameters (S_{11} and S_{21}) from simulations, measurements (before tuning) and tuning screw adjustment, and (b) picture of the filter with the incorporated tuning screw system at the 6 couplings and 5 resonators (11 screws in total). The inset details the losses (IL) at the passband.

are compared to the HFSS simulation outcomes incorporating the ABSplus losses and the aluminum conductivity (green and light blue lines with triangle symbols and yellow line with square symbols from Figure 6.3a): $\tan \delta_{ABSplus} = 0.0053$ and $\sigma_{Al} = 3.8 \cdot 10^7$ S/m. As it is shown, the response achieved immediately after manufacturing agrees quite well with the simulation results.

To incorporate the ABSplus loss tangent in HFSS, it has been utilised a value equals to the largest one provided by the company ($0.0046 < \tan \delta < 0.0053$) [176]. On the other hand, it has been checked that the aluminum conductivity has little impact on the overall

IL parameter for both filters. This investigation verifies that the main problem regarding the losses comes from the ABSplus loss tangent. As depicted in the inset from Figure 6.3a, the lowest IL value at the passband is $IL = 3.7$ dB.

Apart from the IL performance, the other observed parameters are the central frequency $f_c = 3.671$ GHz, the return loss $RL = 12$ dB and the bandwidth $BW = 117$ MHz. When compared to the simulation design results, the response from the manufactured structure demonstrates excellent agreement in terms of f_c and BW. This is a strong indicator that the ABSplus relative permittivity is quite close to the value provided by the company ($\varepsilon_r = 2.55$) [176]. However, the observed minimum RL parameter value inside the passband is significantly greater than the predicted one. Also, it can be observed that several reflection poles are complex. This indicates that the filter is not properly adjusted (or tuned). Generally speaking, this is typical of low-accuracy production mechanisms. The RL is, undoubtedly, the parameter with the highest sensitivity performance in a microwave filter response.

The detuning detected in the filter response, on the other hand, may be addressed by installing tuning screws in the produced prototype, as illustrated in Figure 6.3b. *M4* tuning screws were utilised in this circumstance. As it can be observed, 11 tuning screws were utilised to fine-tune the response of the structure. To adjust the interresonator and input / output couplings, six screws are situated in the middle of the air cylinders. Five extra screws are put in the centre of the resonators (inside the dielectric areas between adjacent air cylinders) for tuning the resonant frequencies of the subcavities. The dielectric material has been pierced at the proper areas for the placement of these 5 screws. It is worth noting here that the screw perforating holes will cause the resonances to move to higher frequencies. Nevertheless, the existence of the screws in the resonator sections lowers their resonant frequencies, balancing the frequency changes. This explain why the structure with the incorporated tuning system (see Figure 6.3b) can be adjusted while maintaining the same f_c value as the previous prototype without screws.

Note that metric M4 screws were used to create the required adjusting mechanism. Then, air holes with a depth of 14.5 mm and a diameter of 5 mm were drilled in the AB-Splus material. This resulted in a 29 MHz rise in the resonant frequency of each subcavity. Following that, *M4* screws were inserted into the perforations, giving a 23.2 MHz/mm tuning sensitivity. This means that with a depth of little more than 1 mm, the screws compensate for the first frequency shift caused by the air perforation holes. It should be noted that this tuning approach might also be used in other comparable cases, such as if the initial measured f_c value is too small. To solve this situation, the air perforation holes might be made larger (higher diameters and depths) to induce a higher increase in the subcavity resonant frequencies. In this case, using screws with smaller metrics could be more suitable in order to have more control over these resonant frequencies, although

their penetration should be higher.

For the tuning of the structure with this system, the following steps were carried out:

- First, all screws are extracted to the maximum.

- Secondly, only by operating with the 4 screws on the interresonator couplings it is searched an equiripple response, where all poles (5 in the case of this filter) are visible.

- Then, the 5 screws on the resonators are adjusted for the fixing of the central frequency ($f_c = 3.68$ GHz in this case), but always being careful to keep all poles in the real frequency axis.

- Later, the first and last screws, those on the input / output couplings, are tuned for the adjustment of the bandwidth ($BW = 120$ MHz in this case).

- Finally, an iterative process is performed adjusting all the screws taking into account the functionality of each one according to the previous steps for improving the response until the target specifications are met.

The final tuned response of the first filter is visible in the plot from Figure 6.3a (yellow, purple and red lines with square symbols). The results suggest that the tuning procedure was definitely successful. The structure response provided the same f_c and BW values as the initial specs. Additionally, using a $RL = 21$ dB, a nearly equiripple response was achieved. Unfortunately, the passband enhancements come at the price of a modest rise in the IL parameter, which now deteriorates to $IL = 3.9$ dB, as it is depicted in the inset of Figure 6.3a. In general, the built structure displayed good filter properties. Furthermore, the tuning procedure has proven to be successful in adjusting for manufacturing defects induced by 3D printing.

After obtaining the tuned prototype, it was investigated the manufacturing tolerance sensitivity of this filter. It was used the theory described in [181] to compute the mechanical precision required to ensure a deterioration in the RL parameter of less than 2 dB. According to the findings of this research, the required accuracy is of $20\,\mu$m. Modern state-of-the-art AM methods provide less accurate processes ($\sim 250\,\mu$m). This work demonstrates that the production of these type of filters necessitates the use of a tuning or adjustment system to compensate for imperfections in AM techniques.

As a final research with this filter, in this PhD thesis it is illustrated how the hybrid manufacturing technique suggested in this work may generate multiple types of transfer functions with a simple and cost effective technique. The concept is based on utilising the same housing to produce multiple responses by 3D printing additional dielectric structures. To demonstrate this principle, it is now proposed the design of a new evanescent filter with air cylinders and the identical requirements as previously, but with a

bandwidth increased to $BW = 175$ MHz.

A significant dimension constraint must be considered while designing this new version: the overall length of the evanescent section (l_{ev}) must be the same as that of the previous version (this is, $l_{ev} = 258.847$ mm). The dielectric structure of the first design (Piece 1) is depicted in Figure 6.4a, and it is compared with the new prototype with larger bandwidth (Piece 2). As it can be observed, both designs keep the same evanescent section
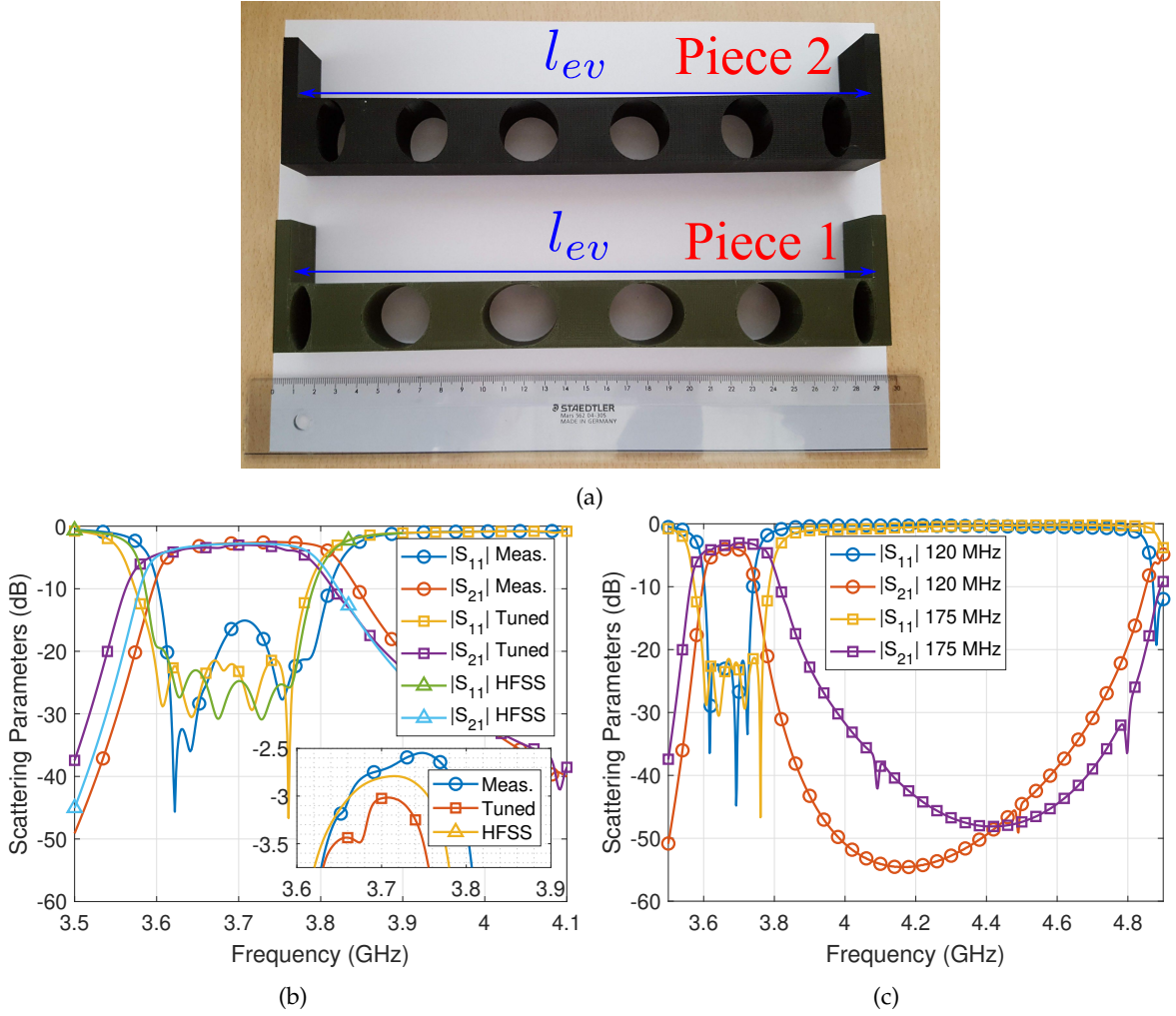
Figure 6.4: Results from the straight evanescent RF filter with enhanced bandwidths: (a) picture of the two 3D-printed ABSplus dielectric versions with different bandwidth value ($BW = 120$ MHz for Piece 1 and $BW = 175$ MHz for Piece 2), (b) Scattering Parameters (S_{11} and S_{21}) from simulations, measurements (before tuning) and tuning screw adjustment of the filter employing the Piece 2, and (c) broad band response with the tuned measurements comparing both versions.

length (l_{ev}). Nevertheless, the new dielectric component has air cylinders with smaller dimensions to provide higher coupling values. Also, the smaller the elliptical air cylinders, the greater the loading effects of the interresonator couplings. As a result, the subcavity lengths are decreased, resulting in air holes that are closer together than in the previous ABSplus piece. It is crucial to note that the length l_{ev} may be the same in both struc-

tures thanks to the extra degree of freedom offered by the length l_1 indicated in Figure 6.1a.

The process for designing the filter with larger bandwidth follows the same concepts as the first version. Table 6.3 contains the final dimensions for the filter version with the Piece 2, referred to the variables from the sketch depicted in Figure 6.1a. The new

Variable	Value (mm)	Variable	Value (mm)	Variable	Value (mm)
l_{port}	10	l_1	8.25	r_1	6.752
l_d	7	l_2	22.059	r_2	11.702
l_{ev}	258.847	l_3	23.255	r_3	13.623
l_{tot}	292.847	l_4	23.411	r_x	14

Table 6.3: Final dimensions for the straight evanescent filter with an enhanced bandwidth ($BW = 175$ MHz). The dimensions are referred to the sketch from Figure 6.1a.

filter version is provided by substituting the structure Piece 1 with Piece 2 employing the same aluminum case (see Figure 6.1c). Figure 6.4b depicts the measurements acquired immediately after production (blue and red lines with circle symbols).

In terms of f_c and BW, the overall performance is fairly good: $f_c = 3.71$ GHz, $BW = 180$ MHz. Because of the increased bandwidth, the minimum IL value inside the bandpass is now better ($IL = 2.5$ dB). Moreover, the RL value is good, being higher than $RL = 15$ dB within the bandpass. We also employed the tuning screw system as in the first version to increase this parameter (see Figure 6.3b). Figure 6.4b depicts the filter response after tuning adjustment (yellow, purple and red lines with square symbols). As it can be observed, the passband after tuning shows a central frequency of $f_c = 3.687$ GHz and a bandwidth of $BW = 172$ MHz. In addition, the measurements demonstrate a nearly equiripple S_{11} parameter with a return loss value higher than $RL = 21$ dB. These passband enhancements come at the trade-off of a greater IL value, whose minimal obtained value is $IL = 3$ dB. The simulated response (with HFSS) is also given in Figure 6.4b for comparison (green, blue and yellow lines with triangular symbols). The losses in these simulations are implemented using the same aluminium conductivity and ABSplus losses as in the previous version. As it is shown, the losses anticipated by HFSS are fairly comparable to those observed immediately after manufacture, however after tuning the prototype exhibits greater losses owing to the impact of the screws.

Figure 6.4c shows a final comparison of the two evanescent filters with elliptical air cylinders and different bandwidths. For this comparison, the response measurements, after tuning, were chosen. It can be clearly observed the bandwidth differences between the two versions. The return loss parameter in both filters is quite good (better than $RL = 20$ dB). In this plot, the responses are displayed across a wide frequency range so that the SFR value may be seen. As it can be observed, the next non-desired mode is located at $f_{sp} \approx 4.8$ GHz for both versions, producing $SFR \approx 1$ GHz. In general, the findings in the straight evanescent filters demonstrate that the hybrid CNC machining and 3D printing method that is proposed in this PhD thesis may be utilised to produce flexible and low-cost

microwave filters with fairly good electrical characteristics. The sole disadvantage found in in these prototypes, is that the insertion losses are slightly greater compared to traditional machining methods. Nevertheless, if the accessibility of enhanced materials for the 3D printing increases, this disadvantage could be overcome in the future.

6.1.3.2 *Evanescent folded filter*

The measurements results of the second filter, obtained from the manufactured structure, are shown in Figure 6.5. As can be seen, unlike the previous case, the response of this
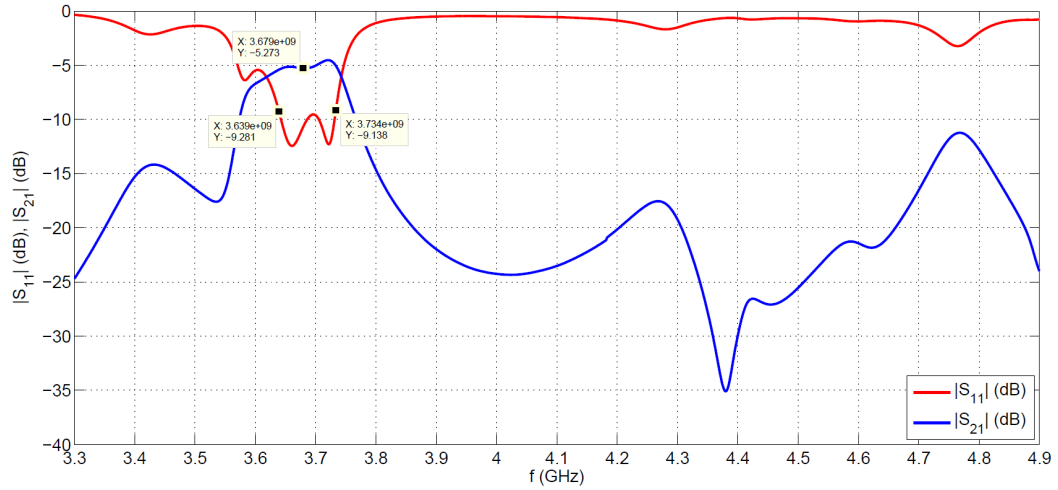
Figure 6.5: Measurements from the manufactured prototype of the evanescent folded design before the tuning.

filter has somewhat poor passband characteristics, giving a return loss of $RL = 9.5$ dB and a insertion loss of $IL = 5.27$ dB. On the other hand, the bandwidth and central frequency are quite good compared to the HFSS simulation results (see Figure 6.2b): $BW = 95$ MHz and $f_c = 3.679$ GHz, respectively.

Similarly to the straight evanescent filter, it has been concluded that the aluminum conductivity impact on the overall insertion losses is not very high. However, the IL parameter is very sensitive with the ABSplus loss tangent and its manufacturing process (roughness, for instance). In addition, it is believed that the extra losses may be due to poor electric contact between the dielectric and the metallic housing, where unwanted small air gaps may be created. Two of the possible solutions that have been considered are: 1) applying conductive paint on the inner walls of the metallic housing and on the outer walls of the dielectric part, and 2) sanding the top / bottom dielectric faces (to increase the contact between the housing parts). Further research has led to the conclusion that this high level of IL may also be due to the 25 MHz difference in bandwidth between the synthesis and the designed responses, discussed in section 6.1.2.

Also, it can be seen that the four reflection poles (see Figure 6.5) are not in the response. This suggests again that the filter is not properly tuned. For this reason, the detuned response of this filter can be adjusted by installing and employing a similar

tuning screw system in the manufactured prototype as in the previous filter. As depicts Figure 6.6a, the reflection coefficient S_{11} has been corrected, which has been obtained by following the steps described in the previous subsection. $M4$ tuning screws were
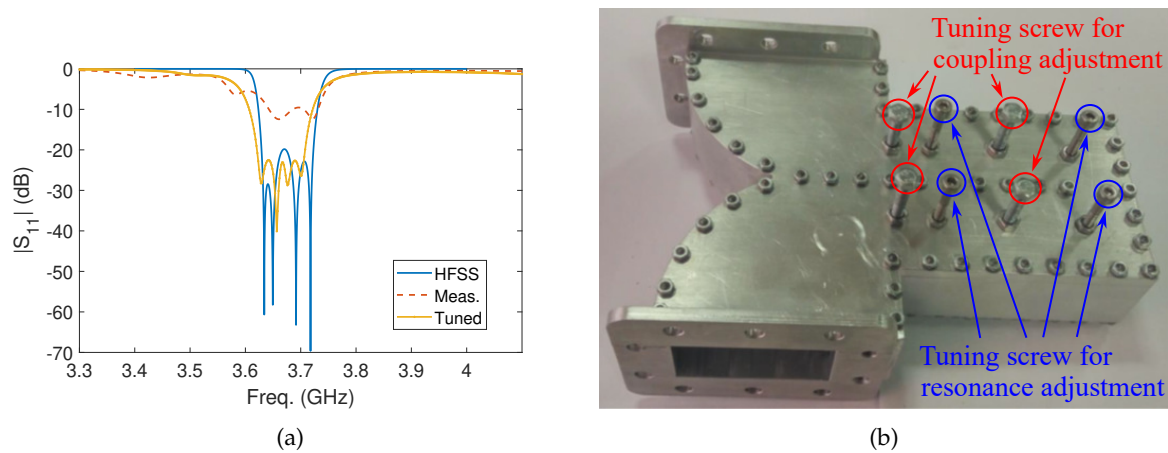
Figure 6.6: Folded evanescent RF filter: (a) S_{11} parameter from simulations, measurements (before tuning) and tuning screw adjustment, and (b) picture of the filter with the installed tuning screw system at 4 air cylinder couplings and 4 resonators (8 screws in total).

used as well for the tuning of this filter (see Figure 6.6b). As it can be seen, 8 screws were employed to fine-tune the response of the prototype. To adjust the two of the interresonator couplings and the input / output couplings, four screws are situated in the middle of the air holes. For the time being, no screws have been introduced in the inductive iris window coupling between resonators 2 and 3 (although it could be implemented if necessary). Four extra screws are put in the centre of the resonators (between adjacent air holes) for tuning the resonant frequencies of the resonators. The ABSplus structure has been pierced at the center of the resonators for the placement of these four screws, as in the previous case. Again, the screw perforating holes cause the resonances to shift to higher frequencies. However, the existence of the screws in the reson-ators compensates this effects, maintaining the same f_c value as in the case without screws.

As in the scenario with the straight evanescent filter, it has been employed the metric $M4$ for the screws to create the required tuning system. Thus, air cylinders with a depth of 14.5 mm and a diameter of 5 mm were bored in the ABSplus material at the center of the resonators. This resulted in a similar resonant frequency increase and tuning sensitivity (once $M4$ screws were inserted into the perforations) as in the pre-vious structure. In addition, using screws with other metrics could also be useful if needed.

Following the tuning screw steps, the final tuned response of the second filter is plot in Figure 6.6a. The results suggest that the tuning procedure was definitely successful in terms of S_{11}. The structure response provided the similar f_c and BW values as the initial specs. Additionally, using a $RL = 22.5$ dB, a nearly equiripple response was obtained. In general, the manufactured structure displayed good filter properties in terms of reflection coefficient. In addition, the tuning procedure has proven to be successful in adjusting for

manufacturing errors caused by 3D printing. However, insertion losses have not improved, and this clearly indicates that there is a contact problem between the cover and the housing body.

6.2 ALTERNATING IRIS FILTER

6.2.1 *Introduction*

As previously mentioned, the interest in the development of new geometries and topologies for waveguide bandpass filters for satellite communications purposes has increased in recent years. One of the limiting factors in the design of such filters is the weight, volume, and footprint inside the satellite, the reduction of which will be key to cost decrease. On the other hand, it is well known that the electromagnetic spectrum is occupied by a multitude of applications, so the selectivity of the filters (how steep the S_{21} parameter slopes fall outside the passband) will be a very important factor in the design of this type of structures for improving the out-band rejection. Such selectivity increases if transmission zeros are implemented in the filter responses, which are used in haloscopes for the rejection of unwanted modes, as covered in previous chapters.

In this line of work, in the previous section the design, manufacture and measurement of an horizontal folding filter with $N = 4$ resonators and five inductive couplings (three of interresonator type, and two of input / output type) has been shown. In addition, few investigations have been carried out in [155] to try to implement transmission zeros in this structure by an inductive cross-coupling between the first and last resonators (see topology in Figure 6.7a), this is, with an element $M_{14} > 0$. However, this topology
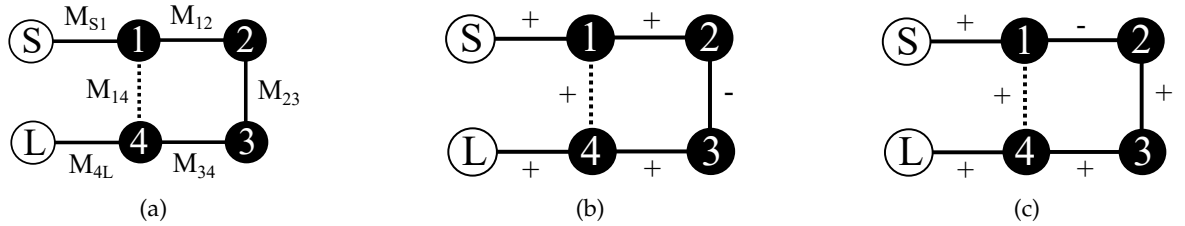
Figure 6.7: (a) Topology of a bandpass filter based on 4 resonators with a cross-coupling M_{14}. Cases for implementing real transmission zeros on a filter with all inductive couplings except (b) the M_{23} element, and (c) the M_{12} element, which are of capacitive type. A positive symbol ($+$) represents an inductive coupling, while a negative symbol ($-$) depicts a capacitive coupling. On the other hand, a solid line means an in-line coupling, while a dashed line represents a cross-coupling.

implemented complex zeros which, while they can help in improving the group delay equalisation, do not enhance the out-of-band rejection [74, 155]. To make these complex zeros real for better rejection, the sign of the M_{14} element must be changed, which was accomplished in [155] by a vertical folding in the structure. The solution proposed in this PhD thesis is to change the sign in non-cross-couplings with asymmetrical horizontally folded structures, which can provide flexibility in the design of higher order filters with

different implementations of zeros.

After an extensive search in the state of the art, it was found that the solution to this problem is through the use of a mix of iris types, as it is shown in [182] for symmetrical structures, the base of the concept that was discussed in previous chapters (mostly in section 3.1.2) with haloscopes in order to increase the separation between configuration modes (the alternating idea). Unlike haloscopes based on alternating multicavities, this technique is based on implementing a specific number of capacitive irises (or inductive irises if the structure is originally based on an all capacitive multicavity). In the case of the structure designed by [182], it is based on a symmetrical and vertically folded structure with $N = 4$ resonators and 6 couplings (4 of interresonator type, and 2 of input / output type), where one of them, the coupling between resonators 2 and 3 (M_{23}), is capacitive and the rest are of inductive type. This design is composed by standard waveguides without dielectrics or evanescent sections (so easier structures for analysing the mentioned concepts). The topology on which this filter is based is the one from Figure 6.7b where the element $M_{23} < 0$ is of capacitive type, and the rest are all inductive couplings (> 0).

However, the selected orientation in the case of this PhD thesis is horizontally folded, whose footprint could be useful in some cases depending on the satellite requirements. It was found that in [183] it is implemented the same topology as in [182] ($M_{23} < 0$) but with a waveguide multicavity folded horizontally instead of vertically. In this work, it has been investigated the implementation of this kind of structures but asymmetrically, this is, the design of a filter based on the topology from Figure 6.7c with all inductive couplings (> 0) except for the interresonator coupling between the first and second resonators, which is of capacitive type ($M_{12} < 0$).

Due to the complexity of this structure, it was decided to employ the *Step by step* technique and the *Coupling Matrix Segmentation* (presented in [84]) for the design process, which systematically yield to the design of the final structure dimensions. The benefits of this approach include the fact that the number of parameters involved in each stage is significantly less than the total number of parameters in the filter structure, as well as the fact that the interactions between nearby elements are taken into account in each iteration.

6.2.2 *Horizontally folded asymmetric filter design*

As it is said in the previous section, an asymmetrical fourth order filter with a quartet topology folded horizontally has been designed with two transmission zeros on both sides of the passband. This is a canonical topology with only one cross-coupling, the M_{14} iris window. The architecture enables for the incorporation of two real transmission zeros in the filter response (one in each side of the passband). Figures 6.7a and 6.7c depict the coupling topology, where the white circles represent the source and load ports (or input / output ports) and the black circles reproduce the resonators (1, 2, 3 and 4). The couplings

along the main path are shown with solid lines, while the cross-coupling is represented by a dashed line. Figure 6.7c shows the type of coupling irises in this case (positive for inductive windows, and negative for capacitive windows).

The fundamental shape of all irises may be investigated further in Figure 6.8a. In these
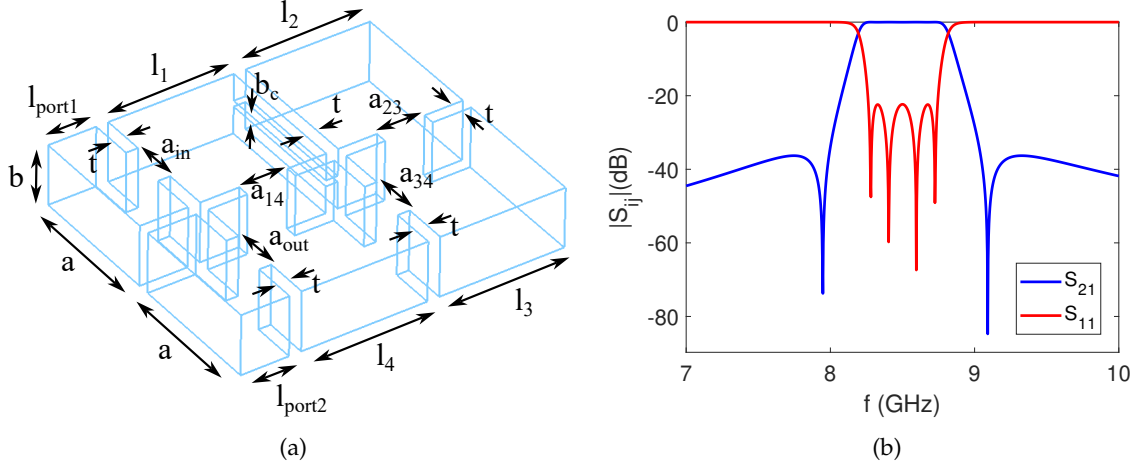
Figure 6.8: Horizontally folded asymmetric filter: (a) 3D model with its dimensions, and (b) ideal response with two real transmission zeros on both sides of the passband. This structure implements the topology from Figure 6.7c.

illustrations, the coupling M_{ij} is controlled by the iris width a_{ij}, between adjacent resonators i and j. For the capacitive case, the element M_{12} is controlled by the window height b_c. In addition, the diagram depicts all the geometrical parameters that will be optimised during the design phase. The thickness of all walls (t) is fixed at 3 mm for practical reasons.

We employ the standard rectangular waveguide WR-90 (a = 22.86 mm and b = 10.16 mm) for the physical implementation. Center frequency f_0 = 8.5 GHz, bandwidth BW = 500 MHz, and minimum return loss RL = 22 dB are the filter specs. In addition, the quartet topology has two transmission zeros, which will be located at f_{z1} = 7.93 GHz and f_{z2} = 9.08 GHz (symmetrically arranged with regard to the filter centre frequency). These specs produce the scattering parameters shown in Figure 6.8b, that will be the target for the response of this design

The design process begins with getting the normalised coupling matrix using the approach outlined in [74], with the necessary filter characteristics above-mentioned, resulting to

$$M_{N+2} = \begin{pmatrix} 0 & 1.0587 & 0 & 0 & 0 & 0 \\ 1.0587 & 0 & -0.9 & 0 & 0.13 & 0 \\ 0 & -0.9 & 0 & 0.75 & 0 & 0 \\ 0 & 0 & 0.75 & 0 & 0.9 & 0 \\ 0 & 0.13 & 0 & 0.9 & 0 & 1.0587 \\ 0 & 0 & 0 & 0 & 1.0587 & 0 \end{pmatrix}. \tag{6.3}$$

This matrix, like the examples in the preceding section, has all of its diagonal elements equal to zero. This indicates that the topology is synchronously tuned, and all resonators are adjusted at the passband centre frequency. This is the situation, as previously stated,

when the frequency response to be synthesised is symmetrical with regard to the central frequency. It is also worth noting that one of the matrix couplings has a negative sign, the capacitive element M_{12}.

The scaled coupling matrix (M') is now calculated, utilising the resonant mode TE_{101} in the rectangular waveguide cavities as resonators. The details of this process are found in [182]. Following [182], applying the filter specifications above-mentioned the scaled coupling matrix can be extracted:

$$M'_{N+2} = 10^{-4} \cdot \begin{pmatrix} 0 & 8.4533 & 0 & 0 & 0 & 0 \\ 8.4533 & 0 & -3.3971 & 0 & 0 & 0 \\ 0 & -3.3971 & 0 & 2.8309 & 0 & 0 \\ 0 & 0 & 2.8309 & 0 & 3.3971 & 0 \\ 0 & 0 & 0 & 3.3971 & 0 & 8.4533 \\ 0 & 0 & 0 & 0 & 8.4533 & 0 \end{pmatrix}. \tag{6.4}$$

Note how it has been imposed on this matrix that the element M_{14} is equal to zero. This is because the cross window (between resonators 1 and 4) will not be implemented until the last design step, where an optimisation will be applied to the necessary dimensions.

For applying the step by step design approach, the filter structure (see Figure 6.8a) and its scaled matrix (see equation 6.4) are divided in several steps, as illustrated in Figure 6.9. The design procedure begins by considering only the first iris window, namely the input coupling (see Figure 6.9a). This circuit response is quite basic, as seen by the black line in Figure 6.10a, and it is employed to improve the physical structure input iris, which is made up of the input inductive window (a_{in}) depicted in Figure 6.8a. Figure 6.9a depicts the portion of the physical structure that corresponds to the first step. It is important to note that the waveguide corresponding to the first resonator in this construction is simply terminated by a waveguide port (red surface from Figure 6.9a). Due to the intrinsic dispersion of inductive irises, the response of the iris is frequency-dependent. Nevertheless, the iris width a_{in} is tuned until the correct transmission parameter value is obtained at the passband centre frequency (this is, at $f_0 = 8.5$ GHz), as seen in Figure 6.10a. To analyse the structures in all the steps, full-wave simulations are applied using FEST3D software [78]. Just the width of the input iris a_{in} is adjusted in this first phase, as seen in Table 6.4.

Variables (mm)	Step 1	Step 2	Step 3	Step 4	Step 5	Final
a_{in}	15.615	15.568	15.568	15.666	15.672	15.989
b_c		0.979	0.939	0.972	0.966	0.985
a_{23}			11.69	11.878	11.88	12.002
a_{34}				11.864	11.776	11.632
a_{out}					15.295	15.108
a_{14}						7.425
l_1		23.68	23.664	23.601	23.613	22.533
l_2			26.412	26.261	26.205	26.199
l_3				22.9	22.884	22.959
l_4					19.99	19.214

Table 6.4: Values of all the filter dimensions (referred to the Figure 6.8a) acquired during each step.

$$M_1' = 10^{-4} \cdot \begin{pmatrix} 0 & 8.4533 \\ 8.4533 & 0 \end{pmatrix}$$

$$M_2' = 10^{-4} \cdot \begin{pmatrix} 0 & 8.4533 & 0 \\ 8.4533 & 0 & -3.3971 \\ 0 & -3.3971 & 0 \end{pmatrix}$$

$$M_3' = 10^{-4} \cdot \begin{pmatrix} 0 & 8.4533 & 0 & 0 \\ 8.4533 & 0 & -3.3971 & 0 \\ 0 & -3.3971 & 0 & 2.8309 \\ 0 & 0 & 2.8309 & 0 \end{pmatrix}$$

(a)　　　　　　　(b)　　　　　　　(c)

$$M_4' = 10^{-4} \cdot \begin{pmatrix} 0 & 8.4533 & 0 & 0 & 0 \\ 8.4533 & 0 & -3.3971 & 0 & 0 \\ 0 & -3.3971 & 0 & 2.8309 & 0 \\ 0 & 0 & 2.8309 & 0 & 3.3971 \\ 0 & 0 & 0 & 3.3971 & 0 \end{pmatrix}$$

$$M_5' = 10^{-4} \cdot \begin{pmatrix} 0 & 8.4533 & 0 & 0 & 0 & 0 \\ 8.4533 & 0 & -3.3971 & 0 & 0 & 0 \\ 0 & -3.3971 & 0 & 2.8309 & 0 & 0 \\ 0 & 0 & 2.8309 & 0 & 3.3971 & 0 \\ 0 & 0 & 0 & 3.3971 & 0 & 8.4533 \\ 0 & 0 & 0 & 0 & 8.4533 & 0 \end{pmatrix}$$

(d)　　　　　　　　　　　　(e)

Figure 6.9: Steps for the design procedure of the presented filter dimensions based on the subdivision of the structure. The red walls represent the position of the port excitations.

The element M_{12} is combined with the first resonator in the second stage of the design process, yielding the coupling matrix illustrated in Figure 6.9b. Figure 6.10b depicts the response, which is utilised to adjust the second section of the physical structure, which is also illustrated in Figure 6.9b. The coupling M_{12} in the filter construction is generated with the capacitive iris b_c depicted in Figure 6.8a. Lastly, the length l_1 is used to change the resonant frequency of the first resonator. The waveguide corresponding to the second resonator is terminated with a waveguide port, as shown in Figure 6.9b.

As indicated, b_c and l_1 are the major geometrical parameters involved in the optimisation processes for this second phase of the design process. The two geometrical parameters are first tuned until the response is regained, as indicated in Figure 6.10b by the black line. It should be noted here that, following an initial optimisation with these two dimensions, a little refinement with the input iris (a_{in}) is frequently necessary. In this method, all of the structure interactions and tiny couplings are strictly accounted for during the final computation of the necessary geometrical parameters.

(a)

(b)

(c)
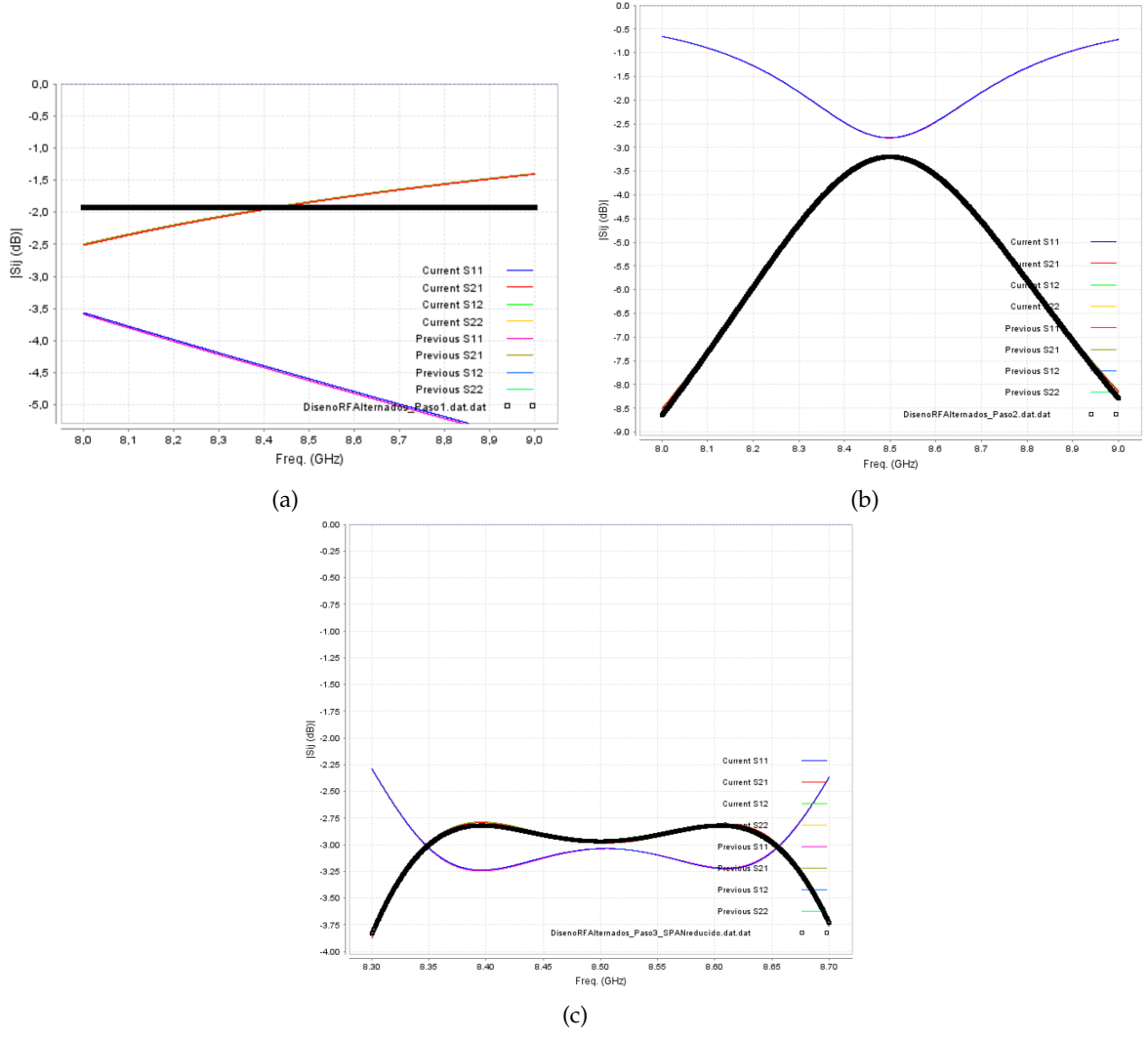
Figure 6.10: Responses at the optimization process for (a) the first, (b) the second, and (c) the third steps. The black lines represent the target response. The scattering parameter S_{21} (red lines) is employed in these steps for the optimization. The rest of the lines (blue line (S_{11}), for example) are not used here.

The geometrical variables acquired at this point in the design process are also listed in Table 6.4 (Step 2). The input iris has been changed from $a_{in} = 15.615$ mm in Step 1 to $a_{in} = 15.568$ mm in Step 2. This suggests that, despite their small variations, the interactions and loading effects of the 1st resonator on this iris are significant. The study also emphasises the significance of accounting for coupling effects and interactions from nearby elements during the final optimization of the various portions of the filter.

As illustrated in Figure 6.9c, it is added a new coupling (the element M_{23}) and the second resonator in the third phase of the design process. As shown, the new coupling is adjusted with the inductive iris a_{23} (see Figure 6.8a), while the new resonator is adjusted with the length l_2. The waveguide associated with the third resonator is again terminated on the front side with a waveguide port, as shown in Figure 6.9c.

The new geometrical parameters (a_{23} and l_2) are first tuned to restore the response displayed by the black line (S_{21}) in Figure 6.10c, using the same technique as previously. Following this first optimisation step, a refinement that includes nearby elements is carried out (b_c and l_1). It should be noted that the input iris (a_{in}) does not need to be included in the optimisation procedure at this point. This refining method recovers the goal function with good precision, as demonstrated by the red line in Figure 6.10c.

Table 6.4 contains the geometrical dimensions obtained following this stage (Step 3). The capacitive height (b_c) and the first resonator length (l_1) differ only little from the preceding step. Anyway, these small variations highlight the need of taking neighbouring structures into account while finalising the design of the different parts of the filter structure.

Then, it is added the following section, as shown in Figure 6.9d, based on a new coupling (the element M_{34}) and the third resonator in the fourth step of the design process. The new coupling is adjusted with the inductive iris width a_{34}, while the new resonator is tuned with the length l_3 (see Figure 6.8a). As illustrated in Figure 6.9d, the waveguide associated with the fourth resonator is terminated on the front side with a waveguide port (red surfaces shown in Figure 6.9d).

Using the approach from previous steps, the new geometrical parameters (a_{34} and l_3) are first modified to recover the response seen in Figure 6.11a. Following this initial round
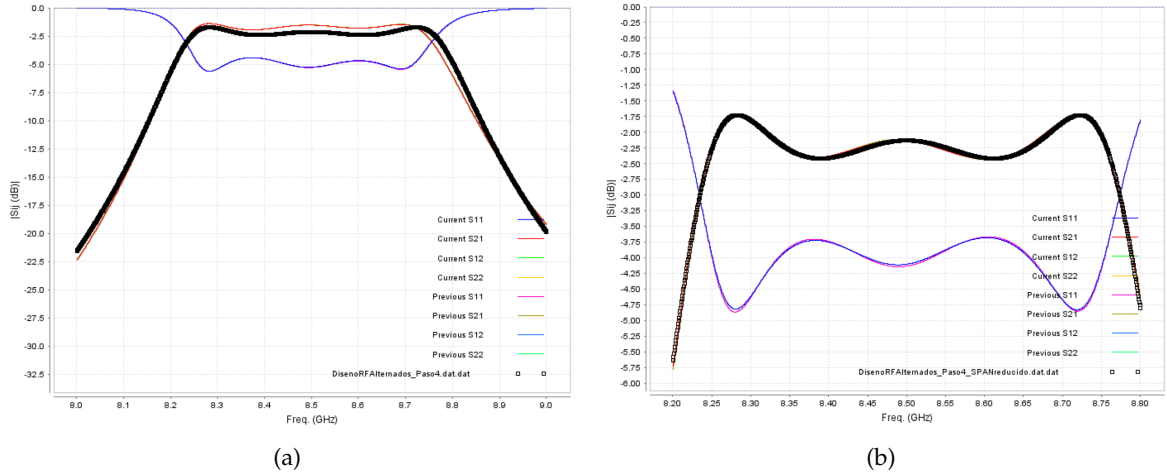
Figure 6.11: Response at the optimization process for the fourth step: (a) wide frequency span, and (b) reduced span. The black lines represent the target response. The scattering parameter S_{21} (red line) is employed in this step for the optimization. The rest of the lines (blue line (S_{11}), for example) are not used here.

of optimisation, a refinement that includes nearby elements is performed (a_{23} and l_2). The red line in Figure 6.11a shows that this refining approach recovers the goal function with high precision. Next, as illustrated in Figure 6.11b, additional finer optimisation with a reduced frequency span is used to adjust the previous elements of the filter structure (b_c, l_1, and even a_{in}), resulting in a more precise response.

Table 6.4 (Step 4) also lists the dimension variables obtained at this phase in the design process. The geometrical dimensions used in the previous three steps are also slightly altered in this phase. This shows that the interactions and loading effects of all the structure parts are substantial. This conclusion is consistent with the notion that an asymmetric filter is far more sensitive to its dimensions than a symmetrical construction, although the parameter that makes a filter most sensitive is the bandwidth (if *BW* is large, the interaction between elements is stronger and more corrections have to be made).

The last section (excluding the cross-coupling) is now implemented for the fifth step. In this case, a new coupling is introduced, the M_{4L} element (modelled by an inductive iris), and the last resonator, modelled by the fourth resonant cavity, as shown in Figure 6.9e. This coupling and resonator are adjusted by the dimensions a_{out} and l_4, respectively (see Figure 6.8a). Now, the waveguide associated with the filter output is terminated on the front side with a waveguide port, which will be the final path of the whole structure once designed.

The variables a_{out} and l_4 are then adjusted to obtain the response (utilising now both S_{21} and S_{11} parameters) seen in Figure 6.12a (black lines). After a first optimization, the rest

(a)   (b)
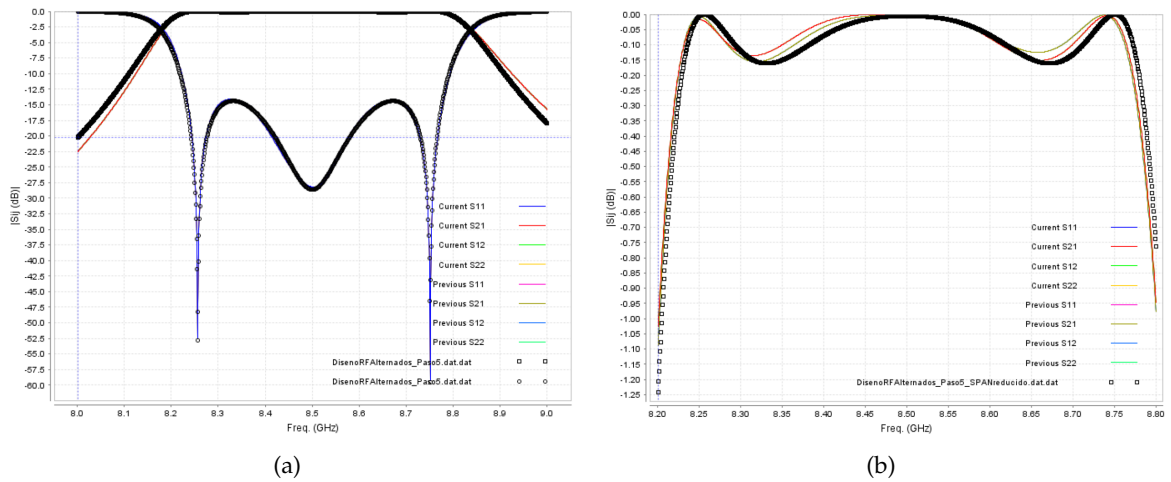
Figure 6.12: Step 5 response: (a) wide frequency span, and (b) reduced span. The black lines represent the target response. The scattering parameter S_{21} (red line) is employed in this step for the optimization. The S_{11} parameter is also utilised in (a) for higher accuracy. The rest of the lines are not used here.

of the variables are also tuned. The read and blue lines in Figure 6.12a show the outcomes with a good agreement compared to the target (black lines). Furthermore, as shown in Figure 6.12b, another optimisation with a reduced frequency span and employing only the S_{21} parameter is carried out to adjust all the filter sections, resulting in a higher accuracy.

The dimension variables collected at this stage in the design procedure are shown in Table 6.4 (Step 5). At this phase, the geometrical parameters employed in the previous four steps are also tuned.

As a final step, the cross-coupling M_{14} is implemented with the structure dimensions from Step 5 (see Figure 6.13a). This element is modelled by an inductive iris window

(a)

(b)

(c)
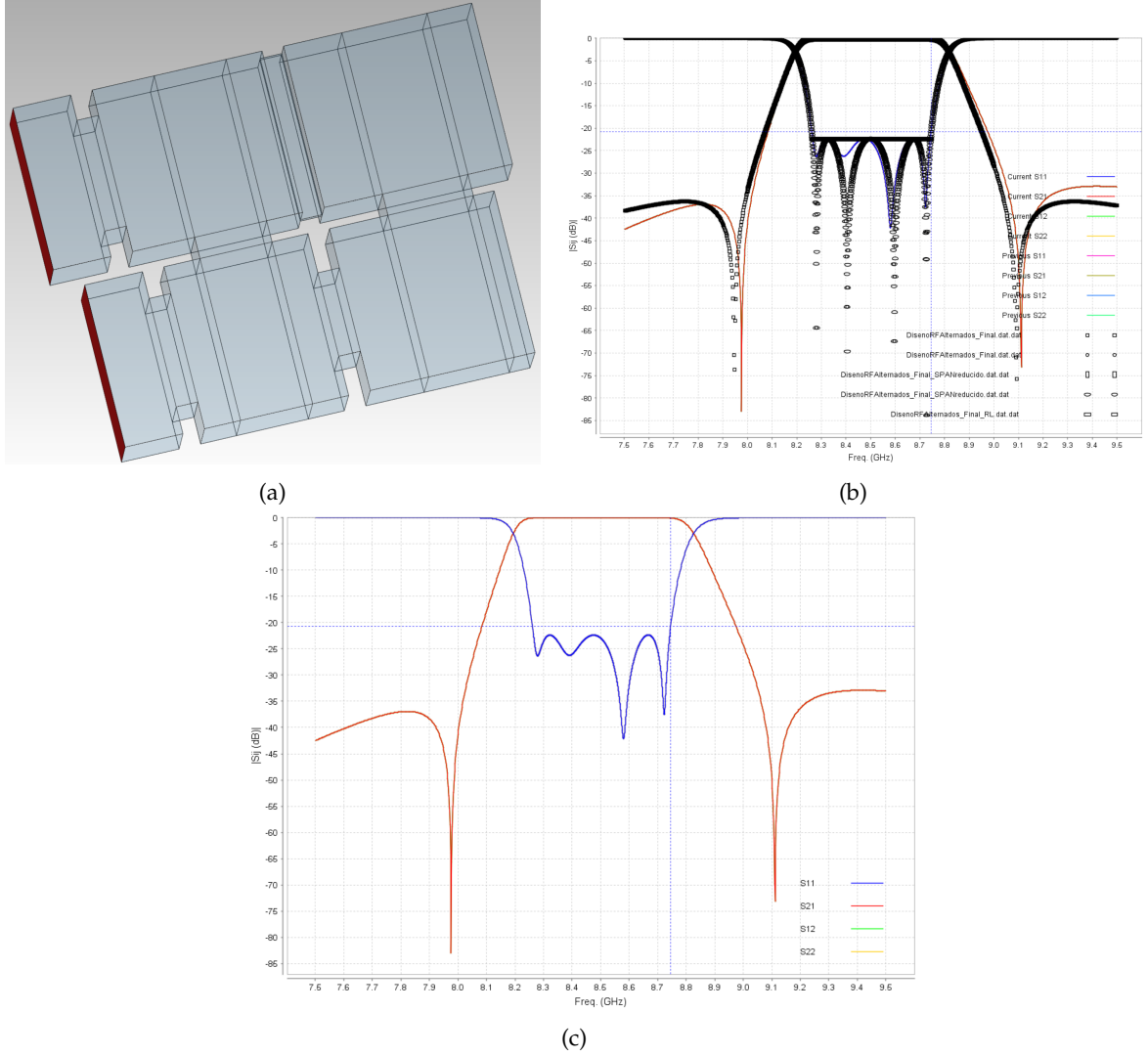
Figure 6.13: Final step: (a) 3D model, (b) response at the optimization process, and (c) final response of the filter. The black lines in (b) represent the target response.

that connects the first and last resonators thanks to the structure folding. This coupling is adjusted with the iris width (a_{14}, referred to the dimensions from Figure 6.8a). The optimization process for this final phase is based on the target response from the matrix shown in equation 6.3 (see Figure 6.8b).

Figure 6.13b depicts the coupling matrix goal response as well as the physical structure response with optimised dimensions. Once again, the optimization is carried out employing both scattering parameters (S_{21} and S_{11}) for higher accuracy. In general, attending the frequency values f_c (the central frequency), f_{z1} and f_{z1} (the position of the transmission zeros below and above the passband, respectively), and BW (the bandwidth), it can be stated that there is good agreement between both responses. Figure 6.13c shows the filter response in detail for ease of visualisation. The initial return loss level inside the passband

of $RL = 22$ dB was also successfully reached. In Table 6.4 (Final) the final dimensions obtained after optimization are included.

The next objective for this study is the fabrication of the filter and its electromagnetic characterisation with the VNA. Although such manufacture has been left as a future line, some of the considerations to be taken into account for it have been analysed. Firstly, in order to allow WR-90 flanges to be positioned in the ports, it is necessary to implement a small section of orientation change (in opposite directions) in each port. For the filter studied in the previous section a 90° waveguide bend was utilised, however this time a 30° one will be sufficient. Figure 6.14 depicts the structure with these 30° sections at both ports. These extra sections at the ports hardly vary the already optimised response.
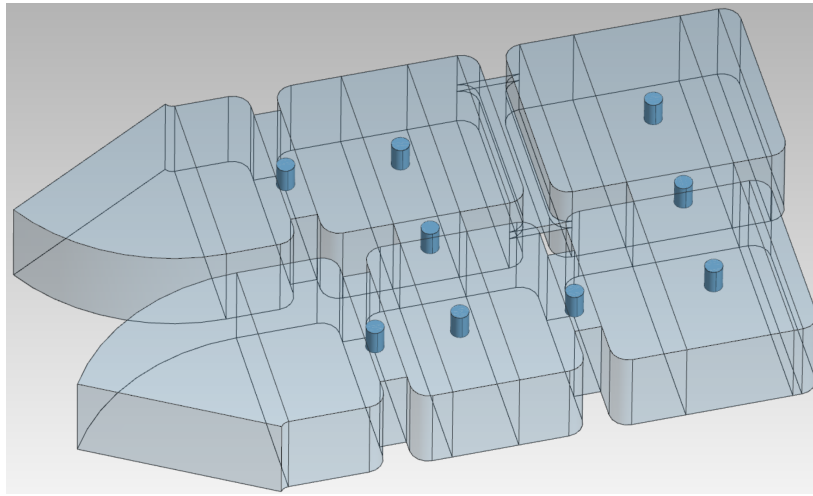
Figure 6.14: 3D model of the designed horizontally folded asymmetric filter with 30° waveguide bends at the ports, rounded chamfers at the vertical corners, and tuning screws at the resonators and irises.

On the other hand, as has been seen in the manufacture of the housings of all the structures investigated in this PhD thesis, the machining drills that outline the walls of the cavities and irises will impose rounded chamfers (of radius 2 mm for this filter) in some of the corners, which will depend directly on the manufacturing cut. In this case, an horizontal cut has been chosen due to the high complexity for the other two types of cuts (transversal and vertical), so the chamfers will have to be implemented on the vertical axis (see Figure 6.14). This implies a new optimization of the response, which has been reserved as future work. Finally, as it is such a sensitive structure (due to its asymmetry, the low bandwidth value and the presence of transmission zeros close to the passband), the implementation of a tuning screw system has been taken into account before its manufacture, as illustrated in Figure 6.14[1]. To this end, a study was carried out to predict the sensitivity of the response on the penetration of the screws in each position (both in the centres of the resonators and in the centres of the iris windows).

---

1 In order to reduce the complexity of the problem, the implementation of a tuning screw in the capacitive iris has been avoided for the time being and can be introduced later in production if necessary.

To have enough space to tune the filter with the screws, it has been decided to optimise the response with these screws inserted 3 mm into the cavities and irises. For this purpose, it has to be studied how much the lengths of the resonant cavities and the widths of the irises have to be corrected. Firstly, for the resonators, it has been simulated the behaviour of a single cavity with a tuning screw varying its depth at the centre, obtaining a sensitivity in the resonant frequency of -113 MHz/mm at our operation frequency ($f_0 = 8.5$ GHz). Simulating a resonator without screws, it has been obtained a sensitivity with its length of -130 MHz/mm. Then, for a compensation of the 3 mm screw depth at all the resonators, a 2.6 mm reduction of the resonator lengths should be applied. On the other hand, for the inductive irises, the simulations provided a sensitivity of the physical coupling k with the screw depth of 3.17×10^{-3} per mm. Without tuning screws, the iris windows give a dependence with its widths of 0.014 per mm. Therefore, to correct for the 3 mm screw depth at all the inductive iris windows, a 0.7 mm reduction of the iris widths should also be applied. These corrections in both resonators and couplings serve as starting point for the new optimization, that should also be realised due to the implementation of the vertical chamfers, as previously stated.

6.2.3 *Topologies with N > 4*

In this line of work, investigations have been carried out for the extension (to more than 4 resonators) of the concept of implementing pairs of real transmission zeros at both sides of the passband in asymmetric filters by mixing signs in the main path couplings (non-cross-couplings) with horizontally folded structures. In particular, this effect has been studied in a filter with $N = 6$ resonators, where studies have been conducted to obtain a response with two pairs of transmission zeros, for an even higher out-of-band rejection. After several tests, a matrix has been found that provides a response with specifications similar to those used in the previous filter (horizontally folded quartet):

$$M_{N+2} = \begin{pmatrix} 0 & 1.023 & 0 & 0 & 0 & 0 & 0 & 0 \\ 1.023 & 0 & -0.868 & 0 & 0 & 0 & 0.01 & 0 \\ 0 & -0.868 & 0 & 0.61 & 0 & 0.13 & 0 & 0 \\ 0 & 0 & 0.61 & 0 & 0.7 & 0 & 0 & 0 \\ 0 & 0 & 0 & 0.7 & 0 & -0.61 & 0 & 0 \\ 0 & 0 & 0.13 & 0 & -0.61 & 0 & 0.868 & 0 \\ 0 & 0.1 & 0 & 0 & 0 & 0.868 & 0 & 1.023 \\ 0 & 0 & 0 & 0 & 0 & 0 & 1.023 & 0 \end{pmatrix}. \tag{6.5}$$

This matrix provides the response shown in Figure 6.15a, which is based on the topology shown in the inset. As it can be seen, the structure needs the implementation of two capacitive irises (negative sign) in the in-line interresonator couplings M_{12} and M_{45}, and two inductive irises (positive sign) in the interresonator cross-couplings M_{16} and M_{25}. The rest of the couplings are all of inductive type. A 3D model of this filter is depicted in Figure 6.15b. It is important to note that the number of transmission zeros that will appear in the filter response will be equal to the number of resonators in the structure (N) minus the minimum number of resonators needed to go from port 1 to port 2. This is known as the *Minimum Path Rule* [74].In this case, the number of transmission zeros are
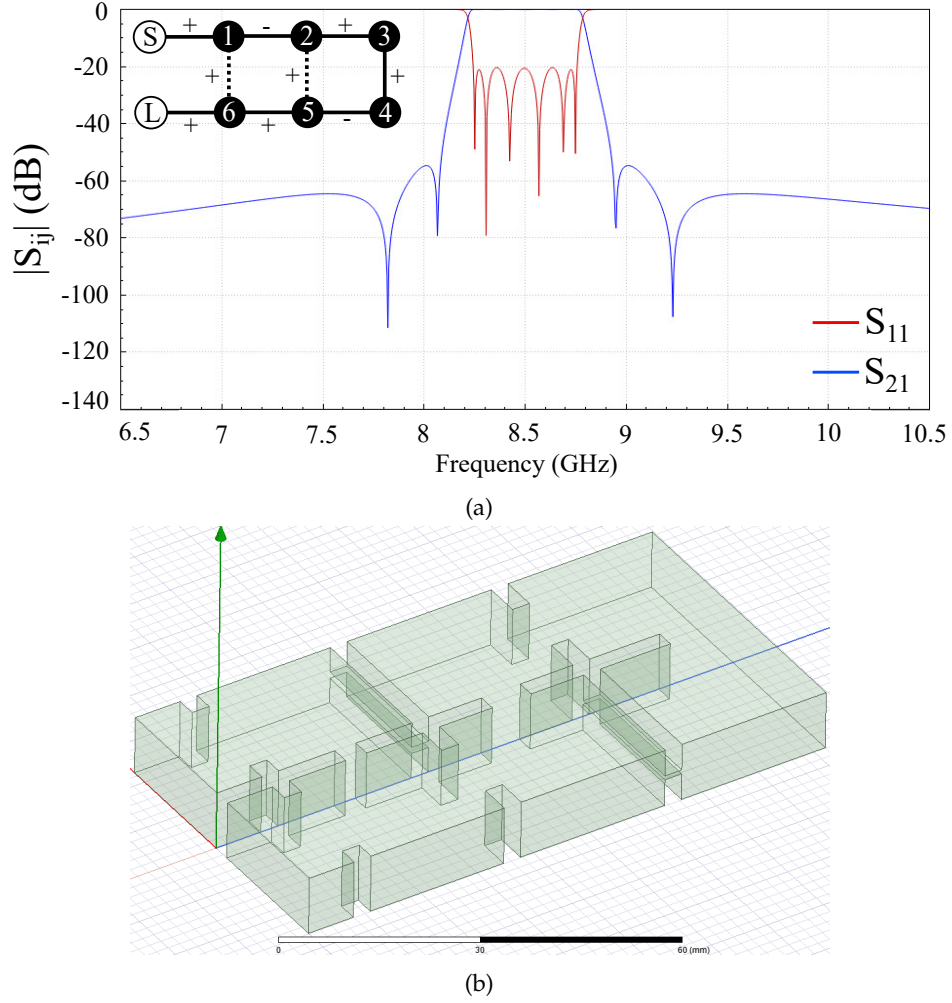
Figure 6.15: Horizontally folded asymmetric filter with $N = 6$ resonators: (a) response with two pairs of transmission zeros, and (b) 3D model of the prototype to be designed. The inset in (a) depicts the topology necessary for obtaining such response. As it can be observed, M_{12} and M_{45} are capacitive couplings.

$n_{tz} = 6 - 2 = 4$.

An asymmetric structure based on 8 resonators could be used for the implementation of 3 pairs of transmission zeros, achieving even higher out-of-band rejection, although its design and tuning can be quite complex. For the design of these structures, a more efficient technique employing the coupling matrix segmentation based on multi-port networks [182] could be necessary due to its high complexity. The design of the prototype from Figure 6.15b has been left as future work.

6.3 CONCLUSIONS

In the first section of this chapter, the primary goal of the study is to demonstrate experimentally that using 3D-printed ABSplus material as a dielectric element for the construction of cheap evanescent bandpass filters operating in the C-band is feasible. Two filter designs made of dielectrics and evanescent waveguide cases were designed, pro-

duced, and successfully measured for this purpose. Both filters have an in-line topology and use low-cost AM dielectrics in conjunction with machined metallic components for the housing.

In the case of the first filter designed, which is based on a straight structure with elliptical air cylinders, it exhibits a good performance in the S_{21} parameter as compared to the second filter based on an horizontal folding geometry. The second filter yields to an almost square footprint, and to the possibility of implementing cross-couplings if needed. It has also been proved that several transfer functions may be implemented by 3D printing distinct dielectric structures that are then inserted within the same metallic housing. Because of the electrical qualities of the used ABSplus material, the electrical response of the measurements are fairly good, although with somewhat increased IL. Enhancements in this parameter are expected to come when new 3D printing materials with better electrical characteristics become widely available.

It is concluded that the hybrid CNC machining and 3D printing or AM technique presented in this research is a highly important industrial approach for the quick, cheap and flexible prototyping of microwave filters based on the proposed idea.

On the other hand, in the second section, the design of a filter based on an asymmetric folding canonical topology that mixes inductive and capacitive couplings was presented. The idea is to implement capacitive irises at the main path couplings in an all-inductive topology for applying real transmission zeros at both sides of the filter passband. Due to the complexity of this type of filters, the design method is based on scaling the normalised coupling matrix to identify appropriate partial responses of the filter. The approaches were successfully used to the design and construction of a filter prototype with two real transmission zeros in quartet topology. Several recommendations are provided for the manufacture of this filter, such as the application of a tuning system, which has been studied with simulations in order to assess its capability to effectively tune the response.

A study was also conducted for the development of an asymmetric matrix able to implement four real transmission zeros by a structure with six resonators and two cross-couplings. All couplings in this structure are inductive except for two, which are on the M_{12} and M_{45} elements (couplings in the main path). A similar technique, as described previously, may be used to create different filters with higher order folded canonical topologies or with extra cross-couplings.

7

CONCLUSIONS AND FUTURE RESEARCH

7.1 CONCLUSIONS

This PhD thesis has focused on the development and improvement of new dark matter axion detection systems based on single resonant cavities or multicavities, commonly known as haloscopes. These systems have been carried out in waveguide technology. In addition, novel bandpass filter designs for satellite communications have been developed in this same technology, as spin-off activity of the haloscopes designs.

As it has been seen in Chapter 2, the field of haloscope research has been booming in the last decade and most of its parameters have yet to be improved by the axion community. In this sense, the present PhD thesis offers many improvements in order to increase the possibilities of detecting the long-awaited axion particles, which could explain the composition and confirm the existence of dark matter, which corresponds to one of the big questions in Physics today. Some of these improvements have been to increase the performance of the haloscopes by increasing their volume, quality factor and form factor, and to design a novel electronic tuning system. Axions can be found by converting them into photons in the presence of a strong magnetic field. To boost the strength of the converted photon signal, the haloscope approach employs a cavity resonating at the axion frequency.

Throughout the last 20 years, the haloscope approach has been utilised to search for axions. Yet, the majority of the experiments have looked for masses less than 25 μeV. The RADES team (within which this PhD thesis has been developed) searches for axion above 25 μeV using single cavities or the multicavity concept. The latter is based on connecting N subcavities with inductive or / and capacitive iris windows for resonating at a single frequency, a parameter directly proportional to the mass of the axion. This approach allows the increase of the haloscope volume without lowering its resonant frequency. Some of the designs developed by the RADES group have been installed on the CAST and SM18 magnets, working at high magnetic fields and at cryogenic temperatures, conducting axion data campaigns in the last years where, after analysing the data, the axion has not yet been found.

An all-inductive $N = 5$ multicavity was designed and manufactured using the coupling matrix technique and CST simulations, being the first haloscope developed by the RADES

team. By the end of 2017, this structure was installed inside the CAST magnet. The major goal of this PhD thesis was to implement enhancements to these types of structures increasing the competence of the team among the experimental axion groups. The first section of Chapter 3 has shown the progress made in efficiently increasing the volume, quality factor and form factor of haloscopes with rectangular geometry that would fit in any type of magnet (dipole or solenoid). These three parameters are very important in a haloscope design and the axion detection capability depends directly on its values. This study may serve as a guide for any axion group seeking to develop a dark matter detector with high performances. In addition, different designs and fabrications carried out are shown, validating all the simulations presented. In the second section of this chapter, the manufacturing quality factor results of various RADES prototypes have been analysed. Throughout this analysis, new ideas for improving this factor are proposed, along with other ideas for enhancing other issues, like the development of a novel identification mode technique. Special interest has been put on a new idea developed in this PhD thesis: the modularity, which is based on applying fabrication cuts at efficient positions in order to improve the surface current flow (and therefore improve the quality factor) in the resonant waveguide cavities. The last two sections of this chapter show the studies carried out for the implementation of a tuning system (both mechanical and electronic) and input / output coupling readjustment. For the latter, a preliminary prototype has been designed and manufactured giving good results that could lead to the development of a new version to be used in the real axion measurement campaigns.

Chapter 4 has focused on the development of a new idea of electronic tuning based on ferroelectric materials, which have also served to propose a new system to implement interresonator couplings, that can be adjusted electronically. These devices are able to change their permittivity ε_r by applying a DC voltage or a temperature change. The variations of ε_r gives a resonant frequency (which is the axion frequency) shift in the haloscope. Unfortunately, because haloscopes must work at cryogenic temperatures, the chosen ferroelectrics are KTOs, which have extremely high permittivity (~ 4500), making the problem enormously difficult. In this work, an idea based on efficiently positioning KTO films of a certain thickness has been developed in order to obtain a high tuning range with very good performance in the haloscope parameters (quality factor, form factor, and volume). This work constitutes one of the great advances introduced by the PhD thesis since it contributes a great value to the axion community, since previously only superficial work had been done on this type of electronic tuning. These electronic systems could replace or complement mechanical tuning systems, which present problems at cryogenic temperatures and have virtually no scalability. Additional investigations have been carried out for the use of these ferroelectric films as a replacement for metallic iris (both inductive and capacitive), which sometimes imply a challenge in production when a very high quality factor is desired. Also, a setup for the characterization of the future KTO films has been designed. The simulations provided promising results, verifying the viability of the

prototype.

Then, in Chapter 5, other improvements studied in this work have been shown. Among these studies, particular emphasis has been placed on the sum of the signals from several ports of the same haloscopes using the phase-matching method. The idea of this technique is based on the increase of the resonant mode separation, which is a parameter of great interest throughout the developments carried out in this PhD thesis. Various simulations have been conducted for the sum of up to 8 coaxial ports, rejecting some modes that are close to the axion resonance. These results are very useful because the axion mode should ideally be isolated to avoid problems like: the axion mode identification, the quality factor calculation, and the reduction of the form factor. To validate these techniques experimentally, a prototype has been designed and manufactured to combine with the phase-matching concept its coaxial ports. The results of the measurements and post-processing have shown excellent results, confirming the possibility of rejecting resonances close to the axion mode, thus being able to design haloscopes with larger volumes. In the following sections of this chapter, other secondary studies carried out as an extension of the main ones have been covered: development of a QuBit system to decrease the system temperature, design of haloscopes in the UHF and W bands, implementation of superconducting elements in haloscopes (HTS design), and development of a full-wave modal technique for the efficient analysis of the axion-photon coupling in a haloscope.

Finally, in Chapter 6 the results obtained from the investigations conducted for the development of bandpass filters based on multicavities in waveguide technology have been presented. As it has been demonstrated, this technology allows both the development of axion dark matter detectors or haloscopes, as well as radiofrequency bandpass filters for satellite communications. In line with the latter, improvements have been made to two evanescent filters that use a hybrid machining CNC system together with the use of dielectric elements produced from 3D printing, in order to greatly reduce the cost. In this PhD thesis, a tuning system with screws has been proposed, which has allowed producing a response in the manufactured filters with good agreement with respect to simulations, thus validating the experimental results for this concept. The structures from this section make it possible to reduce the weight on board the satellite, which is a key characteristic for launching them into space due to the strong dependence between weight and cost, as it is well known. On the other hand, the study of new asymmetric topologies with cross-couplings has been carried out to produce transmission zeros on both sides of the passband, through the mix of inductive and capacitive irises. This technique gives responses with higher rejection capabilities. The design of a filter based on four resonators has been carried out, providing a very effective response, and the necessary guidelines for its manufacture have been presented. The filters and topologies studied in this section are of special interest when the needs of the devices that must go on board (in communications satellites) imply an increase in the out-of-band rejection, with an almost square footprint.

The work addressed in this PhD thesis has given rise to a high number of future lines of research due to the fact that satisfactory progress has been made and the high demand for improvement both in dark matter haloscopes and in satellite communication filters. Thus, the future lines extracted from the work carried out will consist of:

- Haloscope designs: Design of a competitive haloscope with high volume operating at X-Band for the BabyIAXO magnet. All the ideas shown in section 3.1 (the multicavity concept, the alternating irises technique, the large dimensions, and the 3D geometries) could be combined for the creation of the *definitive haloscope*. In this sense, two studies has been left as future work: tall multicavity designs employing different lengths for each subcavity to utilise practically the whole bore of a solenoid magnet, and optimization of the form factor in the large multicavity example presented in section 3.1.2.3. Also, the application of all the research presented in section 3.1 but with cylindrical geometries (both cavities and multicavities) is a pending issue that is expected to be accomplished soon. On the other hand, for the implementation of transmission zeros in multicavities, two investigations have raised as future work: synthesis of haloscope designs with transmission zeros and arbitrary coupling topology, and implementation of an internal bypass metallic loop structure (wire) for obtaining a cross coupling with in-line structure (1D geometries) [184]. The latter idea could be useful in dipole magnets with small diameter, where 2D geometries could generate space issues.

- Studies in the alternating 6-subcavities haloscope with vertical cut: Application of screw holes in the horizontal axis, and implementation of a new soldering strategy to increase the quality factor. Additionally, the possibility of designing the 6-subcavities alternating haloscope with movable screws as coupling elements (that could act as inductive or capacitive coupling), instead of fixed window irises, is being explored. Following this idea, the unloaded quality factor Q_0 could be increased because only a vertical cut would be needed, without capacitive cuts. However, the quality factor reduction due to the screws is something that must be assessed in manufacturing.

- Modularity: Study of the concept of modularity with modules using inductive irises and / or with a higher number of subcavities (30, for example). In this line, it is also expected to explore the feasibility of mixing inductive and capacitive modules to implement multitude of different topologies without the need for additional fabrications.

- Investigations in the alternating 30-subcavities haloscope: Analysis of the measurements taken at CAST by the Time Gating method to extract the information of the input coupling coefficient β at such installation, and implementation of the same reprocessing carried out on the 6-subcavities haloscope (desoldering, vertical cutting, re-coating and soldering).

- Mechanical tuning control system for vertical cut haloscopes: Adaptation of the control device presented in Figure 3.65 to all the RADES designs, particularly in the 6-subcavities and 30-subcavities haloscopes. More vertical cut tuning investigations with manual opening are needed before the construction of theses control systems.

- Ferromagnetic tuning: Experimental implementation of the ferromagnetic YIG designs shown in section 3.3.2.2. In order to conduct this study, the ferromagnetic material must first be characterised and various simulations must be performed with the results for subsequent adjustment.

- Adjustable coaxial system: Performance tests of the system presented in section 3.4.1 with the acquired stepping motor (the *HT23-595 - NEMA 23 High Torque Step Motor*) and its controller (the *STR2 - DC Powered Advanced Microstep Drive*), and, later, with the nanopositioner Cryo Linear Actuator *CLA2603* device. Manufacturing and testing of the second version of the previous system employing finger gaskets for reducing the losses from radiation (see Figure 3.75).

- Ferroelectric elements: Experimental implementation of the ferroelectric KTO designs (both as tuning and coupling element) presented in Chapter 4 with the help of the *Euclid Techlabs* company [133]. Similarly to the ferromagnetic experiments, the KTO films must first be electrically characterised and various studies must be conducted with the outcomes for subsequent adjustment. In section 4.4 it is shown a setup developed in this work for this characterization. Once these investigations have been carried out, the next step will be to adapt these ferroelectric systems to all RADES haloscopes for future axion data campaigns. In addition, the study of cylindrical cavity designs with ferroelectric elements has been reserved as a future line of research. The adaptation of the techniques shown in section 4.1.1 employing ferroelectric films close to the side walls would be investigated for cylindrical cavities. Figure 7.1a depicts a preliminary design developed at the end of this PhD thesis. On the other hand, Figure 7.1b shows one of the investigated strategies, based on the division of a cylindrical cavity into two halves with an interleaved geometry where a positive and negative voltage (or GND) could be applied to each half to bias the KTO located between them (avoiding the implementation of high resistivity contacts). Other geometries, such as the one shown in Figure 7.1c, are also being studied to reduce the effect on the surface currents while implementing choke sections at the ports to have a simpler adjustment system for the input / output coaxial coupling. In this case, the KTO would be positioned at the regions between the cavity walls, as in the case depicted in Figure 7.1b. Finally, research is being conducted into the doping of KTO materials with lithium, in order to decrease the ferroelectric permittivity to much lower values (from 4500 to 500, for example), which would make electromagnetic designs much easier.

- Multi-port combination for mode rejecting: Investigation of loop ports at tall structures for rejecting the TE_{121} resonant mode is also an interesting topic. In addition, structures with more than two loops could be studied to cancel other TE_{1y1} modes,

(a) (b) (c)
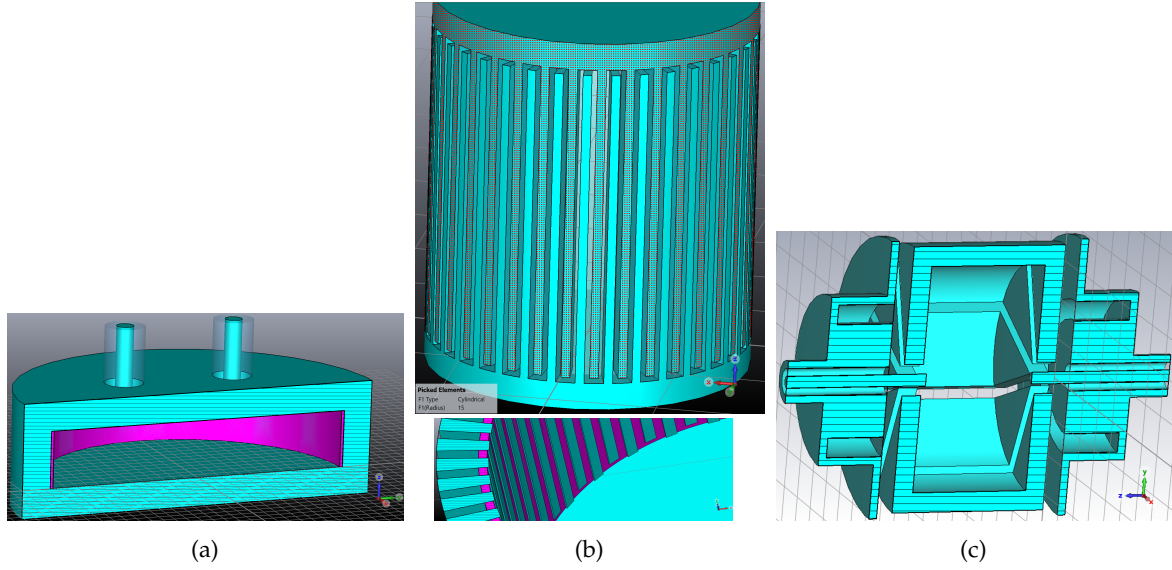
Figure 7.1: 3D models of the cylindrical cavity designs to be studied in a future for the implementation of KTO ferroelectrics as tuning elements: (a) KTO films at sides, (b) design with interleaved cuts, and (c) the *Cake cavity* idea with choke sections. The pink color represents the ferroelectric KTO. The bottom picture from (b) shows the inner section of the design for the visualisation of the position of the ferroelectric material. (a) and (c) depict the symmetric half of the structure, being the dashed regions the symmetry plane.

being y an even number, by strategically positioning these ports in the null E-field regions of the mode. Additionally, the optimisation of the S_{11} level to achieve critical coupling combining the 8 coaxial ports of the prototype shown in section 5.1 (see Figure 5.7) has been left as pending work. Another future direction that has emerged from this PhD thesis is to apply the investigations presented in this topic to a prototype with more and larger subcavities. Lastly, this research has resulted in the study of a new design method, which is still being investigated, based on the usage of pyramidal waveguide transitions (with geometry comparable to that of horn antennas) to avoid excitation of resonant modes along the height in tall multicavities. The combination of KTO films with these ideas is also a future line of work.

- Other studies: Development of the additional ideas (QuBits technology (section 5.2.1), haloscope design in UHF and W bands (section 5.2.2), HTS haloscopes (section 5.2.3), and BI-RME 3D method (section 5.2.4)).

- RF bandpass filters for satellite communications: Improvement of the transmission parameter response in the manufactured prototype employing the folded evanescent filter design presented in section 6.1.3.2. It is thought that the problem may stem from a poor contact between the metallic parts of the housing. First of all, the dielectric will be sanded for a better fit. If this method does not work, a new ABSplus part would be produced with a more suitable size, which is a simple and inexpensive task due to the low cost of 3D printing manufacturing. On the other hand, the production of the asymmetric folded filter with transmission zeros shown in section 6.2.2 has also been reserved as a future line. Prior to such fabrication, a re-optimisation must

be applied considering the implementation of a tuning screw system, 30° waveguide bend sections at the ports, and rounded vertical chamfers at the corners. Finally, the design and fabrication of the structure presented in section 6.2.3 (horizontally folded asymmetric filter with 6 resonators to obtain 4 transmission zeros) is also one of the future lines of research of this PhD thesis.

APPENDIX I: TECHNICAL DRAWINGS

A.1 ALL-INDUCTIVE 5-SUBCAVITIES HALOSCOPE WITH HORIZONTAL CUT
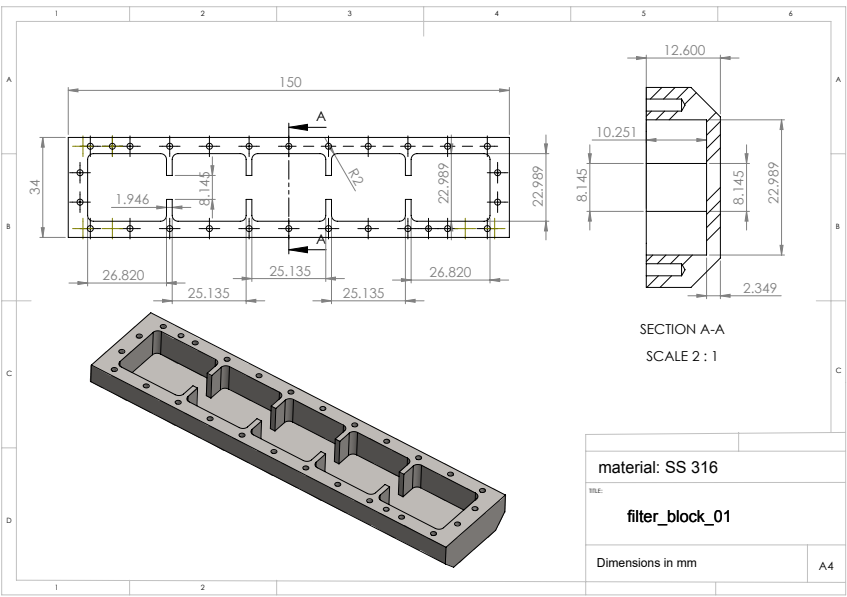
Figure A.1: Body of the all-inductive 5-subcavities haloscope.
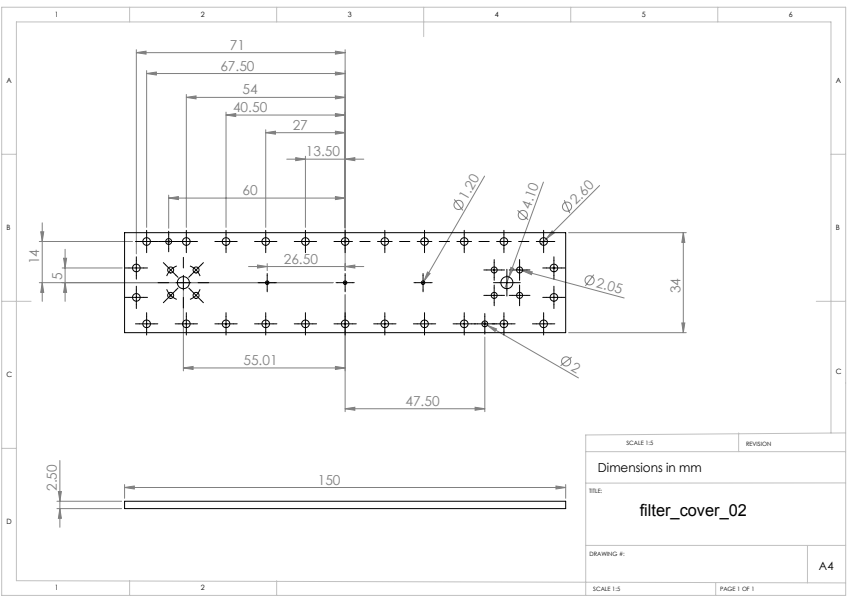
Figure A.2: Cover of the all-inductive 5-subcavities haloscope.

Figure A.3: Dimensions of the alternating 6-subcavities haloscope.

A.3 ALTERNATING 30-SUBCAVITIES HALOSCOPE WITH HORIZONTAL CUT

Figure A.4: Body of the alternating 30-subcavities haloscope.

Figure A.5: Cover of the alternating 30-subcavities haloscope.

A.4 ALL-INDUCTIVE TALL 4-SUBCAVITIES HALOSCOPE WITH VERTICAL CUT

Figure A.6: Symmetrical half of the all-inductive tall 4-subcavities haloscope.
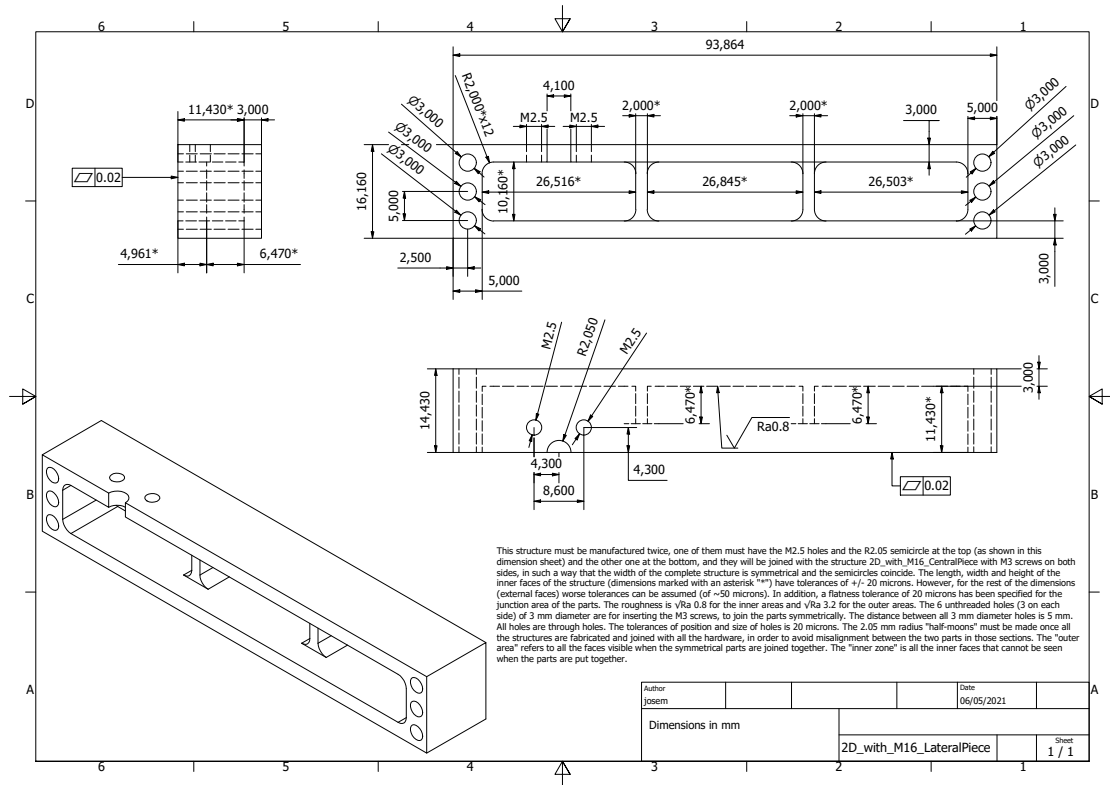
Figure A.7: Lateral piece of the all-inductive 2D 6-subcavities haloscope with M_{16} cross-coupling.
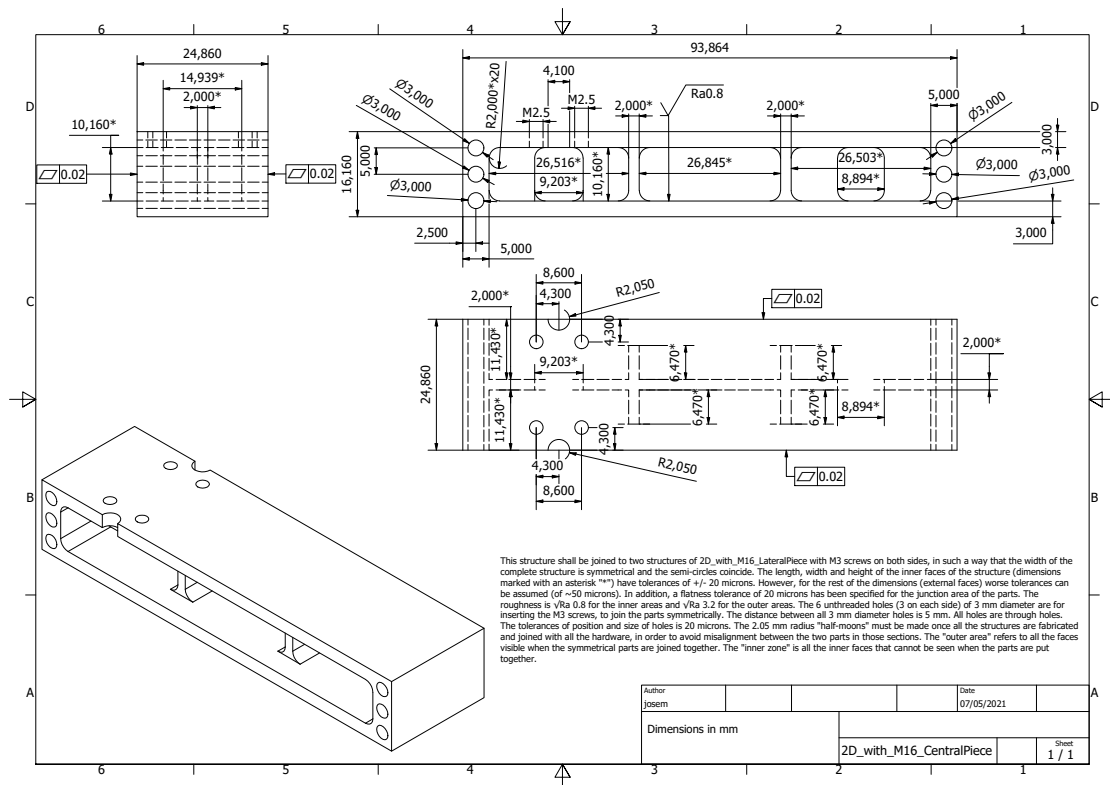
Figure A.8: Central piece of the all-inductive 2D 6-subcavities haloscope with M_{16} cross-coupling.
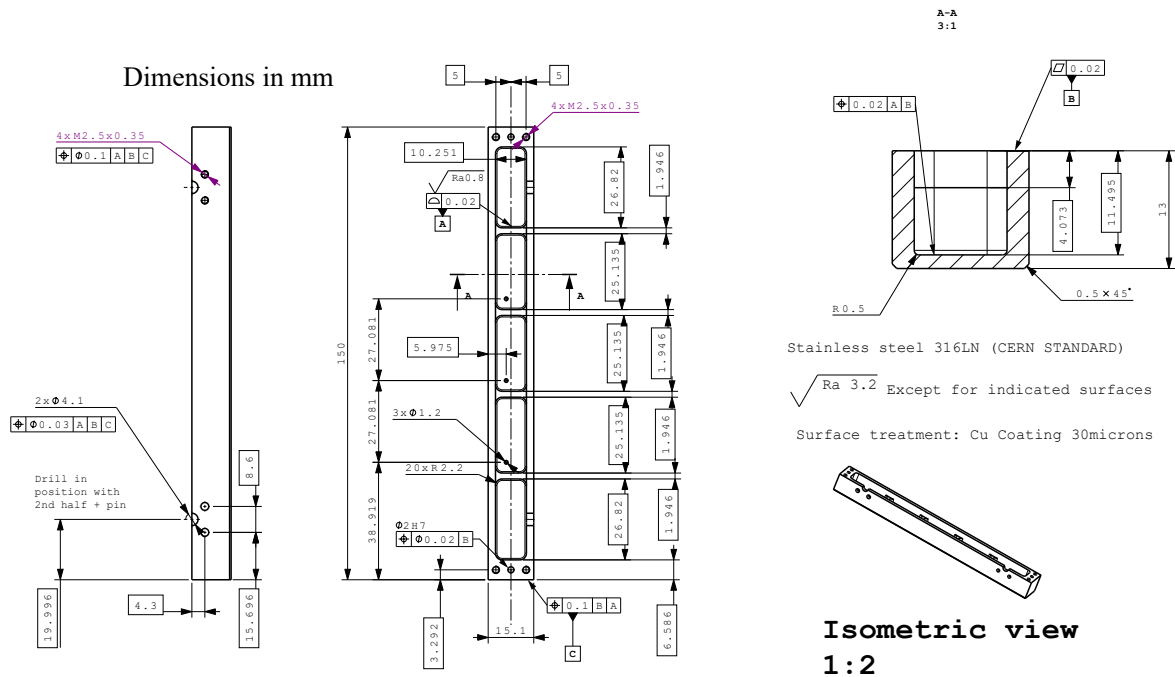
Figure A.9: Symmetrical half of the vertical cut haloscope.

A.7 MODULARITY WITH TRANSVERSAL CUTS
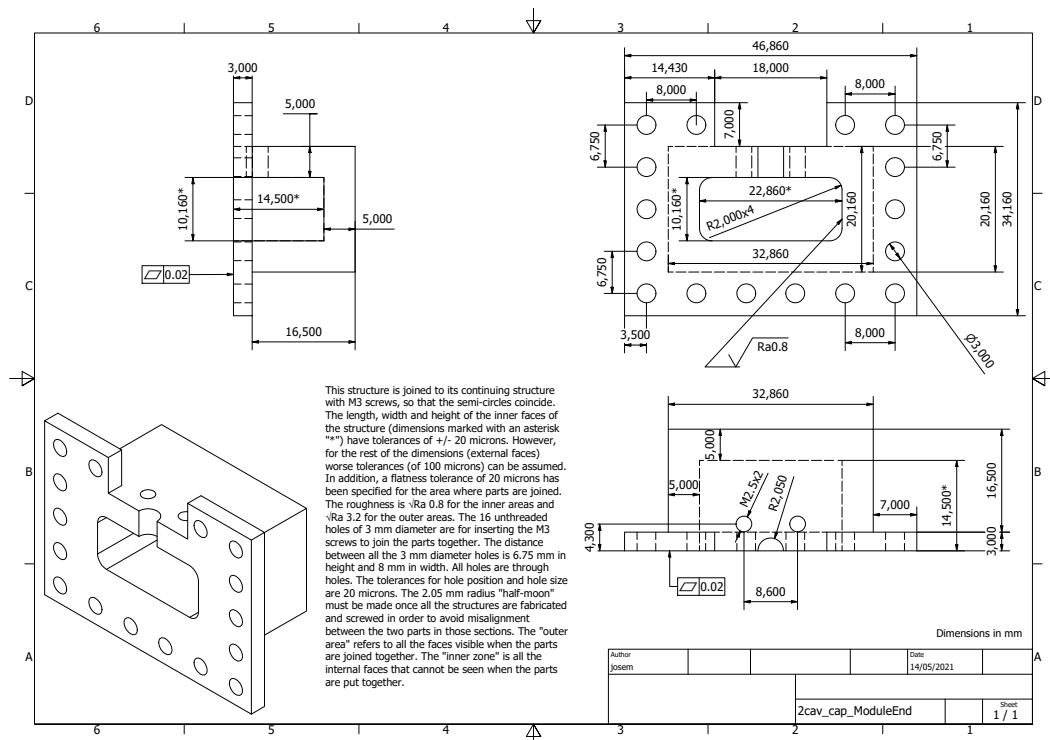
Figure A.10: *2cav-Cap-ModuleEnd* module of the modularity.
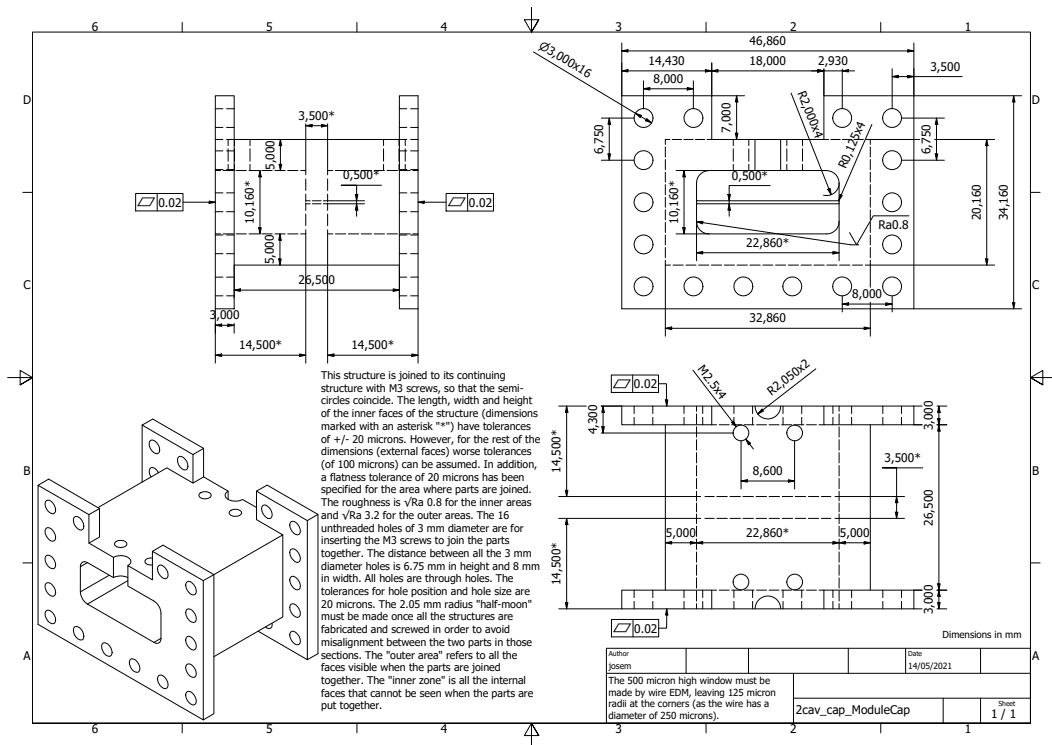
Figure A.11: *2cav-Cap-ModuleCap* module of the modularity.

A.8 HTS HALOSCOPE WITH VERTICAL CUT
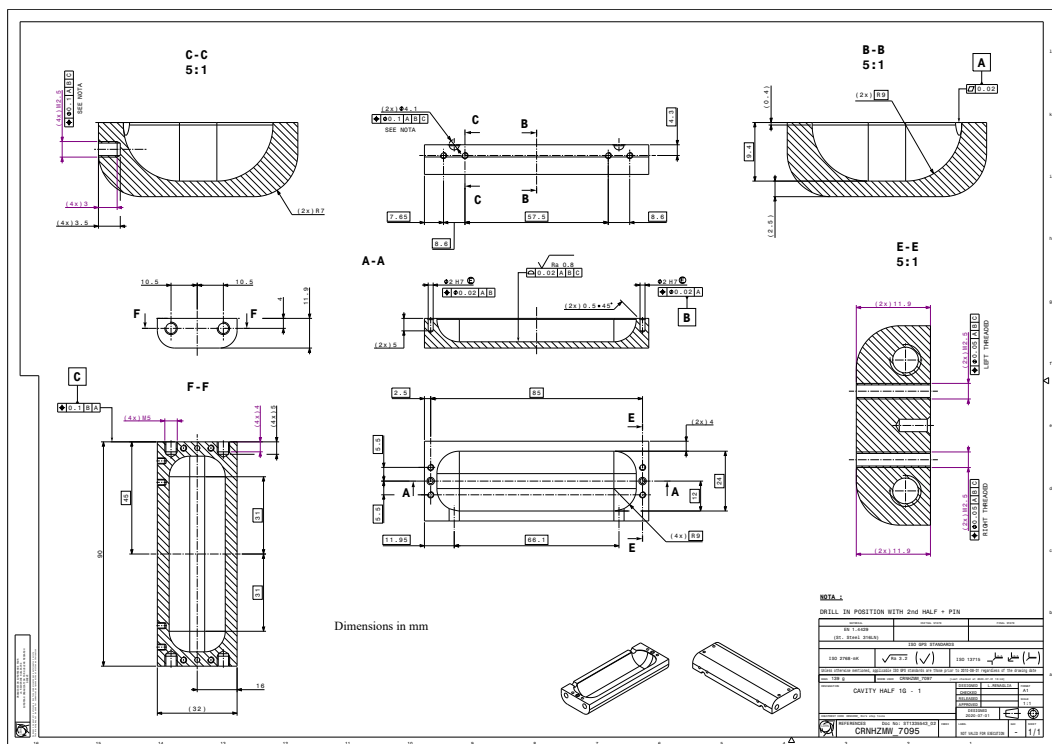
Figure A.12: First half of the HTS haloscope.
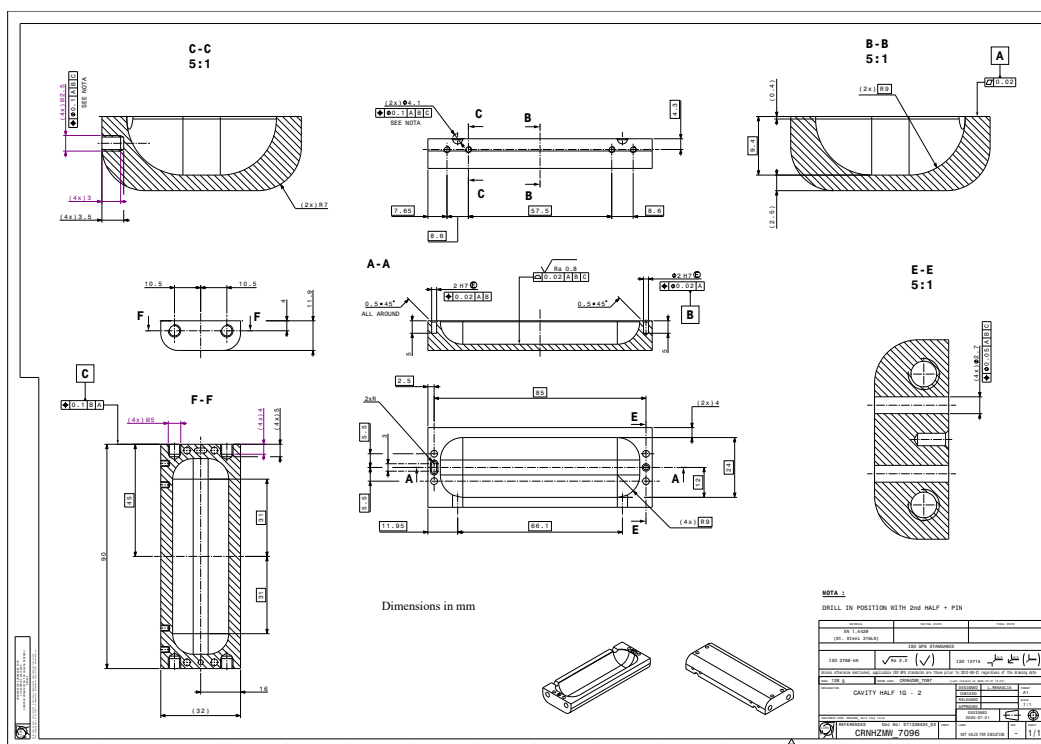
Figure A.13: Second half of the HTS haloscope.

Figure A.14: Body of the straight evanescent bandpass filter.

210
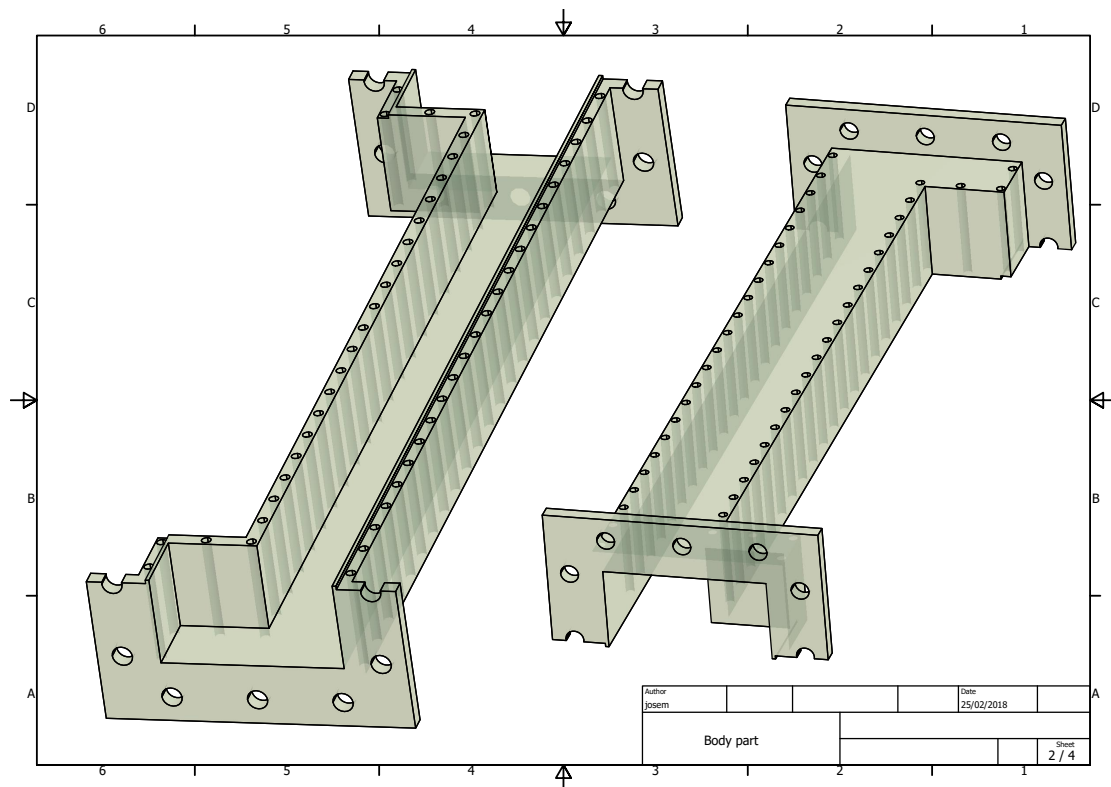
Figure A.15: More body details of the straight evanescent bandpass filter.
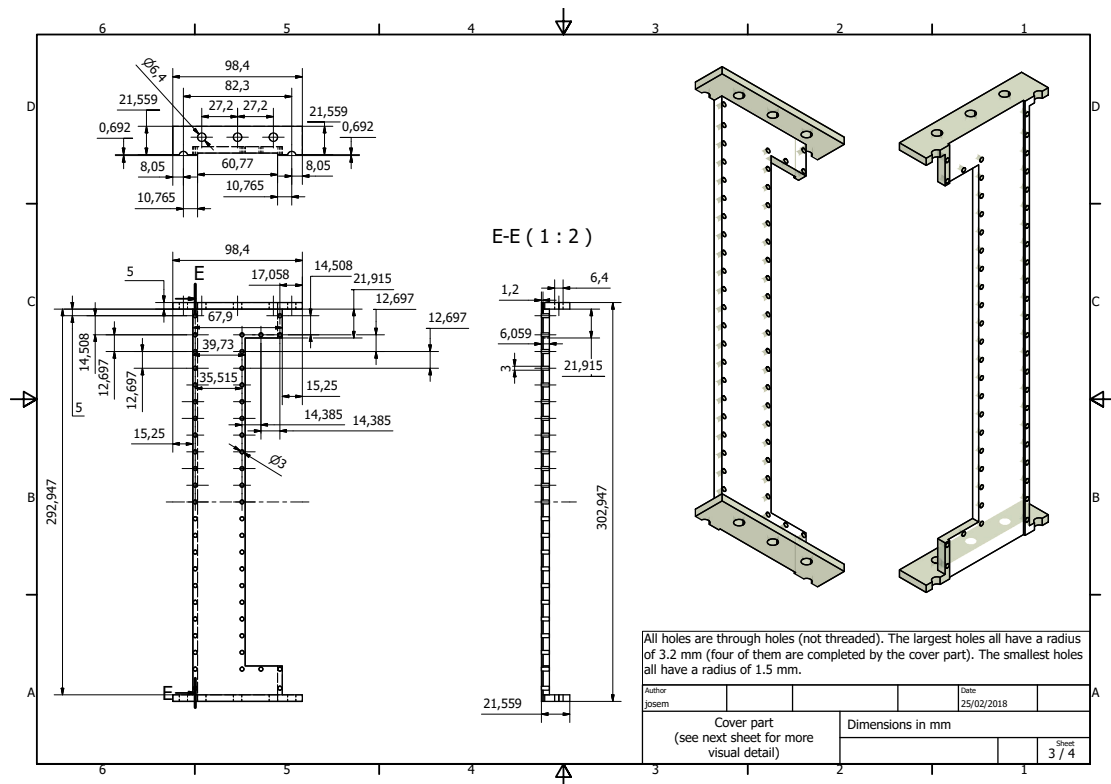
Figure A.16: Cover of the straight evanescent bandpass filter.
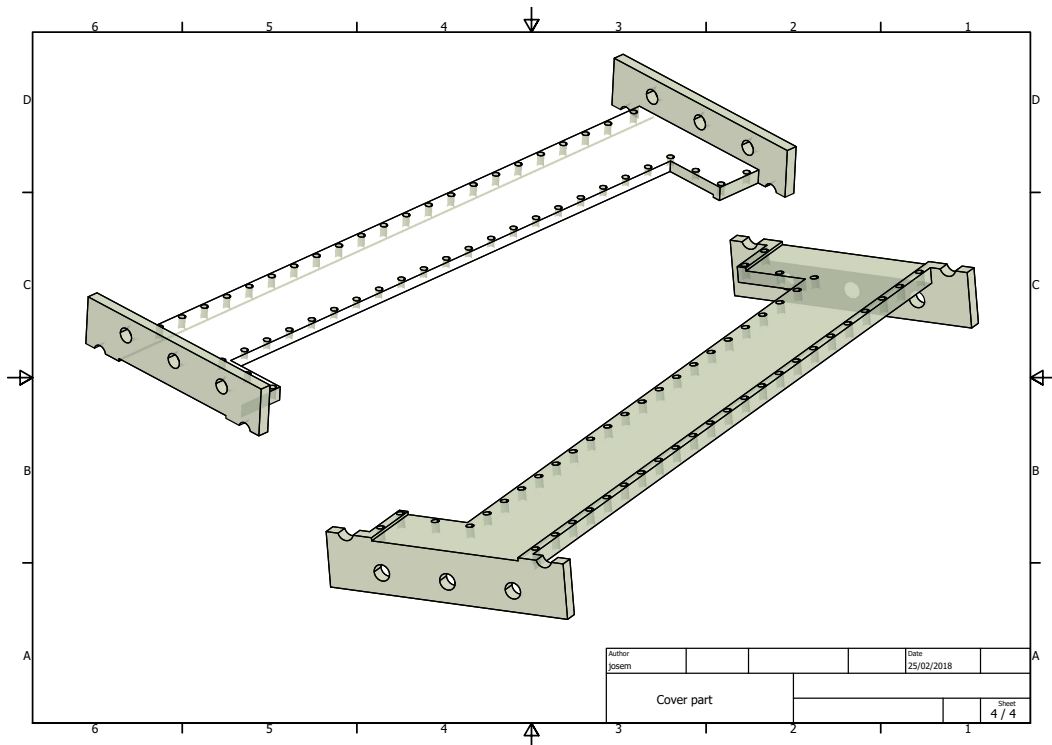
Figure A.17: More cover details of the straight evanescent bandpass filter.

A.10 FOLDED EVANESCENT FILTER WITH HORIZONTAL CUT
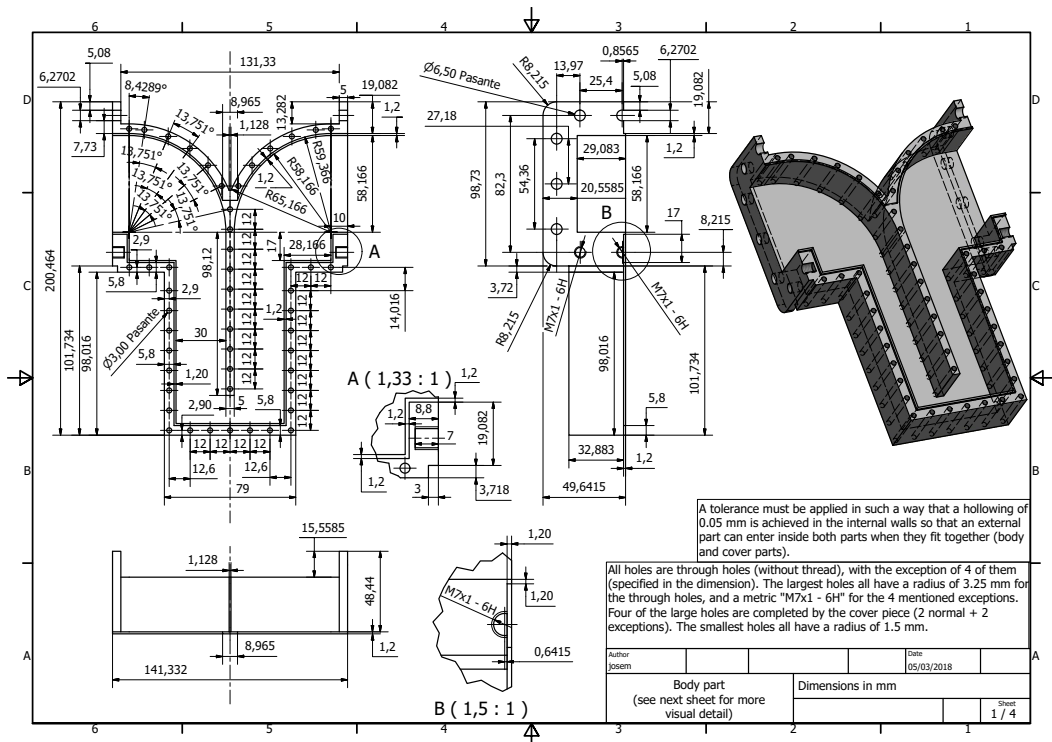
Figure A.18: Body of the folded evanescent bandpass filter.

Figure A.19: More body details of the folded evanescent bandpass filter.

Figure A.20: Cover of the folded evanescent bandpass filter.

213
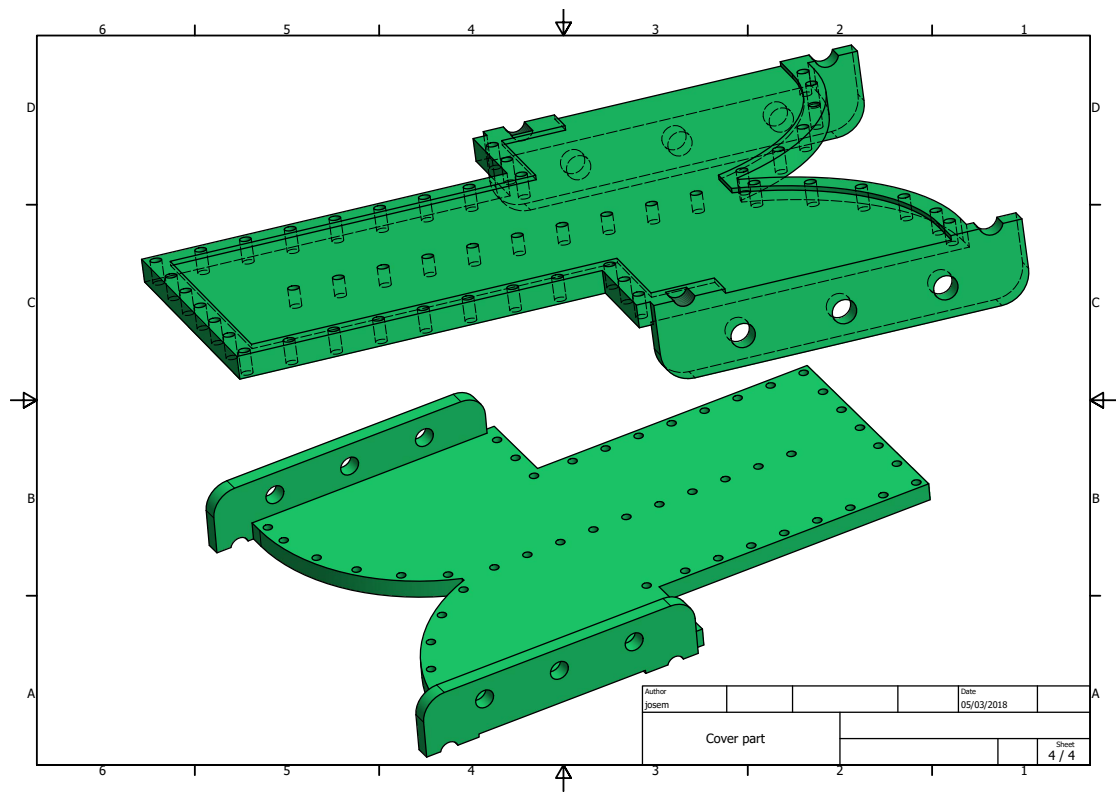
Figure A.21: More cover details of the folded evanescent bandpass filter.

APPENDIX II: CRITICAL COUPLING COMBINING 2 PORTS

As it is explained in subsection 3.2.1.4, to obtain a critical coupling level (situation with the highest axion-photon conversion sensitivity in a haloscope) in a cavity or multicavity with a single port (or with two ports, with one of them very weakly coupled), it must be configured in such a way that it provides a minimum S_{11} level or, in other words, a value of $\beta = 1$. It was seen that this can be achieved by performing a sweep of coaxial antenna lengths, in case of using this type of ports, until such a value is obtained.

On the other hand, as it is explained in section 5.1, when the combination of 2 or more ports are desired with the phase matching method, in order to eliminate some unwanted modes in the response of a haloscope, they must have the same characteristics (e.g. the same antenna length).

To combine the above two concepts, i.e. to achieve the critically coupled case when combining ports, a slightly more complex analysis must be performed. In this PhD thesis, the study of this analysis has been carried out for the case of combining two ports. For this porpoise, the one-port scenario is reviewed. Figure B.1 depicts the circuit of this case.
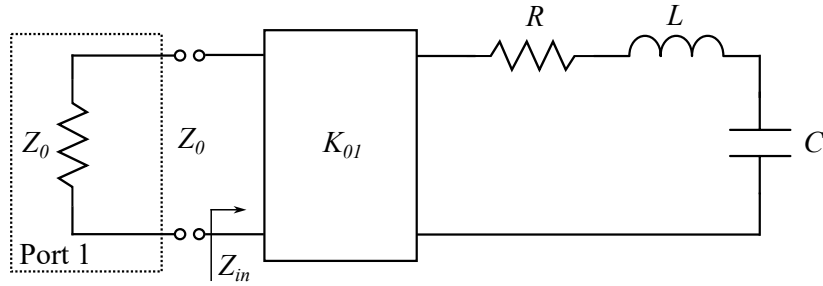
Figure B.1: Series *RLC* resonant circuit with a Z_0 port and an impedance inverter of value K_{01} to model the external coupling.

From [74] it can be extracted that

$$Z_{in} = \frac{K_{01}^2}{R},$$
(B.1)

at the resonant frequency, where Z_{in} is the input impedance from the port to the circuit (including the external coupling plus the *RLC* resonator), K_{01} is the value of the impedance inverter, and R is the resistance value of the resonator and models the resonator losses.

On the other hand, the reflection scattering parameter S_{11} can be related with the input impedance by [69]

$$S_{11} = \frac{Z_{in} - Z_0}{Z_{in} + Z_0},$$

(B.2)

where Z_0 is the characteristic impedance of the port (50 Ω is our case). For a critical coupling scenario, it is needed that $S_{11} = 0$ at resonance. This implies that

$$Z_{in} = Z_0 = \frac{K_{01}^2}{R}.$$

(B.3)

Therefore, it is obtained a critical coupling with

$$K_{01} = \sqrt{Z_0 R}.$$

(B.4)

From equation B.4 it can be seen that for a lossless resonator ($R = 0$) there is no solution.

Now, considering the case with two symmetrical and equivalent ports, the circuit from Figure B.2 should be analysed.
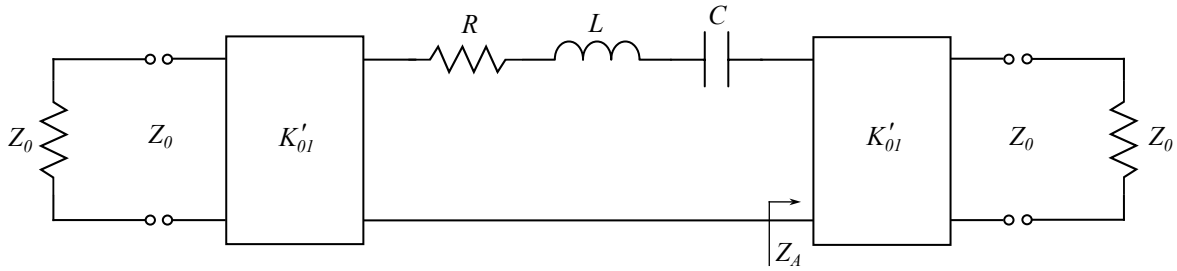
Figure B.2: Series RLC resonant circuit with two Z_0 ports and two impedance inverters of value K_{01}' to model the external couplings.

Unlike in the case of one port, the impedance inverter now has a K_{01}' value. In addition, the parameter Z_A from this scheme is the impedance as viewed from the resonator to the right side (including the second impedance inverter and port), and it can be expressed as

$$Z_A = \frac{K_{01}'^2}{Z_0}.$$

(B.5)

At resonance, this circuit is converted into the scheme shown in Figure B.3 , where its input impedance is computed as

$$Z_{in} = \frac{K_{01}'^2}{R + Z_A} = \frac{K_{01}'^2}{R + \frac{K_{01}'^2}{Z_0}} = \frac{K_{01}'^2 Z_0}{RZ_0 + K_{01}'^2}.$$

(B.6)

As the desired situation is to obtain $K_{01} = K_{01}'$, employing equation B.4, it is extracted that

$$Z_{in} = \frac{Z_0 R Z_0}{RZ_0 + Z_0 R} = \frac{Z_0^2 R}{2Z_0 R} = \frac{Z_0}{2}.$$

(B.7)
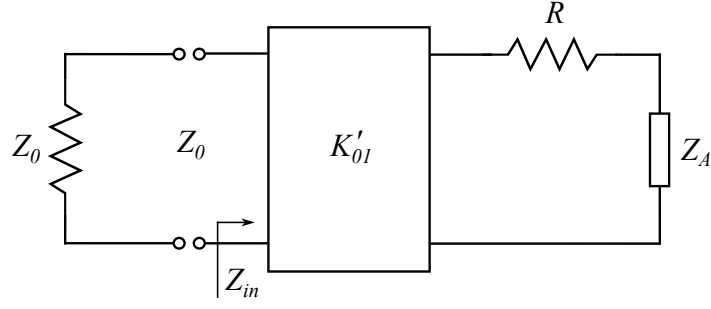
Figure B.3: Conversion of the circuit from Figure B.2 into a series R circuit with a Z_0 port, an impedance inverter of value K'_{01} to model the external couplings, and the impedance Z_A. This scenario is valid at the resonant frequency.

With this, and utilising equation B.2, the final S_{11} value (at resonance) can be obtained as

$$S_{11} = \frac{Z_0/2 - Z_0}{Z_0/2 + Z_0} = \frac{-Z_0/2}{3Z_0/2} = -\frac{Z_0}{3Z_0} = -1/3 = -0.33. \tag{B.8}$$

It is important to note that the sign of this parameter is important for obtaining the critical coupling case (a condition $S_{11} = 1/3$ would only work at the parallel RLC circuit analysis). In terms of magnitude in dB and phase in degree, this parameter acquires the value of $|S_{11}| = -9.5$ dB and $\phi_{S_{11}} = 180^o$.

PUBLICATIONS AND RESEARCH STAYS

This PhD thesis includes work by the author that has been published or accepted for publication. These publications are the own work of the author of this PhD thesis, and the author has the permission of the publishers to reproduce the contents of these publications for academic purposes.

In particular, some data, ideas, opinions and figures presented in this work have previously appeared or may appear shortly after the submission of this PhD thesis mainly in the following scientific outcome:

- National conferences:

    1. Jose María García Barceló et al. "**Estudio de la sintonización electrónica en tecnología guía de onda a temperaturas criogénicas para un detector de axiones de materia oscura**"in *XXXIV edición del Simposium URSI*, Sevilla, Spain, 2019

    2. Jose María García Barceló et al. "**Avances en el proyecto RADES: Sintonización electrónica con detectores axiónicos de materia oscura en tecnología guía de onda a bajas temperaturas**"in *V Jornadas Doctorales Campus Mare Nostrum*, Murcia, Spain, 2019

    3. Jose María García Barceló et al. "**Diseño de filtros paso banda en tecnología guía de onda mediante fabricación aditiva**"in *XXXIII edición del Simposium URSI*, Granada, Spain, 2018

- International conferences:

    1. Jose María García Barceló et al. "**Evanescent Mode Filters Composed of Dielectric Parts Built Using 3D-Printing Methods**"in *International Microwave Filter Workshop 2021*, Perugia, Italy, 2021. Online: https://ieeexplore.ieee.org/document/9642351

    2. Jose María García Barceló "**Haloscopes for axion dark matter detection in the 30 μeV range with RADES**"in *Snowmass October Workshop on Wave-like Dark Matter*, MIT, Online, 2021

    3. Jose María García Barceló "**The RADES project progress: alternating formalism and ferroelectric tuning**"in *11th IAXO Collaboration Meeting*, CERN, Geneva, Switzerland, 2020

    4. Jose María García Barceló "**The CAST-RADES project progress: electrical tuning ideas and a new 30 sub-cavities axion detector design**"in *15th Patras Workshop on Axions, WIMPs and WISPs*, Freiburg, Germany, 2019

5. Jose María García Barceló et al. "**Electrically Tunable Systems**"in *1st RADES Collaboration Meeting*, Zaragoza, Spain, 2019

- Scientific journals:

1. Jose María García Barceló et al. "**Methods and restrictions to increase the volume of resonant rectangular-section haloscopes for detecting dark matter axions**" under revision in *JHEP*, ArXiv preprint: https://arxiv.org/abs/2302.10569

2. Jose María García Barceló et al. "**On the development of new tuning and inter-coupling techniques using ferroelectric materials in the detection of dark matter axions**" published in *IEEE Access*, 2023, 11, 30360-30372 DOI: https://doi.org/10.1109/ACCESS.2023.3260783

3. Alejandro Díaz Morcillo, Jose María García Barceló et al. "**Design of New Resonant Haloscopes in the Search for the Dark Matter Axion: A Review of the First Steps in the RADES Collaboration**" published in *Universe*, 2021, 8 (1), 5 DOI: https://doi.org/10.3390/universe8010005

4. Alejandro Álvarez Melcón et al. "**Scalable haloscopes for axion dark matter detection in the 30 μeV range with RADES**" published in *Journal of High Energy Physics*, 2020, 84 (2020) DOI: https://doi.org/10.1007/JHEP07(2020)084

5. Alejandro Pons Abenza, Jose María García Barceló et al. "**Design and implementation of evanescent mode waveguide filters using dielectrics and additive manufacturing techniques**" published in *AEU - International Journal of Electronics and Communications*, 2020, 116 (2020), 153065 DOI: https://doi.org/10.1016/j.aeue.2020.153065

Below is a summary of the scientific works that resulted from other partnerships during this doctoral period:

- National conferences:

1. Jose Ramón Navarro Madrid, Alejandro Díaz Morcillo and Jose María García Barceló et al. "**Comparativa de prestaciones entre cavidades resonantes y multicavidad para detección de axiones de materia oscura**"in *XXXVII edición del Simposium URSI*, Málaga, Spain, 2022

- Scientific journals:

1. Beatriz Aja et al. "**The Canfranc Axion Detection Experiment (CADEx): search for axions at 90 GHz with Kinetic Inductance Detectors**" published in *Journal of Cosmology and Astroparticle Physics*, 2022, 11 (2022) DOI: https://dx.doi.org/10.1088/1475-7516/2022/11/044

2. P. Navarro et al. "**Wide-band full-wave electromagnetic modal analysis of the coupling between dark-matter axions and photons in microwave resonators**" published in *Physics of the Dark Universe*, 2022, 36 (2022), 101001 DOI: https://doi.org/10.1016/j.dark.2022.101001

3. J. Golm et al. "**Thin Film (High Temperature) Superconducting Radiofrequency Cavities for the Search of Axion Dark Matter**" published in *IEEE Transactions on Applied Superconductivity*, 2022, 32 (4) DOI: https://doi.org/10.1109/TASC.2022.3147741

4. Alejandro Álvarez Melcón et al. "**First results of the CAST-RADES haloscope search for axions at 34.67 μeV**" published in *Journal of High Energy Physics*, 2021, 75 (2021) DOI: https://doi.org/10.1007/JHEP10(2021)075

- White papers:

1. Snowmass collaboration "**Snowmass 2021 Axion Dark Matter White Paper**", *Proceedings of the 2021 US Community Study on the Future of Particle Physics (Snowmass 2021)*, ArXiv preprint: https://arxiv.org/abs/2203.14923v1. Full Snowmass report: https://www.slac.stanford.edu/econf/C210711/index.html

Except where reference is made in the text of the work, this PhD thesis contains no other material published elsewhere or extracted in whole or in part from a PhD thesis accepted for the award of any other degree or diploma. No other person's work has been used without due acknowledgment in the main text of the PhD thesis. This work has not been submitted for the award of any degree or diploma in any other tertiary institution.

On the other hand, the author of this work has carried out 3 research stays abroad where he has realised part of the experiments shown in this PhD thesis. The stays have been executed at CERN, located on the French-Swiss border near the city of Geneva, which is the largest research laboratory in *Elementary Particle Physics* or *High Energy Physics* in the world.

- Research stays:

1. From the 5th of February 2019 to the 8th of March 2019 at CERN, Geneva, Switzerland, under the supervision of Dr. Babette Döbrich.

2. From the 1st of March 2020 to the 1st of June 2020 at CERN, Geneva, Switzerland, under the supervision of Dr. Babette Döbrich.

3. From the 3rd of May 2021 to the 20th of May 2021 at CERN, Geneva, Switzerland, under the supervision of Dr. Babette Döbrich.

The tasks conducted have been related to the CAST experiment, within the RADES research project.

REFERENCES

[1] S. Weinberg, 'A new light boson?', *Phys. Rev. Lett.*, vol. 40, pp. 223–226, 1978. DOI: https://doi.org/10.1103/PhysRevLett.40.223.

[2] F. Wilczek, 'Problem of strong P and T invariance in the presence of instantons', *Phys. Rev. Lett.*, vol. 40, pp. 279–282, 1978. DOI: https://doi.org/10.1103/PhysRevLett.40.279.

[3] R. Peccei and H. Quinn, 'CP conservation in the presence of pseudoparticles', *Phys. Rev. Lett.*, vol. 38, pp. 1440–1443, 1977. DOI: https://doi.org/10.1103/PhysRevLett.38.1440.

[4] J. Ipser and P. Sikivie, 'Can Galactic Halos Be Made of Axions?', *Phys. Rev. Lett.*, vol. 50, pp. 925–927, 12 1983. DOI: https://doi.org/10.1103/PhysRevLett.50.925.

[5] C. Patrignani *et al.*, 'Review of Particle Physics', *Chin. Phys. C*, vol. 40, no. 10, p. 100 001, 2016. DOI: https://doi.org/10.1088/1674-1137/40/10/100001.

[6] P. Sikivie, 'Experimental Tests of the Invisible Axion', *Phys. Rev. Lett.*, vol. 51, M. A. Srednicki, Ed., pp. 1415–1417, 1983, [Erratum: Phys.Rev.Lett. 52, 695 (1984)]. DOI: https://doi.org/10.1103/PhysRevLett.51.1415.

[7] H. Primakoff, 'Photoproduction of neutral mesons in nuclear electric fields and the mean life of the neutral meson', *Phys. Rev.*, vol. 81, p. 899, 1951. DOI: https://doi.org/10.1103/PhysRev.81.899.

[8] K. Van Bibber, N. R. Dagdeviren, S. E. Koonin, A. K. Kerman and H. N. Nelson, 'Proposed experiment to produce and detect light pseudoscalars', *Phys. Rev. Lett.*, vol. 59, pp. 759–762, 7 1987. DOI: https://doi.org/10.1103/PhysRevLett.59.759.

[9] Y. Fukuda, T. Kohmoto, S. ichi Nakajima and M. Kunitomo, 'Production and detection of axions by using optical resonators', *Progress in Crystal Growth and Characterization of Materials*, vol. 33, no. 1, pp. 363–366, 1996, ISSN: 0960-8974. DOI: https://doi.org/10.1016/0960-8974(96)83672-2.

[10] P. Sikivie, D. B. Tanner and K. van Bibber, 'Resonantly Enhanced Axion-Photon Regeneration', *Phys. Rev. Lett.*, vol. 98, p. 172 002, 17 2007. DOI: https://doi.org/10.1103/PhysRevLett.98.172002.

[11] D. M. Lazarus, G. C. Smith, R. Cameron, A. C. Melissinos, G. Ruoso, Y. K. Semertzidis and F. A. Nezrick, 'Search for solar axions', *Phys. Rev. Lett.*, vol. 69, pp. 2333–2336, 16 1992. DOI: https://doi.org/10.1103/PhysRevLett.69.2333.

[12] Y. Inoue, T. Namba, S. Moriyama, M. Minowa, Y. Takasu, T. Horiuchi and A. Yamamoto, 'Search for sub-electronvolt solar axions using coherent conversion of axions into photons in magnetic field and gas helium', *Physics Letters B*, vol. 536, no. 1, pp. 18–23, 2002, ISSN: 0370-2693. DOI: https://doi.org/10.1016/S0370-2693(02)01822-1.

[13] S. Moriyama, M. Minowa, T. Namba, Y. Inoue, Y. Takasu and A. Yamamoto, 'Direct search for solar axions by using strong magnetic field and X-ray detectors', *Physics Letters B*, vol. 434, no. 1, pp. 147–152, 1998, ISSN: 0370-2693. DOI: https://doi.org/10.1016/S0370-2693(98)00766-7.

[14] Y. Inoue, Y. Akimoto, R. Ohta, T. Mizumoto, A. Yamamoto and M. Minowa, 'Search for solar axions with mass around 1 eV using coherent conversion of axions into photons', *Physics Letters B*, vol. 668, no. 2, pp. 93–97, 2008, ISSN: 0370-2693. DOI: https://doi.org/10.1016/j.physletb.2008.08.020.

[15] V. Anastassopoulos, S. Aune, K. Barth *et al.*, 'New CAST Limit on the Axion-Photon Interaction', *Nature Physics*, vol. 13, pp. 584–590, May 2017. DOI: https://doi.org/10.1038/nphys4109.

[16] CAST Collaboration, 'Search for Sub-eV Mass Solar Axions by the CERN Axion Solar Telescope with ^{3}He Buffer Gas', *Phys. Rev. Lett.*, vol. 107, p. 261 302, 26 2011. DOI: https://doi.org/10.1103/PhysRevLett.107.261302.

[17] IAXO Collaboration, 'Physics potential of the International Axion Observatory (IAXO)', *Journal of Cosmology and Astroparticle Physics*, vol. 2019, no. 06, pp. 047–047, 2019. DOI: https://doi.org/10.1088/1475-7516/2019/06/047.

[18] P. W. Graham, I. G. Irastorza, S. K. Lamoreaux, A. Lindner and K. A. van Bibber, 'Experimental Searches for the Axion and Axion-Like Particles', *Annual Review of Nuclear and Particle Science*, vol. 65, no. 1, pp. 485–514, 2015. DOI: https://doi.org/10.1146/annurev-nucl-102014-022120.

[19] I. G. Irastorza and J. Redondo, 'New experimental approaches in the search for axion-like particles', *Progress in Particle and Nuclear Physics*, vol. 102, pp. 89–159, 2018, ISSN: 0146-6410. DOI: https://doi.org/10.1016/j.ppnp.2018.05.003.

[20] L. Di Luzio, M. Giannotti, E. Nardi and L. Visinelli, 'The landscape of QCD axion models', *Physics Reports*, vol. 870, pp. 1–117, 2020, ISSN: 0370-1573. DOI: https://doi.org/10.1016/j.physrep.2020.06.002.

[21] P. Sikivie, 'Invisible axion search methods', *Rev. Mod. Phys.*, vol. 93, p. 015 004, 1 2021. DOI: https://doi.org/10.1103/RevModPhys.93.015004.

[22] L. Abbott and P. Sikivie, 'A cosmological bound on the invisible axion', *Physics Letters B*, vol. 120, no. 1, pp. 133–136, 1983, ISSN: 0370-2693. DOI: https://doi.org/10.1016/0370-2693(83)90638-X.

[23] M. Dine and W. Fischler, 'The not-so-harmless axion', *Physics Letters B*, vol. 120, no. 1, pp. 137–141, 1983, ISSN: 0370-2693. DOI: https://doi.org/10.1016/0370-2693(83)90639-1.

[24] I. Stern, 'ADMX Status', *Proceedings of the Science, 38th International Conference on High Energy Physics*, vol. ICHEP2016, p. 198, 2016. DOI: https://doi.org/10.22323/1.282.0198. arXiv: 1612.08296 [physics.ins-det].

[25] W. U. Wuensch, S. De Panfilis-Wuensch, Y. K. Semertzidis, J. T. Rogers, A. C. Melissinos, H. J. Halama, B. E. Moskowitz, A. G. Prodell, W. B. Fowler and F. A. Nezrick, 'Results of a laboratory search for cosmic axions and other weakly coupled light particles', *Phys. Rev. D*, vol. 40, pp. 3153–3167, 10 1989. DOI: https://doi.org/10.1103/PhysRevD.40.3153.

[26] C. Hagmann, P. Sikivie, N. S. Sullivan and D. B. Tanner, 'Results from a search for cosmic axions', *Phys. Rev. D*, vol. 42, pp. 1297–1300, 4 1990. DOI: https://doi.org/10.1103/PhysRevD.42.1297.

[27] A. Á. Melcón, S. A. Cuendis, C. Cogollos *et al.*, 'Axion searches with microwave filters: the RADES project', *Journal of Cosmology and Astroparticle Physics*, vol. 2018, no. 05, pp. 040–040, 2018. DOI: https://doi.org/10.1088/1475-7516/2018/05/040.

[28] D. Alesini, D. Babusci, D. Di Gioacchino, C. Gatti, G. Lamanna and C. Ligi, 'The KLASH Proposal', 2017. arXiv: 1707.06010 [physics.ins-det].

[29] S. Al Kenany, M. Anil, K. Backes *et al.*, 'Design and operational experience of a microwave cavity axion detector for the $20 - 100$ μeV range', *Nuclear Instruments and Methods in Physics Research Section A: Accelerators, Spectrometers, Detectors and Associated Equipment*, vol. 854, pp. 11–24, 2017, ISSN: 0168-9002. DOI: https://doi.org/10.1016/j.nima.2017.02.012.

[30] B. T. McAllister, G. Flower, E. N. Ivanov, M. Goryachev, J. Bourhill and M. E. Tobar, 'The ORGAN experiment: An axion haloscope above 15 GHz', *Physics of the Dark Universe*, vol. 18, pp. 67–72, 2017, ISSN: 2212-6864. DOI: https://doi.org/10.1016/j.dark.2017.09.010.

[31] D. Alesini, C. Braggio, G. Carugno *et al.*, 'Search for invisible axion dark matter of mass $m_a = 43$ μeV with the QUAX–$a\gamma$ experiment', *Phys. Rev. D*, vol. 103, p. 102 004, 10 2021. DOI: https://doi.org/10.1103/PhysRevD.103.102004.

[32] J. Jeong, S. Youn, S. Ahn, J. E. Kim and Y. K. Semertzidis, 'Concept of multiple-cell cavity for axion dark matter search', *Physics Letters B*, vol. 777, pp. 412–419, 2018, ISSN: 0370-2693. DOI: https://doi.org/10.1016/j.physletb.2017.12.066.

[33] G. Bertone, D. Hooper and J. Silk, 'Particle dark matter: evidence, candidates and constraints', *Physics Reports*, vol. 405, no. 5, pp. 279–390, 2005, ISSN: 0370-1573. DOI: https://doi.org/10.1016/j.physrep.2004.08.031.

[34] V. C. Rubin, 'Dark Matter in the Universe', *Proceedings of the American Philosophical Society*, vol. 132, no. 4, pp. 434–443, 1988, ISSN: 0003049X. [Online]. Available: http://www.jstor.org/stable/986963 (visited on 29/03/2023).

[35] R. D. Blandford and R. Narayan, 'Cosmological Applications of Gravitational Lensing', *Annual Review of Astronomy and Astrophysics*, vol. 30, no. 1, pp. 311–358, 1992. DOI: https://doi.org/10.1146/annurev.aa.30.090192.001523.

[36] D. Maity and P. Saha, 'Connecting CMB anisotropy and cold dark matter phenomenology via reheating', *Phys. Rev. D*, vol. 98, p. 103 525, 10 2018. DOI: https://doi.org/10.1103/PhysRevD.98.103525.

[37] A. Yahalom, 'The Effect of Retardation on Galactic Rotation Curves', *Journal of Physics: Conference Series*, vol. 1239, no. 1, p. 012 006, 2019. DOI: https://doi.org/10.1088/1742-6596/1239/1/012006.

[38] NASA, ESA, CSA, and STScI, *NASA's Webb Produces the Most Detailed Image of the Early Universe to Date*, [accessed July 11, 2022], 2022. [Online]. Available: https://webbtelescope.org/contents/news-releases/2022/news-2022-038.

[39] E. Kolb and M. Turner, *The Early Universe*, First. CRC Press, 1990. DOI: https://doi.org/10.1201/9780429492860.

[40] D. S. Akerib, S. Alsum, H. M. Araújo *et al.*, 'Results from a Search for Dark Matter in the Complete LUX Exposure', *Phys. Rev. Lett.*, vol. 118, p. 021 303, 2 2017. DOI: https://link.aps.org/doi/10.1103/PhysRevLett.118.021303.

[41] ATLAS Collaboration, *ATLAS releases new results in search for weakly-interacting supersymmetric particles*, [Physics Briefing], 2017. [Online]. Available: http://atlas.cern/updates/physics-briefing/atlas-releases-new-results-search-weakly-interacting-supersymmetric.

[42] A. Arvanitaki, S. Dimopoulos, S. Dubovsky, N. Kaloper and J. March-Russell, 'String axiverse', *Phys. Rev. D*, vol. 81, p. 123 530, 12 2010. DOI: https://doi.org/10.1103/PhysRevD.81.123530.

[43] J. E. Kim, 'Light pseudoscalars, particle physics and cosmology', *Physics Reports*, vol. 150, no. 1, pp. 1–177, Jan. 1987. DOI: https://doi.org/10.1016/0370-1573(87)90017-2.

[44] S. L. Adler, 'Axial-Vector Vertex in Spinor Electrodynamics', *Phys. Rev.*, vol. 177, pp. 2426–2438, 5 1969. DOI: https://doi.org/10.1103/PhysRev.177.2426.

[45] R. Jackiw and C. Rebbi, 'Vacuum Periodicity in a Yang-Mills Quantum Theory', *Phys. Rev. Lett.*, vol. 37, pp. 172–175, 3 1976. DOI: https://doi.org/10.1103/PhysRevLett.37.172.

[46] G. 't Hooft, 'Computation of the quantum effects due to a four-dimensional pseudoparticle', *Phys. Rev. D*, vol. 14, pp. 3432–3450, 12 1976. DOI: https://doi.org/10.1103/PhysRevD.14.3432.

[47] V. Baluni, 'CP-nonconserving effects in quantum chromodynamics', *Phys. Rev. D*, vol. 19, pp. 2227–2230, 7 1979. DOI: https://doi.org/10.1103/PhysRevD.19.2227.

[48] E. P. Shabalin, 'Electric dipole moment of the neutron in gauge theory', *Sov. Phys. Usp.*, vol. 26, p. 297, 1983. DOI: https://doi.org/10.1070/pu1983v026n04abeh004331.

[49] J. M. Pendlebury, S. Afach, N. J. Ayres *et al.*, 'Revised experimental upper limit on the electric dipole moment of the neutron', *Phys. Rev. D*, vol. 92, p. 092 003, 9 2015. DOI: https://doi.org/10.1103/PhysRevD.92.092003.

[50] C. A. Baker, D. D. Doyle, P. Geltenbort *et al.*, 'Improved Experimental Limit on the Electric Dipole Moment of the Neutron', *Phys. Rev. Lett.*, vol. 97, p. 131 801, 13 2006. DOI: https://doi.org/10.1103/PhysRevLett.97.131801.

[51] M. S. Turner, 'Windows on the axion', *Physics Reports*, vol. 197, no. 2, pp. 67–97, 1990, ISSN: 0370-1573. DOI: https://doi.org/10.1016/0370-1573(90)90172-X.

[52] J. D. Bjorken, S. Ecklund, W. R. Nelson, A. Abashian, C. Church, B. Lu, L. W. Mo, T. A. Nunamaker and P. Rassmann, 'Search for neutral metastable penetrating particles produced in the SLAC beam dump', *Phys. Rev. D*, vol. 38, pp. 3375–3386, 11 1988. DOI: https://doi.org/10.1103/PhysRevD.38.3375.

[53] J. E. Kim, 'Weak-Interaction Singlet and Strong CP Invariance', *Phys. Rev. Lett.*, vol. 43, pp. 103–107, 2 1979. DOI: https://doi.org/10.1103/PhysRevLett.43.103.

[54] M. Shifman, A. Vainshtein and V. Zakharov, 'Can confinement ensure natural CP invariance of strong interactions?', *Nuclear Physics B*, vol. 166, no. 3, pp. 493–506, 1980, ISSN: 0550-3213. DOI: https://doi.org/10.1016/0550-3213(80)90209-6.

[55] A. R. Zhitnitsky, 'On Possible Suppression of the Axion Hadron Interactions. (In Russian)', *Sov. J. Nucl. Phys.*, vol. 31, p. 260, 1980.

[56] M. Dine, W. Fischler and M. Srednicki, 'A simple solution to the strong CP problem with a harmless axion', *Physics Letters B*, vol. 104, no. 3, pp. 199–202, 1981, ISSN: 0370-2693. DOI: https://doi.org/10.1016/0370-2693(81)90590-6.

[57] J. Preskill, M. B. Wise and F. Wilczek, 'Cosmology of the invisible axion', *Physics Letters B*, vol. 120, no. 1, pp. 127–132, 1983, ISSN: 0370-2693. DOI: https://doi.org/10.1016/0370-2693(83)90637-8.

[58] J. E. Kim and G. Carosi, 'Axions and the strong CP problem', *Rev. Mod. Phys.*, vol. 82, pp. 557–601, 1 2010. DOI: https://doi.org/10.1103/RevModPhys.82.557.

[59] A. Abeln, K. Altenmüller, S. Cuendis *et al.*, 'Conceptual design of BabyIAXO, the intermediate stage towards the International Axion Observatory', *Journal of High Energy Physics*, vol. 2021, May 2021. DOI: https://doi.org/10.1007/JHEP05(2021)137.

[60] C. O'Hare, *Cajohare/axionlimits: Axionlimits*, https://cajohare.github.io/AxionLimits/, version v1.0, Jul. 2020. DOI: https://doi.org/10.5281/zenodo.3932430.

[61] A. K. Yi, S. Ahn, C. Kutlu *et al.*, 'Axion Dark Matter Search around 4.55 μeV with Dine-Fischler-Srednicki-Zhitnitskii Sensitivity', *Phys. Rev. Lett.*, vol. 130, p. 071 002, 7 2023. DOI: https://doi.org/10.1103/PhysRevLett.130.071002. [Online]. Available: https://link.aps.org/doi/10.1103/PhysRevLett.130.071002.

[62] S. Arguedas Cuendis, *Dark matter axion search using novel RF resonant cavity geometries in the CAST experiment*, 2021. [Online]. Available: https://doi.org/10.25365/thesis.70391.

[63] Zioutas, K. et al., 'A Decommissioned LHC model magnet as an axion telescope', *Nucl. Instrum. Meth. A*, vol. 425, pp. 480–489, 1999. DOI: https://doi.org/10.1016/S0168-9002(98)01442-9.

[64] Aalseth, C. E. and others, 'A Solar axion search using a decommissioned LHC test magnet: Proposal to the SPSC', Aug. 1999.

[65] T. Dafni and J. Galán, 'Digging into Axion Physics with (Baby)IAXO', *Universe*, vol. 8, no. 1, 2022, ISSN: 2218-1997. DOI: https://doi.org/10.3390/universe8010037. [Online]. Available: https://www.mdpi.com/2218-1997/8/1/37.

[66] Y. Kim, D. Kim, J. Jeong, J. Kim, Y. C. Shin and Y. K. Semertzidis, 'Effective approximation of electromagnetism for axion haloscope searches', *Physics of the Dark Universe*, vol. 26, p. 100 362, 2019, ISSN: 2212-6864. DOI: https://doi.org/10.1016/j.dark.2019.100362.

[67] D. Kim, J. Jeong, S. Youn, Y. Kim and Y. K. Semertzidis, 'Revisiting the detection rate for axion haloscopes', *Journal of Cosmology and Astroparticle Physics*, vol. 2020, no. 03, pp. 066–066, DOI: https://doi.org/10.1088/1475-7516/2020/03/066.

[68] A. Díaz-Morcillo, J. M. García Barceló, A. J. Lozano Guerrero *et al.*, 'Design of New Resonant Haloscopes in the Search for the Dark Matter Axion: A Review of the First Steps in the RADES Collaboration', *Universe*, vol. 8, no. 1, 2022, ISSN: 2218-1997. DOI: https://doi.org/10.3390/universe8010005.

[69] D. Pozar, *Microwave Engineering*, Second. Wiley, 1998.

[70] C. A. Balanis, *Advanced Engineering Electromagnetics*. John Wiley & Sons, 1989.

[71] T. Braine, R. Cervantes, N. Crisosto *et al.*, 'Extended Search for the Invisible Axion with the Axion Dark Matter Experiment', *Phys. Rev. Lett.*, vol. 124, p. 101 303, 10 2020. DOI: https://doi.org/10.1103/PhysRevLett.124.101303.

[72] B. M. Brubaker, *First results from the HAYSTAC axion search*, 2018. [Online]. Available: https://arxiv.org/abs/1801.00835.

[73] J. M. García-Barceló, A. A. Melcón, A. Díaz-Morcillo, B. Gimeno, A. J. Lozano-Guerrero, J. Monzo-Cabrera, J. R. Navarro-Madrid and P. Navarro, 'Methods and restrictions to increase the volume of resonant rectangular-section haloscopes for detecting dark matter axions', Feb. 2023. arXiv: 2302.10569 [physics.ins-det].

[74] R. J. Cameron *et al.*, *Microwave filters for communication systems: fundamentals, design, and applications*. 2nd edition, Wiley, 2018.

[75] M. Goryachev, B. T. McAllister and M. E. Tobar, 'Axion detection with negatively coupled cavity arrays', *Physics Letters A*, vol. 382, no. 33, pp. 2199–2204, 2018, Special Issue in memory of Professor V.B. Braginsky, ISSN: 0375-9601. DOI: https://doi.org/10.1016/j.physleta.2017.09.016.

[76] J. Jeong, S. Youn, S. Bae, J. Kim, T. Seong, J. E. Kim and Y. K. Semertzidis, 'Search for Invisible Axion Dark Matter with a Multiple-Cell Haloscope', *Phys. Rev. Lett.*, vol. 125, p. 221 302, 22 2020. DOI: https://doi.org/10.1103/PhysRevLett.125.221302.

[77] J. M. García Barceló, A. Álvarez Melcón, S. Arguedas Cuendis, A. Díaz-Morcillo, B. Gimeno, A. Kanareykin, A. J. Lozano Guerrero, P. Navarro and W. Wuensch, *Applications of ferroelectric materials for dark matter axions detection haloscopes*, 2022. DOI: https://doi.org/10.48550/ARXIV.2204.11919.

[78] https://www.3ds.com/products-services/simulia/products/cst-studio-suite/.

[79] A. Álvarez Melcón, S. Arguedas-Cuendis, J. Baier *et al.*, 'First results of the CAST-RADES haloscope search for axions at 34.67 µeV', *J. High Energ. Phys.*, vol. 2021, p. 75, 2021. DOI: https://doi.org/10.1007/JHEP10(2021)075. arXiv: 2104.13798 [hep-ph].

[80] A. Álvarez Melcón, S. Arguedas-Cuendis, C. Cogollos *et al.*, 'Scalable haloscopes for axion dark matter detection in the 30 µeV range with RADES', *Journal of High Energy Physics*, vol. 084, pp. 1 –28, 2020. DOI: https://doi.org/10.1007/JHEP07(2020)084.

[81] P. Navarro, B. Gimeno, A. Álvarez Melcón *et al.*, 'Wide-band full-wave electromagnetic modal analysis of the coupling between dark-matter axions and photons in microwave resonators', *Physics of the Dark Universe*, vol. 36, p. 101 001, 2022, ISSN: 2212-6864. DOI: https://doi.org/10.1016/j.dark.2022.101001.

[82] D. Bak, 'Rapid prototyping or rapid production? 3D printing processes move industry towards the latter', *Assembly Automation*, vol. 23, no. 4, 2003, ISSN: 0144-5154. DOI: https://doi.org/10.1108/01445150310501190.

[83] A. P. Abenza, A. Á. Melcón, F. D. Q. Pereira, P. V. Castejón, J. H. Jiménez and A. R. Pérez, *Compact Evanescent Rectangular Waveguide Dual-Channel Bandpass Filters for Additive 3-D Manufacturing*, 2016. [Online]. Available: https://indico.esa.int/event/154/contributions/999/contribution.pdf.

[84] M. Guglielmi, 'Simple CAD procedure for microwave filters and multiplexers', *IEEE Transactions on Microwave Theory and Techniques*, vol. 42, no. 7, pp. 1347–1352, 1994. DOI: https://doi.org/10.1109/22.299728.

[85] F. Vanin, D. Schmitt and R. Levy, 'Dimensional synthesis for wide-band waveguide filters and diplexers', *IEEE Transactions on Microwave Theory and Techniques*, vol. 52, no. 11, pp. 2488–2495, 2004. DOI: https://doi.org/10.1109/TMTT.2004.837146.

[86] D. Swanson and G. Macchiarella, 'Microwave filter design by synthesis and optimization', *IEEE Microwave Magazine*, vol. 8, no. 2, pp. 55–69, 2007. DOI: https://doi.org/10.1109/MMW.2007.335529.

[87] E. Musonda and I. C. Hunter, 'Microwave Bandpass Filters Using Re-Entrant Resonators', *IEEE Transactions on Microwave Theory and Techniques*, vol. 63, no. 3, pp. 954–964, 2015. DOI: https://doi.org/10.1109/TMTT.2015.2389216.

[88] F. J. Perez Soler, M. Martinez Mendoza, F. D. Quesada Pereira, D. Canete Rebenaque, A. Alvarez Melcon and R. J. Cameron, 'Design of Bandpass Elliptic Filters Employing Inductive Windows and Dielectric Objects', *IEEE Transactions on Microwave Theory and Techniques*, vol. 55, no. 11, pp. 2393–2398, 2007. DOI: https://doi.org/10.1109/TMTT.2007.908673.

[89] F. D. Quesada Pereira, A. Romera Perez, P. Vera Castejón and A. Alvarez Melcon, 'Integral-Equation Formulation for the Analysis of Capacitive Waveguide Filters Containing Dielectric and Metallic Arbitrarily Shaped Objects and Novel Applications', *IEEE Transactions on Microwave Theory and Techniques*, vol. 63, no. 12, pp. 3862–3873, 2015. DOI: https://doi.org/10.1109/TMTT.2015.2490073.

[90] J. Golm, S. A. Cuendis, S. Calatroni *et al.*, 'Thin Film (High Temperature) Superconducting Radiofrequency Cavities for the Search of Axion Dark Matter', *IEEE Transactions on Applied Superconductivity*, vol. 32, no. 4, pp. 1–5, 2022. DOI: https://doi.org/10.1109/TASC.2022.3147741.

[91] A. V. Dixit, S. Chakram, K. He, A. Agrawal, R. K. Naik, D. I. Schuster and A. Chou, 'Searching for Dark Matter with a Superconducting Qubit', *Physical Review Letters*, vol. 126, no. 14, Apr. 2021, ISSN: 0031-9007. DOI: https://doi.org/10.1103/PhysRevLett.126.141302.

[92] A. V. Dixit, *Searching for Dark Matter with Superconducting Qubits*, Jan. 2021. [Online]. Available: https://doi.org/10.6082/uchicago.2942.

[93] C. Bartram, 'Venturing a glimpse of the dark matter halo with ADMX (Talk in Cambridge Workshop on Axion Physics)', 2021.

[94] G. Carosi and K. Van Bibber, 'Status of the ADMX and ADMX-HF experiments (Talk in 8th Patras Workshop on Axions, WIMPs, and WISPs)', 2013. [Online]. Available: https://www.osti.gov/biblio/1078551.

[95] M. Simanovskaia and K. van Bibber, 'Status of the ADMX-HF Experiment', in *11th Patras Workshop on Axions, WIMPs and WISPs*, 2015, pp. 157–163. DOI: https://doi.org/10.3204/DESY-PROC-2015-02/simanovskaia_maria.

[96] B. Aja *et al.*, 'The Canfranc Axion Detection Experiment (CADEx): Search for axions at 90 GHz with Kinetic Inductance Detectors', Jun. 2022. arXiv: 2206.02980 [hep-ex].

[97] J. Choi, S. Ahn, B. Ko, S. Lee and Y. Semertzidis, 'CAPP-8TB: Axion dark matter search experiment around 6.7 μev', *Nucl. Instrum. Methods. Phys. Res. B*, vol. 1013, p. 165 667, 2021. DOI: https://doi.org/10.1016/j.nima.2021.165667.

[98] G. Carosi, G. Rybka and K. van Bibber, Eds., *Proceedings, 2nd Workshop on Microwave Cavities and Detectors for Axion Research: Livermore, California, USA, January 10-13, 2017*, vol. 211, 2018, pp. 1–161. DOI: https://doi.org/10.1007/978-3-319-92726-8.

[99] W Ma, R Viznichenko, A Twin, A Varney, N Clarke, D Warren, R Wotherspoon and T Hollis, 'A New Member of High Field Large Bore Superconducting Research Magnets Family', *IOP Conference Series: Materials Science and Engineering*, vol. 502, no. 1, p. 012 104, 2019. DOI: https://doi.org/10.1088/1757-899X/502/1/012104. [Online]. Available: https://dx.doi.org/10.1088/1757-899X/502/1/012104.

[100] Y. Lee, B. Yang, H. Yoon, M. Ahn, H. Park, B. Min, D. Kim and J. Yoo, 'Searching for Invisible Axion Dark Matter with an 18 T Magnet Haloscope', *Phys. Rev. Lett.*, vol. 128, p. 241 805, 24 2022. DOI: https://doi.org/10.1103/PhysRevLett.128.241805.

[101] H. Yoon, M. Ahn, B. Yang, Y. Lee, D. Kim, H. Park, B. Min and J. Yoo, 'Axion Haloscope Using an 18 T High Temperature Superconducting Magnet', Jun. 2022. arXiv: 2206.12271 [hep-ex].

[102] N. Crescini, *Towards the development of the ferromagnetic axion haloscope*, 2019. [Online]. Available: http://hdl.handle.net/11577/3425918.

[103] B. R. Ko, H. Themann, W. Jang, J. Choi, D. Kim, M. J. Lee, J. Lee, E. Won and Y. K. Semertzidis, 'Electric and magnetic energy at axion haloscopes', *Phys. Rev. D*, vol. 94, p. 111 702, 11 2016. DOI: https://doi.org/10.1103/PhysRevD.94.111702. [Online]. Available: https://link.aps.org/doi/10.1103/PhysRevD.94.111702.

[104] J. Choi, H. Themann, M. J. Lee, B. R. Ko and Y. K. Semertzidis, 'First axion dark matter search with toroidal geometry', *Phys. Rev. D*, vol. 96, p. 061 102, 6 2017. DOI: https://doi.org/10.1103/PhysRevD.96.061102. [Online]. Available: https://link.aps.org/doi/10.1103/PhysRevD.96.061102.

[105] C. Ramella, M. Pirola and S. Corbellini, 'Accurate Characterization of High-*Q* Microwave Resonances for Metrology Applications', *IEEE Journal of Microwaves*, vol. 1, no. 2, pp. 610–624, 2021. DOI: https://doi.org/10.1109/JMW.2021.3063247.

[106] S. Arguedas-Cuendis, A. Álvarez Melcón, C. Cogollos *et al.*, 'The 3 Cavity Prototypes of RADES: An Axion Detector Using Microwave Filters at CAST', in *Microwave Cavities and Detectors for Axion Research. Springer Proceedings in Physics*, vol. 245, 2020. DOI: https://doi.org/10.1007/978-3-030-43761-9_6.

[107] M. Guglielmi, F. Montauti, L. Pellegrini and P. Arcioni, 'Implementing transmission zeros in inductive-window bandpass filters', *IEEE Transactions on Microwave Theory and Techniques*, vol. 43, no. 8, pp. 1911–1915, 1995. DOI: https://doi.org/10.1109/22.402281.

[108] A. D. M. *et al.*, *Microondas: líneas de transmisión, guías de onda y cavidades resonantes*. Universidad Politécnica de Cartagena, 2015.

[109] J. E. Aitken, 'Swept-frequency microwave Q-factor measurement', 1976. DOI: https://doi.org/10.1049/piee.1976.0184.

[110] K. Leong, J. Mazierska and J. Krupka, 'Measurements of unloaded Q-factor of transmission mode dielectric resonators', in *1997 IEEE MTT-S International Microwave Symposium Digest*, vol. 3, 1997, pp. 1639–1642. DOI: https://doi.org/10.1109/MWSYM.1997.596696.

[111] K. T. M. Leong, *Precise measurements of surface resistance of high temperature superconducting thin films using a novel method of Q-factor computations for sapphire dielectric resonators in the transmission mode*, 2000. [Online]. Available: https://researchonline.jcu.edu.au/41458/.

[112] Mecanizados JJ Celdran S.L.U. [Online]. Available: https://jjceldran.com/.

[113] Alta Precisión del Mecanizado S.L. [Online]. Available: http://www.apmsl.com/APM/home_IN.html.

[114] *https://uk.mathworks.com/products/matlab.html*.

[115] Alge S. Coop. [Online]. Available: https://www.algemecanizados.es/.

[116] Finitec Electrolisis S.L. [Online]. Available: http://finitec-electrolisis.com/.

[117] C. Boutan, M. Jones, B. H. LaRoque *et al.*, 'Piezoelectrically Tuned Multimode Cavity Search for Axion Dark Matter', *Phys. Rev. Lett.*, vol. 121, p. 261 302, 2018. DOI: https://doi.org/10.1103/PhysRevLett.121.261302.

[118] L. Zhong, S. Al Kenany, K. M. Backes *et al.*, 'Results from phase 1 of the HAYSTAC microwave cavity axion experiment', *Phys. Rev. D*, vol. 97, p. 092 001, 2018. DOI: https://doi.org/10.1103/PhysRevD.97.092001.

[119] D. Alesini, C. Braggio, G. Carugno *et al.*, 'Realization of a high quality factor resonator with hollow dielectric cylinders for axion searches', *Nucl. Instrum. Methods. Phys. Res. B*, vol. 985, p. 164 641, 2020. DOI: https://doi.org/10.1016/j.nima.2020.164641.

[120] L. Miceli, 'Haloscope axion searches with the cast dipole magnet: the CAST-CAPP/IBS detector', in *11th Patras Workshop on Axions, WIMPs and WISPs*, 2015, pp. 164–168. DOI: https://doi.org/10.3204/DESY-PROC-2015-02/miceli_lino.

[121] V. Bilik and J. Bezek, 'Noncontacting R26-Waveguide Sliding Short for Industrial Applications', in *2006 European Microwave Conference*, 2006, pp. 1032–1035. DOI: https://doi.org/10.1109/EUMC.2006.281100.

[122] S. Gevorgian, *Ferroelectrics in Microwave Devices, Circuits and Systems: Physics, Modeling, Fabrication and Measurements*, First. Springer-Verlag London, 2009. DOI: https://doi.org/10.1007/978-1-84882-507-9.

[123] A. Kanareykin, E. Nenasheva, S. Kazakov, A. Kozyrev, A. Tagantsev, V. Yakovlev and C. Jing, 'Ferroelectric Based Technologies for Accelerators', in *AIP Conference Proceedings*, vol. 1086, 2009, pp. 380–385. DOI: https://doi.org/10.1063/1.3080935.

[124] E. González-Rodríguez, H. Maune, Y. Zheng, M. Sazegar, L. Shen, I. A. Shah, D. Dahlhaus, K. Hofmann and R. Jakoby, 'Tunable ferroelectric impedance matching networks and their impact on digital modulation system performance', *AEU - International Journal of Electronics and Communications*, vol. 67, no. 12, pp. 1107–1117, 2013, ISSN: 1434-8411. DOI: https://doi.org/10.1016/j.aeue.2013.08.012. [Online]. Available: https://www.sciencedirect.com/science/article/pii/S1434841113002173.

[125] D. Bowring, T. Connolly, M. Kang, M. Ortega, S. Priya, C. Salemi, M. Silezin, A. Sonnenschein and A. Tollestrup, 'Dielectric tuning of cavities', in *3rd Workshop on Cavities and Detectors for Axion Research*, 2018. [Online]. Available: https://indico.fnal.gov/event/17488/contributions/43471.

[126] M. Ortega and D. Bowring, 'Next Generation Tunable Microwave Cavities for the search of Dark Matter Axions using Nonlinear Dielectric Films', in *SIST/GEM Final Presentations 2017*, 2017. [Online]. Available: https://indico.fnal.gov/event/14933.

[127] R. G. Geyer, B. Riddle, J. Krupka and L. A. Boatner, 'Microwave dielectric properties of single-crystal quantum paraelectrics $KTaO_3$ and $SrTiO_3$ at cryogenic temperatures', *Journal of Applied Physics*, vol. 97, p. 104 111, 2005. DOI: https://doi.org/10.1063/1.1905789.

[128] N. Crescini *et al.*, 'Operation of a ferromagnetic axion haloscope at $m_a = 58 \, \mu eV$', *Eur. Phys. J. C*, vol. 78, no. 9, p. 703, 2018, [Erratum: Eur.Phys.J.C 78, 813 (2018)]. DOI: https://doi.org/10.1140/epjc/s10052-018-6163-8. arXiv: 1806.00310 [hep-ex].

[129] J. R. Everts, G. G. G. King, N. J. Lambert, S. Kocsis, S. Rogge and J. J. Longdell, 'Ultrastrong coupling between a microwave resonator and antiferromagnetic resonances of rare-earth ion spins', *Phys. Rev. B*, vol. 101, p. 214 414, 21 2020. DOI: https://doi.org/10.1103/PhysRevB.101.214414. [Online]. Available: https://link.aps.org/doi/10.1103/PhysRevB.101.214414.

[130] M. M. Abraham, J. M. Baker, B. Bleaney, J. Z. Pfeffer and M. R. Wells, 'Antiferromagnetic resonance in $GdVO_4$', *Journal of Physics: Condensed Matter*, vol. 4, no. 24, p. 5443, 1992. DOI: 10.1088/0953-8984/4/24/014. [Online]. Available: https://dx.doi.org/10.1088/0953-8984/4/24/014.

[131] T. Tsutaoka, T. Kasagi and K. Hatakeyama, 'Permeability spectra of yttrium iron garnet and its granular composite materials under dc magnetic field', *Journal of Applied Physics*, vol. 110, no. 5, 053909-053909-12, pp. 053 909–053909–12, Sep. 2011. DOI: https://doi.org/10.1063/1.3626057.

[132] H. Peng, S. Asztalos, E. Daw *et al.*, 'Cryogenic cavity detector for a large-scale cold dark-matter axion search', *Nuclear Instruments and Methods in Physics Research Section A: Accelerators, Spectrometers, Detectors and Associated Equipment*, vol. 444, no. 3, pp. 569–583, 2000, ISSN: 0168-9002. DOI: https://doi.org/10.1016/S0168-9002(99)00971-7.

[133] https://www.euclidtechlabs.com/all-products.

[134] R. Bradley, J. Clarke, D. Kinion, L. J. Rosenberg, K. van Bibber, S. Matsuki, M. Mück and P. Sikivie, 'Microwave cavity searches for dark-matter axions', *Rev. Mod. Phys.*, vol. 75, pp. 777–817, 3 2003. DOI: https://doi.org/10.1103/RevModPhys.75.777. [Online]. Available: https://link.aps.org/doi/10.1103/RevModPhys.75.777.

[135] F. Souris, H. Christiani and J. Davis, 'Tuning a 3D Microwave Cavity via Superfluid Helium at MilliKelvin Temperatures', *Applied Physics Letters*, vol. 111, Jul. 2017. DOI: https://doi.org/10.1063/1.4997641.

[136] A. Romera Perez, A. Pons Abenza, F. D. Quesada Pereira, J. Hinojosa Jimenez, A. Alvarez Melcon and J. S. Gomez Diaz, 'A novel low-pass filter based on dielectric impedance inverters to enhance the multipactor breakdown threshold', *AEU - International Journal of Electronics and Communications*, vol. 143, p. 154 040, 2022, ISSN: 1434-8411. DOI: https://doi.org/10.1016/j.aeue.2021.154040. [Online]. Available: https://www.sciencedirect.com/science/article/pii/S1434841121004374.

[137] V. Skoromets, C. Kadlec, H. Němec, D. Fattakhova-Rohlfing and P. Kužel, 'Tunable dielectric properties of $KTaO_3$ single crystals in the terahertz range', *J. Phys. D: Appl. Phys.*, vol. 49, p. 065 306, 2016. DOI: https://doi.org/10.1088/0022-3727/49/6/065306.

[138] C. Ang, A. S. Bhalla and L. E. Cross, 'Dielectric behavior of paraelectric $KTaO_3$, $CaTiO_3$, and $(Ln_{1/2}Na_{1/2})TiO_3$ under a dc electric field', *Phys. Rev. B*, vol. 64, p. 184 104, 18 2001. DOI: https://doi.org/10.1103/PhysRevB.64.184104. [Online]. Available: https://link.aps.org/doi/10.1103/PhysRevB.64.184104.

[139] http://www.crystal-material.com/Substrate-Materials/KTaO3-substrate.html.

[140] D. Kajfez and P. Guillon, *Dielectric Resonators*. Artech House Inc., 1986.

[141] H. Aghayari, J. Nourinia and C. Ghobadi, 'Incorporated substrate integrated waveguide filters in propagative and evanescent mode: Realization and comparison', *AEU - International Journal of Electronics and Communications*, vol. 91, pp. 150–159, 2018, ISSN: 1434-8411. DOI: https://doi.org/10.1016/j.aeue.2018.05.008. [Online]. Available: https://www.sciencedirect.com/science/article/pii/S1434841118306083.

[142] J. W. Elam, A. U. Mane, J. A. Libera *et al.*, 'Synthesis, Characterization, and Application of Tunable Resistance Coatings Prepared By Atomic Layer Deposition', *ECS Meeting Abstracts*, vol. MA2013-02, no. 24, p. 1858, 2013. DOI: https://doi.org/10.1149/MA2013-02/24/1858. [Online]. Available: https://dx.doi.org/10.1149/MA2013-02/24/1858.

[143] C. M. Adair *et al.*, 'Search for Dark Matter Axions with CAST-CAPP', *Nature Commun.*, vol. 13, no. 1, p. 6180, 2022. DOI: https://doi.org/10.1038/s41467-022-33913-6. arXiv: 2211.02902 [hep-ex].

[144] H.-x. Xu, G.-m. Wang and K. Lu, 'Microstrip Rat-Race Couplers', *IEEE Microwave Magazine*, vol. 12, no. 4, pp. 117–129, 2011. DOI: https://doi.org/10.1109/MMM.2011.940600.

[145] https://www.keysight.com/gb/en/products/software/pathwave-design-software/pathwave-advanced-design-system/pathwave-ads-software-bundles.html.

[146] E. Wilkinson, 'An N-Way Hybrid Power Divider', *IRE Transactions on Microwave Theory and Techniques*, vol. 8, no. 1, pp. 116–118, 1960. DOI: https://doi.org/10.1109/TMTT.1960.1124668.

[147] https://www.minicircuits.com.

[148] C. Lee and O. Reimann, 'T-RAX: Transversely Resonant Axion eXperiment', *Journal of Cosmology and Astroparticle Physics*, vol. 2022, no. 09, p. 007, 2022. DOI: https://doi.org/10.1088/1475-7516/2022/09/007. [Online]. Available: https://dx.doi.org/10.1088/1475-7516/2022/09/007.

[149] B. Schumacher, 'Quantum coding', *Phys. Rev. A*, vol. 51, pp. 2738–2747, 4 1995. DOI: https://doi.org/10.1103/PhysRevA.51.2738. [Online]. Available: https://link.aps.org/doi/10.1103/PhysRevA.51.2738.

[150] H. Paik, D. I. Schuster, L. S. Bishop *et al.*, 'Observation of High Coherence in Josephson Junction Qubits Measured in a Three-Dimensional Circuit QED Architecture', *Phys. Rev. Lett.*, vol. 107, p. 240 501, 24 2011. DOI: https://doi.org/10.1103/PhysRevLett.107.240501. [Online]. Available: https://link.aps.org/doi/10.1103/PhysRevLett.107.240501.

[151] D. Schuster, A Houck, J Schreier *et al.*, 'Resolving photon number states in a superconducting circuit', *Nature*, vol. 445, pp. 515–8, Mar. 2007. DOI: https://doi.org/10.1038/nature05461.

[152] A. Blais, R.-S. Huang, A. Wallraff, S. M. Girvin and R. J. Schoelkopf, 'Cavity quantum electrodynamics for superconducting electrical circuits: An architecture for quantum computation', *Phys. Rev. A*, vol. 69, p. 062 320, 6 2004. DOI: https://doi.org/10.1103/PhysRevA.69.062320. [Online]. Available: https://link.aps.org/doi/10.1103/PhysRevA.69.062320.

[153] A. Romanov, P. Krkotić, G. Telles, J. O'Callaghan, M. Pont, F. Perez, X. Granados, S. Calatroni, T. Puig and J. Gutierrez, 'High frequency response of thick REBCO coated conductors in the framework of the FCC study', *Sci. Rep.*, vol. 10, no. 1, p. 12 325, 2020. DOI: https://doi.org/10.1038/s41598-020-69004-z.

[154] F. Savary *et al.*, 'Design, Assembly, and Test of the CERN 2-m Long 11 T Dipole in Single Coil Configuration', *IEEE Trans. Appl. Supercond.*, vol. 25, no. 3, p. 4 004 105, 2015. DOI: https://doi.org/10.1109/TASC.2015.2395381.

[155] J. M. García Barceló, *Diseño de filtros de microondas utilizando técnicas de fabricación 3D para aplicaciones espaciales*, Jun. 2018. [Online]. Available: http://hdl.handle.net/10317/7073.

[156] V. E. Boria and B. Gimeno, 'Waveguide filters for satellites', *IEEE Microwave Magazine*, vol. 8, no. 5, pp. 60–70, 2007. DOI: https://doi.org/10.1109/MMM.2007.903649.

[157] X. Shang, M. Lancaster and Y.-L. Dong, 'W-band waveguide filter based on large TM120 resonators to ease CNC milling', *Electronics Letters*, vol. 53, no. 7, pp. 488–490, 2017. DOI: https://doi.org/10.1049/el.2016.4131. eprint: https://ietresearch.onlinelibrary.wiley.com/doi/pdf/10.1049/el.2016.4131. [Online]. Available: https://ietresearch.onlinelibrary.wiley.com/doi/abs/10.1049/el.2016.4131.

[158] M. D'Auria, W. J. Otter, J. Hazell, B. T. W. Gillatt, C. Long-Collins, N. M. Ridler and S. Lucyszyn, '3-D Printed Metal-Pipe Rectangular Waveguides', *IEEE Transactions on Components, Packaging and Manufacturing Technology*, vol. 5, no. 9, pp. 1339–1349, 2015. DOI: https://doi.org/10.1109/TCPMT.2015.2462130.

[159] O. A. Peverini, M. Lumia, F. Calignano, G. Addamo, M. Lorusso, E. P. Ambrosio, D. Manfredi and G. Virone, 'Selective Laser Melting Manufacturing of Microwave Waveguide Devices', *Proceedings of the IEEE*, vol. 105, no. 4, pp. 620–631, 2017. DOI: https://doi.org/10.1109/JPROC.2016.2620148.

[160] V. Kyovtorov, I. Georgiev, S. Margenov, D. Stoychev, F. Oliveri and D. Tarchi, 'New antenna design approach - 3D polymer printing and metallization. experimental test at 14–18GHz', *AEU - International Journal of Electronics and Communications*, vol. 73, pp. 119–128, 2017, ISSN: 1434-8411. DOI: https://doi.org/10.1016/j.aeue.2016.12.017. [Online]. Available: https://www.sciencedirect.com/science/article/pii/S1434841116315643.

[161] A. Genc, I. B. Basyigit, B. Colak and S. Helhel, 'Investigation of the characteristics of low-cost and lightweight horn array antennas with novel monolithic waveguide feeding networks', *AEU - International Journal of Electronics and Communications*, vol. 89, pp. 15–23, 2018, ISSN: 1434-8411. DOI: https://doi.org/10.1016/j.aeue.2018.03.024. [Online]. Available: https://www.sciencedirect.com/science/article/pii/S1434841117330273.

[162] F. Calignano, D. Manfredi, E. P. Ambrosio, S. Biamino, M. Lombardi, E. Atzeni, A. Salmi, P. Minetola, L. Iuliano and P. Fino, 'Overview on Additive Manufacturing Technologies', *Proceedings of the IEEE*, vol. 105, no. 4, pp. 593–612, 2017. DOI: https://doi.org/10.1109/JPROC.2016.2625098.

[163] J. R. Montejo-Garai, I. O. Saracho-Pantoja, C. A. Leal-Sevillano, J. A. Ruiz-Cruz and J. M. Rebollar, 'Design of microwave waveguide devices for space and ground application implemented by additive manufacturing', in *2015 International Conference on Electromagnetics in Advanced Applications (ICEAA)*, 2015, pp. 325–328. DOI: https://doi.org/10.1109/ICEAA.2015.7297128.

[164] S. Khan, N. Vahabisani and M. Daneshmand, 'A Fully 3-D Printed Waveguide and Its Application as Microfluidically Controlled Waveguide Switch', *IEEE Transactions on Components, Packaging and Manufacturing Technology*, vol. 7, no. 1, pp. 70–80, 2017. DOI: https://doi.org/10.1109/TCPMT.2016.2631545.

[165] K. Y. Chan, R. Ramer and R. Sorrentino, 'Low-Cost Ku-Band Waveguide Devices Using 3-D Printing and Liquid Metal Filling', *IEEE Transactions on Microwave Theory and Techniques*, vol. 66, no. 9, pp. 3993–4001, 2018. DOI: https://doi.org/10.1109/TMTT.2018.2851573.

[166] J. A. Lorente, M. M. Mendoza, A. Z. Petersson, L. Pambaguian, A. A. Melcon and C. Ernst, 'Single part microwave filters made from selective laser melting', in *2009 European Microwave Conference (EuMC)*, 2009, pp. 1421–1424. DOI: https://doi.org/10.23919/EUMC.2009.5296127.

[167] C. Guo, X. Shang, J. Li, F. Zhang, M. J. Lancaster and J. Xu, 'A Lightweight 3-D Printed X-Band Bandpass Filter Based on Spherical Dual-Mode Resonators', *IEEE Microwave and Wireless Components Letters*, vol. 26, no. 8, pp. 568–570, 2016. DOI: https://doi.org/10.1109/LMWC.2016.2587838.

[168] C. Guo, X. Shang, M. J. Lancaster and J. Xu, 'A 3-D Printed Lightweight X-Band Waveguide Filter Based on Spherical Resonators', *IEEE Microwave and Wireless Components Letters*, vol. 25, no. 7, pp. 442–444, 2015. DOI: https://doi.org/10.1109/LMWC.2015.2427653.

[169] P. Booth and E. V. Lluch, 'Enhancing the Performance of Waveguide Filters Using Additive Manufacturing', *Proceedings of the IEEE*, vol. 105, no. 4, pp. 613–619, 2017. DOI: https://doi.org/10.1109/JPROC.2016.2616494.

[170] K. Salonitis, G Tsoukantas, P. Stavropoulos and A Stournaras, *Virtual Modelling and Rapid Manufacturing - Advanced Research in Virtual and Rapid Prototyping*. CRC Press, 2003, ch. A critical review of stereolithography process modeling.

[171] N.-H. Tran, V.-N. Nguyen, A.-V. Ngo and V. Nguyen, 'Study on the Effect of Fused Deposition Modeling (FDM) Process Parameters on the Printed Part Quality', *Int. Journal of Engineering Research and Application*, vol. 7, no. 12, pp. 71–77, 2017.

[172] C. Carceller, F. Gentili, D. Reichartzeder, W. Bösch and M. Schwentenwein, 'Practical considerations in the design of monoblock TM dielectric resonator filters with additive manufacturing', in *2017 International Conference on Electromagnetics in Advanced Applications (ICEAA)*, 2017, pp. 364–367. DOI: https://doi.org/10.1109/ICEAA.2017.8065251.

[173] Y. Marchives, N. Delhote, S. Verdeyme and P. M. Iglesias, 'Wide-band dielectric filter at C-band manufactured by stereolithography', in *2014 44th European Microwave Conference*, 2014, pp. 187–190. DOI: https://doi.org/10.1109/EuMC.2014.6986401.

[174] A. Perigaud, O. Tantot, N. Delhote, S. Verdeyme, S. Bila and D. Baillargeat, 'Bandpass Filter Based on Skeleton-like Monobloc Dielectric Pucks Made by Additive Manufacturing', in *2018 48th European Microwave Conference (EuMC)*, 2018, pp. 296–299. DOI: https://doi.org/10.23919/EuMC.2018.8541710.

[175] H. Aghayari, J. Nourinia, C. Ghobadi and B. Mohammadi, 'Realization of dielectric loaded waveguide filter with substrate integrated waveguide technique based on incorporation of two substrates with different relative permittivity', *AEU - International Journal of Electronics and Communications*, vol. 86, pp. 17–24, 2018, ISSN: 1434-8411. DOI: https://doi.org/10.1016/j.aeue.2018.01.008. [Online]. Available: https://www.sciencedirect.com/science/article/pii/S1434841117325967.

[176] https://www.stratasys.com/en/materials/materials-catalog/polyjet-materials/abs-plus/.

[177] A. Pons-Abenza, A. Alvarez-Melcon, F. D. Quesada-Pereira and L. Arche-Andradas, 'Frequency Correction Design Technique for Additive Manufactured Cavity Filters', in *2018 48th European Microwave Conference (EuMC)*, 2018, pp. 288–291. DOI: https://doi.org/10.23919/EuMC.2018.8541362.

[178] G. L. Matthaei *et al.*, *Microwave Filters, Impedance-Matching Networks, and Coupling Structures*. Artech House, 1980.

[179] *https://www.ansys.com/products/electronics/ansys-hfss*.

[180] *https://support.stratasys.com/en/printers/fdm/dimension-family*.

[181] M. Martinez-Mendoza, C. Ernst, J. A. Lorente, A. Alvarez-Melcon and F. Seyfert, 'On the Relation Between Stored Energy and Fabrication Tolerances in Microwave Filters', *IEEE Transactions on Microwave Theory and Techniques*, vol. 60, no. 7, pp. 2131–2141, 2012. DOI: https://doi.org/10.1109/TMTT.2012.2195023.

[182] A. Romera Perez, A. Pons Abenza, D. Martinez Martinez, A. Alvarez Melcon and F. D. Quesada Pereira, 'Filter design for folded canonical topologies based on equivalent circuit segmentation', *AEU - International Journal of Electronics and Communications*, vol. 109, pp. 157–165, 2019, ISSN: 1434-8411. DOI: https://doi.org/10.1016/j.aeue.2019.07.010. [Online]. Available: https://www.sciencedirect.com/science/article/pii/S1434841119313263.

[183] I. Bouchachi, J. Mateu and R. Mohamed Lahdi, 'Waveguide Filter Modeling and Simulation using Mode-matching, Fullwave Network Analysis and Swarm Optimization', *Applied Computational Electromagnetics Society Journal (ACES)*, vol. 32, no. 02, 169–177, Feb. 2017. [Online]. Available: https://journals.riverpublishers.com/index.php/ACES/article/view/9747.

[184] M. Latif, G. Macchiarella and F. Mukhtar, 'A Novel Coupling Structure for Inline Realization of Cross-Coupled Rectangular Waveguide Filters', *IEEE Access*, vol. 8, pp. 107 527–107 538, 2020. DOI: https://doi.org/10.1109/ACCESS.2020.3000847.

INSTITUTIONAL ACKNOWLEDGMENTS